Syracuse University

SURFACE

December 2020

CHARACTERIZATION OF CRYSTALLINE PIGMENTS WITH LOW-FREQUENCY VIBRATIONAL SPECTROSCOPY AND SOLID-STATE DENSITY FUNCTIONAL THEORY

Elyse M. Kleist
Syracuse University

Follow this and additional works at: https://surface.syr.edu/etd

Part of the Physical Sciences and Mathematics Commons

Abstract

Although historical pigments are seldom found in the modern artist's palette, their characterization is a critical aspect of designing effective conservation and restoration protocols, establishing provenance, and detecting forgeries. Ideal characterization methods are nondestructive, noninvasive, and able to distinguish between pure and mixed pigment samples. Spectroscopic techniques are commonly used to identify pigment composition because of their non-ionizing nature, rapid acquisition times, and safety. Unfortunately, the majority of these methods have difficulty distinguishing between pigments with similar chemical and physical properties. Recent advancements in instrument technology have increased the broader availability of terahertz time-domain spectroscopy (THz-TDS) and low-frequency Raman spectroscopy (LFRS). In this work, the capabilities of THz-TDS and LFRS for identification and characterization of historic and modern pigments were evaluated. These experimental studies were supported with solid-state density functional theory (ss-DFT) simulations of the pigment structures and vibrations to gain insight into the molecular and intermolecular origins of the observed spectral features. These results demonstrate the powerful combination of low-frequency (≤ 200 cm^{-1}) vibrational spectroscopic methods and computational techniques for the identification and characterization of pigments and establish the compelling abilities of THz-TDS and LFRS as new tools for characterization of pigment components in artworks and artifacts.

CHARACTERIZATION OF CRYSTALLINE PIGMENTS
WITH LOW-FREQUENCY VIBRATIONAL SPECTROSCOPY
AND SOLID-STATE DENSITY FUNCTIONAL THEORY

by

Elyse M. Kleist

B.S. Indiana University of Pennsylvania, 2013
M.Phil. Syracuse University, 2015

Dissertation
Submitted in partial fulfillment of the requirements for the degree of
Doctor of Philosophy in Chemistry.

Syracuse University
December 2020

Acknowledgements

Table of Contents

List of Tables and Figures

List of Abbreviations

ABS	Acrylonitrile butadiene styrene
BZ	Brillouin zone
CA	Cellulose acetate
CPHF	Coupled Perturbed Hartree-Fock
DFT	Density functional theory
DPP	Diketopyrrolopyrrole
FTIR	Fourier-transform infrared spectroscopy
FWHM	Full width at half maximum
GGA	Generalized gradient approximation
HDPE	High-density polyethylene
HF	Hartree-Fock
IR	Infrared
LDA	Local density approximation
LFRS	Low-frequency Raman spectroscopy
LO/TO	Longitudinal optical/transverse optical
LOD	Limit of detection
LOQ	Limit of quantitation
MS	Mass spectrometry
NIR	Near-infrared spectroscopy
PBC	Periodic boundary conditions
PC	Photoconductive antennas
PES	Potential energy surface
PMMA	Poly(methyl methacrylate)
PS	Polystyrene
PTFE	Polytetrafluoroethylene
PVC	Polyvinyl chloride
PXRD	Powder X-ray diffraction
SAN	Styrene acrylonitrile resin
SCF	Self-consistent field method
SS-DFT	Solid-state density functional theory
THz	Terahertz
THz-TDS	Terahertz time-domain spectroscopy
XFS	X-ray fluorescence spectroscopy
XRF	X-ray fluorescence

Chapter 1. Introduction

1.1 Motivation

In 2011, one of the most elaborate forgery rings in European history was discovered through the examination of pigments in a painting. Chemical analysis revealed that the painting, which was dated from the late 19th century, contained titanium white, a pigment not used by artists until the mid-20th century. The discovery of this counterfeit is one example that demonstrates the need for reliable detection and identification of the component materials of artifacts. In addition to authentication purposes, pigment characterization plays a key role in the determination of provenance, design of conservation strategies, and monitoring physio-chemical and biological degradation in paintings and artifacts. [1-9] Due to the delicate and irreplaceable nature of many artifacts, ideal characterization methods will nondestructively and noninvasively determine the pigment composition and condition of an artifact.[10-17] The motivation for this work is predicated on this need for additional analysis techniques capable of overcoming complications from the diversity and availability of pure pigments and pigment mixtures.

Here, a multi-disciplinary approach of THz-TDS, LFRS, and ss-DFT is used to characterize pure pigments **(Chapter 4** and **Chapter 6)** and pigment mixtures **(Chapter 5)**. These low-frequency (≤ 200 cm^{-1}) vibrational spectroscopies reveal the intermolecular motions unique to a crystalline pigment, making them ideal for differentiating chemically related **(Chapter 4)** and visually similar pigments (**Chapters 5, 6)**. In addition to the pigment research in **Chapters 4-6**, the application of Raman spectroscopy in the identification of polymer components found in plastic artifacts has been demonstrated **(Chapter 7)**. The subjects for the polymer study were actual museum artifacts and part of a collection in the Syracuse University Libraries' Special Collections Research Center.

1.2 Introduction

Common analytical techniques currently in use for *in situ* pigment identification include: powder X-ray diffraction (PXRD), X-ray fluorescence spectroscopy (XFS),[18] mass spectrometry (MS),[19] Fourier-transform infrared spectroscopy (FTIR),[20-24] and Raman spectroscopy.[19, 24-29] However, PXRD data collection is difficult *in situ*[30] and has been shown to produce incorrect crystal structures in pigments that are chemically similar.[31] XFS studies are unable to detect light elements and have difficulty differentiating between chemically similar pigments.[32-35] MS is unfavorable because analysis requires destruction of a small sample from the artifact. FTIR has previously been used for pigment identification; however, several classes of inorganic pigments are inactive in the mid-infrared (mid-IR, 4000 – 400 cm^{-1}) region (e.g. oxides or sulfides).[36 20, 24] In these cases, complementary Raman spectroscopy is used to overcome such limitations. Nevertheless, Raman analysis requires vigilance to avoid damage from higher photon energies and spectra can be affected by fluorescence signals from organic components.[37-38] The near-infrared (near-IR, 12,800 – 4000 cm^{-1}) and far-infrared (far-IR) have also been used for pigment identification. Near-IR studies are unsatisfactory because only functional groups containing NH, CH, OH, CO, and CC bonds produce significant vibrational bands in this range, limiting applicability to many historic inorganic pigments.[20, 39]

THz spectroscopy, which refers to the far-IR, has been used to overcome the limitations of near-IR, mid-IR, and Raman spectroscopies in pigment identification, especially for inorganic compounds derived from minerals.[40,41] THz radiation excites lattice vibrations that are unique to specific crystalline structures. These vibrations can be studied with vibrational techniques that access this low-frequency region. Recent improvements in technology[42-44] and instrumentation[45] have increased the accessibility of two low-frequency vibrational spectroscopic techniques:

terahertz time-domain spectroscopy (THz-TDS) and low-frequency Raman spectroscopy (LFRS).

1.3 Low-Frequency Vibrational Spectroscopy

THz-TDS and LFRS are appealing methods for pigment identification because of their specificity, short acquisition times, and non-destructive nature.[12, 46-47] These two low-frequency ($\leq$ 200 cm^{-1}) vibrational techniques have been used to probe the intermolecular interactions in various solid materials including explosives,[48-49] pharmaceuticals,[50-51] pigments,[48-49, 52-53] and more.[38, 44, 54-64] As opposed to the intramolecular vibrations in the mid-IR, low-frequency vibrations correspond to weak intermolecular motions of the species in the crystalline lattice.[65] Intermolecular motions in crystalline materials are dependent on the packing of the unit cell and component identities. As a result, these spectral features form 'fingerprints' that are unique to each sample. These spectral 'fingerprints' make it possible to use THz-TDS and LFRS for the identification and characterization of materials that are otherwise indistinguishable.[56, 66] The complex origins of the spectral features in THz-TDS and LFRS spectra are not easily identifiable, therefore applications of these techniques in identification studies have been largely predicated on the existence of high-quality spectra for pure pigments. Experimental THz-TDS and Raman spectral databases of artists' materials have been constructed,[53, 67-70] but they primarily focus on pure materials, when historically, pigment mixtures were commonly used to achieve desired hues in artifacts.[6]

Raman, mid-IR, and first-derivative reflectance visible spectroscopies have been demonstrated to be useful in the analysis of various pigment mixtures and binders[21-23, 71] but the overlapping spectral signals from mixtures often present challenges in analysis as compared to pure samples. THz-TDS and LFRS are likely useful in pigment mixture studies given the reported successes of these techniques in pharmaceutical mixtures.[57, 72-75] In order to evaluate the analytical

capability of THz-TDs or LFRS in pigment mixture studies, the sensitivity of each instrument to specific pigments must be determined. This sensitivity is described as the limits of detection (LOD) and quantitation (LOQ). The pigment composition of binary mixtures can then be estimated using calibration curves specific to the instrument and standard samples of known mixture proportions. These measurements depend on the signal-to-noise ratio of the data and the degree of spectral separation between individual component peaks. The LOD and LOQ can be dramatically different between THz-TDS and LFRS investigations of the same sample because the spectroscopic selection rules of each technique may yield a unique pattern of peak positions and intensities. The chemical-specificity and successful application of THz-TDS and LFRS in pigment mixture studies could prove useful in elucidating the contrast mechanisms underlying the 2D and 3D images of artworks that have been obtained with THz imaging systems.[12, 76-82] Additionally, solid-state density functional theory (ss-DFT) simulations may be beneficial in understanding spectra of mixed pigments.[83]

1.4 Solid-State Density Functional Theory

Although THz-TDS and LFRS have been demonstrated to be ideal techniques for pigment identification, interpretation of the vibrational origins of the observed spectral features is difficult if not impossible with experimental data alone. This complication can be overcome with ss-DFT simulations of crystalline pigments. These simulations utilize periodic boundary conditions[84] to include the effects of the solid-state environment on the crystalline pigment structure and dynamics. Simulations with ss-DFT also provide insight into the intermolecular modes that dominate the low-frequency spectral region and enable unambiguous spectral assignments.[39, 85] Simulating THz-TDS and LFRS spectra with ss-DFT highlights the connection between chemical identity, crystalline structure, and the intermolecular forces that collectively

contribute to the characteristic low-frequency vibrational spectra of these materials. This approach has been successfully demonstrated on both organic[86] and inorganic pigments.[87-88]

1.5 Summary of Chapters

The first part of this work (**Chapters 2** and **3**) covers the theory behind low-frequency vibrational spectroscopy and solid-state density functional theory. **Chapter 2** presents an overview of the quantum mechanical origins of vibrations and relationship to solid-state vibrations. A simple model, carbon dioxide, is used to illustrate the differences in spectral features when moving from molecular vibrational spectroscopy to solid-state vibrational spectroscopy. This model compound is also used to highlight the selection rules of infrared and Raman spectroscopies. This chapter also includes descriptions of the THz-TDS and LFRS commercial instruments used in this work. **Chapter 3** covers DFT and ss-DFT, beginning with the quantum mechanical foundations of DFT that led to the development of density functionals and basis sets. The extension of this theory into the solid-state includes periodic boundary conditions, reciprocal space, and Bloch's theorem. An overview of the ss-DFT software, CRYSTAL[89], and the calculations most used in this work, are described.

The second part of this work utilizes the experimental methods described in **Chapter 2** to demonstrate the capabilities of THz-TDS and LFRS in pure pigment and mixed pigment samples. In addition to the low-frequency vibrational characterization, the ss-DFT methods described in **Chapter 3** were used to assign the low-frequency spectral features. **Chapters 4** and **6** utilize THz-TDS and ss-DFT to characterize pigments that are visually and chemically similar. **Chapter 4** presents the experimental THz-TDS spectra and ss-DFT simulations of three blue/green copper-containing pigments: azurite, malachite, and verdigris. **Chapter 6** follows the same structure but with two modern red pigments, PR254 and PR3. **Chapter 5** focuses on two

pigments commonly used by artists' in pure and mixed forms, minium and vermilion. These two inorganic crystalline pigments were used to investigate the capabilities of THz-TDS and LFRS in examining mixtures. Data from pure samples and binary mixtures of minium and vermilion enabled LOD and LOQ values for the pigments to be established for both THz-TDS and LFRS measurements. The ss-DFT spectral simulations enabled complete assignments of the observed (sub-200 cm^{-1}) spectral features.

In **Chapter 7**, the results of a collaboration with the Plastics Artifacts Collection in the Syracuse University Libraries' Special Collections Research Center are presented. This study aimed to develop Raman spectroscopy as a practical nondestructive method for unambiguous characterization of the composition of plastic artifacts in the collection. The identification of the polymer components of these artifacts will be used to develop strategies for conservation and storage of these pieces.

1.6 References

1.   Chaplin, T. D.; Clark, R. J. H.; Beech, D. R., Comparison of Genuine (1851–1852 Ad) and Forged or Reproduction Hawaiian Missionary Stamps Using Raman Microscopy. *Journal of Raman Spectroscopy* **2002**, *33*, 424-428.

2.   Berrie, B. H.; Leona, M.; McLaughlin, R., Unusual Pigments Found in a Painting by Giotto (C. 1266-1337) Reveal Diversity of Materials Used by Medieval Artists. *Heritage Science* **2016**, *4*, 1.

3.   Doménech-Carbó, M. T.; Osete-Cortina, L., Another Beauty of Analytical Chemistry: Chemical Analysis of Inorganic Pigments of Art and Archaeological Objects. *ChemTexts* **2016**, *2*, 14.

4.   Feller, R. L.; Roy, A., *Artists' Pigments: A Handbook of Their History and Characteristics*; National Gallery of Art: Washington, 1986.

5.   Walter, P.; de Viguerie, L., Materials Science Challenges in Paintings. *Nature Materials* **2018**, *17*, 106.

6.   Eastaugh, N., *Pigment Compendium: A Dictionary and Optical Microscopy of Historical Pigments*; Butterworth-Heinemann: Oxford, 2008.

7.   Gage, J., *Color in Art*; Thames & Hudson: London, 2006.

8.   Carvalho, I.; Casanova, C.; Araújo, R.; Lemos, A., Colour Identification, Degradation Processes and Findings in a Fifteenth-Century Book of Hours: The Case Study of *Cofre N.º 31* from Mafra National Palace. *Heritage Science* **2018**, *6*, 9.

9.   Castro, K.; Vandenabeele, P.; Rodríguez-Laso, M. D.; Moens, L.; Madariaga, J. M., Micro-Raman Analysis of Coloured Lithographs. *Analytical and Bioanalytical Chemistry* **2004**, *379*, 674-683.

10.   Derrick, M. R.; Stulik, D.; Landry, J. M., *Infrared Spectroscopy in Conservation Science*; Getty Conservation Institute, 2000.

11.   Bardon, T.; May, R. K.; Taday, P. F.; Strlic, M., Systematic Study of Terahertz Time-Domain Spectra of Historically Informed Black Inks. *Analyst* **2013**, *138*, 4859-4869.

12.   Jackson, J. B.; Bowen, J.; Walker, G.; Labaune, J.; Mourou, G.; Menu, M.; Fukunaga, K., A Survey of Terahertz Applications in Cultural Heritage Conservation Science. *IEEE Transactions on Terahertz Science and Technology* **2011**, *1*, 220-231.

13.   Fukunaga, K.; Ogawa, Y.; Hayashi, S. i.; Hosako, I., Application of Terahertz Spectroscopy for Character Recognition in a Medieval Manuscript. *IEICE Electronics Express* **2008**, *5*, 223-228.

14.   Cosentino, A., Terahertz and Cultural Heritage Science: Examination of Art and Archaeology. *Technologies* **2016**, *4*, 6.

15.   Alcantara-Garcia, J.; Ploeger, R., Teaching Polymer Chemistry through Cultural Heritage. *Journal of Chemical Education* **2018**, *95*, 1118-1124.

16.   Shashoua, Y., *Inhibiting the Deterioration of Plasticized Poly (Vinyl Chloride)-a Museum Perspective*; Denmark's Technical University, 2001.

17.   Vandenabeele, P.; Rousaki, A.; Costa, M.; Moens, L.; Edwards, H. G. M., Chapter 5 Pigments and Colourants. In *Raman Spectroscopy in Archaeology and Art History: Volume 2*, The Royal Society of Chemistry: London, 2019; Vol. 2, pp 61-67.

18.   Fikri, I.; El Amraoui, M.; Haddad, M.; Ettahiri, A. S.; Bellot-Gurlet, L.; Falguères, C.; Lebon, M.; Nespoulet, R.; Ait Lyazidi, S.; Bejjit, L., Xrf and Uv-Vis-Nir Analyses of Medieval Wall Pintings of Al-Qarawiyyin Mosque (Morocco). *IOP Conference Series: Materials Science and Engineering* **2018**, *353*, 012020.

19.   Dowsett, M.; Adriaens, A., The Role of Sims in Cultural Heritage Studies. *Nuclear Instruments and Methods in Physics Research Section B* **2004**, *226*, 38-52.

20.   Vagnini, M.; Miliani, C.; Cartechini, L.; Rocchi, P.; Brunetti, B. G.; Sgamellotti, A., Ft-Nir Spectroscopy for Non-Invasive Identification of Natural Polymers and Resins in Easel Paintings. *Analytical and Bioanalytical Chemistry* **2009**, *395*, 2107-2118.

21.   Wiesinger, R.; Pagnin, L.; Anghelone, M.; Moretto, L. M.; Orsega, E. F.; Schreiner, M., Pigment and Binder Concentrations in Modern Paint Samples Determined by Ir and Raman Spectroscopy. *Angewandte Chemie International Edition* **2018**, *57*, 7401-7407.

22.   Pottier, F.; Gerardin, M.; Michelin, A.; Hébert, M.; Andraud, C., Simulating the Composition and Structuration of Coloring Layers in Historical Painting from Non-Invasive Spectral Reflectance Measurements. *Comptes Rendus Physique* **2018**, *19*, 599-611.

23.   González-Vidal, J. J.; Perez-Pueyo, R.; Soneira, M. J.; Ruiz-Moreno, S., Automatic Identification System of Raman Spectra in Binary Mixtures of Pigments. *Journal of Raman Spectroscopy* **2012**, *43*, 1707-1712.

24.   Bruni, S.; Cariati, F.; Casadio, F.; Toniolo, L., Identification of Pigments on a Xv-Century Illuminated Parchment by Raman and Ftir Microspectroscopies. *Spectrochimica Acta Part A* **1999**, *55*, 1371-1377.

25.   Buzzini, P.; Suzuki, E., Forensic Applications of Raman Spectroscopy for the *in Situ* Analyses of Pigments and Dyes in Ink and Paint Evidence. *Journal of Raman Spectroscopy* **2016**, *47*, 16-27.

26.   Shabunya-Klyachkovskaya, E. V.; Kulakovich, O. S.; Gaponenko, S. V., Surface Enhanced Raman Scattering of Inorganic Microcrystalline Art Pigments for Systematic Cultural Heritage Studies. *Spectrochimica Acta Part A* **2019**, *222*, 117235.

27.   Smith, G. D.; Clark, R. J. H., Raman Microscopy in Art History and Conservation Science. *Studies in Conservation* **2001**, *46*, 92-106.

28.   Vandenabeele, P.; Edwards, H. G. M.; Moens, L., A Decade of Raman Spectroscopy in Art and Archaeology. *Chemical Reviews* **2007**, *107*, 675-686.

29.   Casadio, F.; Leona, M.; Lombardi, J. R.; Van Duyne, R., Identification of Organic Colorants in Fibers, Paints, and Glazes by Surface Enhanced Raman Spectroscopy. *Accounts of Chemical Research* **2010**, *43*, 782-791.

30.   Lomax, S. Q., The Application of X-Ray Powder Diffraction for the Analysis of Synthetic Organic Pigments. Part 2: Artists' Paints. *Journal of Coatings Technology and Research* **2010**, *7*, 325-330.

31.   Buchsbaum, C.; Schmidt, M. U., Rietveld Refinement of a Wrong Crystal Structure. *Acta Crystallographica Section B* **2007**, *63*, 926-932.

32.   Zeitler, J. A.; Taday, P. F.; Newnham, D. A.; Pepper, M.; Gordon, K. C.; Rades, T., Terahertz Pulsed Spectroscopy and Imaging in the Pharmaceutical Setting □ a Review. *J. Pharm. Pharmacol.* **2007**, *59*, 209-223.

33.   Neelmeijer, C.; Brissaud, I.; Calligaro, T.; Demortier, G.; Hautojärvi, A.; Mäder, M.; Martinot, L.; Schreiner, M.; Tuurnala, T.; Weber, G., Paintings— a Challenge for Xrf and Pixe Analysis. *X-Ray Spectrometry* **2000**, *29*, 101-110.

34.   de Courlon, C.; Ives, S.; Dredge, P., Fields of Colour: The Conservation of Matt, Synthetic Paintings by Michael Johnson. *AICCM Bulletin* **2015**, *36*, 136-146.

35.   Dredge, P.; Ives, S.; Howard, D. L.; Spiers, K. M.; Yip, A.; Kenderdine, S., Mapping Henry: Synchrotron-Sourced X-Ray Fluorescence Mapping and Ultra-High-Definition Scanning of an Early Tudor Portrait of Henry Viii. *Applied Physics A* **2015**, *121*, 789-800.

36.   Albert, S., et al., Synchrotron-Based Highest Resolution Terahertz Spectroscopy of the N24 Band System of 1,2-Dithiine ($C_4H_4S_2$): A Candidate for Measuring the Parity Violating Energy Difference between Enantiomers of Chiral Molecules. *The Journal of Physical Chemistry Letters* **2016**, *7*, 3847-3853.

37.   Kendix, E. L.; Prati, S.; Joseph, E.; Sciutto, G.; Mazzeo, R., Atr and Transmission Analysis of Pigments by Means of Far Infrared Spectroscopy. *Analytical and Bioanalytical Chemistry* **2009**, *394*, 1023-1032.

38.   Zhang, F.; Wang, H. W.; Tominaga, K.; Hayashi, M.; Lee, S.; Nishino, T., Elucidation of Chiral Symmetry Breaking in a Racemic Polymer System with Terahertz Vibrational Spectroscopy and Crystal Orbital Density Functional Theory. *J Phys Chem Lett* **2016**, *7*, 4671-4676.

39.   El Haddad, J.; Bousquet, B.; Canioni, L.; Mounaix, P., Review in Terahertz Spectral Analysis. *TrAC, Trends Anal. Chem.* **2013**, *44*, 98-105.

40.   Brusentsova Tatiana, N.; Peale Robert, E.; Maukonen, D.; Harlow George, E.; Boesenberg Joseph, S.; Ebel, D., Far Infrared Spectroscopy of Carbonate Minerals. *Am. Mineral.* **2010**, *95*, 1515.

41.   Kendix, E.; Moscardi, G.; Mazzeo, R.; Baraldi, P.; Prati, S.; Joseph, E.; Capelli, S., Far Infrared and Raman Spectroscopy Analysis of Inorganic Pigments. *J. Raman Spectrosc.* **2008**, *39*, 1104-1112.

42.   Zhang, X. C.; Xu, J., *Introduction to Thz Wave Photonics*; Springer US, 2009.

43.   Auston, D. H.; Nuss, M. C., Electrooptical Generation and Detection of Femtosecond Electrical Transients. *IEEE Journal of Quantum Electronics* **1988**, *24*, 184-197.

44.   Baxter, J. B.; Guglietta, G. W., Terahertz Spectroscopy. *Analytical Chemistry* **2011**, *83*, 4342-4368.

45.   Smith, G. D.; Clark, R. J. H., Raman Microscopy in Archaeological Science. *Journal of Archaeological Science* **2004**, *31*, 1137-1160.

46.   Centeno, S. A., Identification of Artistic Materials in Paintings and Drawings by Raman Spectroscopy: Some Challenges and Future Outlook. *Journal of Raman Spectroscopy* **2016**, *47*, 9-15.

47.   Casadio, F.; Daher, C.; Bellot-Gurlet, L., Raman Spectroscopy of Cultural Heritage Materials: Overview of Applications and New Frontiers in Instrumentation, Sampling Modalities, and Data Processing. *Top. Curr. Chem.* **2016**, *374*, 62.

48.   Allis, D. G.; Prokhorova, D. A.; Korter, T. M., Solid-State Modeling of the Terahertz Spectrum of the High Explosive Hmx. *The Journal of Physical Chemistry A* **2006**, *110*, 1951-1959.

49.   Sleiman, J., Bou. Terahertz Imaging and Spectroscopy: Application to Defense and Security in Front of the Examination Panel. Université de Bordeaux, 2016.

50.   Sibik, J.; Zeitler, J. A., Direct Measurement of Molecular Mobility and Crystallisation of Amorphous Pharmaceuticals Using Terahertz Spectroscopy. *Advanced Drug Delivery Reviews* **2016**, *100*, 147-157.

51.   Li, Q.; Zaczek, A. J.; Korter, T. M.; Zeitler, J. A.; Ruggiero, M. T., Methyl-Rotation Dynamics in Metal–Organic Frameworks Probed with Terahertz Spectroscopy. *Chemical Communications* **2018**, *54*, 5776-5779.

52.   Squires, A. D.; Lewis, R. A., Terahertz Analysis of Phthalocyanine Pigments. *Journal of Infrared, Millimeter, and Terahertz Waves* **2019**, *40*, 738-751.

53.   Fukunaga, K.; Picollo, M., Terahertz Spectroscopy Applied to the Analysis of Artists' Materials. *Appl. Phys. A* **2010**, *100*, 591-597.

54.   Kawano, Y., Terahertz Waves: A Tool for Condensed Matter, the Life Sciences and Astronomy. *Contemporary Physics* **2013**, *54*, 143-165.

55.   Zhang, W.; Song, Z.; Ruggiero, M. T.; Mittleman, D. M., Assignment of Terahertz Modes in Hydroquinone Clathrates. *Journal of Infrared, Millimeter, and Terahertz Waves* **2020**.

56.   Neu, J.; Nemes, C. T.; Regan, K. P.; Williams, M. R. C.; Schmuttenmaer, C. A., Exploring the Solid State Phase Transition in Dl-Norvaline with Terahertz Spectroscopy. *Physical Chemistry Chemical Physics* **2018**, *20*, 276-283.

57.   Sasaki, T.; Sakamoto, T.; Otsuka, M., Detection of Impurities in Organic Crystals by High-Accuracy Terahertz Absorption Spectroscopy. *Anal. Chem.* **2018**, *90*, 1677-1682.

58.   Jepsen, P. U.; Clark, S. J., Precise Ab-Initio Prediction of Terahertz Vibrational Modes in Crystalline Systems. *Chem. Phys. Lett.* **2007**, *442*, 275-280.

59.   Trafela, T.; Mizuno, M.; Fukunaga, K.; Strlič, M., Quantitative Characterisation of Historic Paper Using Thz Spectroscopy and Multivariate Data Analysis. *Applied Physics A* **2013**, *111*, 83-90.

60.   Beard, M. C.; Turner, G. M.; Schmuttenmaer, C. A., Terahertz Spectroscopy. *The Journal of Physical Chemistry B* **2002**, *106*, 7146-7159.

61.   Fukunaga, K.; Hosako, I., Innovative Non-Invasive Analysis Techniques for Cultural Heritage Using Terahertz Technology. *Comptes Rendus Physique* **2010**, *11*, 519-526.

62.   Larkin, P. J.; Dabros, M.; Sarsfield, B.; Chan, E.; Carriere, J. T.; Smith, B. C., Polymorph Characterization of Active Pharmaceutical Ingredients (Apis) Using Low-Frequency Raman Spectroscopy. *Applied Spectroscopy* **2014**, *68*, 758-776.

63.   Dampf, S. J.; Korter, T. M., Anomalous Temperature Dependence of the Lowest-Frequency Lattice Vibration in Crystalline Γ-Aminobutyric Acid. *The Journal of Physical Chemistry A* **2019**, *123*, 2058-2064.

64.   Parrott, E. P. J.; Zeitler, J. A., Terahertz Time-Domain and Low-Frequency Raman Spectroscopy of Organic Materials. *Applied Spectroscopy* **2015**, *69*, 1-25.

65.   Mizuno, M.; Fukunaga, K.; Saito, S.; Hosako, I., Analysis of Calcium Carbonate for Differentiating between Pigments Using Terahertz Spectroscopy. *Journal of the European Optical Society Rapid Publications* **2009**, *4*.

66.   Parrott, E. P. J.; Fischer, B. M.; Gladden, L. F.; Zeitler, J. A.; Jepsen, P. U., Terahertz Spectroscopy of Crystalline and Non-Crystalline Solids. In *Terahertz Spectroscopy and Imaging*, Peiponen, K.-E.; Zeitler, A.; Kuwata-Gonokami, M., Eds. Springer Berlin Heidelberg: Berlin, Heidelberg, 2013; pp 191-227.

67.   Price, B. A.; Pretzel, B.; Lomax, S. Q., Infrared and Raman Users Group Spectral Database. 2007 ed.; IRUG: Philadelphia, 2009; Vol. 1 & 2.

68.   Fukunaga, K., Terahertz Spectral Database: Construction of Open Terahertz Spectral Database. *J. Nat. Inst. Inf. Commun. Technol.* **2008**, *55*, 61-66.

69.   Castro, K.; Pérez-Alonso, M.; Rodríguez-Laso, M. D.; Fernández, L. A.; Madariaga, J. M., On-Line Ft-Raman and Dispersive Raman Spectra Database of Artists' Materials (E-Visart Database). *Analytical and Bioanalytical Chemistry* **2005**, *382*, 248-258.

70.   Caggiani, M. C.; Cosentino, A.; Mangone, A., Pigments Checker Version 3.0, a Handy Set for Conservation Scientists: A Free Online Raman Spectra Database. *Microchemical Journal* **2016**, *129*, 123-132.

71.   Pallipurath, A. R.; Skelton, J. M.; Ricciardi, P.; Elliott, S. R., Estimation of Semiconductor-Like Pigment Concentrations in Paint Mixtures and Their Differentiation from Paint Layers Using First-Derivative Reflectance Spectra. *Talanta* **2016**, *154*, 63-72.

72.   Strachan, C. J.; Pratiwi, D.; Gordon, K. C.; Rades, T., Quantitative Analysis of Polymorphic Mixtures of Carbamazepine by Raman Spectroscopy and Principal Components Analysis. *J. Raman Spectrosc.* **2004**, *35*, 347-352.

73.   El Haddad, J.; de Miollis, F.; Bou Sleiman, J.; Canioni, L.; Mounaix, P.; Bousquet, B., Chemometrics Applied to Quantitative Analysis of Ternary Mixtures by Terahertz Spectroscopy. *Anal. Chem.* **2014**, *86*, 4927-4933.

74.   King, M. D.; Buchanan, W. D.; Korter, T. M., Identification and Quantification of Polymorphism in the Pharmaceutical Compound Diclofenac Acid by Terahertz Spectroscopy and Solid-State Density Functional Theory. *Anal. Chem.* **2011**, *83*, 3786-3792.

75.   Warnecke, S.; Wu, J. X.; Rinnan, Å.; Allesø, M.; Van Den Berg, F.; Jepsen, P. U.; Engelsen, S. B., Quantifying Crystalline A-Lactose Monohydrate in Amorphous Lactose Using Terahertz Time Domain Spectroscopy and near Infrared Spectroscopy. *Vib. Spectrosc.* **2019**, *102*, 39-46.

76.   Koch Dandolo, C. L.; Guillet, J.-P.; Ma, X.; Fauquet, F.; Roux, M.; Mounaix, P., Terahertz Frequency Modulated Continuous Wave Imaging Advanced Data Processing for Art Painting Analysis. *Optics Express* **2018**, *26*, 5358-5367.

77.   Locquet, A.; Dong, J.; Melis, M.; Citrin, D. In *Terahertz Pulsed Imaging Reveals the Stratigraphy of a Seventeenth-Century Oil Painting*, Unconventional Optical Imaging, International Society for Optics and Photonics: 2018; p 106771Z.

78.   Koch Dandolo, C. L.; Picollo, M.; Cucci, C.; Jepsen, P. U., Fra Angelico's Painting Technique Revealed by Terahertz Time-Domain Imaging (Thz-Tdi). *Appl. Phys. A-Mater.* **2016**, *122*, 898.

79.   Guillet, J.-P.; Roux, M.; Wang, K.; Ma, X.; Fauquet, F.; Balacey, H.; Recur, B.; Darracq, F.; Mounaix, P., Art Painting Diagnostic before Restoration with Terahertz and Millimeter Waves. *J. Infrared Millim. Terahertz Waves* **2017**, *38*, 369-379.

80.   Adam, A. J. L.; Planken, P. C. M.; Meloni, S.; Dik, J., Terahertz Imaging of Hidden Paint Layers on Canvas. *Optics Express* **2009**, *17*, 3407-3416.

81.   Koch Dandolo, C. L.; Filtenborg, T.; Skou-Hansen, J.; Jepsen, P. U., Analysis of a Seventeenth-Century Panel Painting by Reflection Terahertz Time-Domain Imaging (Thz-Tdi):

Contribution of Ultrafast Optics to Museum Collections Inspection. *Appl. Phys. A* **2015**, *121*, 981-986.

82.   Koch-Dandolo, C. L.; Filtenborg, T.; Fukunaga, K.; Skou-Hansen, J.; Jepsen, P. U., Reflection Terahertz Time-Domain Imaging for Analysis of an 18th Century Neoclassical Easel Painting. *Applied Optics* **2015**, *54*, 5123-5129.

83.   Yang, Y.; Zhai, D.; Zhang, Z.; Zhang, C., Thz Spectroscopic Identification of Red Mineral Pigments in Ancient Chinese Artworks. *J. Infrared, Millimeter, Terahertz Waves* **2017**, *38*, 1232-1240.

84.   Pascale, F.; Zicovich-Wilson, C. M.; Gejo, F. L.; Civalleri, B.; Orlando, R.; Dovesi, R., The Calculation of the Vibrational Frequencies of Crystalline Compounds and Its Implementation in the Crystal Code. *J. Comput. Chem.* **2004**, *25*, 888-897.

85.   Jepsen, P. U.; Cooke, D. G.; Koch, M., Terahertz Spectroscopy and Imaging – Modern Techniques and Applications. *Laser Photonics Rev.* **2011**, *5*, 124-166.

86.   Squires, A. D.; Lewis, R. A.; Zaczek, A. J.; Korter, T. M., Distinguishing Quinacridone Pigments Via Terahertz Spectroscopy: Absorption Experiments and Solid-State Density Functional Theory Simulations. *J. Phys. Chem. A* **2017**, *121*, 3423-3429.

87.   Ruggiero, M. T.; Bardon, T.; Strlic, M.; Taday, P. F.; Korter, T. M., Assignment of the Terahertz Spectra of Crystalline Copper Sulfate and Its Hydrates Via Solid-State Density Functional Theory. *J. Phys. Chem. A* **2014**, *118*, 10101-10108.

88.   Kleist, E. M.; Koch Dandolo, C. L.; Guillet, J.-P.; Mounaix, P.; Korter, T. M., Terahertz Spectroscopy and Quantum Mechanical Simulations of Crystalline Copper-Containing Historical Pigments. *The Journal of Physical Chemistry A* **2019**, *123*, 1225-1232.

89.   Dovesi, R., et al., Quantum□Mechanical Condensed Matter Simulations with Crystal. *Wiley Interdiscip. Rev. Comput. Mol. Sci.*, *0*, e1360.

Chapter 2. Experimental Methods

2.1 Introduction

Terahertz time-domain spectroscopy (THz-TDS) and low-frequency Raman spectroscopy (LFRS) are ideal techniques for the characterization of historic and modern pigments. In addition to their nondestructive and noninvasive natures, THz-TDS and LFRS produce chemically specific spectra that are essential to distinguishing pigments that are visually similar or chemically related. In order to demonstrate the utility of these techniques for potential analytical applications, spectral characterization of pure pigments is necessary. In support of this vibrational study, powder X-ray diffraction (PXRD) measurements have been used as a non-spectroscopic tool for evaluating sample identity and purity in bulk samples. After successful characterization of the low-frequency spectral behaviors of pure pigments, these methods can be applied with greater confidence in the analysis of pigment mixtures.

This chapter focuses on the theory behind THz-TDS and LFRS techniques beginning with the fundamentals of vibrational spectroscopy and the extension of these fundamentals to low-frequency vibrations. A brief introduction to the theory and instrumentation for PXRD is also included. Throughout this discussion, carbon dioxide (CO_2) will be used as a simple model system to demonstrate spectral differences between infrared and Raman spectroscopic studies of solids and single molecules. CO_2 makes a simple, yet ideal, model due to its $D_{\infty h}$ point group symmetry and crystallizes into space group 205, Pa3. These symmetries permit both infrared-active and Raman-active vibrations to exist within a single molecule of CO_2 and a crystallized array of bulk CO_2. Diffraction data for CO_2 is also included as a general example of a PXRD pattern.

2.2 Vibrational Spectroscopy

Understanding the low-frequency intermolecular vibrations of crystalline materials requires discussion of the quantum mechanical vibrational behaviors of a simple model.[1-3] The simplest vibration is the stretching motion in a diatomic molecule and it can be described with the Schrödinger equation for a quantum harmonic oscillator[2, 4-7]

$$-\frac{\hbar^2}{2m}\frac{d^2\psi(x)}{dx^2} + \frac{1}{2}k_f x^2 \psi(x) = E\psi \qquad (2.1)$$

In the quantum harmonic oscillator model, the discreet vibrational energy levels (E_n) are defined

$$E_n = \hbar v\left(n + \frac{1}{2}\right) \qquad (2.2)$$

where v, the vibrational frequency is equal to

$$v = \frac{1}{2\pi}\sqrt{\frac{k}{m_r}} \qquad (2.3)$$

where k is the force constant and μ is the reduced mass.

This harmonic oscillator model is an overly-simplified approximation that breaks down when describing vibrations beyond the stretching motion of diatomic molecule. Realistically, vibrations deviate from harmonic behavior and require corrections to account for complexities for each oscillator but also possible coupling between oscillators in a system.[4] These oscillators are considered anharmonic and, unlike the symmetric harmonic oscillator, are asymmetric (**Figure 2-1[8]**)
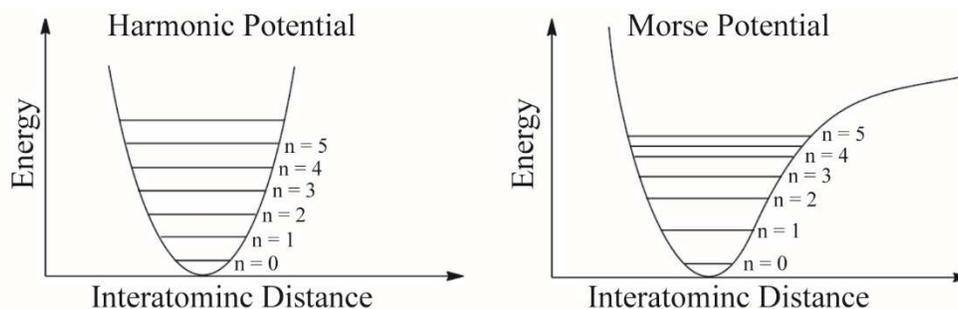
Figure 2-1 Depictions of harmonic oscillator (left) and Morse potential (right). Adapted from Reference 8.

Anharmonic oscillators are best approximated with a Morse potential:

$$V = D_e\left(1 - e^{-\beta(r-r_0)^2}\right) \tag{2.4}$$

where D_e corresponds to the depth of the potential energy well, β is the curvature at the bottom of the well, and $(r - r_0)$ is the internuclear distance. The vibrational energy levels of a Morse potential are defined as an expanded Taylor series

$$E_n = \left(n + \frac{1}{2}\right)v_e - \left(n + \frac{1}{2}\right)^2 v_e x_e.... \tag{2.5}$$

in which the first term accounts for the harmonic behavior and the second term (and terms beyond) are for anharmonic corrections.[9] Unlike the evenly-spaced vibrational energy levels in the harmonic approximation, the difference between the vibrational energy levels in the Morse potential are inversely proportional to n and asymptotically approach the dissociation energy.

This vibrational theory can be extended to low-frequency vibrational theory, although the vibrational spectra will change drastically since the atomic-level nature of the vibrations in the mid-IR correspond to intramolecular motions and those in the far-IR are dominated by intermolecular motions. These spectral differences can be easily described with the simple model, CO_2. In vibrational spectra of molecular CO_2, modes originate from intramolecular motions. For example, in the infrared spectrum, modes near 667 cm^{-1} and 2349 cm^{-1} are

attributed to bending and asymmetric stretching motions, and in the Raman spectrum, the only mode at 1932 cm^{-1} corresponds to a symmetric stretch.[10-11] In the vibrational spectra of crystalline CO_2, the same intramolecular vibrations still exist (with shifting of energies), but new intermolecular vibrations result from the solid form. The new vibrational motions in the solid are seen as three modes in the IR spectrum (68, 110, and 114 cm^{-1}) and correspond to translational lattice motions, while three modes (73, 90, and 131 cm^{-1}) in the Raman spectrum are hindered rotations of CO_2 molecules in the crystalline lattice.[10, 12-13] Intermolecular vibrations such as translations and hindered rotations are not present in isolated molecules since they arise from interactions of the molecules within the crystal lattice. The differences in spectral frequencies between molecular and crystalline CO_2 can be explained with Eq. 2.2 and 2.3 which show the dependence of the vibrational frequency on the force constant and reduced mass of the motion. From these two equations, low-frequency modes will either be characterized by small force constants or large reduced masses; two conditions that are both satisfied by crystals with weak intermolecular van der Waals forces or involve simultaneous motions of many atoms (e.g. translations).

In crystals, the displacement of atoms from the equilibrium position is restricted by the periodicity of the solid and the symmetry elements of the unit cell. This is best understood with a simplified periodic model of one dimensional chains of atoms. In these chains, vibrations are the displacement of atoms only along the direction of the chain. These displacements are referred to as longitudinal modes. If the dimensionality is removed the restrictions are no longer restricted to one dimension. Displacements will occur along the direction of the chain and also perpendicular to the chain. The displacements perpendicular to the original chain are transverse modes. Since

the displacements of atoms are restricted in in crystalline lattices, the forces constants of these motions are considerable smaller and occur at lower frequencies.

2.3 Selection Rules

The discussion of the vibrational origins of changes in spectral frequencies between molecular and crystalline CO_2 warrants an explanation of the differences between the IR and Raman spectra. In the molecular spectra of CO_2, the IR spectrum had three modes and the Raman only had one,[10-11] while there are three low-frequency modes in both the IR and Raman spectra of crystalline CO_2. In molecular vibrations, the origins of modes in IR spectra are characterized by the change in the dipole moment of a molecule during a vibrational motion, whereas modes in Raman spectra originate from the change in the polarizability. In crystals, the same theories apply but rather than observing the changes in a molecule's dipole moment and polarizability, the changes are in relation to the unit cell.

Considering IR spectroscopy first, the absorption of quantized radiation will induce a transition between vibrational energy levels (shown in **Figure 2-2**). The only allowed transitions follow: $\Delta v = \pm 1$ and will be active if the dipole moment of a system changes during the vibration. This is defined by the magnitude of the dipole moment, M:

$$M = \int \psi^*_{final} \hat{\mu} \, \psi_{initial} d\tau \tag{2.6}$$

Where, $\hat{\mu}$, the electric dipole operator is defined as the sum over all particles with the charge (e) and particle position (x, y, z):

$$\hat{\mu} = \hat{\mu}_x + \hat{\mu}_y + \hat{\mu}_z = \sum e(x + y + z) \tag{2.7}$$

From Eq. 2.6 and Eq. 2.7, the magnitude of the dipole moment is equal to $\hat{\mu}$ over the wavefunction of the transition, where $\hat{\mu}$ is dependent on the charges of particles and their positions

Rather than inducing molecular vibrations with direct absorption, vibrations can also be probed using light scattering. The light scattered by a sample can be elastic or inelastic and is classified as Rayleigh and Raman scattering, respectively.[14] Raman scattering is further classified as Stokes and anti-Stokes scattering. Raman scattering has intensities on the order of 10^{-5} - 10^{-8} of Rayleigh scattering. The frequencies of the scattered photons are reported as shifts from the incident photon beam frequency and are dependent on internal vibrational interactions or lattice vibrations. In Stokes scattering, photons from the incoming beam are absorbed to virtual state and upon release will fall to a higher vibration energy level than that of the ground state. This process results in a frequency shift that is lower than the incident beam frequency. In anti-Stoke scattering, some excited states are already populated and will relax to the ground state from a virtual state when a photon is released. Stokes scattering is more intense due to the dependence of anti-Stokes scattering on the thermal population of higher vibrational energy states. This process causes a frequency shift in the light that is higher than the incident beam frequency. This behavior is shown in **Figure 2.2[15]**, as well as a comparison between the transitions observed in infrared and Raman spectroscopies.
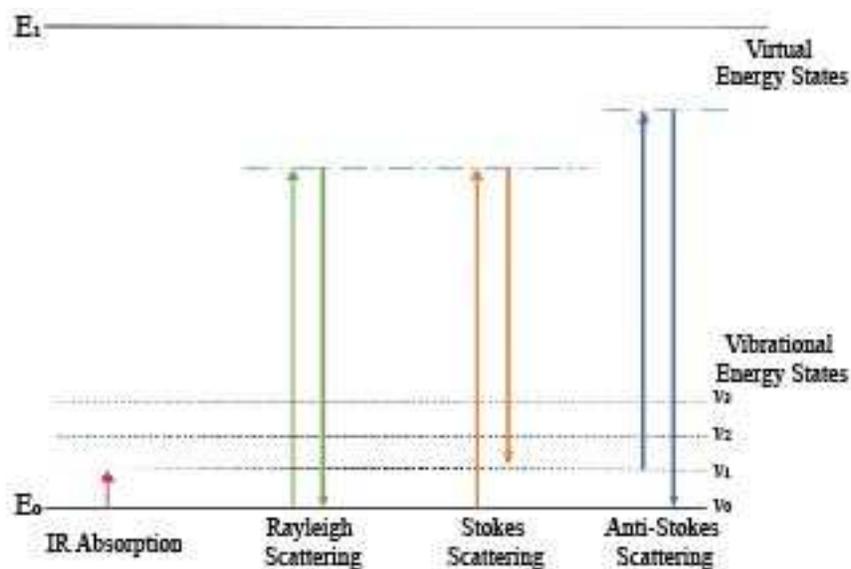
Figure 2-2 Allowed transitions in IR and Raman spectroscopies. Adapted from Reference 15.

A Raman-active mode will undergo a change in its polarizability during the transition. The selection rule for Raman-active modes is related to Eq. 2.6, with the transition moment $[\alpha]$ defined in terms of polarizability of the molecule:

$$[\alpha] = \int \psi_{final}^* \alpha \, \psi_{initial} d\tau \qquad (2.8)$$

The change in polarizability, α, during a Raman-active transition is defined as the response of the induced dipole moment $[\alpha]$ within an electric field (E):

$$\alpha = [\alpha]E \qquad (2.9)$$

In IR-active vibrations, the change in dipole moment was only concerned with the x, y, and z coordinate positions. In Raman-active vibrations, the response of the induced dipole moment within an electric field is defined with a tensor:

19

$$[\alpha] = \begin{bmatrix} \alpha_{xx} & \alpha_{xy} & \alpha_{xz} \\ \alpha_{yx} & \alpha_{yy} & \alpha_{yz} \\ \alpha_{zx} & \alpha_{yz} & \alpha_{zz} \end{bmatrix} \begin{bmatrix} E_x \\ E_y \\ E_z \end{bmatrix} \tag{2.10}$$

The electric field, along the $x, y,$ and z directions, is defined by the diagonal, $(\alpha_{xx}, \alpha_{yy}, \alpha_{zz})$. The response of the induced dipole moment along the directions of the other matrix values define the strength of polarization in that direction.

2.4 Toptica TeraFlash Time-Domain Spectrometer

In this work, a Toptica TeraFlash Time-Domain Spectrometer (**Figure 2.3)**, which uses a Toptica FemtoFiber femtosecond laser with fiber InGaAs photoconductive switches, was used for optoelectronic terahertz generation.[16-18] In this spectrometer, near-infrared radiation is generated with a femtosecond laser centered on 1560 nm and converted to terahertz waves using photoconductive switches comprised of a semiconducting multilayer structure of InGaAs and InAlAs on InP. Terahertz waves are then generated when the near-infrared radiation generates free charge carriers in the photoconductive switches creating a photocurrent of terahertz waves.[19-20]

Figure 2-3 Commercially available Toptica TeraFlash Time-Domain Spectrometer

All pigment samples for THz measurements were prepared in a polytetrafluoroethylene (PTFE) matrix with concentrations determined by the sample's absorption behavior. Polymer matrices show little to no THz absorption, making them ideal for measurements.[21-23] Here, PTFE was used because it has a low hygroscopicity[24] and high compressibility.[25] The pigments and matrix were homogenized and finely ground using a Dentsply-Rinn 3110-3A ball mill. Homogenized pigment/matrix powders were pressed into 13 mm diameter x 2 mm thick pellets using a hydraulic press (~2000 psi). A pellet of pure PTFE with the same dimensions was prepared for use as a blank. During data collection, samples were held under vacuum while the spectrometer was purged with dry air to minimize peaks from water vapor, which is a strong terahertz radiation absorber.[26]

THz-TDS measurements were usually collected at 293 K and again at 78 K when greater peak resolution was needed. Spectral peaks will narrow upon cooling, because the number of thermally excited states decreases at low temperatures. In addition, when a sample is cooled the spectrum will shift to higher frequencies. This shift is due to the contraction of the unit cell at low temperatures, in turn increasing the vibrational force constants.

During a measurement, the THz-induced optical changes of a sample were recorded as time-domain waveforms with current signals as a function of the signal delay in picoseconds using a 100 ps window and an average of 20000 scans. The observed bandwidth was 0.3 - 4.8 THz (10-150 cm^{-1}), with a spectral resolution of 0.005 THz (0.167 cm^{-1}).Time-domain waveforms were converted into the frequency-domain using Fourier transforms. The ratio of the transformed waveforms for the sample/matrix and blank pellets yields the absorption coefficients that are used to construct the final THz-TDS spectra. The absorbance values are transformed

from optical density to units of ε (M^{-1} cm^{-1}) using Beer's law and the concentrations (mol L^{-1}) and thicknesses (cm) of the sample pellet.

2.5 Ondax SureBlock XLF-CLM THz-Raman Spectrometer

In LFRS spectra, the THz region lies very close to the Rayleigh excitation peak, which has been a large complication in accessing the sub-200 cm^{-1} region with Raman spectroscopy. This strong peak must be attenuated in order to reveal useful signals in this region.[27] Recent developments in volume holographic grating filters[28-29] have enabled development of notch filters that are able to reject the specific wavelength of the incoming laser while preserving the transmission of other Raman signals.

In this work, an Ondax SureBlock XLF-CLM THz-Raman spectrometer was used. This spectrometer used a stabilized diode laser centered at 785 nm (Surelock LM series). A series of ultra-narrowband VGH suppression filters (NoiseBlock series) removed spontaneous emission from the diode laser. The beam was directed to a dichroic 90/10 VHG beam splitter that refocused the beam to the sample then measures the scattering off the sample. The beam splitter separated the Rayleigh scatter from the Raman signal, sending the Rayleigh scatter back to the laser and transmitting the Raman signals.[27] The Ondax THz-Raman spectrometer was fiber-coupled to an Andor Shamrock SR-750 spectrograph and Andor iDus 416 CCD camera detector. The combination of this spectrograph and CCD camera detector optimizes sensitivity and spectral resolution.
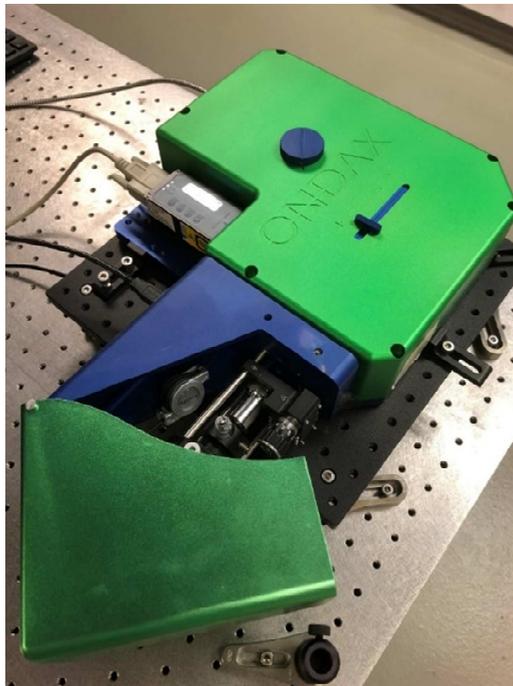
Figure 2-4 Commercially available Ondax SureBlock XLF-CLM THz-Raman spectrometer

In comparison to the sample pellets needed for THz-TDS spectroscopy, the samples for

Raman methods are simply the material of interest. Precautions were taken to eliminate

interference from ambient laboratory fluorescent lighting and to minimize damage to the samples

from heating due to excessive laser power. These samples were held in a 10-mm glass vial which

was placed in the spectrometer sample holder. The collected spectra were averaged over 225

exposures with exposure times ranging between 1 to 3 seconds. The collected spectral range

(with respect to the Rayleigh line) was from -100 to 300 cm^{-1} with a spectral resolution of 0.7

cm^{-1}. For comparison purposes, the intensity data for each sample was normalized.

2.6 Powder X-ray Diffraction

In solid-state materials, the crystalline lattice is defined as a three-dimensional periodic

arrangement of atoms continuously moving (vibrating) around their equilibrium positions. These

motions are influenced by the interatomic interactions and the symmetry elements of the lattice.

The periodic nature of lattices allows for simplification of the structure with a unit cell. Unit cells are defined by lattice parameters including lengths of the cell edges and the angles between them. These parameters are used to categorize unit cells into one of the seven crystal systems and further into one of 230 space groups defined unique atomic positions and symmetry elements of the unit cell.[30-31] Crystals will reflect high-energy X-ray radiation and produce diffraction patterns that yield structural details including crystal systems, space groups, lattice parameters, and atomic positions.[32-33] Bragg's law[34-35] relates the scattering angles of diffracted X-rays to the atomic plane distances in a crystal:

$$2d \sin(\theta) = n\lambda \qquad\qquad (2.1)$$

Where d is the distance between atom planes, θ is the angle between the incident X-ray and atom plane, and λ is the wavelength of the incoming X-ray beam. Powder X-ray diffraction (PXRD) is used to measure diffraction of bulk powder samples. PXRD data is used to determine the space group and unit cell lattice dimensions of crystalline samples. PXRD is relatively quick data collection but requires a considerable amount of sample. In this work, PXRD was used to confirm sample identity, purity, and crystallinity of the representative pure pigments. An example PXRD powder pattern is shown in **Figure 2-5** for crystalline CO_2.[36]
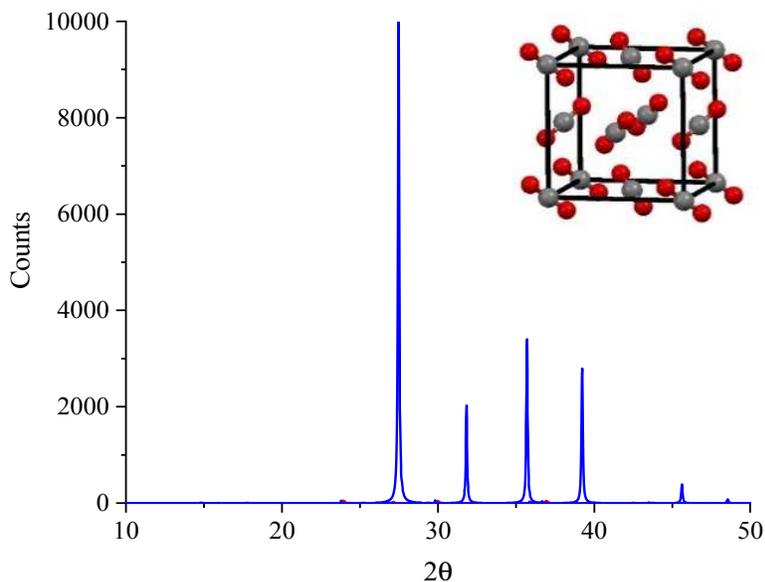
Figure 2-5 Predicted PXRD pattern for crystalline CO₂. Adapted from Reference

The PXRD measurements used a Bruker D2 Phaser diffractometer (**Figure 2-6**) with a LYKXEYE 1D silicon strip detector. Data collected with the Bruker D2 Phaser diffractometer was analyzed with the DIFFRAC.SUITE software package. During a data collection, the diffractometer held the sample position constant while the x-ray radiation beam (Cu Kα radiation, λ=1.5406 Å) was rotated around the sample.
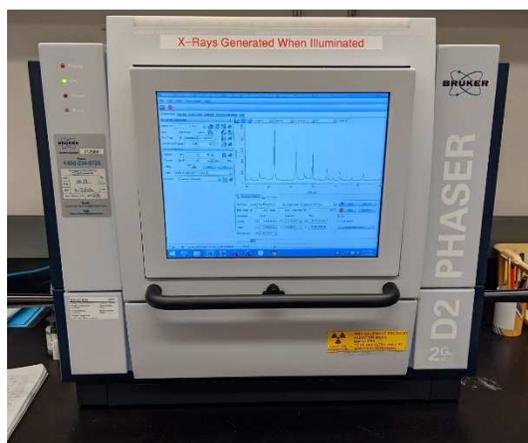
Figure 2-6 Commercially available Bruker D2 Phaser diffractometer.

2.7 Reference

1.	Bratos, S.; Pick, R. M., *Vibrational Spectroscopy of Molecular Liquids and Solids*; Springer US, 2012.

2.	Schmuttenmaer, C. A., Exploring Dynamics in the Far-Infrared with Terahertz Spectroscopy. *Chemical Reviews* **2004**, *104*, 1759-1780.

3.	Woolfson, M., Solid State Physics 3. Theory of Lattice Dynamics in the Harmonic Approximation by A. A. Maradudin, E. W. Montroll, G. H. Weiss and I. P. Ipatova. *Acta Crystallographica Section A* **1973**, *29*, 314.

4.	Wilson, E. B.; Decius, J. C.; Cross, P. C.; Sundheim, B. R., Molecular Vibrations: The Theory of Infrared and Raman Vibrational Spectra. *Journal of The Electrochemical Society* **1955**, *102*, 235C.

5.	Harris, D. C.; Bertolucci, M. D., *Symmetry and Spectroscopy: An Introduction to Vibrational and Electronic Spectroscopy*; Dover Publications, 1989.

6.	Engel, T.; Reid, P., *Physical Chemistry*; Pearson Education, 2012.

7.	Atkins, P.; de Paula, J., *Atkins' Physical Chemistry*; OUP Oxford, 2010.

8.	Takahashi, M., Terahertz Vibrations and Hydrogen-Bonded Networks in Crystals. *Crystals* **2014**, *4*, 74-103.

9.	Silbey, R. J.; Alberty, R. A.; Bawendi, M. G., *Solutions Manual to Accompany Physical Chemistry, 4e*; Wiley, 2004.

10.	Osberg, W. E.; Hornig, D. F., The Vibrational Spectra of Molecules and Complex Ions in Crystals. Vi. Carbon Dioxide. *The Journal of Chemical Physics* **1952**, *20*, 1345-1347.

11.	Jr., D. F. E.; Jr., B. L. C., Vibrational Intensities. Iii. Carbon Dioxide and Nitrous Oxide. *The Journal of Chemical Physics* **1951**, *19*, 1554-1561.

12.	Carter, R. S.; Rush, J. J.; Research, I. f. M., *Molecular Dynamics and Structure of Solids*; National Bureau of Standards, 1969.

13.	Cahill, J. E.; Leroi, G. E., Raman Spectra of Solid Co2, N2o, N2, and Co. *The Journal of Chemical Physics* **1969**, *51*, 1324-1332.

14.	Dubessy, J.; Caumon, M. C.; Rull, F., *Raman Spectroscopy Applied to Earth Sciences and Cultural Heritage*; European Mineralogical Union, 2012.

15.	Mamede, A. P.; Gonçalves, D.; Marques, M. P. M.; Batista de Carvalho, L. A. E., Burned Bones Tell Their Own Stories: A Review of Methodological Approaches to Assess Heat-Induced Diagenesis. *Applied Spectroscopy Reviews* **2018**, *53*, 603-635.

16.	Rulliere, C., *Femtosecond Laser Pulses: Principles and Experiments*; Springer, 2005.

17.	Saeedkia, D., 1 - Optoelectronic Techniques for the Generation and Detection of Terahertz Waves. In *Handbook of Terahertz Technology for Imaging, Sensing and Communications*, Saeedkia, D., Ed. Woodhead Publishing: 2013; pp 3-27.

18.	Georgiou, G.; Tyagi, H. K.; Mulder, P.; Bauhuis, G. J.; Schermer, J. J.; Rivas, J. G., Photo-Generated Thz Antennas. *Scientific Reports* **2014**, *4*, 3584.

19.   Zhang, X. C.; Xu, J., *Introduction to Thz Wave Photonics*; Springer US, 2009.

20.   Rullière, C., *Femtosecond Laser Pulses: Principles and Experiments*; Springer Berlin Heidelberg, 2013.

21.   Wietzke, S.; Jansen, C.; Reuter, M.; Jung, T.; Kraft, D.; Chatterjee, S.; Fischer, B. M.; Koch, M., Terahertz Spectroscopy on Polymers: A Review of Morphological Studies. *Journal of Molecular Structure* **2011**, *1006*, 41-51.

22.   Cunningham, P. D.; Valdes, N. N.; Vallejo, F. A.; Hayden, L. M.; Polishak, B.; Zhou, X.-H.; Luo, J.; Jen, A. K.-Y.; Williams, J. C.; Twieg, R. J., Broadband Terahertz Characterization of the Refractive Index and Absorption of Some Important Polymeric and Organic Electro-Optic Materials. *Journal of Applied Physics* **2011**, *109*, 043505-043505-5.

23.   Bründermann, E.; Hübers, H.-W.; Kimmitt, M. F., Spectroscopic Methods. In *Terahertz Techniques*, Springer Berlin Heidelberg: Berlin, Heidelberg, 2012; pp 247-300.

24.   Balakrishnan, J.; Fischer, B. M.; Abbott, D., Sensing the Hygroscopicity of Polymer and Copolymer Materials Using Terahertz Time-Domain Spectroscopy. *Appl Opt* **2009**, *48*, 2262-6.

25.   Rae, P. J.; Dattelbaum, D. M., The Properties of Poly(Tetrafluoroethylene) (Ptfe) in Compression. *Polymer* **2004**, *45*, 7615-7625.

26.   Exter, M.; Fattinger, C.; Grischkowsky, D., Terahertz Time-Domain Spectroscopy of Water Vapor. *Opt Lett* **1989**, *14*, 1128-30.

27.   Heyler, R.; Carriere, J. T.; Havermeyer, F., *Thz-Raman: Accessing Molecular Structure with Raman Spectroscopy for Enhanced Chemical Identification, Analysis, and Monitoring*; SPIE, 2013; Vol. 8726.

28.   Moser, C.; Havermeyer, F., Ultra-Narrow-Band Tunable Laserline Notch Filter. *Applied Physics B* **2009**, *95*, 597-601.

29.   Moser, C.; Havermeyer, F., *Compact Raman Spectrometer System for Low Frequency Spectroscopy*; SPIE, 2010; Vol. 7598.

30.   Suh, I. H.; Kim, K. J.; Choo, G. H.; Lee, J. H.; Choh, S. H.; Kim, M. J., The Asymmetric Unit of X-Ray Intensity Data of the Seven Crystal Systems. *Acta Crystallographica Section A* **1993**, *49*, 369-371.

31.   Buerger, M., Tables of the Characteristics of the Vector Representations of the 230 Space Groups. *Acta Crystallographica* **1950**, *3*, 465-471.

32.   Cullity, B. D., *Elements of X-Ray Diffraction*; Addison-Wesley Publishing Company, 1978.

33.   Berger, M.; Yang, Q.; Maier, A., X-Ray Imaging. In *Medical Imaging Systems: An Introductory Guide*, Maier, A.; Steidl, S.; Christlein, V.; Hornegger, J., Eds. Springer International Publishing: Cham, 2018; pp 119-145.

34.   Bragg, W. H., The Reflection of X-Rays by Crystals. *Nature* **1913**, *91*, 477-477.

35.   Kapitza, P. L.; Dirac, P. A. M., The Reflection of Electrons from Standing Light Waves. *Mathematical Proceedings of the Cambridge Philosophical Society* **1933**, *29*, 297-300.

36.   De Smedt, J.; Keesom, W. In *The Structure of Solid Nitrous Oxide and Carbon Dioxide*, Proceedings of the Koninklijke Akademie Van Wetenschappen Te Amsterdam, 1924; pp 839-846.

Chapter 3. Density Functional Theory

3.1 Introduction

The spectral features in THz-TDS and LFRS spectra (**Chapter 2**) correspond to complex intermolecular motions in crystalline samples. In this work, the origins of these spectral features are determined with ss-DFT.[1] In order to discuss the aspects of ss-DFT that make it ideal for modeling crystalline solids, the theoretical framework of DFT must first be considered.

This chapter examines the fundamentals of DFT including descriptions of the quantum mechanical behavior of electrons and the orbitals they occupy with the Hohenberg-Kohn theorems, the Kohn/Sham method, exchange/correlation functionals, and basis sets. These foundational concepts are extended into solid-state models with periodic boundary conditions, reciprocal space, and Bloch's theorem. The ss-DFT software package, CRYSTAL, and its applications in this research are also discussed.

3.2 Quantum Mechanical Foundations of Density Functional Theory

In the time-independent Schrödinger equation,[2-3] the Hamiltonian operator returns the energy of a sub-atomic particle, which can be deconstructed into the kinetic and potential energy terms.[4-5] This equation was initially used to explicitly derive the wavefunction and energy levels of the one-electron hydrogen atom,[6] but explicit solutions for larger systems are nearly impossible because the number of terms needed in the Hamiltonian to adequately describe electronic and nuclear interactions increases as the electrons increase.[7] Solving many-electron systems is possible by limiting the terms in the Hamiltonian to those that describe the electronic interactions in a system.[4] The exclusion of nuclear interactions, referred to as the Born-Oppenheimer approximation,[8] is predicated on the assumption that atomic nuclei are stationary

in comparison to electrons because of the large mass difference between the two.[9] As a result,

the time-independent Schrödinger equation for a particle becomes

$$H\psi = \left[-\frac{\hbar}{2m} \sum_{i=1}^{N} \nabla_i^2 + \sum_{i=1}^{N} V(r_i) + \sum_{i=1}^{N}\sum_{j<1} U(r_i r_j) \right] \psi = E\psi \tag{3.1}$$

Where ψ is the electronic wavefunction, E is the ground state energy of a system, and H

is the Hamiltonian. The Hamiltonian is defined by three terms, respectively: the kinetic energy of

each electron, the interaction energy between the atomic nuclei and each electron, and the

interaction energy between the electrons in a system.[10-12]

Although exclusion of the nuclear terms simplifies the time-independent Schrödinger

equation, difficulties remain in defining the wavefunction for a particle: a multi-body problem

and 3N dimensionality. The last term of the Hamiltonian in Eq. 3.1 describes the interactions

between electrons. Consequently, in multi-electron (multi-body) models this implies that

determination of the wavefunction for one electron requires knowing the wavefunctions for the

other electrons in a model. The other difficulty, 3N dimensionality, arises from the treatment of

each electron as a single particle in space with unique coordinates. Rather than characterizing

electrons as single points in space, defining the collective of electrons as a density eliminates the

multi-body problem and reduces the dimensionality to a function of three coordinates. The

electron density (n) is defined as

$$n(r) = \sum_i \psi_i^*(r)\psi_i(r) \tag{3.2}$$

where the summation of the individual wavefunctions is equal to the probability that an electron

$(\psi_i(r))$ is at a point in space, (r).

Although Eq. 3.2 eliminated the multi-body and dimensionality complications, describing

$\psi_i(r)$ for $n(r)$ was not possible. Pierre Hohenberg and Walter Kohn theorized that ground state

energy of these wavefunctions can be determined from the solutions to a set of non-interacting

electronic equations based on the electron density.[13] This theory was centered on two theorems:

first, the ground-state energy is defined as a functional of electron density,[10, 13-14] and second, the

electron density that minimizes the energy of the overall functional is the true electron density of

a system.[14-15]

The second Hohenberg-Kohn theorem[16] can be expressed as:

$$E[\{\psi_i\}] = E_{known}[\{\psi_i\}] + E_{XC}[\{\psi_i\}] \tag{3.3}$$

where the minimized energy of a system depends on $E_{XC}[\{\psi_i\}]$. This term is the

exchange/correlation functional which accounts for the effects not included in $E_{known}[\{\psi_i\}]$.

Although, the Hohenberg-Kohn theorems simplified Eq. 3.1, there were no methods for defining

a functional that related the ground-state energy with electronic density, leaving solutions to Eq.

3.3 with the same problems encountered in Eq. 3.1. A definition for this functional, developed

by Walter Kohn and Lu Jeu Sham, was based on wavefunctions for single electrons rather than

wavefunctions that included contributions from each electron.[16] A single-electron wavefunction

is defined as

$$\left[-\frac{\hbar}{2m}\nabla^2 + V(\boldsymbol{r}) + V_H(\boldsymbol{r}) + V_{XC}(\boldsymbol{r})\right]\psi_i(\boldsymbol{r}) = \varepsilon_i\psi_i(\boldsymbol{r}) \tag{3.4}$$

where the second term of the Hamiltonian describes the interaction between an electron and the

atomic nuclei. This term is also in Eq. 3.1 and is included in the $E_{known}[\{\psi_i\}]$ term of Eq. 3.3.

The third term of Eq. 3.4 is the Hartree potential:

$$V_H(\boldsymbol{r}) = e^2 \int \frac{n(\boldsymbol{r'})}{|\boldsymbol{r} - \boldsymbol{r'}|} d^3\boldsymbol{r'} \tag{3.5}$$

which accounts for the Coulombic repulsion between an electron and the electronic density of a system. The fourth term is the exchange-correlation potential contribution to the wavefunction described by

$$V_{XC}(\boldsymbol{r}) = \frac{\delta E_{XC}(\boldsymbol{r})}{\delta n(\boldsymbol{r})} \tag{3.6}$$

As a result, the wavefunction of a single electron (Eq. 3.4) depends on the Hartree potential (Eq. 3.5) which hinges on the electron density (Eq. 3.2) that can only be solved with known single-electron wavefunctions (Eq. 3.4). This circular process and along with the undefined exchange/correlation contribution (Eq. 3.6) form the iterative basis of the self-consistent field (SCF) energy calculations in DFT.[12]

3.3 Density Functionals

In the prior section, both the minimized energy of a system (Eq. 3.3) and the single-electron wavefunction (Eq. 3.4) include the undefined exchange/correlation terms, $E_{XC}[\{\psi_i\}]$ and $V_{XC}(\boldsymbol{r})$. The definition of a functional that yields exact exchange-correlation energy is unknown, resulting in the development of various approximations of the energy as functionals of electron density, referred to as exchange/correlation functionals.[10, 12] Categorization of functionals has classically been depicted as a ladder composed of five rungs that correspond to the sophistication of the model.[10, 17] Each rung includes a new physical constant. Theoretically, the inclusion of more constants will increase accuracy but the tradeoff between computational cost and accuracy must be considered.

Here, the focus is on local density approximations, generalized gradient approximations, and hybrid models. Other classes of functionals exist (range-corrected hybrid functionals[18-21] and meta-global gradient approximation functionals[10, 22-23]) but are not covered in this work.

Many density functionals do not account for the long-range London dispersion forces.[24] Although corrections for these weak interactions are small, [25] they are not negligible, and have been accounted for with the addition of two- three- and many-body terms. [26] In crystals, these forces contribute to the formation and stabilization of the lattice structure, prompting the development of two, and three-body dispersion terms for use in ss-DFT.[25, 27-31]

3.3.1 Local Density Approximation Functionals

The simplest functionals are local density approximation (LDA) functionals. LDAs were developed with the assumption that electron density is uniform in all directions. The LDA exchange-correlation energy depends on electron density and is the sum of independent exchange and correlation terms[10]

$$E_{XC}^{LDA}[n(\boldsymbol{r})] = E_X^{LDA} + E_C^{LDA} \tag{3.7}$$

Exact solutions for these terms are possible in systems with high electron delocalization or slow-changing electron densities.[10, 12, 32-34] Examples of LDAs include: PW92,[35] VWN,[36] and PZ.[37]

3.3.2 Generalized Gradient Approximation Functionals

In addition to the electron density, generalized gradient approximation (GGAs) functionals include the gradient of the electron density in a system.[38] This additional parameter allows for improved local behavior models of the electron density in a real structure.[39] The generic form of a GGA functional is defined by the addition of a gradient correction to the LDA functional:

$$\varepsilon_{XC}^{GGA}(\boldsymbol{r}) = \varepsilon_{XC}^{LDA}[n(\boldsymbol{r})] + \Delta \left[\frac{|\nabla n(\boldsymbol{r})|}{n^{\frac{4}{3}}(\boldsymbol{r})} \right] \tag{3.8}$$

Additionally, the exchange functionals[40] and correlation[41] functionals of GGAs have been independently developed for use in development of hybrid functionals.

3.3.3 Hybrid functionals

Although GGAs were an improvement from LDAs, further development showed additional accuracy was possible upon mixing exact HF exchange with exchange-correlation energy from GGAs to create a hybrid functional.[42-43] This mixing increases the applicability of hybrid functionals, making them one of the most utilized functionals in computational chemistry.[44-45] The general form of a hybrid functional is

$$E_{XC}^{hybrid} = (1-a)E_{XC}^{GGA} + aE_X^{HF} \tag{3.9}$$

where a represents the mixing ratios of GGA exchange-correlation energy and HF exchange.[12]

In this research, B3LYP and PBE0, two well-known hybrid functionals, were used. B3LYP (Beck-3-parameter-Lee-Yang-Parr) was built with the B88 exchange functional[46] and the Lee-Yang-Par[40, 47] correlation functionals. The three empirical parameters (a, b, c) determined the ratio of mixing between the LDA exchange-correlation energies and the HF/GGA exchange-correlation energies,

$$E_{XC}^{B3LYP} = E_{XC}^{LDA} + a(E_X^{HF} - E_X^{LDA}) + b(E_X^B - E_X^{LDA}) + E_c^{LDA} + c(E_c^{LYP} - E_c^{LDA}) \tag{3.10}$$

PBE0 is the parameter-free hybrid model of the non-empirical GGA functional, PBE (Perdew–Burke-Ernzerhof)[48-50]

$$E_{XC}^{PBE0} = E_{XC}^{GGA} + \frac{1}{4}(E_X^{HF} - E_X^{GGA}) \tag{3.11}$$

3.4 Basis Sets

In addition to estimating electronic behavior, it is necessary to describe the atomic orbitals the electrons occupy. These atomic orbitals are defined with sets of functions (basis sets) for the electronic wavefunctions. In modern DFT software, atomic orbitals are defined with either plane-wave basis sets,[51-52] atom-centered basis sets,[53-54] or a combination of the two.[55] Although plane-wave basis set calculations offer advantages over atom-centered basis sets, such as the elimination of basis set superposition error, intrinsic periodicity in three dimensions, and faster calculations of energies and gradients in solid-state calculations, they have an extraordinarily high computational cost when paired with hybrid functionals.[56-57] This incompatibility with hybrid functionals requires the use of GGA functionals that are usually less accurate than hybrid functionals.[56-57] The compatibility of atom-centered basis sets with hybrid functionals makes them more advantageous for crystalline systems where higher accuracy is needed to model the sometimes subtle features of the crystal lattice. For this reason, only atom-centered basis sets were used in this work and will be covered.

Atomic orbitals are defined with atom-centered basis sets built with either Slater-type orbitals (STOs) or Gaussian-type orbitals (GTOs). Although basis sets built with STOs yield higher computational accuracy, they have a high computational cost that only increases as a system grows. This high computational cost has contributed to the wider use of Gaussian-type basis sets.[58] The form of Gaussian-type orbitals is expressed in Cartesian coordinates for atom b as

$$g_{ijk} = N x_b^i y_b^j z_b^k e^{-\alpha\, r_b^2} \tag{3.12}$$

where N is a normalization constant, (x, y, z) are the Cartesian coordinates originating from b's nucleus, α is the orbital exponent, and r is the distance to the nucleus.

The smallest Gaussian-type basis sets, minimal basis sets, use single functions to describe the core and valence orbitals. Although they have a low computational cost, they are poor models for systems beyond a gas-phase atom.[59] Split-valence basis sets are larger than minimal basis sets and define the core orbitals with one function and valence orbitals with more than one function. The inclusion of more functions increases the accuracy of these models by allowing the electron density to shift away from the atom nucleus.[60-61] Considerable attention has focused towards the development of Gaussian-type basis sets that are optimized for solid-state calculations by improving the quality of functions used to describe crystalline orbitals.[62-63] Solid-state specific basis sets used in this research were developed by Peintinger, et al.[62] and Weigend, et al.[61]

Combining polarization and diffuse functions with minimal and split-valence basis sets can improve electronic structure calculations by including orbitals beyond the valence orbitals. Adding more orbitals provides electrons the freedom to shift towards bonding regions.[12, 58] Inclusion of these functions are especially important in models with delocalized electrons.[58, 64] Although it is reasonable to assume that increasing the number of polarization and diffuse functions results yields simulations with higher accuracy, this does not always hold true[65] and could complicate convergence as well as increase computational costs.[66]

Historically, modeling heavy atoms (transition metals and heavy metals) been challenging due to the computation costs associated with treating many electrons, the inability to account for relativistic effects, and complications in simulation convergence.[67] These difficulties have been reduced through the development of effective core potentials (ECPs).[10, 12, 67] ECPs reduce the computational costs of electronic structure calculations using a pseudopotential to describe the nucleus and all the core electrons. The pseudopotential replaces the second term of

the Hamiltonian in Eq. 3.4 with a modified potential that accounts for the interactions of the tightly-bound core electrons and the atomic nucleus. This frees up computational resources, by shrinking basis sets for heavy atoms, to focus on approximations of the effects on the valence electrons.[12, 68-69] Although ECPs greatly reduce the complications to modeling heavy atoms, they are built on the assumption that there is no overlap in the wavefunctions of core and valence electrons.[10]

3.5 Modeling Crystalline Materials with Solid-State Density Functional Theory

3.5.1 Periodic Boundary Conditions, Reciprocal Space, and Bloch's Theorem

Implementation of DFT methods in solid-state models is predicated on the periodicity of crystals.[70] These solid-state density functional theory (ss-DFT) models utilize periodic boundary conditions (PBCs) (**Figure 3-1**) to define an infinite crystal lattice with only the unit cell as the starting point.[12]
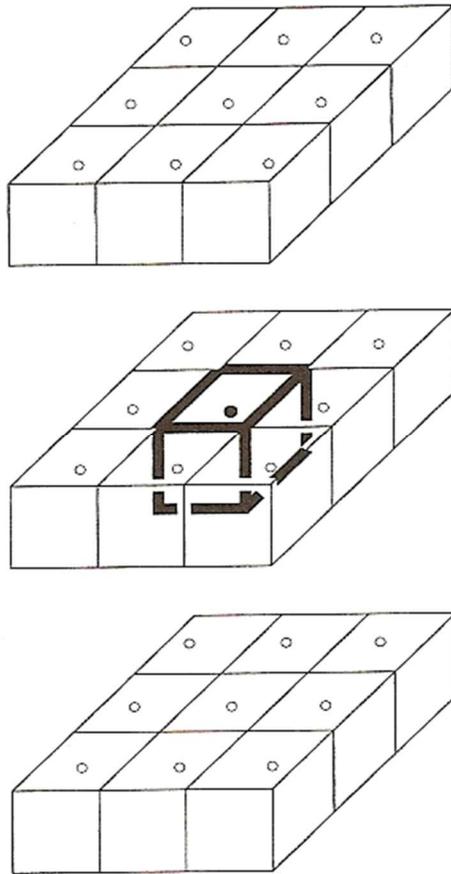
Figure 3-1 Example of a three-dimensional PBC. The bolded cell is surrounded by images generated with PBCs. Adapted from Reference 12.

Further simplification of ss-DFT simulations comes from the transformation of the unit cell in real space into reciprocal space with the unit cell defined as the Brillouin zone (BZ).[71] The BZ is defined with **k** (sampling) points and reciprocal space lattice vectors. The real space vectors of a unit cell (a, b, c) are transformed into reciprocal space lattice vectors (a^*, b^*, c^*) via

$$a^* = 2\pi \frac{b \times c}{a \cdot b \times c} \tag{3.13}$$

$$b^* = 2\pi \frac{c \times a}{b \cdot c \times a} \tag{3.14}$$

$$c^* = 2\pi \frac{a \times b}{c \cdot a \times b} \tag{3.15}$$

which demonstrates the inverse relationship between real and reciprocal space. In reciprocal space, atom-centered basis sets are transformed into periodic Bloch functions that define crystalline orbitals.[72-73] These Bloch functions will satisfy Bloch's theorem:

$$\Psi(\mathrm{r}) = e^{ikr} u(r) \tag{3.16}$$

where the number of **k** points needed to describe a solid system is determined when the periodicity of Bloch wavefunction matches the periodicity of the original crystal.[74] The periodicity of a wavefunction, R, is described with Bloch functions of the form

$$V(R + r) = V(r) \tag{3.17}$$

This periodic definition of $V(r)$ can be substituted into the Kohn-Sham Hamiltonian (Eq. 3.4) to determine the ground-state energy with the SCF method described in Sec. 3.2.1.

3.5.2 Computational Techniques Used Specifically in CRYSTAL Software

Solid-state density functional simulations were carried out with the commercial software package, CRYSTAL.[75-76] This software utilizes PBCs to reduce computational costs of crystalline models. In this research, CRYSTAL was used to model the crystalline structures and normal mode frequencies of solid pigments.

3.5.3 Geometry Optimizations

Prior to a geometry optimization, the number of **k** points needed to describe a system must be determined. In CRYSTAL,[75] this value is defined with shrinking factors via the keyword, SHRINK. The shrinking factors are used to construct the Pack-Monkhorst[77] grid that is proportional to the number of **k** points and reciprocal space. Shrinking factors are determined with single-point energy calculations that hold the geometry constant while manually changing the **k** points. Calculations with differing **k** points are carried out until the energy difference between two single-point calculations converges to limits set with the keyword, TOLDEE.

In a geometry optimization, a PES is constructed using a user-defined initial geometry.[78-80] The minima of PESs are found using a Quasi-Newton optimization scheme, where the gradients (analytical first-derivatives) of the PES are continuously evaluated until the stationary point of the PES is determined. During this optimization, the unit cell parameters and atomic positions are free to relax to the lowest electronic energy. Aspects of convergence on the PES (with the keywords in parentheses) that can be controlled include the gradient of the potential energy surface (TOLDEG) and the displacements along the PES (TOLDEX).[76]

3.5.4 Vibrational Normal Modes and Intensities

Harmonic frequencies are calculated at the Γ point in the Brillouin zone by displacing atomic positions along Cartesian coordinates to determine the gradient numerical derivatives of symmetrically unique atoms.[81-83] The second-order derivatives are found with numerical methods and used to construct the mass-weighted Hessian matrix (mass-weighted force constant) to generate the eigenvalues and eigenvectors of the vibrations. These eigenvalues and eigenvectors are then used to calculate the normal modes.

As demonstrated in **Chapter 2**, the activity of an IR normal mode is proportional to the change in dipole moments with respect to the atomic displacements.[84] In CRYSTAL, the intensities are determined using the Berry phase method[85] which evaluates the derivatives of the dipole moment with respect to the atomic displacements as differences in polarization between the equilibrium and distorted geometries. Intensities are printed with units of km mol^{-1} which are not directly comparable with experimental intensities (ε). Transformation of the simulated intensities is carried out using experimentally determined full-width half-maximum values of the spectral peaks from Lorentzian line-shape analyses.

In CRYSTAL, the Raman polarizability tensor, calculated with a coupled-perturbed Hartree-Fock / Kohn Sham method, is evaluated over the normal mode coordinates to calculate Raman intensities.[85-89] The intensities for a polycrystalline spectrum are found by averaging over all orientations of the tensor. Once Raman intensities are calculated, the keyword RAMEXP can be used to account for effects from temperature and the wavelength of the incident beam on the intensities.[90] The intensities generated with CRYSTAL are arbitrary in units and require normalization for comparison to experimental spectra. Scaling of the predicted intensities is

usually necessary, so comparisons are better focused on relative peak heights within a single

spectrum.

3.6 References

1.   Jepsen, P. U.; Clark, S. J., Precise Ab-Initio Prediction of Terahertz Vibrational Modes in Crystalline Systems. *Chem. Phys. Lett.* **2007**, *442*, 275-280.

2.   Schrödinger, E., Quantisierung Als Eigenwertproblem. *Annalen der Physik* **1926**, *384*, 361-376.

3.   Schrödinger, E., An Undulatory Theory of the Mechanics of Atoms and Molecules. *Physical Review* **1926**, *28*, 1049-1070.

4.   Atkins, P.; de Paula, J., *Atkins' Physical Chemistry*; OUP Oxford, 2010.

5.   Cohen, L., Hamiltonian Operators Via Feynman Path Integrals. *Journal of Mathematical Physics* **1970**, *11*, 3296-3297.

6.   Stebbings, R. F.; Dunning, F. B.; Dunning, F. W., *Rydberg States of Atoms and Molecules*; Cambridge University Press, 1983.

7.   Levine, I. N., *Quantum Chemistry*; Pearson Prentice Hall, 2009.

8.   Born, M.; Oppenheimer, R., Zur Quantentheorie Der Molekeln. *Annalen der Physik* **1927**, *389*, 457-484.

9.   Pilar, F. L., *Elementary Quantum Chemistry*; McGraw-Hill, 1990.

10.   Sholl, D.; Steckel, J. A., *Density Functional Theory: A Practical Introduction*; Wiley, 2009.

11.   Hehre, W. J., *A Guide to Molecular Mechanics and Quantum Chemical Calculations*; Wavefunction, 2003.

12.   Cramer, C. J., *Essentials of Computational Chemistry: Theories and Models*; Wiley, 2013.

13.   Kryachko, E. S., Hohenberg-Kohn Theorem. *International Journal of Quantum Chemistry* **1980**, *18*, 1029-1035.

14.   Sahni, V., The Hohenberg-Kohn Theorems and Kohn-Sham Density Functional Theory. In *Quantal Density Functional Theory*, Springer Berlin Heidelberg: Berlin, Heidelberg, 2004; pp 99-123.

15.   Epstein, S. T.; Rosenthal, C. M., The Hohenberg–Kohn Theorem. *The Journal of Chemical Physics* **1976**, *64*, 247-249.

16.   Kohn, W.; Sham, L. J., Self-Consistent Equations Including Exchange and Correlation Effects. *Physical Review* **1965**, *140*, A1133-A1138.

17.   Perdew, J. P.; Ruzsinszky, A.; Tao, J.; Staroverov, V. N.; Scuseria, G. E.; Csonka, G. I., Prescription for the Design and Selection of Density Functional Approximations: More Constraint Satisfaction with Fewer Fits. *The Journal of Chemical Physics* **2005**, *123*, 062201.

18.   Ruggiero, M. T.; Gooch, J.; Zubieta, J.; Korter, T. M., Evaluation of Range-Corrected Density Functionals for the Simulation of Pyridinium-Containing Molecular Crystals. *The Journal of Physical Chemistry A* **2016**, *120*, 939-947.

19.   Krukau, A. V.; Vydrov, O. A.; Izmaylov, A. F.; Scuseria, G. E., Influence of the Exchange Screening Parameter on the Performance of Screened Hybrid Functionals. *The Journal of Chemical Physics* **2006**, *125*, 224106.

20.   Henderson, T. M.; Izmaylov, A. F.; Scuseria, G. E.; Savin, A., Assessment of a Middle-Range Hybrid Functional. *Journal of Chemical Theory and Computation* **2008**, *4*, 1254-1262.

21.   Weintraub, E.; Henderson, T. M.; Scuseria, G. E., Long-Range-Corrected Hybrids Based on a New Model Exchange Hole. *Journal of Chemical Theory and Computation* **2009**, *5*, 754-762.

22.   Tao, J.; Perdew, J. P.; Staroverov, V. N.; Scuseria, G. E., Climbing the Density Functional Ladder: Nonempirical Meta--Generalized Gradient Approximation Designed for Molecules and Solids. *Physical Review Letters* **2003**, *91*, 146401.

23.   Zhao, Y.; Truhlar, D. G., The M06 Suite of Density Functionals for Main Group Thermochemistry, Thermochemical Kinetics, Noncovalent Interactions, Excited States, and Transition Elements: Two New Functionals and Systematic Testing of Four M06-Class Functionals and 12 Other Functionals. *Theoretical Chemistry Accounts* **2008**, *120*, 215-241.

24.   Kristyán, S.; Pulay, P., Can (Semi)Local Density Functional Theory Account for the London Dispersion Forces? *Chemical Physics Letters* **1994**, *229*, 175-180.

25.   Reilly, A. M.; Tkatchenko, A., Van Der Waals Dispersion Interactions in Molecular Materials: Beyond Pairwise Additivity. *Chemical Science* **2015**, *6*, 3289-3301.

26.   Otero-de-la-Roza, A.; LeBlanc, L. M.; Johnson, E. R., What Is "Many-Body" Dispersion and Should I Worry About It? *Physical Chemistry Chemical Physics* **2020**, *22*, 8266-8276.

27.   Elrod, M. J.; Saykally, R. J., Many-Body Effects in Intermolecular Forces. *Chemical Reviews* **1994**, *94*, 1975-1997.

28.   Becke, A. D.; Johnson, E. R., A Density-Functional Model of the Dispersion Interaction. *The Journal of Chemical Physics* **2005**, *123*, 154101.

29.   Grimme, S., Density Functional Theory with London Dispersion Corrections. *WIREs Computational Molecular Science* **2011**, *1*, 211-228.

30.   Grimme, S.; Ehrlich, S.; Goerigk, L., Effect of the Damping Function in Dispersion Corrected Density Functional Theory. *Journal of Computational Chemistry* **2011**, *32*, 1456-1465.

31.   Grimme, S., Semiempirical Gga-Type Density Functional Constructed with a Long-Range Dispersion Correction. *Journal of Computational Chemistry* **2006**, *27*, 1787-1799.

32.   Ziegler, T., Approximate Density Functional Theory as a Practical Tool in Molecular Energetics and Dynamics. *Chemical Reviews* **1991**, *91*, 651-667.

33.   Anisimov, V. I. In *First-Principles Calculations of the Electronic Structure and Spectra of Strongly Correlated Systems: Lda + U Method*, Berlin, Heidelberg, Springer Berlin Heidelberg: Berlin, Heidelberg, 1995; pp 106-116.

34.   Ceperley, D. M.; Alder, B. J., Ground State of the Electron Gas by a Stochastic Method. *Physical Review Letters* **1980**, *45*, 566-569.

35.   Perdew, J. P.; Wang, Y., Accurate and Simple Analytic Representation of the Electron-Gas Correlation Energy. *Physical Review B* **1992**, *45*, 13244-13249.

36.   Vosko, S. H.; Wilk, L.; Nusair, M., Accurate Spin-Dependent Electron Liquid Correlation Energies for Local Spin Density Calculations: A Critical Analysis. *Canadian Journal of Physics* **1980**, *58*, 1200-1211.

37.   Perdew, J. P.; Zunger, A., Self-Interaction Correction to Density-Functional Approximations for Many-Electron Systems. *Physical Review B* **1981**, *23*, 5048-5079.

38.   Perdew, J. P.; Chevary, J. A.; Vosko, S. H.; Jackson, K. A.; Pederson, M. R.; Singh, D. J.; Fiolhais, C., Atoms, Molecules, Solids, and Surfaces: Applications of the Generalized Gradient Approximation for Exchange and Correlation. *Physical Review B* **1992**, *46*, 6671-6687.

39.   Perdew, J. P.; Burke, K.; Ernzerhof, M., Generalized Gradient Approximation Made Simple. *Phys. Rev. Lett.* **1996**, *77*, 3865-3868.

40.   Becke, A. D., Density-Functional Exchange-Energy Approximation with Correct Asymptotic Behavior. *Physical Review A* **1988**, *38*, 3098-3100.

41.   Handy, N. C.; Cohen, A. J., Left-Right Correlation Energy. *Molecular Physics* **2001**, *99*, 403-412.

42.   Becke, A. D., Density-Functional Thermochemistry. Iii. The Role of Exact Exchange. *J. Chem. Phys.* **1993**, *98*, 5648-52.

43.   Becke, A. D., A New Mixing of Hartree–Fock and Local Density☐Functional Theories. *The Journal of Chemical Physics* **1993**, *98*, 1372-1377.

44.   Arbuznikov, A. V., Hybrid Exchange Correlation Functionals and Potentials: Concept Elaboration. *Journal of Structural Chemistry* **2007**, *48*, S1-S31.

45.   Stanton, J. F., A Chemist's Guide to Density Functional Theory by Wolfram Koch (German Chemical Society, Frankfurt Am Main) and Max C. Holthausen (Humbolt University Berlin). Wiley-Vch: Weinheim. 2000. Xiv + 294 Pp. $79.95. Isbn 3-527-29918-1. *Journal of the American Chemical Society* **2001**, *123*, 2701-2701.

46.   Becke, A. D.; Johnson, E. R., A Unified Density-Functional Treatment of Dynamical, Nondynamical, and Dispersion Correlations. *The Journal of Chemical Physics* **2007**, *127*, 124108.

47.   Lee, C.; Yang, W.; Parr, R. G., Development of the Colle-Salvetti Correlation-Energy Formula into a Functional of the Electron Density. *Physical Review B* **1988**, *37*, 785-789.

48.   Adamo, C.; Barone, V., Toward Reliable Density Functional Methods without Adjustable Parameters: The Pbe0 Model. *The Journal of Chemical Physics* **1999**, *110*, 6158-6170.

49.   Campo, J. M. d.; Gázquez, J. L.; Trickey, S. B.; Vela, A., Non-Empirical Improvement of Pbe and Its Hybrid Pbe0 for General Description of Molecular Properties. *The Journal of Chemical Physics* **2012**, *136*, 104108.

50.   Perdew, J. P.; Ernzerhof, M.; Burke, K., Rationale for Mixing Exact Exchange with Density Functional Approximations. *The Journal of Chemical Physics* **1996**, *105*, 9982-9985.

51.   Hafner, J., Ab-Initio Simulations of Materials Using Vasp: Density-Functional Theory and Beyond. *Journal of Computational Chemistry* **2008**, *29*, 2044-2078.

52.   Giannozzi, P., et al., Quantum Espresso: A Modular and Open-Source Software Project for Quantum Simulations of Materials. *Journal of Physics: Condensed Matter* **2009**, *21*, 395502.

53.   Dovesi, R., et al., Quantum-Mechanical Condensed Matter Simulations with Crystal. *Wiley Interdiscip. Rev.: Comput. Mol. Sci.* **2018**, *8*, e1360.

54.   Frisch, M. J., et al. *Gaussian 16 Rev. C.01*, Wallingford, CT, 2016.

55.   Kühne, T. D., et al., Cp2k: An Electronic Structure and Molecular Dynamics Software Package - Quickstep: Efficient and Accurate Electronic Structure Calculations. *The Journal of Chemical Physics* **2020**, *152*, 194103.

56.   Tosoni, S.; Tuma, C.; Sauer, J.; Civalleri, B.; Ugliengo, P., A Comparison between Plane Wave and Gaussian-Type Orbital Basis Sets for Hydrogen Bonded Systems: Formic Acid as a Test Case. *The Journal of Chemical Physics* **2007**, *127*, 154102.

57.   Booth, G. H.; Tsatsoulis, T.; Chan, G. K.-L.; Grüneis, A., From Plane Waves to Local Gaussians for the Simulation of Correlated Periodic Systems. *The Journal of Chemical Physics* **2016**, *145*, 084111.

58.   Evarestov, R. A., *Quantum Chemistry of Solids: The Lcao First Principles Treatment of Crystals*; Springer Berlin Heidelberg, 2007.

59.   Engel, T.; Reid, P., *Physical Chemistry*; Pearson Education, 2012.

60.   Schaefer, A.; Horn, H.; Ahlrichs, R., Fully Optimized Contracted Gaussian Basis Sets for Atoms Lithium to Krypton. *J. Chem. Phys.* **1992**, *97*, 2571-7.

61.   Weigend, F.; Ahlrichs, R., Balanced Basis Sets of Split Valence, Triple Zeta Valence and Quadruple Zeta Valence Quality for H to Rn: Design and Assessment of Accuracy. *Physical Chemistry Chemical Physics* **2005**, *7*, 3297-3305.

62.   Peintinger, M. F.; Oliveira, D. V.; Bredow, T., Consistent Gaussian Basis Sets of Triple-Zeta Valence with Polarization Quality for Solid-State Calculations. *J. Comput. Chem.* **2013**, *34*, 451-459.

63.   Laun, J.; Vilela Oliveira, D.; Bredow, T., Consistent Gaussian Basis Sets of Double- and Triple-Zeta Valence with Polarization Quality of the Fifth Period for Solid-State Calculations. *Journal of Computational Chemistry* **2018**, *39*, 1285-1290.

64.   Frisch, M. J.; Pople, J. A.; Binkley, J. S., Self‐Consistent Molecular Orbital Methods 25. Supplementary Functions for Gaussian Basis Sets. *The Journal of Chemical Physics* **1984**, *80*, 3265-3269.

65.   Beran, G. J. O., Modeling Polymorphic Molecular Crystals with Electronic Structure Theory. *Chemical Reviews* **2016**, *116*, 5567-5613.

66.   Papajak, E.; Zheng, J.; Xu, X.; Leverentz, H. R.; Truhlar, D. G., Perspectives on Basis Sets Beautiful: Seasonal Plantings of Diffuse Basis Functions. *Journal of Chemical Theory and Computation* **2011**, *7*, 3027-3034.

67.   Xu, X.; Truhlar, D. G., Performance of Effective Core Potentials for Density Functional Calculations on 3d Transition Metals. *Journal of Chemical Theory and Computation* **2012**, *8*, 80-90.

68.   Seminario, J. M., Chapter 6 - Ab Initio and Dft for the Strength of Classical Molecular Dynamics. In *Theoretical and Computational Chemistry*, Balbuena, P. B.; Seminario, J. M., Eds. Elsevier: 1999; Vol. 7, pp 187-229.

69.   Metz, B.; Stoll, H.; Dolg, M., Small-Core Multiconfiguration-Dirac–Hartree–Fock-Adjusted Pseudopotentials for Post-D Main Group Elements: Application to Pbh and Pbo. *J. Chem. Phys.* **2000**, *113*, 2563-2569.

70.   Kratzer, P.; Neugebauer, J., The Basics of Electronic Structure Theory for Periodic Systems. *Frontiers in Chemistry* **2019**, *7*.

71.   Kittel, C.; Kittel, U. C., *Introduction to Solid State Physics*; Wiley, 1971.

72.   Gazalet, J.; Dupont, S.; Kastelik, J. C.; Rolland, Q.; Djafari-Rouhani, B., A Tutorial Survey on Waves Propagating in Periodic Media: Electronic, Photonic and Phononic Crystals. Perception of the Bloch Theorem in Both Real and Fourier Domains. *Wave Motion* **2013**, *50*, 619-654.

73.   Ashcroft, N. W.; Mermin, N. D., *Solid State Physics*; Harcourt College Publishers: Orlando, 1976.

74.   Woolfson, M., Solid State Physics 3. Theory of Lattice Dynamics in the Harmonic Approximation by A. A. Maradudin, E. W. Montroll, G. H. Weiss and I. P. Ipatova. *Acta Crystallographica Section A* **1973**, *29*, 314.

75.   Dovesi, R., et al., Quantum☐Mechanical Condensed Matter Simulations with Crystal. *Wiley Interdiscip. Rev. Comput. Mol. Sci.*, *0*, e1360.

76.   Dovesi, R., et al., Crystal17 User's Manual. University of Torino, Torino, 2017.

77.   Monkhorst, H. J.; Pack, J. D., Special Points for Brillouin-Zone Integrations. *Phys. Rev. B: Condens. Matter* **1976**, *13*, 5188-5192.

78.   Leach, A. R., *Molecular Modelling: Principles and Applications*; Prentice Hall, 2001.

79.   Wittbrodt, J. M.; Schlegel, H. B., Estimating Stretching Force Constants for Geometry Optimization. *Journal of Molecular Structure: THEOCHEM* **1997**, *398-399*, 55-61.

80.   Bernhard Schlegel, H., Estimating the Hessian for Gradient-Type Geometry Optimizations. *Theoretica chimica acta* **1984**, *66*, 333-340.

81.   Pascale, F.; Zicovich-Wilson, C. M.; Gejo, F. L.; Civalleri, B.; Orlando, R.; Dovesi, R., The Calculation of the Vibrational Frequencies of Crystalline Compounds and Its Implementation in the Crystal Code. *J. Comput. Chem.* **2004**, *25*, 888-897.

82.   Wilson, E. B.; Decius, J. C.; Cross, P. C., *Molecular Vibrations: The Theory of Infrared and Raman Vibrational Spectra*; McGraw-Hill, 1955.

83.   Zicovich-Wilson, C. M.; Pascale, F.; Roetti, C.; Saunders, V. R.; Orlando, R.; Dovesi, R., Calculation of the Vibration Frequencies of A-Quartz: The Effect of Hamiltonian and Basis Set. *J. Comp. Chem.* **2004**, *25*, 1873-1881.

84.   Izmaylov, A. F.; Scuseria, G. E., Analytical Infrared Intensities for Periodic Systems with Local Basis Sets. *Physical Review B* **2008**, *77*, 165131.

85.   Maschio, L.; Kirtman, B.; Orlando, R.; Rerat, M., Ab Initio Analytical Infrared Intensities for Periodic Systems through a Coupled Perturbed Hartree-Fock/Kohn-Sham Method. *J. Chem. Phys.* **2012**, *137*, 204113/1-204113/11.

86.   Ferrero, M.; Rérat, M.; Orlando, R.; Dovesi, R., The Calculation of Static Polarizabilities of 1-3d Periodic Compounds. The Implementation in the Crystal Code. *J. Comput. Chem.* **2008**, *29*, 1450-1459.

87.   Ferrero, M.; Rérat, M.; Orlando, R.; Dovesi, R., Coupled Perturbed Hartree-Fock for Periodic Systems: The Role of Symmetry and Related Computational Aspects. *J. Chem. Phys.* **2008**, *128*, 014110.

88.   Ferrero, M.; Rérat, M.; Kirtman, B.; Dovesi, R., Calculation of First and Second Static Hyperpolarizabilities of One- to Three-Dimensional Periodic Compounds. Implementation in the Crystal Code. *J. Chem. Phys.* **2008**, *129*, 244110.

89.   Maschio, L.; Kirtman, B.; Rérat, M.; Orlando, R.; Dovesi, R., *Ab Initio* Analytical Raman Intensities for Periodic Systems through a Coupled Perturbed Hartree-Fock/Kohn-Sham Method in an Atomic Orbital Basis. Ii. Validation and Comparison with Experiments. *J. Chem. Phys.* **2013**, *139*, 164102.

90.   Prosandeev, S. A.; Waghmare, U.; Levin, I.; Maslar, J., First-Order Raman Spectra of $\mathrm{a}{\mathrm{B}}_{1/2}^{\ensuremath{'}}{\mathrm{B}}_{1/2}^{\ensuremath{''}}{\mathrm{O}}_{3}$ Double Perovskites. *Physical Review B* **2005**, *71*, 214307.

Chapter 4. Terahertz Spectroscopy and Quantum Mechanical Simulations of Crystalline Copper-containing Historical Pigments

Terahertz spectroscopy, a non-invasive and non-destructive analytical technique used in art conservation and restoration, can provide compelling data concerning the composition and condition of culturally valuable and historical objects. Terahertz spectral databases of modern and ancient artists' pigments exist, but lack explanations for the origins of the unique spectral features. Solid-state density functional theory simulations can provide insight into the molecular and intermolecular forces that dominate the observed absorption features, as well as reveal deviations from simple harmonic vibrational behavior that can complicate these spectra. The characteristic terahertz spectra of solid azurite, malachite, and verdigris are presented here, along with simulations of their crystalline structures and sub-3.0 THz lattice vibrations. The powerful combination of theory and experiment enables unambiguous spectral assignment of these complex materials and highlights the challenges that anharmonic peak broadening in organic-containing materials may present in the construction of reference pigment databases.

4.1 Introduction

In the field of heritage science, spectroscopy is an invaluable analytical approach for understanding the component materials of an object, previous restoration and conservation efforts, and artistic technique. The intricacy of the materials and the mixtures used in this field is such that many parameters like sample type, degree of aging, humidity exposure, and temperature control can influence the dielectric behavior of the sample response. While many different spectroscopy types have been applied, terahertz (THz) vibrational spectroscopy (≤ 100 cm^{-1}) has gained recent popularity as a powerful nondestructive technique for understanding the intermolecular interactions in solid materials.[1-3] Terahertz radiation is an ideal source of information for characterization of various fragile artifacts, especially pigment identification, a crucial step for properly addressing dating, authenticity, and other problems encountered in heritage science.[4-7]

Standard techniques for pigment identification include X-ray fluorescence spectroscopy (XRF), mass spectrometry, as well as infrared and Raman spectroscopies.[8,9] The information provided by XRF is not always sufficient to identify the components of the paint under investigation, considering different pigments may contain the same elements and light elements cannot be detected.[10] Mass spectrometry is unfavorable because analysis requires destruction of a small piece from the sample. Fourier-transform infrared spectroscopy (FTIR) has previously been used for pigment identification; however, several classes of inorganic pigments are inactive in the mid-infrared (mid-IR) region (e.g. oxides or sulfides) and cannot be identified with this technique. In these cases, complementary Raman spectroscopy is used to overcome such limitations.[11] Nevertheless, Raman spectra can be affected by fluorescence signal in the presence of organic compounds or ligands despite efforts made to reduce this phenomenon using

mathematical or instrumental methods.[12] Raman analysis also requires vigilance to avoid damage due to higher photon energies.

Less investigated than the mid-IR, the near-infrared (near-IR) and far-infrared (far-IR) regions have also been used for pigment identification. Near-IR is useful when performing non-invasive reflection spectroscopy, as combination and overtone bands found in this spectral range have lower absorptions than fundamental ones in the mid-IR and are not distorted by specular reflection. However, only functional groups containing NH, CH, OH, CO, and CC bonds produce significant vibrational bands in this range, limiting applicability.[13] The spectral region accessed by far-FTIR has been exploited for overcoming the limitations of mid-FTIR and Raman spectroscopy in pigment identification, especially for inorganic compounds derived from minerals.[14,15] Far-IR radiation excites lattice vibrations that are unique to specific solid-state structures with significantly different frequencies found for crystalline polymorphs of the same chemical compound.

Only recently has THz spectroscopy for pigment analysis and identification proven to be an effective tool for characterizing vibrational modes including rotational, torsional, phonon, and intra-/intermolecular modes.[16,17] Compared to the mid-IR, where high-energy molecular vibrations are observed, THz spectroscopy can detect low-energy vibrations and weak interactions between molecules, such as those due to hydrogen bonding and van der Waals forces.[18] The THz response is linked to the collective behavior of molecules in their environment and can be used to distinguish polymorphism and chirality.[19-24] Moreover, pulsed terahertz time-domain spectroscopy (THz-TDS) directly provides the value of the electric field amplitude of the electromagnetic radiation, rather than optical intensity. Accordingly, both the amplitude and phase of the electric field in the frequency domain are directly obtained by Fourier transform

with no need for Kramers-Kronig relations to calculate the desired optical constant from a measured one.[16]

The spectroscopic examination of pigments and their specific fingerprints in the THz region will help researchers understand the source of contrast in the THz frequency parametric images obtained with THz imaging systems, which have been exploited for analysis of artworks.[5, 25-28] Clarification of the spectral features for individual pigments is an essential component in identification of pigment mixtures used by artists, or the degradation of pigments over time. To aid in this understanding, experimental mid-FTIR, Raman, and THz spectral databases of artists' materials have been constructed[29-32] and further spectroscopic examinations of pigments followed.[30, 33-35] These works demonstrate that individual pigments have unique spectral fingerprints, but accurate interpretation of spectra can be difficult given their complexities. Solid-state density functional theory (ss-DFT) simulations are beneficial in elucidating these measured spectra that are comprised of pure or mixed pigments and indistinguishable by visual inspection.[33] Simulating THz frequencies with ss-DFT allows for consideration of the connection between chemical identity, crystalline structure, and the intermolecular forces that collectively contribute to the characteristic THz vibrational spectra of these materials.

In this study, experimental THz spectra and ss-DFT simulations of the crystalline structures and the sub-3.0 THz lattice vibrations of azurite $[Cu_3(CO_3)_2(OH)_2]$, malachite $[Cu_2CO_3(OH)_2]$, and neutral verdigris $[Cu(CH_3COO)_2 \cdot H_2O]$ are presented. The visual appearance and crystal structures of these historical pigments are shown in **Figure 4-1**. Previous studies have reported the THz vibrational spectra of these pigments, but no terahertz-focused computational work has appeared for copper carbonate and acetate complexes, though other

frequency ranges have been considered.[5, 34-43] Related computational analyses of the THz spectra of similar copper sulfate compounds[44] and other dyes[45] have been published.
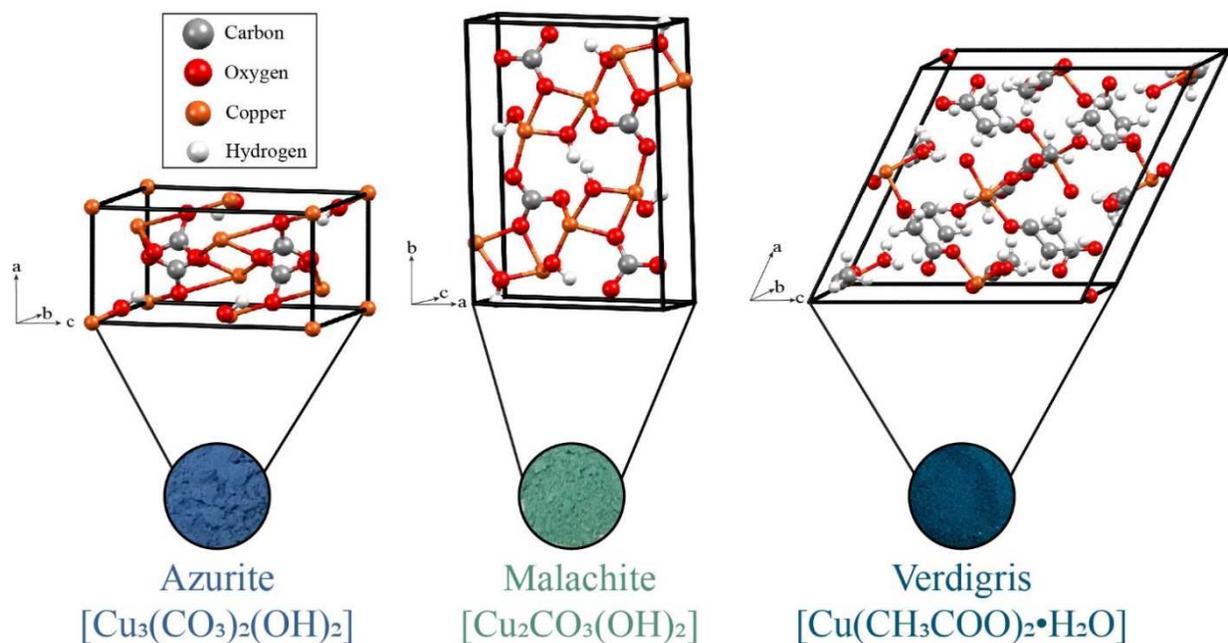
Figure 4-1 Powder samples and crystallographic unit cells of azurite, malachite, and neutral verdigris.

4.2 Materials and Methods

4.2.1 Sample Preparation

Azurite, malachite, and verdigris were purchased from Kremer Pigments Inc. (Munich, Germany), while powdered high-density polyethylene (HDPE) was obtained from Sigma Aldrich (St. Louis, USA). All were used without further purification. The purity and type of verdigris was determined by powder X-ray diffraction (XRD) on a Bruker D8 Advance powder diffractometer using Cu Kα radiation (λ=1.5406 Å), considering that various forms of basic and neutral copper acetate can form upon exposure to different atmospheric or synthetic conditions.[46]

Powder data was collected and analyzed with Diffrac Plus XRD Commander software (version 2.6.1) and compared to calculated powder patterns produced in Mercury CSD 3.10.251 using the published single-crystal X-ray diffraction data for synthetic neutral verdigris. The powder patterns shown in **Figure. A1** in **Appendix A** confirm that the purchased verdigris is the neutral hydrate form.

The pigments and HDPE were mixed and ground to reduce particle size and avoid scattering loss during the measurements, then pressed into uniform pellets with a 13 mm diameter and thicknesses varying from 2.72 to 3.52 mm, (specifics can be found in **Table A1** in **Appendix A**). Particle size effects are a known complication in terahertz spectra of pigments[47], but no corrections for such phenomena have been implemented here. All THz spectra were measured with pellets made with a 20 % w/w concentration of pigment.

4.2.2 THz-TDS Experimental Setup

Terahertz spectra were measured on a TPS Spectra 3000 time-domain spectroscopy system from TeraView (Cambridge, UK) at room temperature (293 K). The system relies on GaAs laser-gated photoconductive antennas (PC-antennas) for terahertz generation and detection, with an 80 fs Ti:Sa ultrashort pulsed laser operating at 800 nm with a repetition rate of 76 MHz used as a probe/pump beam. The THz-TDS system offers a useful frequency range of $0.06 – 3.0$ THz ($2.0 – 100.0$ cm^{-1}) with a maximum dynamic range around 75 dB and a rapid scan mode up to 30 scans/second. Further system specifications can be found elsewhere.[48] The THz signals were acquired from the pellets in a transmission configuration, with the pellet placed between the transmitter and the receiver at the focal point of the THz radiation, midway between two off-axis parabolic mirrors. The pellet, emitter, and receiver are located inside a closed

system compartment, which has been purged with dry air to eliminate undesired absorption bands from water vapor in the acquired THz spectra.

The THz signals were acquired within an 18.8660 ps time-delay window with a time step of 0.0097 ps (1943 data-points, 0.0063 THz step in frequency domain; 100 signal averaging for each pellet). Three THz spectra were recorded for each pellet for a total of 27 THz spectra. Terahertz absorbance spectra were obtained through the base-10 logarithm of the ratio of the sample single-beam spectrum divided by a reference single-beam spectrum. The THz signal collected from a 100 % wt. HDPE pellet (400 mg) was used as the reference signal for this calculation.

4.2.3 Solid-State DFT Simulation Parameters

Solid-state DFT simulations were performed using the CRYSTAL17 software package.[49-50] The Becke−3−Lee−Yang–Parr[51] (B3LYP) exchange correlation functional was used in conjunction with the POB-TZVP basis set for Cu[52], and the Ahlrichs valence triple zeta (VTZ) basis set with polarization functions[53] for all other atom types. Geometry optimizations were carried out using starting atomic positions, lattice dimensions, and space groups from previously published room temperature crystallographic data.[54-57] The structures were allowed to fully relax to energetic minima within the limits of the applied space group symmetries and an energy convergence threshold of $\Delta E < 10^{-8}$ hartree. Harmonic limit vibrational analyses were performed on the optimized structures at the same level of theory, but with an energy convergence of $\Delta E < 10^{-10}$ hartree. Numerical derivatives for frequencies were calculated using the central-difference formula with two displacements per Cartesian axis, per atom.[58] Infrared intensities were calculated using the Berry phase approach.[59-60] Longitudinal optical/transverse optical (LO/TO) phonon splitting was evaluated in the frequency analysis through charge localization via Wannier

functions and coupled-perturbed Hartree-Fock calculation of the high-frequency dielectric tensor.[61-63] Calculated dielectric tensor components and LO/TO split frequencies for all three systems can be found in **Tables A2-A5** in the Supporting Information. In all calculations, tolerances for the Coulomb and exchange series integrals were set to 10^{-10}, 10^{-10}, 10^{-10}, 10^{-12}, and 10^{-24} hartree. The simulations used a pruned DFT integration grid comprised of 99 radial and 1454 angular points. The appropriate number of k-points in the Monkhorst-Pack scheme[64] was determined by monitoring total energy convergence for each solid.

4.3 Results and Discussion

4.3.1 Terahertz Absorption Spectra of Azurite, Malachite, and Verdigris

The THz spectra of malachite, azurite, and verdigris are presented in **Figure 4-2**. While no significant features could be detected in the THz spectrum of malachite, two sharp and distinctive features are found in the spectrum of azurite at 1.83 THz and 2.23 THz (61.0 cm^{-1} and 74.4 cm^{-1}). The THz spectrum of verdigris is more complex than the other pigments and features a sharp peak at 1.02 THz (34.0 cm^{-1}) with a broad (but structured) band found between 1.7 and 2.6 THz (56.7 cm^{-1} and 86.7 cm^{-1}). The conspicuous absence of absorption peaks in the malachite spectrum and the presence of both narrow and broad peaks in the azurite and verdigris data are unexpected observations that deserve greater consideration.

It is common for the THz spectra of molecular solids to exhibit relatively broad line widths that can necessitate the use of cryogenic cooling to uncover hidden features.[65-66] However, narrow bands have previously been observed for various crystalline inorganic pigments at room temperature.[5, 31, 33] In azurite, the first peak at 1.83 THz has a line width of only 0.025 THz (all peak shapes determined via least squares fitting to Lorentzian functions, shown in Supporting Information) making it as sharp as those measured in low-temperature

samples of organic molecular crystals. The thermal broadening of spectral peaks is linked to the anharmonicity of the potential energy surfaces governing the vibrational motions in the solid state, with those most harmonic in nature producing the narrowest line widths. Thus, the THz spectrum of azurite suggests the forces in this solid are largely harmonic in character.

In contrast, the THz spectrum of verdigris shows a mixture of line widths, indicating that different vibrations exist in potential energy surfaces with unequal anharmonicities. The lowest frequency peak has a FWHM of 0.045 THz, ~80 % broader than what is found in azurite, but still narrower than most room-temperature THz data. A peak fitting analysis of the broad feature between 1.7 and 2.6 THz found that the partially resolved absorption features can be well modeled using three peaks with an average linewidth of 0.167 THz, nearly seven times broader than that seen in azurite. The origins of these significantly greater linewidths may be rooted in the acetate polyatomic ion components of verdigris, since they resemble the organic species in the molecular solids that typically show broadened THz spectra. This suggests that the organic components in verdigris are the main contributors to the observed peak broadening and the higher frequency features are the widest due to localization of the underlying vibrations within the organic acetate species.

The lack of any obvious discrete absorptions in the malachite THz spectrum is surprising given its chemical similarity to azurite. An initial supposition is that this may be related to the existence of a large amount of vibrational anharmonicity, resulting in extreme peak broadening and consequent obscuring of the spectral pattern. While sample cooling to liquid nitrogen temperatures or below may help resolve some of the spectral features, emphasis here is on the analysis of ambient temperature THz data since that is the information that would be collected for *in situ* art objects. The underlying chemical origins of these unique THz spectra, including

the lack of THz frequency features, can be explored and revealed using quantum mechanical

simulations to model the structures and vibrational motions of these crystalline systems.
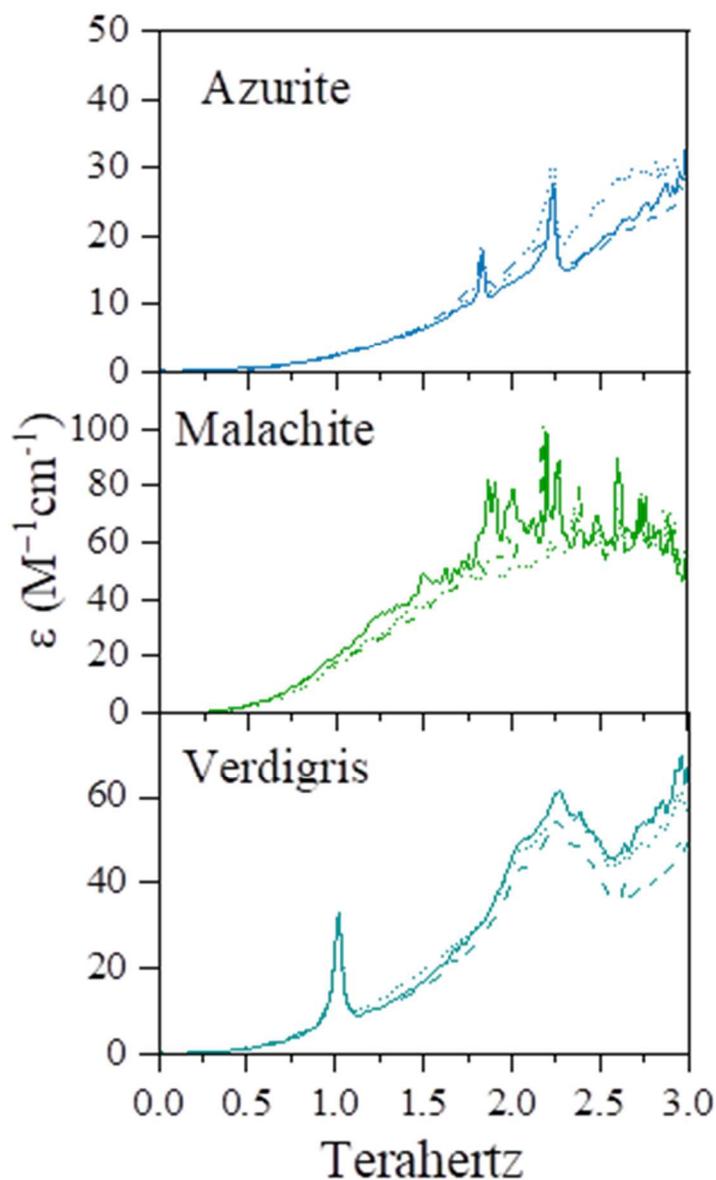
Figure 4-2 Averaged experimental THz spectra of azurite, malachite, and verdigris collected for each sample pellet detailed in Table A1. Each trace represents the averaged data from triplicate measurements of each pellet.

57

4.3.2 Computational Structural and Vibrational Analysis

Solid-state density functional theory simulated lattice parameters are listed in **Table 4-1**

alongside the experimental lattice parameters. The calculated crystal structures are all in

excellent agreement with the observed structures, yielding dimensional errors of ≤ 1.25 % in all

cases. The internal structures of the solids, which can be compared in terms of intramolecular

bond lengths, angles, and dihedrals, also match well with experimental data (see **Appendix A**

Tables A6-A8). The only significant differences occur in the dihedral angles involving

hydrogens due to the poor positional data available in the X-ray crystallographic structures. The

high-quality optimized structures of all three samples were used in the vibrational analyses of

their solid-state motions.

Table 4-1 Space groups, Z values, and comparison of experimental and calculated lattice parameters for azurite, malachite, and verdigris.

	Azurite		Malachite		Verdigris	
space group	P2$_1$/c		P2$_1$/a		C2/c	
Z	2		4		8	
	Exp.	Calcd.	Exp.	Calcd.	Exp.	Calcd.
a (Å)	5.01	5.00	9.50	9.43	13.17	13.31
b (Å)	5.85	5.86	11.97	11.95	8.56	8.66
c (Å)	10.35	10.48	3.24	3.26	13.86	13.92
α (°)	90	90	90	90	90	90
β (°)	92.41	91.63	98.75	98.11	117.02	116.05
γ (°)	90	90	90	90	90	90
V (Å^3)	303.22	306.61	364.35	363.56	1392.20	1440.99

SS-DFT vibrational simulations of the crystalline pigments allowed for assignment of

their observed THz spectra, as shown in **Figure 4-3**. To facilitate comparison with theory, simple

empirical baseline corrections were applied to the experimental spectra with details provided in

Figure A2 of **Appendix A**. The experimental and simulated spectra for malachite are not shown because no significant peaks occur in the experiment or in the simulation (see **Appendix A** for details). Lists of all the calculated infrared-active vibrations of the three pigments including mode character descriptions are provided in **Table 4-2,** a list of the Raman-active modes and animations of the IR-active modes are given in **Appendix A**. While TO/LO vibrational energy splitting magnitudes were calculated for each solid, it was found to be a negligible factor in all cases, with spectroscopically unresolved frequency splittings of ≤ 0.015 THz.

Table 4-2 Calculated infrared-active vibrations (sub-3.0 THz) for crystalline azurite, malachite, and verdigris.

	Frequency (THz)	(cm^{-1})	Intensity (km/mol)	Mode Symmetry	Primary Mode Character
Azurite	1.87	62.43	1.60	A_u	CO_3^{-2} rotation about *b*-axis, anti-parallel translation of Cu^{2+} layers along *a*-axis
	2.30	76.81	5.76	B_u	CO_3^{-2} rotation about *a*-axis, anti-parallel translation of Cu^{2+} layers along *b*-axis
Malachite	2.47	82.39	0.42	A_u	CO_3^{-2} rotation about *b*-axis, translation of Cu^{2+} & OH^- along *c*-axis
Verdigris	1.09	36.52	1.49	B_u	Out-of-phase translation of Cu^{2+} along the *b*-axis
	1.11	36.93	0.48	A_u	Out-of-phase translation of Cu^{2+} along *a*-axis
	1.97	65.59	0.41	A_u	Out-of-phase Cu^{2+} translation along the *c*-axis, rigid rotation of CH_3COO^- and H_2O
	2.12	70.55	6.99	A_u	Rigid rotation of CH_3COO^-
	2.15	71.55	5.72	B_u	Torsion of Cu⋯O−C−O dihedral
	2.34	77.90	0.00[a]	A_u	Torsion of Cu⋯O−C−O dihedral
	2.35	78.23	3.52	B_u	Rigid rotation of CH_3COO^- and H_2O, torsion of Cu⋯O−C−O dihedral in $CH_3COO^- \perp$ to *a-c* plane
	2.51	83.75	6.09	B_u	Rotation of CH_3COO^-, torsion of O⋯Cu⋯O−C dihedral
	2.74	91.46	0.02	A_u	Torsion of Cu⋯O−C−O dihedral

[a]mode predicted to be infrared active, but of negligible intensity

In azurite, the two sharp peaks readily observed in the experimental spectrum at 1.83 and 2.23 THz can be assigned to the 1.87 and 2.30 THz calculated vibrations, respectively. Although the absolute simulated intensities for azurite are higher than the experimentally observed, the relative intensities between the peaks are as expected. The small shift of the calculated modes to higher frequency versus experiment (2.7 % on average) is consistent with there being mostly harmonic curvature in the potential energy surfaces governing these vibrational motions. The azurite absorptions have been assigned to rotation of the CO_3^{-2} ions about the b- and a-axes, along with simultaneous translational motions of the Cu^{2+} ion layers along the a-axis and b-axis of the azurite crystal. These same types of vibrational motions can be found in malachite but are very weakly IR-allowed and lead to its indistinct THz absorption spectrum shown in **Figure 4-2**. Although azurite and malachite are chemically similar (contain the same ionic species) and belong to the same space group, the crystal packing in each solid is markedly different. This leads to unique sets of intra- and intermolecular interactions in each solid, resulting in two obviously different spectra, and highlighting the specific sensitivities of THz spectroscopy versus mid-IR approaches. The quantum mechanical simulations of malachite make it clear that the absence of spectral features is not due to anharmonicity-induced line broadening, but rather is a product of its crystal structure simply not yielding IR-active modes of significant strength in this region.
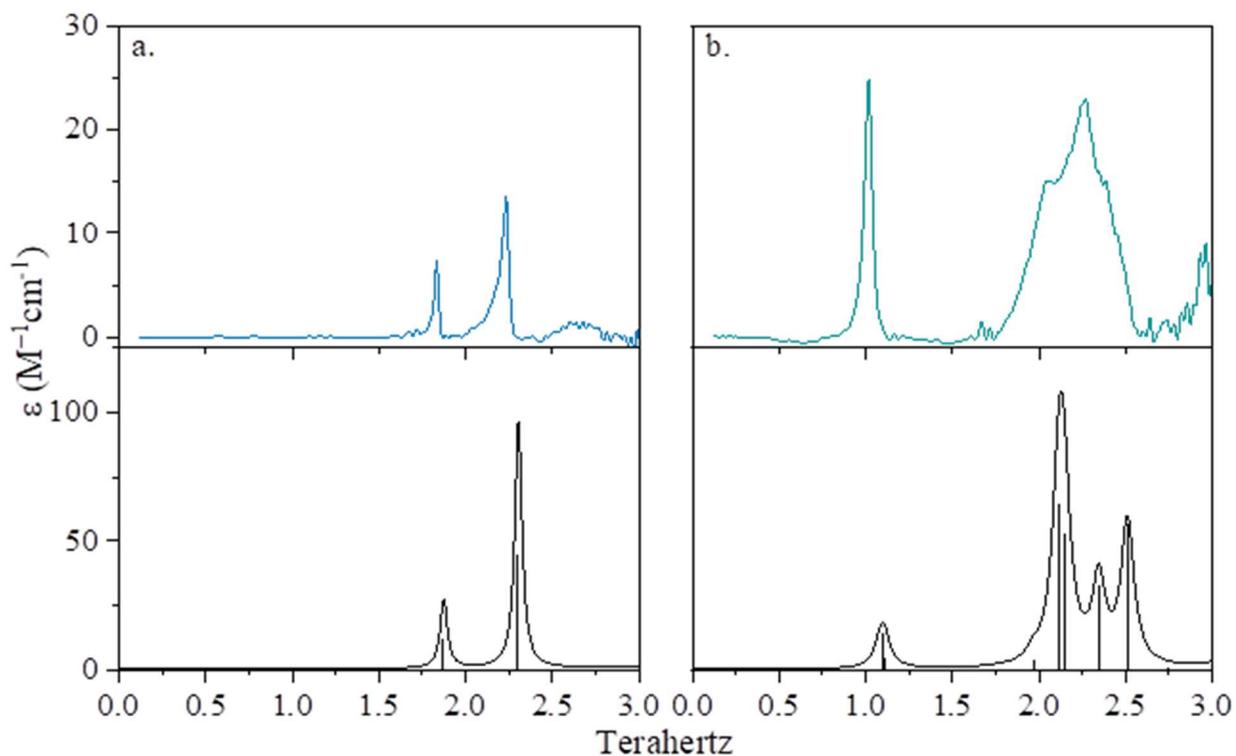
Figure 4-3 Experimental and simulated (black) THz data for azurite (a) and for verdigris (b). The simulated spectra were convolved using Lorentzian line shapes with a FWHM of 0.025 THz for azurite and 0.045 THz for verdigris.

The terahertz spectrum of verdigris shown in panel (b) of **Figure 4-3** has a greater number of absorptions due to the increased molecular complexity of the crystal components. The verdigris spectrum contains one sharp feature at 1.02 THz and a broad absorption with a maximum at 2.27 THz and shoulders at 2.05 and 2.39 THz. The predicted frequencies are in general agreement with these observations, having 2 nearly degenerate vibrations contributing to the first feature (1.09 and 1.11 THz). The less resolved absorption centered near 2.25 THz is more difficult to assign to specific lattice motions since five lattice vibrations (see **Table 4-2**) contribute infrared intensity in this region. The only fully resolved peak in the verdigris spectrum

at 1.02 THz is overestimated by 7.8 % in the simulation (average of the two underlying

vibrations), a nearly 3 times greater shift than in azurite. The significant difference in the

simulated harmonic frequencies as compared to the experiment is consistent with the broader

peak widths indicating increased vibrational anharmonicity is present in the verdigris lattice.

The relatively narrow width of the lowest frequency feature in verdigris suggests that the

vibrational mode is still primarily harmonic in nature, yet less so than azurite. This ranking of

anharmonic character is supported by inspection of potential energy curves constructed by

scanning along the normal mode eigenvectors of the lowest IR-active vibrations in each solid.

The results in **Figure 4-4** clearly show that while the real potential energy curves of azurite and

malachite are essentially harmonic (dashed lines), the equivalent for verdigris deviates

significantly towards anharmonicity at displacement vector magnitudes that replicate zero-point

energy levels (displacement factor of approximately 1.75 on each curve). The unveiling of

vibrational anharmonicity in specific modes, a consistent shifting of the harmonic simulations,

and the broadened features at higher frequencies, collectively demonstrate that verdigris is a

crystalline solid with a very complicated multi-dimensional potential energy surface resulting

from inorganic-organic component interactions. Even motions involving translation of the Cu^{2+}

ions, that are largely harmonic, are perturbed through coupling with anharmonic vibrations

originating in the organic acetate species.
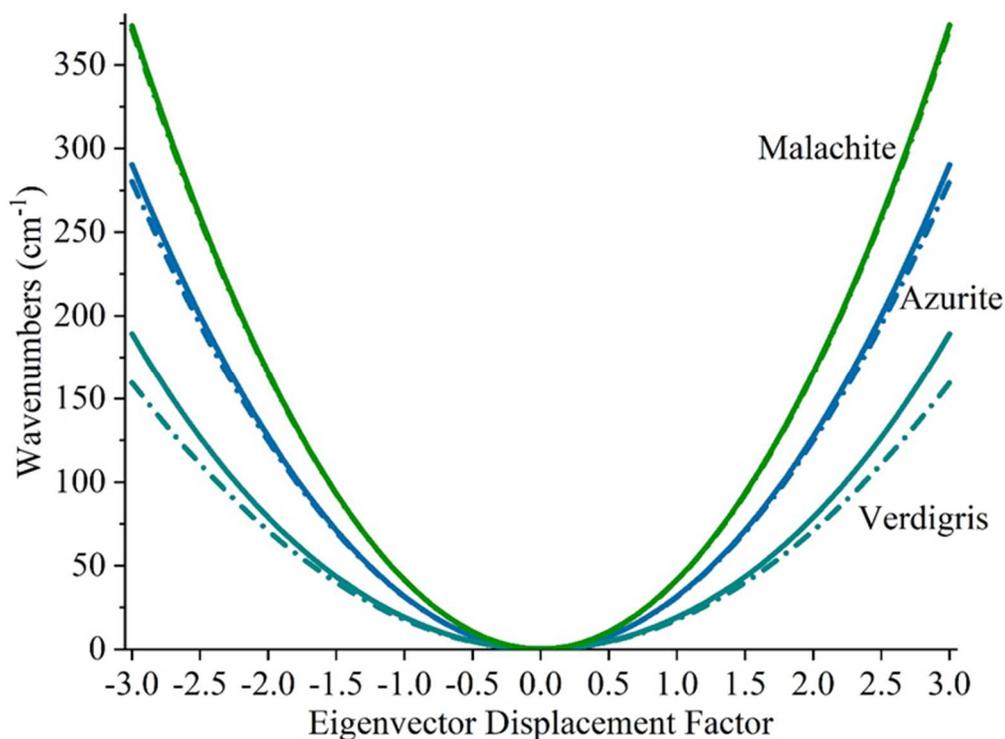
Figure 4-4 Calculated harmonic (dashed) and anharmonic (solid) potential energy curves of the lowest IR-active mode in azurite (1.87 THz), malachite (2.47 THz), and verdigris (1.09 THz).

4.4 Conclusions

Elucidation of the lattice vibration foundations of the experimental terahertz spectral features for the copper-containing pigments azurite, malachite, and verdigris has been achieved using solid-state density functional theory. The ss-DFT characterization of these complex materials greatly increases our understanding of the intermolecular forces contributing to the observed terahertz spectra, especially in situations where distinct absorption features are missing despite expectations or in chemically complex materials where harmonic and anharmonic vibrational behaviors intersect.

The differences in the observed terahertz spectra of chemically related azurite and malachite were rationalized via quantum mechanical simulations of the structures and lattice vibrations. The spectrum of verdigris was assigned by ss-DFT simulations, but the overlap of numerous absorption features in the experimental spectrum due to the presence of considerable anharmonicity, precluded exact vibrational assignments. Comparison of the observed line shapes and calculated potential energy curves for the low-frequency lattice vibrations demonstrate that verdigris exhibits far greater anharmonic character than malachite or azurite.

An appreciation for the chemical origins of terahertz spectra assists in the rigorous analysis of complicated spectra of pigment mixtures and encourages the use of terahertz spectroscopy in the characterization of colorants that are visually indistinguishable. The characterization of these three prominent historical pigments allows for an increased understanding of the intermolecular interactions within the solids that must be accounted for in the construction and validation of spectral databases.

4.5 References

1.   Jepsen, P. U.; Clark, S. J., Precise Ab-Initio Prediction of Terahertz Vibrational Modes in Crystalline Systems. *Chem. Phys. Lett.* **2007**, *442*, 275-280.

2.   Trafela, T.; Mizuno, M.; Fukunaga, K.; Strlič, M., Quantitative Characterisation of Historic Paper Using Thz Spectroscopy and Multivariate Data Analysis. *Applied Physics A* **2013**, *111*, 83-90.

3.   Baxter, J. B.; Guglietta, G. W., Terahertz Spectroscopy. *Anal. Chem.* **2011**, *83*, 4342-4368.

4.   Bardon, T.; May, R. K.; Taday, P. F.; Strlic, M., Systematic Study of Terahertz Time-Domain Spectra of Historically Informed Black Inks. *Analyst* **2013**, *138*, 4859-4869.

5.   Jackson, J. B.; Bowen, J.; Walker, G.; Labaune, J.; Mourou, G.; Menu, M.; Fukunaga, K., A Survey of Terahertz Applications in Cultural Heritage Conservation Science. *IEEE Trans. Terahertz Sci. Technol.* **2011**, *1*, 220-231.

6.   Fukunaga, K.; Ogawa, Y.; Hayashi, S. i.; Hosako, I., Application of Terahertz Spectroscopy for Character Recognition in a Medieval Manuscript. *IEICE Electronics Express* **2008**, *5*, 223-228.

7.   Cosentino, A., Terahertz and Cultural Heritage Science: Examination of Art and Archaeology. *Technologies* **2016**, *4*, 6.

8.   Buzzini, P.; Suzuki, E., Forensic Applications of Raman Spectroscopy for the in Situ Analyses of Pigments and Dyes in Ink and Paint Evidence. *J. Raman Spectrosc.* **2016**, *47*, 16-27.

9.   Dowsett, M.; Adriaens, A., The Role of Sims in Cultural Heritage Studies. *Nucl. Instrum. Methods Phys. Res., Sect. B* **2004**, *226*, 38-52.

10.   Neelmeijer, C.; Brissaud, I.; Calligaro, T.; Demortier, G.; Hautojärvi, A.; Mäder, M.; Martinot, L.; Schreiner, M.; Tuurnala, T.; Weber, G., Paintings— a Challenge for Xrf and Pixe Analysis. *X-Ray Spectrom.* **2000**, *29*, 101-110.

11.   Bruni, S.; Cariati, F.; Casadio, F.; Toniolo, L., Identification of Pigments on a Xv Century Illuminated Parchment by Raman and Ftir Microspectroscopies. *Spectrochim. Acta, Part A* **1999**, *55*, 1371-1377.

12.   Kendix, E. L.; Prati, S.; Joseph, E.; Sciutto, G.; Mazzeo, R., Atr and Transmission Analysis of Pigments by Means of Far Infrared Spectroscopy. *Anal. Bioanal. Chem.* **2009**, *394*, 1023-1032.

13.   Vagnini, M.; Miliani, C.; Cartechini, L.; Rocchi, P.; Brunetti, B. G.; Sgamellotti, A., Ft-Nir Spectroscopy for Non-Invasive Identification of Natural Polymers and Resins in Easel Paintings. *Anal. Bioanal. Chem.* **2009**, *395*, 2107-2118.

14.   Brusentsova Tatiana, N.; Peale Robert, E.; Maukonen, D.; Harlow George, E.; Boesenberg Joseph, S.; Ebel, D., Far Infrared Spectroscopy of Carbonate Minerals. *Am. Mineral.* **2010**, *95*, 1515.

15.   Kendix, E.; Moscardi, G.; Mazzeo, R.; Baraldi, P.; Prati, S.; Joseph, E.; Capelli, S., Far Infrared and Raman Spectroscopy Analysis of Inorganic Pigments. *J. Raman Spectrosc.* **2008**, *39*, 1104-1112.

16.   El Haddad, J.; Bousquet, B.; Canioni, L.; Mounaix, P., Review in Terahertz Spectral Analysis. *TrAC, Trends Anal. Chem.* **2013**, *44*, 98-105.

17.   Jepsen, P. U.; Cooke, D. G.; Koch, M., Terahertz Spectroscopy and Imaging – Modern Techniques and Applications. *Laser Photonics Rev.* **2011**, *5*, 124-166.

18.   Mizuno, M.; Fukunaga, K.; Saito, S.; Hosako, I., Analysis of Calcium Carbonate for Differentiating between Pigments Using Terahertz Spectroscopy. *Journal of the European Optical Society Rapid Publications* **2009**, *4*.

19.   Ruggiero, M. T.; Sibik, J.; Zeitler, J. A.; Korter, T. M., Examination of L-Glutamic Acid Polymorphs by Solid-State Density Functional Theory and Terahertz Spectroscopy. *J Phys Chem A* **2016**, *120*, 7490-5.

20.   Azuri, I.; Hirsch, A.; Reilly, A. M.; Tkatchenko, A.; Kendler, S.; Hod, O.; Kronik, L., Terahertz Spectroscopy of 2,4,6-Trinitrotoluene Molecular Solids from First Principles. *Beilstein J Org Chem.* **2018**, *14*, 381-388.

21.   Taday, P. F.; Bradley, I. V.; Arnone, D. D.; Pepper, M., Using Terahertz Pulse Spectroscopy to Study the Crystalline Structure of a Drug: A Case Study of the Polymorphs of Ranitidine Hydrochloride. *J. Pharm. Sci.* **2003**, *92*, 831-838.

22.   Zeitler, J. A.; Taday, P. F.; Newnham, D. A.; Pepper, M.; Gordon, K. C.; Rades, T., Terahertz Pulsed Spectroscopy and Imaging in the Pharmaceutical Setting □ a Review. *J. Pharm. Pharmacol.* **2007**, *59*, 209-223.

23.   Albert, S., et al., Synchrotron-Based Highest Resolution Terahertz Spectroscopy of the N24 Band System of 1,2-Dithiine ($C_4h_4s_2$): A Candidate for Measuring the Parity Violating Energy Difference between Enantiomers of Chiral Molecules. *J. Phys. Chem. Lett* **2016**, *7*, 3847-3853.

24.   Zhang, F.; Wang, H.-W.; Tominaga, K.; Hayashi, M.; Lee, S.; Nishino, T., Elucidation of Chiral Symmetry Breaking in a Racemic Polymer System with Terahertz Vibrational Spectroscopy and Crystal Orbital Density Functional Theory. *J. Phys. Chem. Lett* **2016**, *7*, 4671-4676.

25.   Guillet, J.-P.; Roux, M.; Wang, K.; Ma, X.; Fauquet, F.; Balacey, H.; Recur, B.; Darracq, F.; Mounaix, P., Art Painting Diagnostic before Restoration with Terahertz and Millimeter Waves. *J. Infrared Millim. Terahertz Waves* **2017**, *38*, 369-379.

26.   Adam, A. J. L.; Planken, P. C. M.; Meloni, S.; Dik, J., Terahertz Imaging of Hidden Paint Layers on Canvas. *Optics Express* **2009**, *17*, 3407-3416.

27.   Koch Dandolo, C. L.; Filtenborg, T.; Skou-Hansen, J.; Jepsen, P. U., Analysis of a Seventeenth-Century Panel Painting by Reflection Terahertz Time-Domain Imaging (Thz-Tdi): Contribution of Ultrafast Optics to Museum Collections Inspection. *Appl. Phys. A* **2015**, *121*, 981-986.

28.   Koch-Dandolo, C. L.; Filtenborg, T.; Fukunaga, K.; Skou-Hansen, J.; Jepsen, P. U., Reflection Terahertz Time-Domain Imaging for Analysis of an 18th Century Neoclassical Easel Painting. *Applied Optics* **2015**, *54*, 5123-5129.

29.   Price, B. A.; Pretzel, B., Infrared and Raman Users Group Spectral Database. 2009 ed.; Philadelphia, 2007; Vol. 1 & 2.

30.   Fukunaga, K., Terahertz Spectral Database: Construction of Open Terahertz Spectral Database. *J. Nat. Inst. Inf. Commun. Technol* **2008**, *55*, 61-66.

31.   Fukunaga, K.; Picollo, M., Terahertz Spectroscopy Applied to the Analysis of Artists' Materials. *Appl. Phys. A* **2010**, *100*, 591-597.

32.   Castro, K.; Pérez-Alonso, M.; Rodríguez-Laso, M. D.; Fernández, L. A.; Madariaga, J. M., On-Line Ft-Raman and Dispersive Raman Spectra Database of Artists' Materials (E-Visart Database). *Analytical and Bioanalytical Chemistry* **2005**, *382*, 248-258.

33.   Yang, Y.; Zhai, D.; Zhang, Z.; Zhang, C., Thz Spectroscopic Identification of Red Mineral Pigments in Ancient Chinese Artworks. *J. Infrared Millim. Terahertz Waves* **2017**, *38*, 1232-1240.

34.   Ha, T.; Lee, H.; Sim, K. I.; Kim, J.; Jo, Y. C.; Kim, J. H.; Baek, N. Y.; Kang, D.-i.; Lee, H. H., Optimal Methodologies for Terahertz Time-Domain Spectroscopic Analysis of Traditional Pigments in Powder Form. *J. Korean Phys. Soc.* **2017**, *70*, 866-871.

35.   Hong, T., et al., Terahertz Time-Domain and Fourier-Transform Infrared Spectroscopy of Traditional Korean Pigments. *J. Korean Chem. Soc.* **2014**, *64*, 727-731.

36.   Li, C. Y.; Shi, N. C.; Li, G. H.; Zhang, Z. W.; Gu, A.; Lei, Y.; Zhang, C. L., Study of the Traditional Chinese Pigments by Terahertz Time-Domain and Fourier-Transform Infrared Spectroscopy. *Applied Optics and Photonics China (AOPC2017)* **2017**, *10459*, 8.

37.   Bardon, T.; May, R. K.; Jackson, J. B.; Beentjes, G.; de Bruin, G.; Taday, P. F.; Strlič, M., Contrast in Terahertz Images of Archival Documents—Part I: Influence of the Optical Parameters from the Ink and Support. *J. Infrared Millim. Terahertz Waves* **2017**, *38*, 443-466.

38.   Abraham, E.; Fukunaga, K., Terahertz Imaging Applied to the Examination of Artistic Objects. *Stud. Conserv.* **2015**, *60*, 343-352.

39.   Fukunaga, K.; Hosako, I., Innovative Non-Invasive Analysis Techniques for Cultural Heritage Using Terahertz Technology. *C. R. Phys.* **2010**, *11*, 519-526.

40.   Bette, S.; Kremer, R. K.; Eggert, G.; Tang, C. C.; Dinnebier, R. E., On Verdigris, Part I: Synthesis, Crystal Structure Solution and Characterisation of the 1-2-0 Phase $(Cu_3(Ch_3coo)_2(Oh)_4)$. *Dalton Trans.* **2017**, *46*, 14847-14858.

41.   Lakshmanan, B. R., Infra-Red Absorption Spectra of Copper Acetate, Copper Propionate, and Copper Butyrate. *Jl of IISc* **1956**, *38*.

42.   Frost, R. L.; Martens, W. N.; Rintoul, L.; Mahmutagic, E.; Kloprogge, J. T., Raman Spectroscopic Study of Azurite and Malachite at 298 and 77 K. *J. Raman Spectrosc.* **2002**, *33*, 252-259.

43.   Goldsmith, J. A.; Ross, S. D., The Infra-Red Spectra of Azurite and Malachite. *Spectrochim. Acta, Part A* **1968**, *24*, 2131-2137.

44.   Ruggiero, M. T.; Bardon, T.; Strlic, M.; Taday, P. F.; Korter, T. M., Assignment of the Terahertz Spectra of Crystalline Copper Sulfate and Its Hydrates Via Solid-State Density Functional Theory. *J. Phys. Chem. A* **2014**, *118*, 10101-10108.

45.   Squires, A. D.; Lewis, R. A.; Zaczek, A. J.; Korter, T. M., Distinguishing Quinacridone Pigments Via Terahertz Spectroscopy: Absorption Experiments and Solid-State Density Functional Theory Simulations. *J. Phys. Chem. A* **2017**, *121*, 3423-3429.

46.   Scott, D. A.; Taniguchi, Y.; Koseto, E., The Verisimilitude of Verdigris: A Review of the Copper Carboxylates. *Stud. Conserv.* **2001**, *46*, 73-91.

47.   Bardon, T.; May, R. K.; Taday, P. F.; Strlič, M., Influence of Particle Size on Optical Constants from Pellets Measured with Terahertz Pulsed Spectroscopy. *IEEE Transactions on Terahertz Science and Technology* **2016**, *6*, 408-413.

48.   Sleiman, J., Bou. Terahertz Imaging and Spectroscopy: Application to Defense and Security in Front of the Examination Panel. Université de Bordeaux, 2016.

49.   Dovesi, R., et al., Quantum-Mechanical Condensed Matter Simulations with Crystal. *Wiley Interdisciplinary Reviews: Computational Molecular Science* **2018**, *8*, e1360.

50.   Dovesi, R., et al., Crystal17 User's Manual. University of Torino, Torino, 2017.

51.   Becke, A. D., Density-Functional Thermochemistry. Iii. The Role of Exact Exchange. *J. Chem. Phys.* **1993**, *98*, 5648-52.

52.	Peintinger, M. F.; Oliveira, D. V.; Bredow, T., Consistent Gaussian Basis Sets of Triple-Zeta Valence with Polarization Quality for Solid-State Calculations. *J. Comput. Chem.* **2013**, *34*, 451-459.

53.	Schaefer, A.; Horn, H.; Ahlrichs, R., Fully Optimized Contracted Gaussian Basis Sets for Atoms Lithium to Krypton. *J. Chem. Phys.* **1992**, *97*, 2571-7.

54.	Belokoneva, E. L.; Gubina, Y. K.; Forsyth, J. B., The Charge Density Distribution and Antiferromagnetic Properties of Azurite $Cu_3[Co_3]_2(Oh)_2$. *Phys. Chem. Miner.* **2001**, *28*, 498-507.

55.	Zigan, F.; Joswig, W.; Schuster, H. D.; Mason, S. A., Refinement of the Structure of Malachite, $Cu_2(Oh)_2co_3$, Using Neutron Diffraction. *Z. Kristallogr., Kristallgeom., Kristallphys., Kristallchem.* **1977**, *145*, 412-26.

56.	Hibbs, D. E.; Kolitsch, U.; Leverett, P.; Sharpe, J. L.; Williams, P. A., Hoganite and Paceite, Two New Acetate Minerals from the Potosi Mine, Broken Hill, Australia. *Mineral. Mag.* **2002**, *66*, 459-464.

57.	Rule, K. C.; Reehuis, M.; Gibson, M. C. R.; Ouladdiaf, B.; Gutmann, M. J.; Hoffmann, J. U.; Gerischer, S.; Tennant, D. A.; Süllow, S.; Lang, M., Magnetic and Crystal Structure of Azurite $Cu_3(Co_3)_2(Oh)_2$ as Determined by Neutron Diffraction. *Physical Review B* **2011**, *83*, 104401.

58.	Pascale, F.; Zicovich-Wilson, C. M.; Gejo, F. L.; Civalleri, B.; Orlando, R.; Dovesi, R., The Calculation of the Vibrational Frequencies of Crystalline Compounds and Its Implementation in the Crystal Code. *J. Comput. Chem.* **2004**, *25*, 888-897.

59.	Zicovich-Wilson, C. M.; Pascale, F.; Roetti, C.; Saunders, V. R.; Orlando, R.; Dovesi, R., Calculation of the Vibration Frequencies of A-Quartz: The Effect of Hamiltonian and Basis Set. *Journal of Computational Chemistry* **2004**, *25*, 1873-1881.

60.	Noel, Y.; Zicovich-Wilson, C. M.; Civalleri, B.; D'Arco, P.; Dovesi, R., Polarization Properties of Zno and Beo: An *Ab Initio* Study through the Berry Phase and Wannier Functions Approaches. *Phys. Rev. B: Condens. Matter Mater. Phys.* **2002**, *65*, 1-9.

61.	Ferrero, M.; Rérat, M.; Orlando, R.; Dovesi, R., The Calculation of Static Polarizabilities of 1-3d Periodic Compounds. The Implementation in the Crystal Code. *J. Comput. Chem.* **2008**, *29*, 1450-1459.

62.	Ferrero, M.; Rérat, M.; Orlando, R.; Dovesi, R., Coupled Perturbed Hartree-Fock for Periodic Systems: The Role of Symmetry and Related Computational Aspects. *J. Chem. Phys.* **2008**, *128*, 014110.

63.	Ferrero, M.; Rérat, M.; Kirtman, B.; Dovesi, R., Calculation of First and Second Static Hyperpolarizabilities of One- to Three-Dimensional Periodic Compounds. Implementation in the Crystal Code. *The Journal of Chemical Physics* **2008**, *129*, 244110.

64.	Monkhorst, H. J.; Pack, J. D., Special Points for Brillouin-Zone Integrations. *Phys. Rev. B: Condens. Matter* **1976**, *13*, 5188-5192.

65.	Shen, Y. C.; Upadhya, P. C.; Linfield, E. H.; Davies, A. G., Temperature-Dependent Low-Frequency Vibrational Spectra of Purine and Adenine. *Appl. Phys. Lett.* **2003**, *82*, 2350-2352.

66.   Takahashi, M.; Ishikawa, Y.; Nishizawa, J.-i.; Ito, H., Low-Frequency Vibrational Modes of Riboflavin and Related Compounds. *Chem. Phys. Lett.* **2005**, *401*, 475-482.

Chapter 5. Quantitative Analysis of Minium and Vermilion Mixtures Using Low-Frequency Vibrational Spectroscopy

Low-frequency vibrational spectroscopy offers a compelling solution for the non-destructive and non-invasive study of pigments in historical artifacts by revealing the characteristic sub-200 cm^{-1} spectral features of component materials. The techniques of terahertz time-domain spectroscopy (THz-TDS) and low-frequency Raman spectroscopy (LFRS) are complementary approaches to accessing this spectral region and are valuable tools for artifact identification, conservation, and restoration. In this investigation of historical pigments, pure and mixed samples of minium (Pb_3O_4) and vermilion (HgS) were studied using a combination of THz-TDS and LFRS experiments to determine the limits of detection (LOD) and quantitation (LOQ) for each compound with both methods. The measurements were also supported using solid-state density functional theory simulations of the pigment structures and vibrations, enabling spectral peaks to be assigned to specific atomic motions in these solids. The THz-TDS LOD was found to be similar for both minium and vermilion at 6 % by mass on average. In comparison, LFRS was found to be more sensitive to both pigments, particularly to the presence of vermilion with an LFRS LOD of 0.2 %. These results demonstrate that low-frequency vibrational spectroscopy can be used for successful quantitative analysis of pigment mixtures and provide reliable new data for use in heritage science.

5.1 Introduction

In heritage science, there is demand for non-invasive and non-destructive techniques for determination of chemically specific data regarding composition and condition of cultural and historical artifacts.[1] Proper characterization and identification of pure and mixed colorants in these artifacts are crucial steps in determining provenance and designing appropriate protocols for conservation and restoration efforts.[2-5] Various approaches for pigment identification are currently employed and include X-ray fluorescence spectroscopy[6] and secondary-ion mass spectrometry[7], as well as near-infrared (near-IR)[8], mid-IR[9], and Raman spectroscopies.[10-14] However, low-frequency vibrational spectroscopies that access ≤ 200 cm^{-1} (≤ 6 THz) vibrational motions in solid samples have attracted great attention in recent years.[15-20] Terahertz time-domain spectroscopy (THz-TDS) and low-frequency Raman spectroscopy (LFRS) are appealing methods for *in situ* studies of artifacts because of their specificities, acquisition times, and non-destructive approaches.[21-23] The utilization of these emerging techniques has been driven largely by improvements in instrumentation capabilities and costs,[24-25] and advances in the quantum mechanical solid-state simulations used to assign and interpret the spectral data.[26-27]

The use of THz-TDS and LFRS methods in heritage science is predicated on the existence of high-quality spectra for pure pigments. Experimental THz-TDS and Raman (though not specifically at low frequencies) spectral databases of artists' materials including pigments, glues, and binding media have been constructed.[28-29] These databases primarily focus on pure materials; however, pigment mixtures were commonly used to achieve desired hues in artifacts.[3] Accurate characterization of pigment mixtures is important not only for identification of artifact composition, but also to provide better understanding of artists' palettes in original works, monitoring degradation of pigments over time, detection of previous damage including prior

restoration and conservation efforts, and artifact authentication.[2, 30-31] Raman and infrared spectroscopies have been utilized in the analyses of various pigment mixtures and binders, as demonstrated in recent reports.[32-34] From an analytical perspective, the multiple spectral signals from mixtures often present a practical challenge for spectroscopic analysis as compared to neat samples. Low-frequency vibrational spectroscopy has the potential to aid in pigment mixture analyses given the already reported successes using THz-TDS and LFRS for molecular solids, including pharmaceuticals.[35-39] Investigating pigments and their mixtures with low-frequency vibrational spectroscopy could also prove useful in elucidating the contrast mechanisms underlying the 2D and 3D images of artworks that have been collected using THz radiation.[40-42]

An important aspect of pure and mixed pigment analyses is determination of the sensitivity of an instrument to particular analytes, which is classified in terms of the limits of detection (LOD) and quantitation (LOQ). The pigment composition of binary mixtures can be estimated from THz-TDS and LFRS spectra using calibration curves specific to the experiment and based on standard samples of known mixture proportions. As for all spectroscopies, determination of LOD and LOQ for THz-TDS and LFRS measurements is dependent on the signal-to-noise ratio of the data and the degree of spectral separation between individual component peaks. The LOD and LOQ can be dramatically different between THz-TDS and LFRS investigations of the same sample since the defining spectroscopic selection rules of each technique yields a unique pattern of peak positions and intensities.

Computational chemistry is becoming an increasingly important part of heritage science given the complexity of artists' materials and the subtle variations in composition that can be significant.[43] The foundational THz-TDS and LFRS experimental spectra of pigments are invaluable to their analytical applications,[44] but detailed explanations are lacking for the origins of

the spectral features specific to each sample. The use of advanced computational models is particularly necessary in low-frequency vibrational spectroscopy of solids, where tabulated characteristic group frequency assignments are not possible due to the complex nature of the lattice vibrations. These complications can be overcome with solid-state density functional theory (ss-DFT) simulations of crystalline pigments, which are based on periodic boundary conditions.[45] These types of calculations explicitly include effects of the solid-state environment on the pigment structure and dynamics, and provide insight into the rotational, torsional, and other phonon modes that dominate the low-frequency spectral region and enable unambiguous spectral assignments.[24, 25] Simulating THz-TDS and LFRS spectra with ss-DFT highlights the connections between chemical identity, crystalline structure, and the intermolecular forces that collectively contribute to the characteristic vibrational spectra of these materials. This approach has been successfully demonstrated on both organic[46] and inorganic pigments.[47-48]

In this work, the focus is on the ancient pigments minium (Pb_3O_4) and vermilion (HgS) because of their frequent use together in artists' palettes and their visual similarity necessitating analytical evaluation for quantification.[5, 9, 34, 49-51] Previous terahertz[44, 52-55] and Raman[56] studies have reported the spectra of pure minium and vermilion, while mixtures of the two have been studied using other techniques including mid-range Raman spectroscopy[57] and first-derivative reflectance visible spectroscopy.[58] Here, these inorganic crystalline pigments were investigated using a combination of THz-TDS, LFRS, and ss-DFT to fully characterize their sub-200 cm^{-1} vibrations. Data from pure samples and binary mixtures of minium and vermilion enabled LOD and LOQ values for the pigments to be established for both THz-TDS and LFRS measurements. The ss-DFT spectral simulations enabled complete assignments of the observed spectral features.

Figure 5-1 Bulk powder samples and crystallographic unit cells of minium and vermilion.

5.2 Materials and Methods

5.2.1 Sample Preparation

Minium and vermilion were purchased from Natural Pigments Inc. (Willets, CA, USA). Micro-fine polytetrafluoroethylene (PTFE) was obtained from Spurlock Specialty Tools (Vacaville, CA, USA). All were used without further purification. Binary mixtures of minium:vermilion with various pigment mass ratios (1:0, 2:1, 3:2, 1:1, 2:3, 1:2, and 0:1) were prepared and homogenized with a mortar and pestle.

5.2.2 X-Ray Powder Diffraction

The purity and bulk crystallinity of powdered minium and vermilion were verified by powder X-ray diffraction (PXRD) on a Bruker D2 Phaser with a LYKXEYE 1D silicon strip detector using Cu Kα radiation ($\lambda = 1.5406$ Å). Experimental PXRD patterns were compared to predicted patterns produced in Mercury[59] using the published 290 K single-crystal X-ray diffraction data for minium[60] and vermilion.[61] These comparisons are shown in **Figure B1** of **Appendix B.**

5.2.3 Terahertz Time-Domain Spectroscopy

Room temperature (290 K) THz-TDS spectra were obtained with a commercial TeraFlash spectrometer from Toptica Photonics (Munich, Germany) based on a $\lambda = 1.5$ μm femtosecond fiber

laser and photoconductive antennas for both THz generation and detection. The pure pigments and pigment mixtures were combined with a PTFE matrix (1.0 wt. % concentration of sample) and ground to reduce particle size and avoid scattering losses during the measurements. No corrections for particle size effects, density fluctuations within the pellet, or non-uniform spatial distribution of the pigments were used in the final data analysis.[62] The samples were pressed into uniform pellets at 2000 psig (details are listed in **Table B1** of **Appendix B**) and a reference pellet of pure PTFE was made under the same conditions. The sample chamber was purged with dry N_2 gas during the experiments to prevent interference from atmospheric water vapor.

THz-TDS waveforms were collected over a 70 ps time window, but the time-domain data for each pellet was truncated to 23 ps past the terahertz pulse center, prior to analysis, to avoid pulse reflections from the pellet surface. The ratio of the Fourier-transformed (Hanning window) data of the sample and reference produced spectra ranging from 10 to 140 cm^{-1} (0.30 to 4.20 THz) with a spectral resolution of 1.45 cm^{-1}. The spectral extinction coefficient (ε) is reported in units of M^{-1}cm^{-1} with concentration (M) expressed in terms of crystallographic unit cell concentration (formula units of $Z = 4$ for minium and $Z = 3$ for vermilion). In order to enhance the signal-to-noise ratio for each sample, three replicate spectra were recorded for each pellet and averaged.

5.2.4 Low-Frequency Raman Spectroscopy

LFRS spectra of powdered pure and mixed samples were collected at 290 K using an Ondax (Monrovia, CA, USA) THz-Raman system. Laser excitation was centered at 784.7 nm and used in a backscattering geometry with fiber-coupling to an Andor Shamrock 750 spectrograph equipped with a cooled (200 K) iDus 416 CCD. A maximum laser power of 10 mW was maintained to avoid sample heating and degradation. Each individual spectrum consisted of 225 acquisitions with 1 second collection windows. The spectral range was 10 to 400 cm^{-1} with an

effective spectral resolution of 0.7 cm^{-1}. Five replicate LFRS spectra were recorded and averaged, then intensity normalized to 1000.0.

5.2.5 Data Analysis of Mixture Spectra

Mean scattering or absorption values and their standard deviations were calculated from replicate measurements of each sample. The 2nd derivative method for baseline detection[63] was used to baseline correct the THz-TDS spectra while no baseline corrections were applied to the LFRS spectra. THz-TDS and LFRS calibration curves, used to determine LOD and LOQ values, were constructed for both pigments using the relative peak areas for both minium and vermilion in the sample spectra and the weight percentages of each pigment. Relative peak areas were determined by fitting Lorentzian profiles to the THz-TDS data after baseline correction, and Voigt profiles to the LFRS data prior to intensity normalization. The LOD and LOQ values for both THz-TDS and LFRS were determined using previously described methodologies.[34, 39, 64-67]

5.2.6 Computational Details

All ss-DFT simulations were performed with the CRYSTAL17 software package, which utilizes periodic boundary conditions to represent the crystalline lattice.[68-69] The PBE[70] (Perdew-Burke-Ernzerhof) and PBE0[71] density functionals were used with the POB-TZVP basis set[72] for non-metal atoms (oxygen and sulfur) in both minium and vermilion, and effective core potential basis sets were used for lead[73-74] and mercury[75] atoms. Simulations for minium accounted for the coexisting divalent Pb (II) and tetravalent Pb (IV) atoms in the crystal lattice. Full geometry optimizations with an energy convergence of $\Delta E < 10^{-8}$ hartree were carried out using initial atomic positions, lattice dimensions, and space groups from the published room-temperature crystallographic data.[60-61] Harmonic vibrational analyses were performed on the optimized structures at the same level of theory, but with an energy convergence of $\Delta E < 10^{-10}$ hartree.

Numerical derivatives for frequencies were calculated using the central-difference formula with two displacements per Cartesian axis, per atom.[45] Infrared intensities for generation of THz-TDS spectra were calculated using the CPHF analytical approach.[76-78] The infrared intensities (km/mol) were converted to extinction coefficients ($M^{-1}cm^{-1}$) for direct comparison to the experimental THz-TDS data. It was found that the simulations consistently overestimated the peak intensities and consequently the simulated THz-TDS intensities in this work have been scaled down by a factor of three for minium and five for vermilion to match observations. Simulated LFRS data utilized Raman tensors calculated with a coupled-perturbed Hartree-Fock/ Kohn-Sham approach and included effects from experimental conditions including temperature and incoming laser frequency.[78-79] The Raman scattering intensities have been normalized to 1000.0 based on the most intense feature in the entire calculated spectrum (found at 128.61 cm^{-1} for minium and 262.05 cm^{-1} for vermilion). Longitudinal optical-transverse optical (LO-TO) phonon splitting was evaluated in the frequency analyses through charge localization via Wannier functions and coupled-perturbed Hartree-Fock/ Kohn-Sham calculation of the high-frequency dielectric tensor.[80-82] Calculated dielectric tensor components and LO-TO split frequencies can be found in **Appendix B**. The overlap-based truncation tolerances for the Coulomb and exchange series integrals were set to 10^{-12}, 10^{-12}, 10^{-12}, 10^{-15}, and 10^{-30} hartree. The simulations used a pruned DFT integration grid comprised of 99 radial and 1454 angular points. The appropriate number of k-points in the Monkhorst-Pack scheme, or the shrinking factor,[83] was determined for each structure by monitoring total energy convergence for each solid as a function of k-point count.

5.3 Results and Discussion

5.3.1 Terahertz-Time Domain Spectroscopy
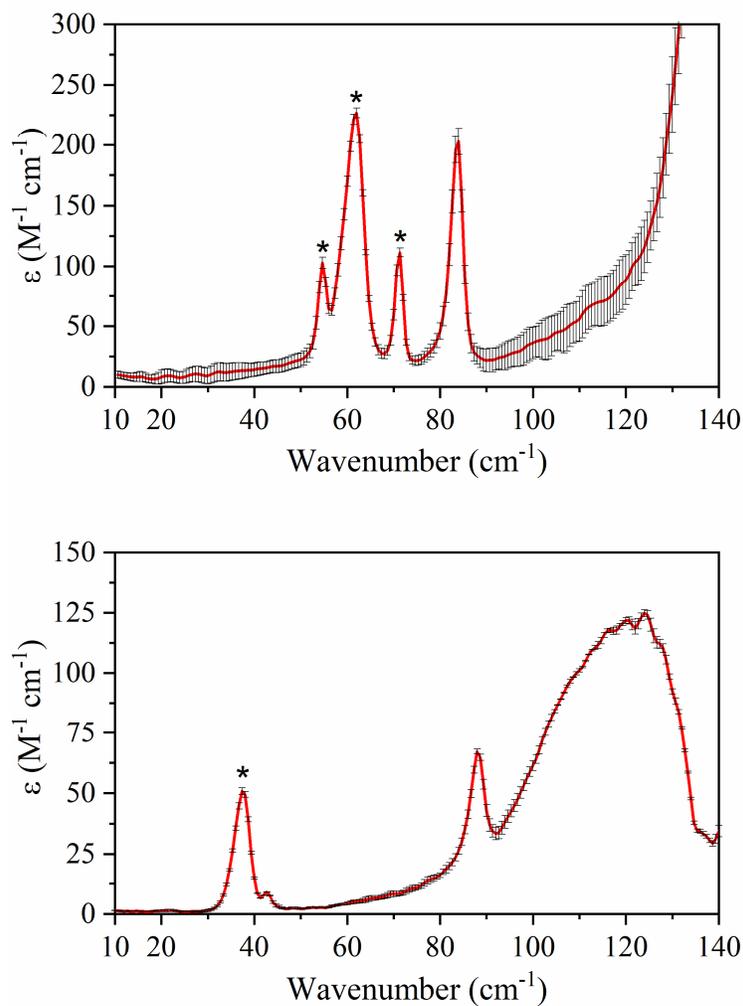
Figure 5-2 THz-TDS spectra of pure minium (top panel) and vermilion (bottom panel). Peaks used in subsequent mixture analyses are denoted with asterisks.

The THz-TDS spectra (not baseline corrected) of pure minium and vermilion are shown in **Figure 5-2**, and a list of the experimental peaks are in **Figure B4** of **Appendix B**. A cluster of THz-TDS absorption features for minium is found between 50 to 90 cm^{-1}, while the three distinct peaks corresponding to vermilion are found between 30 to 45 cm^{-1} and near 90 cm^{-1}. These spectra

are consistent with those reported previously.[54-55] While sample cooling with liquid nitrogen (for example) can help resolve spectral features in molecular solids,[19] emphasis here is on the analysis of ambient temperature data to mimic *in situ* pigment data collection. **Figure 5-3** shows stacked spectral plots (baseline corrected) of the specific peaks of interest in the THz-TDS spectra of the mixture samples used in the LOD and LOQ analyses, and the corresponding calibration curves for each pigment. These standard calibration curves relate the pigment content of a sample to the absorption peak areas. The 37.3 cm^{-1} feature for vermilion could be well fit with a single Lorentzian profile, and the group of peaks found in the THz-TDS spectra of minium (54.7, 62.0, 71.3 cm^{-1}) were fit with a linear combination of three separate Lorentzian profiles. Calibration curves were obtained from linear least squares fits of the relative peak areas in the sample spectra plotted versus the weight percentages of each pigment. Further fit details are provided in **Appendix B**. From the slopes of the calibration curves in **Figure 5-3** and the standard deviations associated with the lowest concentration samples, the THz-TDS LOD for minium was determined to be 5.58 $\pm$ 0.43 % and for vermilion 6.61 $\pm$ 0.28 %. The THz-TDS LOQ for minium and vermilion are 16.91 $\pm$ 0.97 % and 20.04 $\pm$ 0.83 %, respectively.
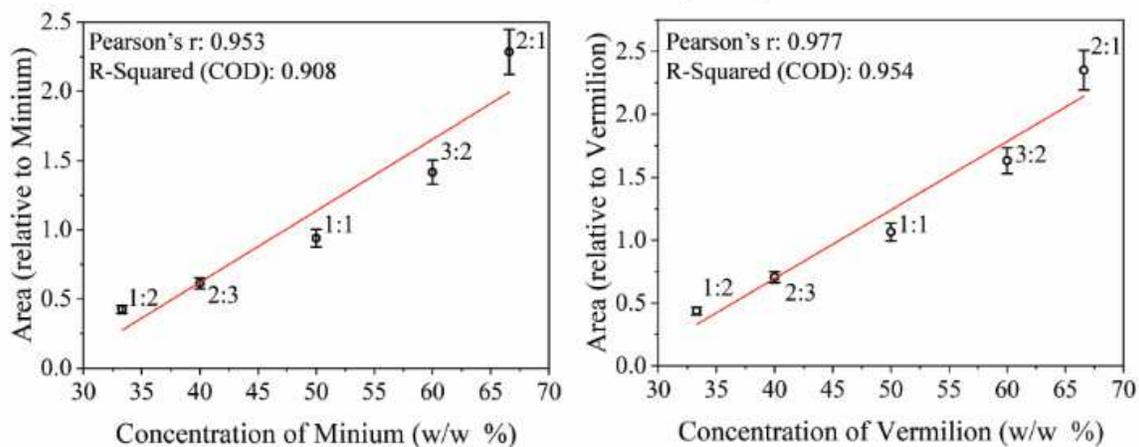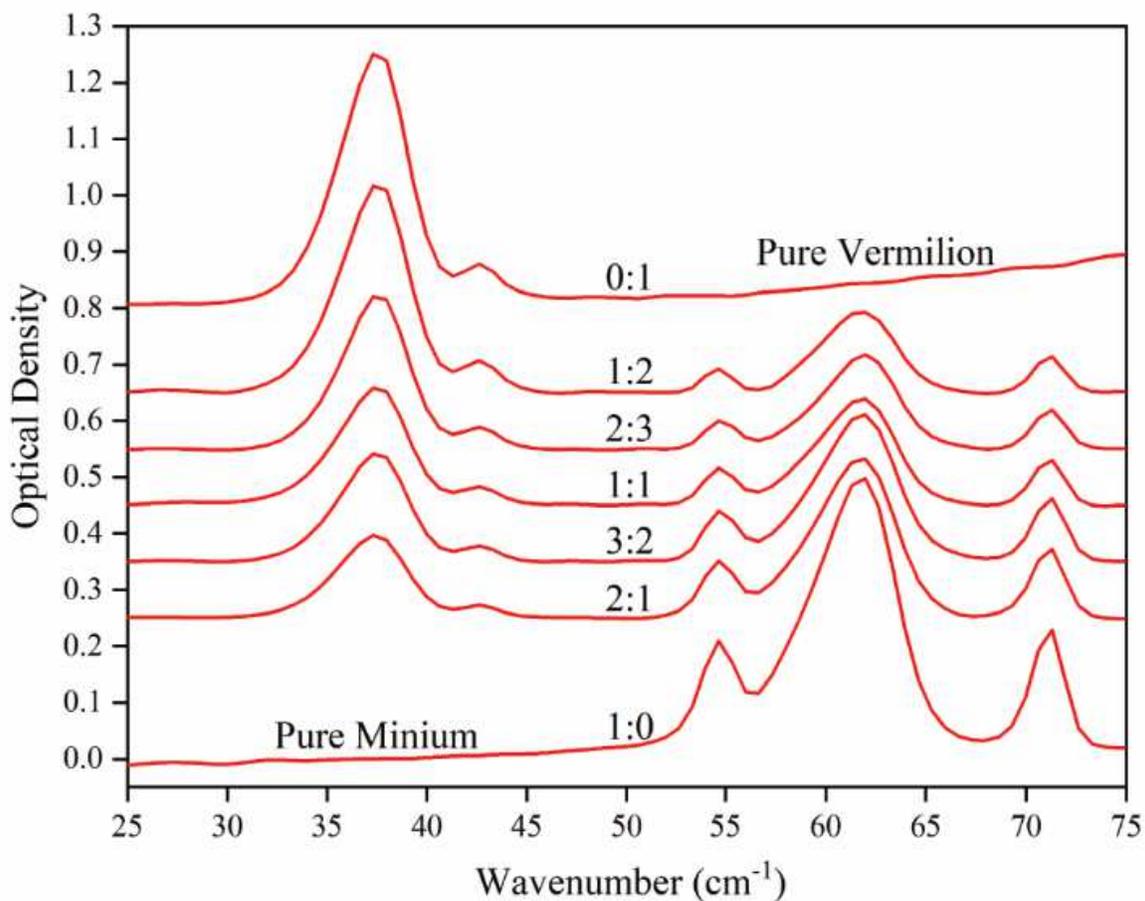
Figure 5-3 THz-TDS data (top panel) for the specific spectral range used in calibration curve (bottom panels) creation and determination of LOD and LOQ values for minium:vermilion mixtures. Spectra are vertically offset for clarity.

5.3.2 Low-Frequency Raman Spectroscopy
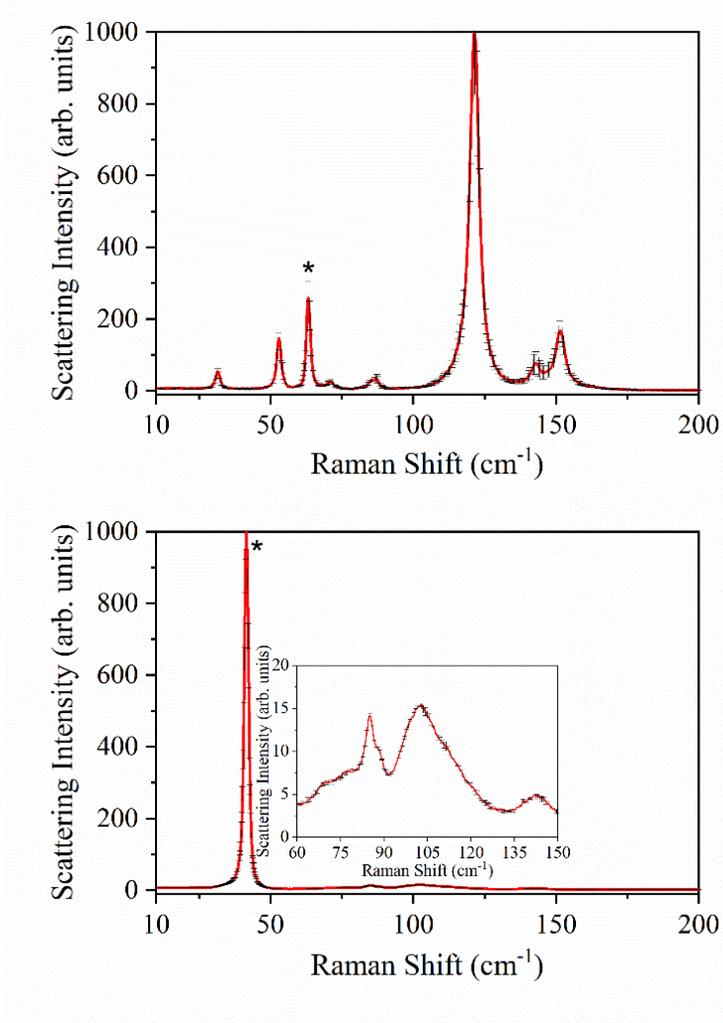
Figure 5-4 Intensity normalized LFRS spectra of minium (top panel) and vermilion (bottom panel). Peaks used in subsequent mixture analyses are denoted with asterisks.

Considering now the LFRS spectra shown in **Figure 5-4**, one strong peak centered at 41.7 cm^{-1} dominates the spectrum for vermilion below 200 cm^{-1}, but other minor features are present between 60 and 150 cm^{-1}. The LFRS spectrum of minium below 100 cm^{-1} shows five well-resolved peaks with the two strongest centered at 53.4 and 63.2 cm^{-1}. These results are consistent with the limited Raman data available in this range.[51, 57] It is important to note that vermilion is an

approximately ~50 % stronger Raman scatterer than minium; this difference is more apparent in the unnormalized data of **Figure B11** of **Appendix B**.

For simplicity reasons and to facilitate comparison with THz-TDS, the LOD and LOQ for each pigment was calculated using the most intense sub-100 cm^{-1} band in the least concentrated sample mixture.[66] In vermilion, the most intense peak at 41.7 cm^{-1} was used for determination of LOD and LOQ values, as was the most intense isolated peak for minium (63.2 cm^{-1}). The relevant spectral regions for the mixture samples are shown in **Figure 5-5**. The same peak area fitting approach was used here as for the THz-TDS data for determination of the LFRS LOD and LOQ values. A difference found in the LFRS data analysis was that a Voigt profile was required to achieve high-quality peak fits due to both intrinsic (Lorentzian) and instrument (Gaussian) contributions to the line shapes, as reported by others.[84]

From measurements of the band areas for the two-component mixtures, the LFRS LOD of minium was found to be 2.52 ± 0.33 % and that for vermilion, 0.21 ± 0.01 %. The LOQ for minium was determined to be 8.41 ± 1.10 % and vermilion yielded 0.69 ± 0.03 %. As already noted, minium is a significantly weaker Raman scatterer than vermilion and the LOD and LOQ of it using LFRS are much higher (less sensitive) than they are for vermilion. This is an important aspect to consider when analyzing unknown mixtures, as one could assume no presence of minium, when in fact the concentration could just simply be below the detection limit, yet still a nontrivial amount (~ 2 %).
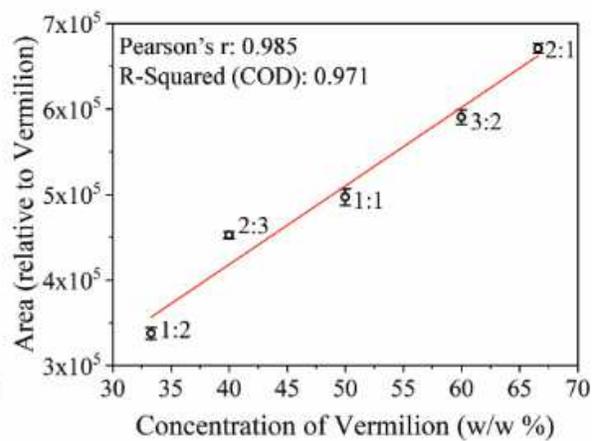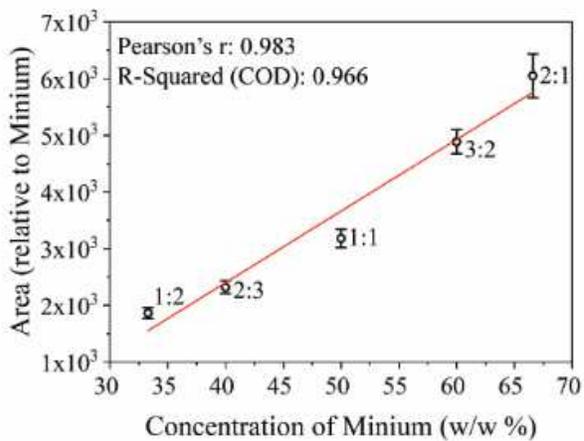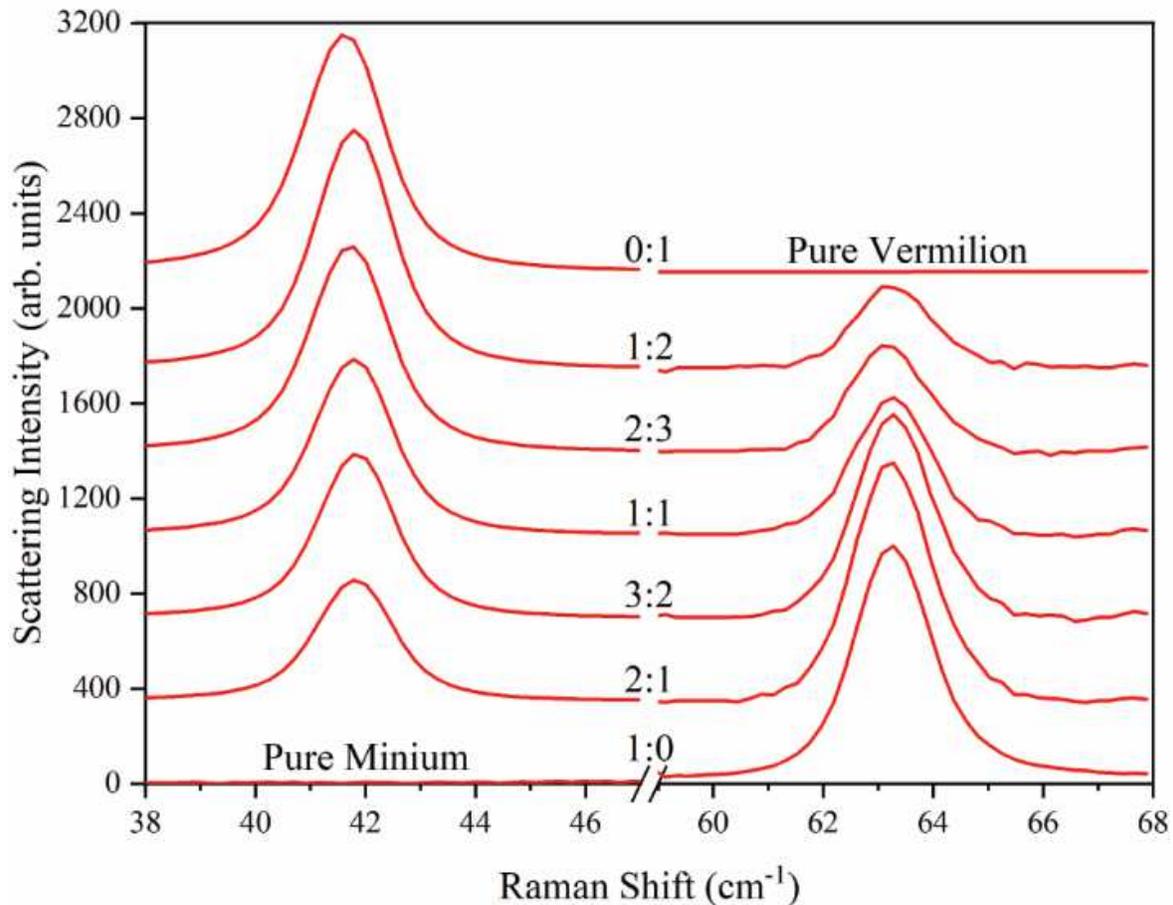
Figure 5-5 LFRS data (top panel) for the specific spectral range used in calibration curve (bottom panels) creation and determination of LOD and LOQ values for minium:vermilion mixtures. Spectra are vertically offset for clarity.

5.3.3 Solid-State Density Functional Theory Analysis

Structural and vibrational ss-DFT simulations supported the experimental line shape analyses by providing additional confidence in the peak assignments. At the very least, ss-DFT low-frequency vibrational simulations are able to confirm the number and relative intensities of features within a particular spectral region which is important for LOD and LOQ evaluation. Adding to their value is that the current work is the first reported ss-DFT analysis and characterization of the crystal structures and low-frequency vibrational motions of minium and vermilion.

In order to obtain high-quality simulated vibrational spectra, accurate lattice and molecular structures must first be produced through full structural optimizations. Comparisons of the experimental and ss-DFT simulated lattice parameters are listed in **Table 5-1**. The need for a hybrid density functional (PBE0) versus a generalized gradient approximation functional (PBE) to accurately model these complex heavy metal systems is clearly demonstrated by the overall dimensional errors for both pigments which decreased from ≤ 4.0 % with PBE to ≤ 0.2 % with PBE0. The superior performance of the hybrid may be attributed to its inclusion of greater HF character (25 %), as this may be especially important to include with inorganic pigments.[85] Simulated and experimental internal structure details of each solid are listed in **Appendix B**.

Table 5-1 Comparison of experimental and calculated lattice parameters for minium and vermilion using the PBE and PBE0 density functionals.

	Minium			Vermilion		
	Exp.[a]	PBE	PBE0	Exp.[b]	PBE	PBE0
a (Å)	8.80	8.845	8.787	4.17	4.198	4.175
b (Å)	8.80	8.845	8.787	4.17	4.198	4.175
c (Å)	6.62	6.778	6.622	9.61	9.684	9.597
α (°)	90	90	90	90	90	90
β (°)	90	90	90	90	90	90
γ (°)	90	90	90	90	90	90
V (Å^3)	512.12	530.303	511.296	144.71	147.774	144.884

[a] ref. 60

[b] ref. 61

While improvement in the simulated solid-state lattices suggests improved vibrational spectra would result, both the PBE and PBE0 methods were still tested for their abilities to produce accurate solid-state vibrations and spectral intensities. The PBE0 predicted modes and intensities for THz-TDS and LFRS are shown in **Figures 5-6** and **5-7**, respectively, while the PBE results can be found in **Appendix B**. The removal of phonon degeneracy by LO-TO frequency splitting, which occurs as a result of long-range dipole-dipole coupling in crystals, was included in the simulations. Accounting for LO-TO split peaks was not nearly as important in reproducing the THz-TDS spectra as it was for the LFRS spectra. In both THz-TDS simulations for minium and vermilion, the LO component peaks accounted for less than 5 % of the observed spectral intensities, but in the LFRS simulation of vermilion, they accounted for nearly 40 % of the observed peak intensities. The LO split peak intensities for minium were negligible in the Raman simulations and therefore not reported here.
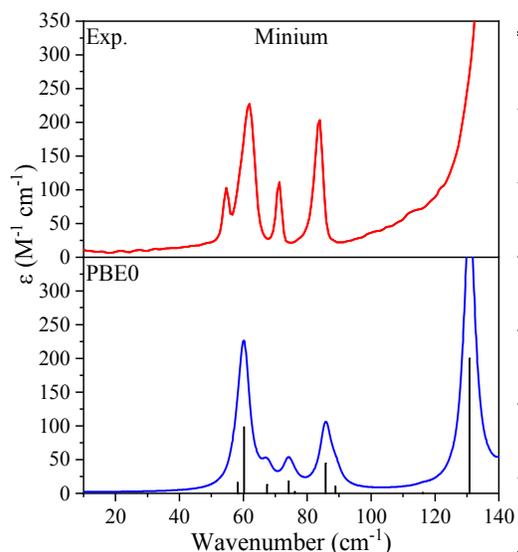
Exp.	Frequency	Intensity	Symmetry
54.7	58.22 (58.45)	35.72 (0.20)	E_u
62.0	60.23 (67.42)	220.35 (28.80)	E_u
71.3	74.17 (76.09)	40.81 (4.70)	A_{2u}
84.0	85.77 (88.81)	100.03 (23.40)	E_u
	116.19 (116.21)	1.62 (0.20)	E_u
	130.83 (146.25)	449.88 (90.60)	A_{2u}
	153.12 (165.82)	829.10 (165.40)	E_u
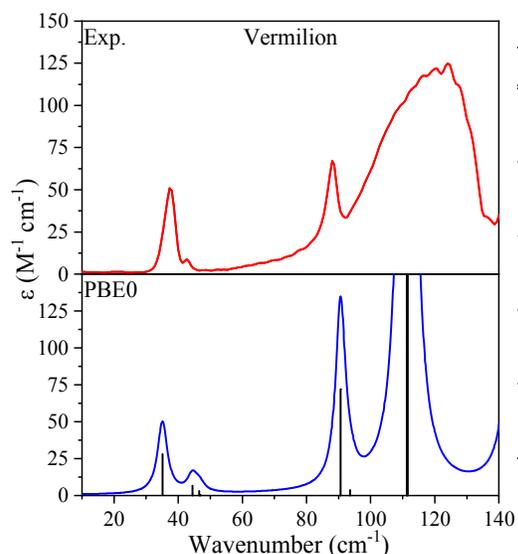
Exp.	Frequency	Intensity	Symmetry
37.3	35.08 (44.39)	32.50 (7.60)	A_2
42.7	46.52 (46.92)	3.47 (0.50)	E
88.0	90.61 (93.62)	83.67 (4.20)	E
119*	111.27 (153.53)	401.53 (325.76)	E
119*	111.54 (144.50)	200.40 (157.50)	A_2

*very broad peak

Figure 5-6 Experimental THz-TDS spectra of minium (top panel) and vermilion (bottom panel), compared to calculated ss-DFT frequencies (cm^{-1}) and intensities (km/mol). Both TO and LO (in parentheses) modes are listed where appropriate. Simulated spectra (blue) were convolved using empirically determined Lorentzian line shapes with a FWHM of 2.2 cm^{-1} for minium and 1.9 cm^{-1} for vermilion.

The mode characters of the observed spectral features in the sub-200 cm^{-1} regions all involve simultaneous translations of the metal and non-metal atoms within the crystal lattices of minium and vermilion. PBE0-generated eigenvector plots[86] for all Raman- and IR-active low-frequency modes (sub-200 cm^{-1}) are shown in **Appendix B**. In short, the THz-TDS peaks at 54.7 and 62.0 cm^{-1} for minium are predominantly due to translations of the O and Pb atoms along the crystallographic *b*-axis. The feature at 71.3 cm^{-1} originates from a similar translational motion, but along the *c*-axis. In the THz-TDS spectrum of vermilion, the 37.3 cm^{-1} peak originates from translations of Hg and S atoms with nearly equal displacement magnitudes along all three crystallographic axes. In the LFRS spectrum of minium, the feature at 63.2 cm^{-1} is attributed to translation of the O and Pb atoms primarily along the *c*-axis. The high intensity peak at 41.7 cm^{-1} in the LFRS spectrum of vermilion is due to translations of all atoms within the *ab*-plane.
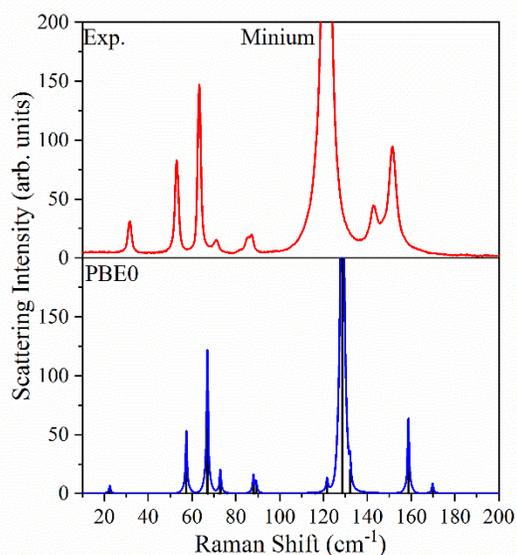
Exp.	Frequency	Intensity	Symmetry
31.8	22.43	6.59	E_g
53.4	57.37	52.86	B_{1g}
63.2	66.95	120.32	E_g
	72.11	0.41	B_{1g}
71.2	72.91	19.64	A_{1g}
	88.06	14.62	B_{2g}
	89.24	8.74	E_g
	121.67	10.80	E_g
	128.61	1000.00	A_{1g}
	132.15	20.53	B_{2g}
	158.79	63.40	E_g
	169.84	8.50	B_{1g}
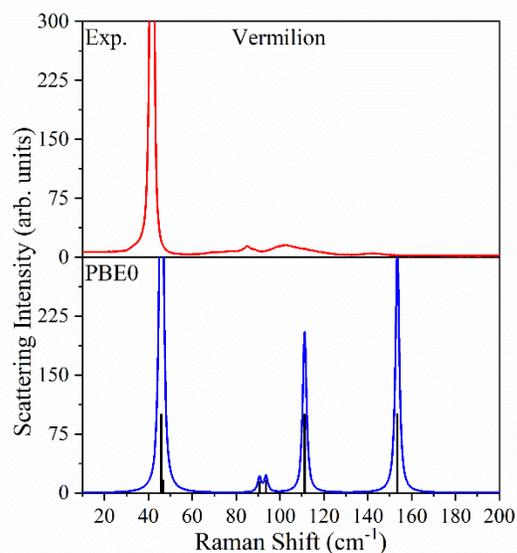
Exp.	Frequency	Intensity	Symmetry
41.7	45.86	548.63	A_1
	46.52 (46.92)	20.81 (20.41)	E
84.5	90.61 (93.62)	18.91 (20.06)	E
101.9	111.27 (153.53)	204.55 (325.76)	E
	(144.50)	0.00	A_2

Figure 5-7 Experimental LFRS spectra of minium (top panel) and vermilion (bottom panel), compared to calculated ss-DFT frequencies (cm^{-1}) and normalized scattering intensities (arb. units). Both TO and LO (in parentheses) modes are listed where appropriate. Simulated spectra (blue) were convolved using empirically determined Voigt profiles (80 % Gaussian / 20 % Lorentzian) with a FWHM of 1.9 cm^{-1} for minium and 2.1 cm^{-1} for vermilion.

5.4 Conclusions

The low-frequency vibrational spectroscopy methods of THz-TDS and LFRS both provide clear spectral fingerprints for minium and vermilion that can be readily used in the quantitative analysis of these pigments in objects and materials of artistic and cultural significance. These distinct and characteristic LFRS and THz-TDS spectra were completely assigned with rigorous ss-DFT simulations of the crystalline pigments, revealing the importance of translational motion in understanding the nature of the sub-200 cm^{-1} vibrations. This work offers the first evaluation and comparison of the analytical capabilities of THz-TDS and LFRS for historical pigment mixture characterization and shows that they provide results that are complementary to each other and at a level that is competitive with more common high-frequency vibrational spectroscopy.[57]

While both low-frequency techniques were successful in quantifying binary pigment mixtures, LFRS was determined to be the preferred method with LOD and LOQ values half those found for THz-TDS of minium and nearly thirty times lower than that for the THz-TDS analysis of vermilion. The THz-TDS derived LOD and LOQ were nearly equal between the two pigments studied here, but the LFRS LOD and LOQ varied considerably, with those for vermilion being about ten times lower than the values for minium. While LFRS is the superior technique for quantifying the composition of specifically minium:vermilion mixtures, this will not necessarily be the case for all mixtures since the THz-TDS absorption profiles of different pigments may produce advantageous LOD and LOQ figures. This is especially true in the investigation of pigments that fluoresce strongly when illuminated by the visible or near-IR lasers commonly used in Raman spectroscopy.[56, 87] Overall, these findings highlight the application of low-frequency vibrational spectroscopies in the study of visually similar pigments, and it is anticipated that the methodology presented here can be extended to a variety of other historic pigments.

5.5 References

1.   Vandenabeele, P.; Rousaki, A.; Costa, M.; Moens, L.; Edwards, H. G. M., Chapter 5 Pigments and Colourants. In *Raman Spectroscopy in Archaeology and Art History: Volume 2*, The Royal Society of Chemistry: London, 2019; Vol. 2, pp 61-67.

2.   Feller, R. L.; Roy, A., *Artists' Pigments: A Handbook of Their History and Characteristics*; National Gallery of Art: Washington, 1986.

3.   Eastaugh, N., *Pigment Compendium: A Dictionary and Optical Microscopy of Historical Pigments*; Butterworth-Heinemann: Oxford, 2008.

4.   Gage, J., *Color in Art*; Thames & Hudson: London, 2006.

5.   Carvalho, I.; Casanova, C.; Araújo, R.; Lemos, A., Colour Identification, Degradation Processes and Findings in a Fifteenth-Century Book of Hours: The Case Study of *Cofre N.º 31* from Mafra National Palace. *Heritage Science* **2018**, *6*, 9.

6.   Fikri, I.; El Amraoui, M.; Haddad, M.; Ettahiri, A. S.; Bellot-Gurlet, L.; Falguères, C.; Lebon, M.; Nespoulet, R.; Ait Lyazidi, S.; Bejjit, L., Xrf and Uv-Vis-Nir Analyses of Medieval Wall Pintings of Al-Qarawiyyin Mosque (Morocco). *IOP Conference Series: Materials Science and Engineering* **2018**, *353*, 012020.

7.   Dowsett, M.; Adriaens, A., The Role of Sims in Cultural Heritage Studies. *Nuclear Instruments and Methods in Physics Research Section B* **2004**, *226*, 38-52.

8.   Vagnini, M.; Miliani, C.; Cartechini, L.; Rocchi, P.; Brunetti, B. G.; Sgamellotti, A., Ft-Nir Spectroscopy for Non-Invasive Identification of Natural Polymers and Resins in Easel Paintings. *Analytical and Bioanalytical Chemistry* **2009**, *395*, 2107-2118.

9.   Bruni, S.; Cariati, F.; Casadio, F.; Toniolo, L., Identification of Pigments on a Xv-Century Illuminated Parchment by Raman and Ftir Microspectroscopies. *Spectrochimica Acta Part A* **1999**, *55*, 1371-1377.

10.   Buzzini, P.; Suzuki, E., Forensic Applications of Raman Spectroscopy for the *in Situ* Analyses of Pigments and Dyes in Ink and Paint Evidence. *Journal of Raman Spectroscopy* **2016**, *47*, 16-27.

11.   Shabunya-Klyachkovskaya, E. V.; Kulakovich, O. S.; Gaponenko, S. V., Surface Enhanced Raman Scattering of Inorganic Microcrystalline Art Pigments for Systematic Cultural Heritage Studies. *Spectrochimica Acta Part A* **2019**, *222*, 117235.

12.   Smith, G. D.; Clark, R. J. H., Raman Microscopy in Art History and Conservation Science. *Studies in Conservation* **2001**, *46*, 92-106.

13.   Vandenabeele, P.; Edwards, H. G. M.; Moens, L., A Decade of Raman Spectroscopy in Art and Archaeology. *Chemical Reviews* **2007**, *107*, 675-686.

14.   Casadio, F.; Leona, M.; Lombardi, J. R.; Van Duyne, R., Identification of Organic Colorants in Fibers, Paints, and Glazes by Surface Enhanced Raman Spectroscopy. *Accounts of Chemical Research* **2010**, *43*, 782-791.

15.   Baxter, J. B.; Guglietta, G. W., Terahertz Spectroscopy. *Analytical Chemistry* **2011**, *83*, 4342-4368.

16.   Beard, M. C.; Turner, G. M.; Schmuttenmaer, C. A., Terahertz Spectroscopy. *The Journal of Physical Chemistry B* **2002**, *106*, 7146-7159.

17.   Fukunaga, K.; Hosako, I., Innovative Non-Invasive Analysis Techniques for Cultural Heritage Using Terahertz Technology. *Comptes Rendus Physique* **2010**, *11*, 519-526.

18.   Larkin, P. J.; Dabros, M.; Sarsfield, B.; Chan, E.; Carriere, J. T.; Smith, B. C., Polymorph Characterization of Active Pharmaceutical Ingredients (Apis) Using Low-Frequency Raman Spectroscopy. *Applied Spectroscopy* **2014**, *68*, 758-776.

19.   Dampf, S. J.; Korter, T. M., Anomalous Temperature Dependence of the Lowest-Frequency Lattice Vibration in Crystalline Γ-Aminobutyric Acid. *The Journal of Physical Chemistry A* **2019**, *123*, 2058-2064.

20.   Parrott, E. P. J.; Zeitler, J. A., Terahertz Time-Domain and Low-Frequency Raman Spectroscopy of Organic Materials. *Applied Spectroscopy* **2015**, *69*, 1-25.

21.   Jackson, J. B.; Bowen, J.; Walker, G.; Labaune, J.; Mourou, G.; Menu, M.; Fukunaga, K., A Survey of Terahertz Applications in Cultural Heritage Conservation Science. *IEEE Transactions on Terahertz Science and Technology* **2011**, *1*, 220-231.

22.   Centeno, S. A., Identification of Artistic Materials in Paintings and Drawings by Raman Spectroscopy: Some Challenges and Future Outlook. *Journal of Raman Spectroscopy* **2016**, *47*, 9-15.

23.   Casadio, F.; Daher, C.; Bellot-Gurlet, L., Raman Spectroscopy of Cultural Heritage Materials: Overview of Applications and New Frontiers in Instrumentation, Sampling Modalities, and Data Processing. *Top. Curr. Chem.* **2016**, *374*, 62.

24.   El Haddad, J.; Bousquet, B.; Canioni, L.; Mounaix, P., Review in Terahertz Spectral Analysis. *TrAC, Trends Anal. Chem.* **2013**, *44*, 98-105.

25.   Jepsen, P. U.; Cooke, D. G.; Koch, M., Terahertz Spectroscopy and Imaging – Modern Techniques and Applications. *Laser Photonics Rev.* **2011**, *5*, 124-166.

26.   Ruggiero, M. T.; Sutton, J. J.; Fraser-Miller, S. J.; Zaczek, A. J.; Korter, T. M.; Gordon, K. C.; Zeitler, J. A., Revisiting the Thermodynamic Stability of Indomethacin Polymorphs with Low-Frequency Vibrational Spectroscopy and Quantum Mechanical Simulations. *Cryst. Growth Des.* **2018**, *18*, 6513-6520.

27.   Zaczek, A. J.; Catalano, L.; Naumov, P.; Korter, T. M., Mapping the Polymorphic Transformation Gateway Vibration in Crystalline 1,2,4,5-Tetrabromobenzene. *Chem. Sci.* **2019**, *10*, 1332-1341.

28.   Price, B. A.; Pretzel, B.; Lomax, S. Q., Infrared and Raman Users Group Spectral Database. 2007 ed.; IRUG: Philadelphia, 2009; Vol. 1 & 2.

29.   Fukunaga, K., Terahertz Spectral Database: Construction of Open Terahertz Spectral Database. *J. Nat. Inst. Inf. Commun. Technol.* **2008**, *55*, 61-66.

30.   Doménech-Carbó, M. T.; Osete-Cortina, L., Another Beauty of Analytical Chemistry: Chemical Analysis of Inorganic Pigments of Art and Archaeological Objects. *ChemTexts* **2016**, *2*, 14.

31.   Walter, P.; de Viguerie, L., Materials Science Challenges in Paintings. *Nature Materials* **2018**, *17*, 106.

32.   Wiesinger, R.; Pagnin, L.; Anghelone, M.; Moretto, L. M.; Orsega, E. F.; Schreiner, M., Pigment and Binder Concentrations in Modern Paint Samples Determined by Ir and Raman Spectroscopy. *Angewandte Chemie International Edition* **2018**, *57*, 7401-7407.

33.   Pottier, F.; Gerardin, M.; Michelin, A.; Hébert, M.; Andraud, C., Simulating the Composition and Structuration of Coloring Layers in Historical Painting from Non-Invasive Spectral Reflectance Measurements. *Comptes Rendus Physique* **2018**, *19*, 599-611.

34.   González-Vidal, J. J.; Perez-Pueyo, R.; Soneira, M. J.; Ruiz-Moreno, S., Automatic Identification System of Raman Spectra in Binary Mixtures of Pigments. *Journal of Raman Spectroscopy* **2012**, *43*, 1707-1712.

35.   Strachan, C. J.; Pratiwi, D.; Gordon, K. C.; Rades, T., Quantitative Analysis of Polymorphic Mixtures of Carbamazepine by Raman Spectroscopy and Principal Components Analysis. *J. Raman Spectrosc.* **2004**, *35*, 347-352.

36.   El Haddad, J.; de Miollis, F.; Bou Sleiman, J.; Canioni, L.; Mounaix, P.; Bousquet, B., Chemometrics Applied to Quantitative Analysis of Ternary Mixtures by Terahertz Spectroscopy. *Anal. Chem.* **2014**, *86*, 4927-4933.

37.   King, M. D.; Buchanan, W. D.; Korter, T. M., Identification and Quantification of Polymorphism in the Pharmaceutical Compound Diclofenac Acid by Terahertz Spectroscopy and Solid-State Density Functional Theory. *Anal. Chem.* **2011**, *83*, 3786-3792.

38.   Sasaki, T.; Sakamoto, T.; Otsuka, M., Detection of Impurities in Organic Crystals by High-Accuracy Terahertz Absorption Spectroscopy. *Anal. Chem.* **2018**, *90*, 1677-1682.

39.   Warnecke, S.; Wu, J. X.; Rinnan, Å.; Allesø, M.; Van Den Berg, F.; Jepsen, P. U.; Engelsen, S. B., Quantifying Crystalline A-Lactose Monohydrate in Amorphous Lactose Using Terahertz Time Domain Spectroscopy and near Infrared Spectroscopy. *Vib. Spectrosc.* **2019**, *102*, 39-46.

40.   Koch Dandolo, C. L.; Guillet, J.-P.; Ma, X.; Fauquet, F.; Roux, M.; Mounaix, P., Terahertz Frequency Modulated Continuous Wave Imaging Advanced Data Processing for Art Painting Analysis. *Optics Express* **2018**, *26*, 5358-5367.

41.   Locquet, A.; Dong, J.; Melis, M.; Citrin, D. In *Terahertz Pulsed Imaging Reveals the Stratigraphy of a Seventeenth-Century Oil Painting*, Unconventional Optical Imaging, International Society for Optics and Photonics: 2018; p 106771Z.

42.   Koch Dandolo, C. L.; Picollo, M.; Cucci, C.; Jepsen, P. U., Fra Angelico's Painting Technique Revealed by Terahertz Time-Domain Imaging (Thz-Tdi). *Appl. Phys. A-Mater.* **2016**, *122*, 898.

43.   Fantacci, S.; Amat, A.; Sgamellotti, A., Computational Chemistry Meets Cultural Heritage: Challenges and Perspectives. *Acc. Chem. Res.* **2010**, *43*, 802-813.

44.   Fukunaga, K.; Picollo, M., Terahertz Spectroscopy Applied to the Analysis of Artists' Materials. *Appl. Phys. A* **2010**, *100*, 591-597.

45.   Pascale, F.; Zicovich-Wilson, C. M.; Gejo, F. L.; Civalleri, B.; Orlando, R.; Dovesi, R., The Calculation of the Vibrational Frequencies of Crystalline Compounds and Its Implementation in the Crystal Code. *J. Comput. Chem.* **2004**, *25*, 888-897.

46.   Squires, A. D.; Lewis, R. A.; Zaczek, A. J.; Korter, T. M., Distinguishing Quinacridone Pigments Via Terahertz Spectroscopy: Absorption Experiments and Solid-State Density Functional Theory Simulations. *J. Phys. Chem. A* **2017**, *121*, 3423-3429.

47.   Ruggiero, M. T.; Bardon, T.; Strlic, M.; Taday, P. F.; Korter, T. M., Assignment of the Terahertz Spectra of Crystalline Copper Sulfate and Its Hydrates Via Solid-State Density Functional Theory. *J. Phys. Chem. A* **2014**, *118*, 10101-10108.

48.   Kleist, E. M.; Koch Dandolo, C. L.; Guillet, J.-P.; Mounaix, P.; Korter, T. M., Terahertz Spectroscopy and Quantum Mechanical Simulations of Crystalline Copper-Containing Historical Pigments. *The Journal of Physical Chemistry A* **2019**, *123*, 1225-1232.

49.   Aze, S.; Vallet, J. M.; Detalle, V.; Grauby, O.; Baronnet, A., Chromatic Alterations of Red Lead Pigments in Artworks: A Review. *Phase Transitions* **2008**, *81*, 145-154.

50.   Gettens, R. J.; Feller, R. L.; Chase, W. T., Vermillion and Cinnabar. *Stud. Cons.* **1972**, *17*, 45-69.

51.   Franquelo, M. L.; Perez-Rodriguez, J. L., A New Approach to the Determination of the Synthetic or Natural Origin of Red Pigments through Spectroscopic Analysis. *Spectrochim. Acta, Part A* **2016**, *166*, 103-111.

52.   Yang, Y.; Zhai, D.; Zhang, Z.; Zhang, C., Thz Spectroscopic Identification of Red Mineral Pigments in Ancient Chinese Artworks. *J. Infrared, Millimeter, Terahertz Waves* **2017**, *38*, 1232-1240.

53.   Ha, T.; Lee, H.; Sim, K. I.; Kim, J.; Jo, Y. C.; Kim, J. H.; Baek, N. Y.; Kang, D.-i.; Lee, H. H., Optimal Methodologies for Terahertz Time-Domain Spectroscopic Analysis of Traditional Pigments in Powder Form. *J. Korean Phys. Soc.* **2017**, *70*, 866-871.

54.   Hong, T., et al., Terahertz Time-Domain and Fourier-Transform Infrared Spectroscopy of Traditional Korean Pigments. *J. Korean Chem. Soc.* **2014**, *64*, 727-731.

55.   Bardon, T.; May, R. K.; Jackson, J. B.; Beentjes, G.; de Bruin, G.; Taday, P. F.; Strlič, M., Contrast in Terahertz Images of Archival Documents—Part I: Influence of the Optical Parameters from the Ink and Support. *J. Infrared, Millimeter, Terahertz Waves* **2017**, *38*, 443-466.

56.   Marucci, G.; Beeby, A.; Parker, A. W.; Nicholson, C. E., Raman Spectroscopic Library of Medieval Pigments Collected with Five Different Wavelengths for Investigation of Illuminated Manuscripts. *Anal. Methods* **2018**, *10*, 1219-1236.

57.   Edwards, H. G. M.; Farwell, D. W.; Newton, E. M.; Fernando, P. R., Minium; Ft-Raman Non-Destructive Analysis Applied to an Historical Controversy. *Analyst* **1999**, *124*, 1323-1326.

58.   Pallipurath, A. R.; Skelton, J. M.; Ricciardi, P.; Elliott, S. R., Estimation of Semiconductor-Like Pigment Concentrations in Paint Mixtures and Their Differentiation from Paint Layers Using First-Derivative Reflectance Spectra. *Talanta* **2016**, *154*, 63-72.

59.   Macrae, C. F.; Bruno, I. J.; Chisholm, J. A.; Edgington, P. R.; McCabe, P.; Pidcock, E.; Rodriguez-Monge, L.; Taylor, R.; van de Streek, J.; Wood, P. A., Mercury Csd 2.0 - New Features for the Visualization and Investigation of Crystal Structures. *J. Appl. Crystallogr.* **2008**, *41*, 466-470.

60.   Gavarri, J.-R.; Weigel, D., Oxydes De Plomb. I. Structure Cristalline Du Minium Pb_3O_4, À Température Ambiante (293 K). *J. Solid State Chem.* **1975**, *13*, 252-257.

61.   Auvray, P.; Genet, F., Refining the Crystal Structure of Cinnabar, A-Mercury(Ii) Sulfide. *Bull. Soc. Fr. Mineral. Cristallogr.* **1973**, *96*, 218-19.

62.   Bardon, T.; May, R. K.; Taday, P. F.; Strlič, M., Influence of Particle Size on Optical Constants from Pellets Measured with Terahertz Pulsed Spectroscopy. *IEEE Trans. Terahertz Sci. Technol.* **2016**, *6*, 408-413.

63.   OriginLab Corporation, *Originlab 2018b*: (Northampton, MA).

64.   Shrivastava, A.; Gupta, V., Methods for the Determination of Limit of Detection and Limit of Quantitation of the Analytical Methods. *Chron. Young Sci.* **2011**, *2*, 21-25.

65.   Currie, L. A., Limits for Qualitative Detection and Quantitative Determination. Application to Radiochemistry. *Anal. Chem.* **1968**, *40*, 586-593.

66.   Vandenabeele, P.; Moens, L., Some Ideas on the Definition of Raman Spectroscopic Detection Limits for the Analysis of Art and Archaeological Objects. *J. Raman Spectrosc.* **2012**, *43*, 1545-1550.

67.   Edwards, H. G. M., Analytical Raman Spectroscopic Discrimination between Yellow Pigments of the Renaissance. *Spectrochim. Acta, Part A* **2011**, *80*, 14-20.

68.   Dovesi, R., et al., Quantum-Mechanical Condensed Matter Simulations with Crystal. *Wiley Interdiscip. Rev.: Comput. Mol. Sci.* **2018**, *8*, e1360.

69.   Dovesi, R., et al., Crystal17 User's Manual. University of Torino, Torino, 2017.

70.   Perdew, J. P.; Burke, K.; Ernzerhof, M., Generalized Gradient Approximation Made Simple. *Phys. Rev. Lett.* **1996**, *77*, 3865-3868.

71.   Adamo, C.; Barone, V., Toward Reliable Density Functional Methods without Adjustable Parameters: The Pbe0 Model. *J. Chem. Phys.* **1999**, *110*, 6158-6170.

72.   Peintinger, M. F.; Oliveira, D. V.; Bredow, T., Consistent Gaussian Basis Sets of Triple-Zeta Valence with Polarization Quality for Solid-State Calculations. *J. Comput. Chem.* **2013**, *34*, 451-459.

73.   Zagorac, D.; Doll, K.; Schön, J. C.; Jansen, M., Ab Initio Structure Prediction for Lead Sulfide at Standard and Elevated Pressures. *Phys. Rev. B* **2011**, *84*, 045206.

74.   Metz, B.; Stoll, H.; Dolg, M., Small-Core Multiconfiguration-Dirac–Hartree–Fock-Adjusted Pseudopotentials for Post-D Main Group Elements: Application to Pbh and Pbo. *J. Chem. Phys.* **2000**, *113*, 2563-2569.

75.   Weihrich, R.; Anusca, I.; Zabel, M., Halbantiperowskite: Zur Struktur Der Shandite $M_{3/2}as$ (M = Co, Ni; a = in, Sn) Und Ihren Typ-Antitypbeziehungen. *Z. Anorg. Allgemeine Chem.* **2005**, *631*, 1463-1470.

76.   Zicovich-Wilson, C. M.; Pascale, F.; Roetti, C.; Saunders, V. R.; Orlando, R.; Dovesi, R., Calculation of the Vibration Frequencies of A-Quartz: The Effect of Hamiltonian and Basis Set. *J. Comp. Chem.* **2004**, *25*, 1873-1881.

77.   Noel, Y.; Zicovich-Wilson, C. M.; Civalleri, B.; D'Arco, P.; Dovesi, R., Polarization Properties of Zno and Beo: An *Ab Initio* Study through the Berry Phase and Wannier Functions Approaches. *Phys. Rev. B: Condens. Matter Mater. Phys.* **2002**, *65*, 1-9.

78.   Maschio, L.; Kirtman, B.; Orlando, R.; Rerat, M., Ab Initio Analytical Infrared Intensities for Periodic Systems through a Coupled Perturbed Hartree-Fock/Kohn-Sham Method. *J. Chem. Phys.* **2012**, *137*, 204113/1-204113/11.

79.   Maschio, L.; Kirtman, B.; Rérat, M.; Orlando, R.; Dovesi, R., *Ab Initio* Analytical Raman Intensities for Periodic Systems through a Coupled Perturbed Hartree-Fock/Kohn-Sham Method in an Atomic Orbital Basis. Ii. Validation and Comparison with Experiments. *J. Chem. Phys.* **2013**, *139*, 164102.

80.   Ferrero, M.; Rérat, M.; Orlando, R.; Dovesi, R., The Calculation of Static Polarizabilities of 1-3d Periodic Compounds. The Implementation in the Crystal Code. *J. Comput. Chem.* **2008**, *29*, 1450-1459.

81.   Ferrero, M.; Rérat, M.; Orlando, R.; Dovesi, R., Coupled Perturbed Hartree-Fock for Periodic Systems: The Role of Symmetry and Related Computational Aspects. *J. Chem. Phys.* **2008**, *128*, 014110.

82.   Ferrero, M.; Rérat, M.; Kirtman, B.; Dovesi, R., Calculation of First and Second Static Hyperpolarizabilities of One- to Three-Dimensional Periodic Compounds. Implementation in the Crystal Code. *J. Chem. Phys.* **2008**, *129*, 244110.

83.   Monkhorst, H. J.; Pack, J. D., Special Points for Brillouin-Zone Integrations. *Phys. Rev. B: Condens. Matter* **1976**, *13*, 5188-5192.

84.   Korepanov, V. I.; Sedlovets, D. M., An Asymmetric Fitting Function for Condensed-Phase Raman Spectroscopy. *Analyst* **2018**, *143*, 2674-2679.

85.   Canepa, P.; Ugliengo, P.; Alfredsson, M., Elastic and Vibrational Properties of A- and B-Pbo. *J. Phys. Chem. C* **2012**, *116*, 21514-21522.

86.   *Jmol: An Open-Source Java Viewer for Chemical Structures in 3d.* *Http://Www.Jmol.Org/*

87.   Clark, R. J. H., Pigment Identification by Spectroscopic Means: An Arts/Science Interface. *C. R. Chimi.* **2002**, *5*, 7-20.

Chapter 6. Evaluating Vibrational Mode Character in the Terahertz Spectra of Solid-State Organic Pigments

The material in this chapter is a completed manuscript currently undergoing revisions. Please see Appendix C for Supporting Information.

Organic pigments have a variety of uses ranging from industrial colorants to a place in artists' palettes. Terahertz time-domain spectroscopy is a promising tool for the identification and characterization of modern organic pigments because of its chemical-specificity and nondestructive natures. Solid-state density functional theory can reliably predict the sub-3.0 THz vibrations and the intermolecular and intramolecular forces that dominate them. Here, characterization of the low-frequency vibrations of two red pigments commonly used in industrial and artistic settings, Pigment Red 3 and Pigment Red 254, is performed using a combination of terahertz time-domain spectroscopy and solid-state density functional theory to gain insight into the origins of the observed spectral features.

6.1 Introduction

Advances in organic synthesis from the late 19th century through the 20th century, enabled the production of modern organic pigments. Widespread use of these novel pigments extended from artists' palettes[1] to industrual applications as colorants in plastics, printing inks, textiles, and paints.[2-3] Their versatility stems from the availability of structural modifications to adjust fastness and coloristic properties.[2] The tunable nature of these properties means that characteristics such as resistance to degradation from light, weather, heat, and chemicals or color variations including hue, saturation, lightness, and intensity can be adjusted with slight changes to the molecular structure.[2, 4-5] Additional benefits of synthetic organic pigments include decreased toxicity, increased availability, durability, and vibrancy;[23, 41, 43-44] all of which contributed to their replacement of historical pigments in modern artists' palettes.

The inclusion of organic pigments in modern artists' palettes necessitates efforts to investigate these pigments with analytical techniques. In heritage science, identification and characterization of artists' materials is a vital aspect in designing effective conservation and restoration protocols, monitoring degradation, and detecting forgeries.[1, 6-13] Current techniques include powder X-ray diffraction (PXRD), mid- and near-infrared (IR) spectroscopy, Raman spectroscopy, and X-ray fluorescence spectroscopy (XRF).[14, 15-16] Data collection methods for PXRD are difficult *in situ*[17] and the analysis of diffraction data has been shown to produce incorrect crystal structures in structurally-similar quinacridone pigments.[18] Mid- and near- IR spectroscopy can only detect certain functional groups, limiting the ability to distinguish chemically similar pigments.[19-20] Raman studies require diligence to prevent damage from higher photon energies, and Raman spectra of organic species can have significant interference from fluorescence.[21] Similar to IR spectroscopies, XRF studies lack chemical specificity and the

sensitivity to detect light elements.[22-24] Limitations of these methods predicate the need for

additional techniques that can overcome these challenges.[25]

Terahertz time-domain spectroscopy (THz-TDS), which accesses vibrations in the ≤ 3.0

THz region, is a nondestructive technique capable of penetrating opaque materials and providing

chemically specific data with relatively quick acquisition times.[26-28] THz methods have proved

useful for analysis of complex crystalline materials in the pharmaceutical industry,[29-30] polymorph

identification,[31-34] and heritage science.[9-11, 35-40] Prior pigment studies focused on the THz-TDS

spectra of historic pigments,[41-43] but recent efforts now include modern organic pigments.[35] In

crystalline solids, low-frequency vibrations involve simultaneous intramolecular and

intermolecular movement of the unit cell components, which are uniquely dependent on 3D

packing arrangements and molecular identities, rendering interpretation of the features in THz-

TDS spectra difficult. This challenge can be reduced with quantum mechanical solid-state

simulations.[44-46] Solid-state density functional theory (ss-DFT) utilizes periodic boundary

conditions to accurately model crystalline environments and their low-frequency motions.[47] The

combination of THz-TDS and ss-DFT has uncovered the origins of THz-TDS spectral features in

complex systems such as clathrates,[48] metal-organic frameworks,[49] polymorphic materials,[33, 46]

disordered crystals,[32] and pigments.[50-53]

In this study, focus is on two modern red pigments, pigment red 3 (PR3) and pigment red

254 (PR254), because of their extensive use in industrial settings and modern artists palettes. PR3,

also known as Toluidine Red, is a versatile and low-cost azo pigment used in printing inks, paints,

and plastics.[4-5, 54] The structures of azo pigments are comprised of a β-naphthol system, in addition

to the azo functional group.[3] Although PR3 is referred to as an azo pigment, a significant number

of studies indicates the predominant resonance structure of these pigments is the hydrazone form

(=N–NH–) rather than the azo form (–N=N–).[4-5, 55-62] PR254, also known as Ferrari Red, is a diketopyrrolopyrrole (DPP) pigment.[16, 63-64] DPP pigments, known for their high-performance and lightfastness, are used in automobile and industrial paint applications,[54, 65] and as functional dyes in optoelectronics.[66] The structures of these pigments include a 1,4-diketopyrrolo(3,4c)pyrrole system which is comprised of two carbonamide-containing five-membered rings.[3, 65]

Here, THz-TDS spectra and solid-state simulations of the crystal structures and sub-3.0 THz modes of PR3 [$C_{17}H_{13}N_3O_3$, CAS#:2425-85-6] and PR254 [$C_{18}H_{10}Cl_2N_2O_2$, CAS#:84632-65-5] are presented. The structures of these modern pigments are shown in **Figures 6-1** and **6-2**. Prior studies have demonstrated the potential of solid-state computational analyses in revealing the effects of crystal packing forces and internal molecular motions on the low-frequency features in THz-TDS spectra of polycyclic aromatic hydrocarbons,[67] as well as the ability of THz-TDS to distinguish between chemically similar species.[51]
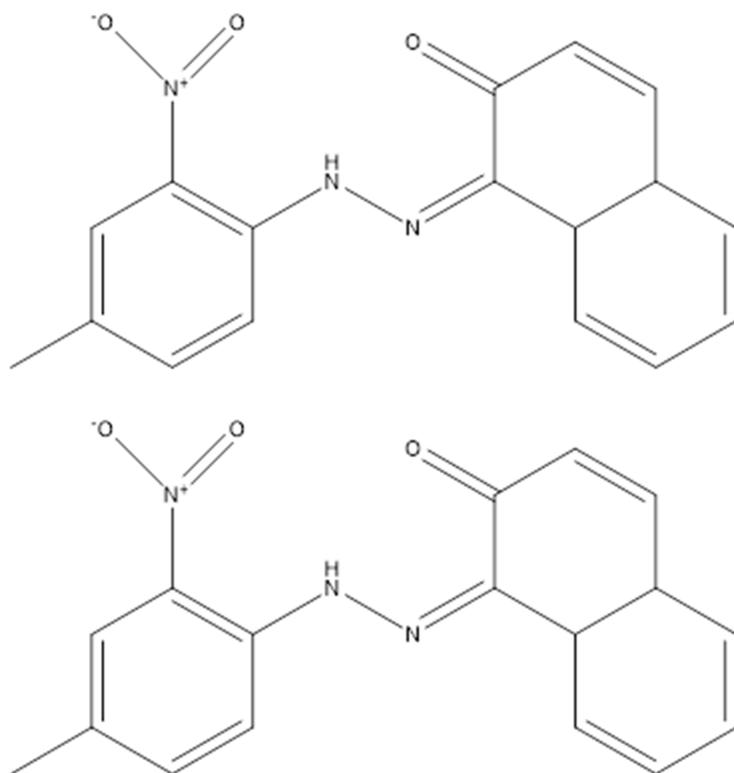
Figure 6-1 Resonance structures of Pigment Red 3: hydrazone form (top) and azo form (bottom).
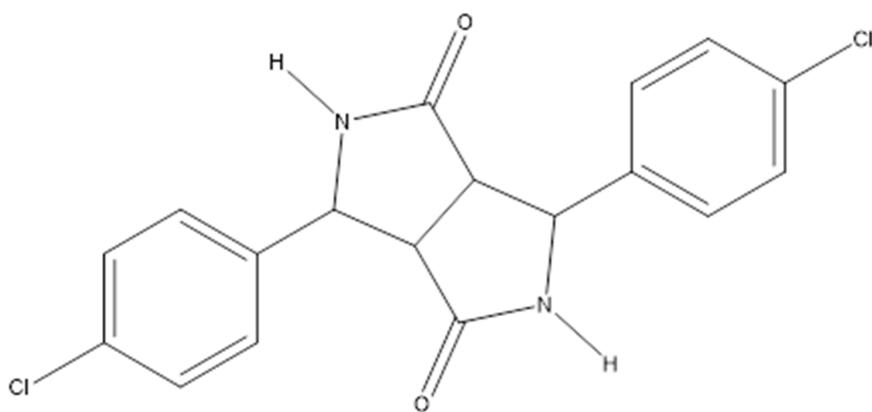
Figure 6-2 Structure of Pigment Red 254.

6.2 Methods

6.2.1 Experimental Details

PR3 (sold under Studio Red) and PR254 (sold under Red DPP BO) were purchased from Kremer Pigments Inc. (Munich, Germany) and used without further purification. Pigment purity and bulk crystallinity was determined by powder X-ray diffraction (PXRD) at 290 K on a Bruker D2 Phaser with a LYKXEYE 1D silicon strip detector using Cu Kα radiation (λ=1.5406 Å). Powder patterns for the pigments were compared to calculated powder patterns (shown in **Appendix C**) produced in Mercury CSD 3.10.251[68] using the single-crystal X-ray diffraction data for PR3 and PR254[69].

Mixed samples of the pigments and HDPE were then pressed into uniform pellets with a 13 mm diameter and thicknesses varying from 3.53 to 3.88 mm. No corrections for particle size effects were applied.[70], All THz spectra were measured with pellets made with a 20 % w/w concentration of pigment. Spectra were collected with a TPS Spectra 3000 time-domain spectroscopy system from TeraView (Cambridge, UK) at room temperature (293 K). The system relies on GaAs laser-gated photoconductive antennas (PC-antennas) for terahertz generation and detection, with an 80 fs Ti:Sa ultrashort pulsed laser operating at 800 nm with a repetition rate of 76 MHz used as a probe/pump beam. The THz-TDS system offers a useful frequency range of $0.06 – 3.0$ THz ($2.0 – 100.0$ cm^{-1}) with a maximum dynamic range around 75 dB and a rapid scan mode up to 30 scans/second.[71] The THz signals were acquired from the pellets in a transmission configuration, with the pellet placed between the transmitter and the receiver at the focal point of the THz radiation, midway between two off-axis parabolic mirrors. The pellet, emitter, and receiver are located inside a closed system compartment, which has been purged

with dry air to eliminate undesired absorption bands from water vapor in the acquired THz spectra.

The THz signals were acquired within an 18.8660 ps time-delay window with a time step of 0.0097 ps (1943 data-points, 0.0063 THz step in frequency domain; 100 signal averaging for each pellet). Three THz spectra were recorded for each pellet for a total of 27 THz spectra. Terahertz absorbance spectra were obtained through the base-10 logarithm of the ratio of the sample single-beam spectrum divided by a reference single-beam spectrum. The THz signal collected from a 100 % wt. HDPE pellet (400 mg) was used as the reference signal for this calculation.

6.2.2 Computational Details

All ss-DFT simulations were performed using the CRYSTAL17 software package.[72-73] Structural optimizations used atomic positions, lattice dimensions, and space groups from the solved crystal structure for PR3 and previously published-ray data for PR254.[69] The structures were allowed to fully relax to energetic minima within the limits of the applied space group symmetries and an energy convergence threshold of $\Delta E < 10^{-9}$ hartree. Simulations were performed with the generalized gradient approximation (GGA) Perdew−Burke−Ernzerhof (PBE)[74-75] exchange-correlation functional was used in conjunction the Ahlrichs valence triple zeta (VTZ) basis set with polarization functions.[76-80] All calculations were augmented with Grimme's London dispersion correction (D3) with the Becke-Johnson damping function and included a three-body repulsion term to better account for intermolecular dispersion forces.[81-83]

Vibrational analyses were carried out on the optimized structures at the same level of theory with an energy convergence of $\Delta E < 10^{-10}$ hartree. Numerical derivatives for frequencies were calculated using the central-difference formula with one displacement per Cartesian axis,

per atom.[84] Normal mode eigenvalues and eigenvectors were calculated within the harmonic approximation and infrared intensities were obtained using the Berry phase approach.[85-86] All IR-active modes and intensities for PR3 and PR254 are listed in **Appendix C**. Coulomb and exchange series integral tolerances were set to 10^{-14}, 10^{-14}, 10^{-14}, 10^{-22}, and 10^{-44} hartree and used a pruned DFT integration grid comprised of 99 radial and 1454 angular points for all calculations. The appropriate number of k-points in the Monkhorst-Pack scheme[87] was determined by monitoring total energy convergence for each solid.

6.3 Results and Discussion

6.3.1 Terahertz Absorption Spectra of PR3 and PR254

The experimental baseline-corrected THz-TDS spectra of PR3 and PR254 are shown in **Figure 6-3**. The spectrum for PR3 contains multiple well-defined peaks located from 0.5 to 3.0 THz. In contrast PR254 is a significantly weaker absorber of THz radiation and only has three apparent absorption features centered at 0.86, 1.88, and 2.05 THz. Frequently, cryogenic cooling is employed in the analysis of molecular solids to uncover hidden features lost to the thermal broadening of spectral peaks, [88-89] but here room temperature studies are emphasized to better replicate the *in situ* analysis of artifacts. In the spectrum of PR3, the average FWHM value is 0.05 THz, while the average FWHM for PR254 is 0.09 THz. The spectral features observed in the room temperature THz-TDS spectra can be further explained using ss-DFT to model the structures and vibrations of these two pigments.
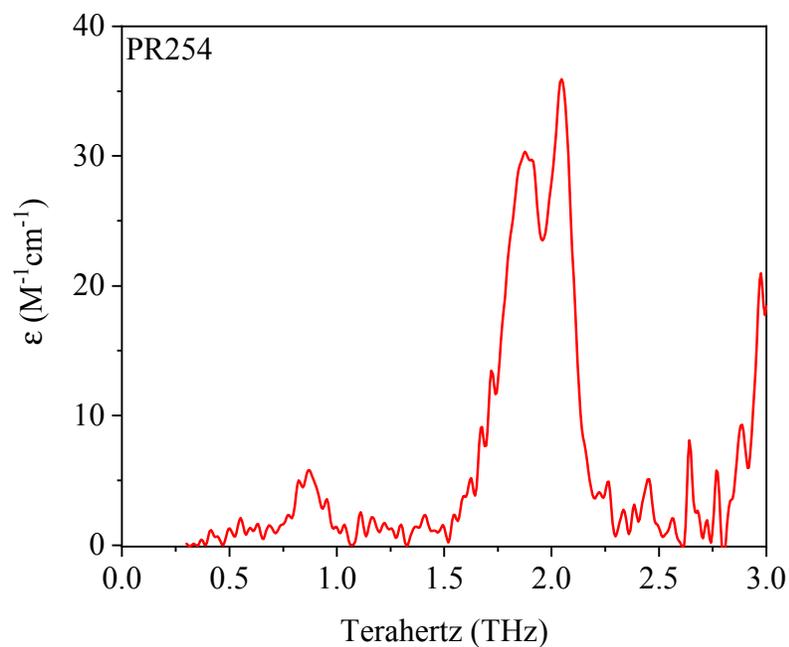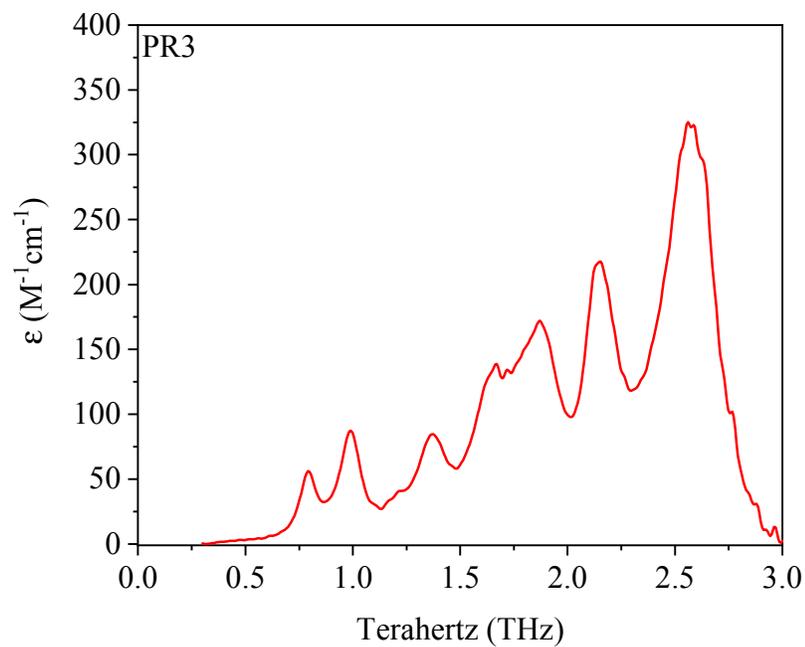
Figure 6-3 Averaged experimental THz-TDS spectra of PR3 (top panel) and PR254 (bottom panel) for each sample pellet. Each spectrum represents the averaged data for triplicate measurements of three pellets.

6.3.2 Computational Structural Analysis

The crystallographic unit cells for both PR3 and PR254 are shown in **Figure 6-4**. Both

pigments crystallize in the monoclinic group as space group *p2₁/c* and *p2₁/n* for PR3 and PR254,

respectively. As previously mentioned, characteristic structural features of organic pigments

include: chromophores, planarity, van der Waals contacts, and functional groups that enable in

hydrogen bonding, insoluble salts or metal complexes. Both PR3 and PR254 are planar

chromophoric systems with functional groups that enable hydrogen bonding. All of these

features lend to the stabilization via π-π stacking and contribute color and fastness properties.
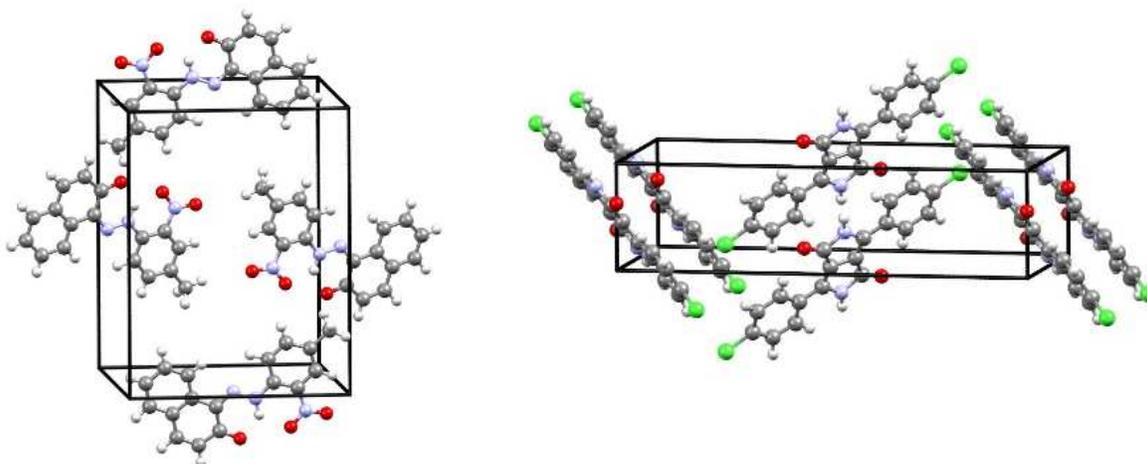
Figure 6-4 Experimental crystallographic unit cells of PR3 (left) and PR254 (right).

The calculated ss-DFT crystallographic unit cell dimensions for both PR3 and PR254 are

listed in **Table 6-1**. The choice to use the PBE functional and VTZP basis set was based on the

demonstrated success of this combination in quinacridone pigments[51] which have structural

similarities to PR3 and PR254. Simulations of the crystal structure for PR3 (hydrazone form)

yielded results with ≤ 1 % dimensional error. In order to address the confusion concerning the

structures of the azo pigments, structural simulations were carried out on the azo and hydrazone

forms of PR3. An energy comparison of the energetically-converged structures confirmed the

hydrazone structure is lower in energy by 76.17 kJ/mol. Although the azo-form relaxed to an energetically favorable minimum, the large energy difference between the forms suggests that was a coincidence. It is interesting to note that the azo structure relaxed to an energetically favorable minimum. The error between the experimental and calculated lattice parameters for PR254 was considerably larger, with an average error of 1.5 %. This larger error in PR254 may be due to limits of the applied theory in modeling the chlorine atoms or hydrogen bonds. The simulated crystal structures, for PR3 and PR254, were used in the following vibrational analysis.

Table 6-1 Comparison of the experimental and calculated crystallographic unit cell dimensions for PR3 and PR254.

	PR3			PR254		
	Exp.	Calc.	Error (%)	Exp.	Calc.	Error (%)
a (Å)	6.82	6.85	0.41	5.66	5.62	-0.76
b (Å)	12.86	12.88	0.13	23.10	23.64	2.32
c (Å)	16.19	16.17	-0.14	5.59	5.45	-2.44
α (°)	90	90		90	90	0.00
β (°)	102.13	102.12	-0.01	99.07	97.89	-1.19
γ (°)	90	90		90	90	0.00
V (Å³)	1389.51	1395.11	0.40	720.80	716.30	-0.62

6.3.3 Computational Vibrational Analysis of PR3 and PR254

Harmonic vibrational calculations with ss-DFT enabled assigned of the observed features from 0.5 – 3.0 THz for PR3 and PR254. Empirical baseline corrections (details are listed in **Appendix C**) were applied to the experimental spectra to simplify comparison with theory. Calculated THz infrared-active vibrations and corresponding mode descriptions are listed in **Tables 6-2** and **6-3**. Complete lists of all infrared-active modes, intensities, and mode symmetries are provided in **Appendix C**. As seen in **Figure 6-5**, simulations with PBE/basis set

produced reasonable simulations that correlated with both the intensities and positions of the experimental peaks.

In PR3, the multiple features THz spectrum were well-reproduced by computational vibrational analysis. The experimental peaks from 0.79 – 2.15 were assigned to motions that are intermolecular in nature involving translations and rotations of the aromatic groups coupled with intramolecular motions. In contrast, the four modes predicted to contribute to observed absorption at 2.57 THz are largely dominated by intramolecular motion localized in the nitro and methyl groups. The mode characters for the three predominant features in PR254 were all found to be intermolecular in nature. The features at 0.86 THz and 1.88 THz are due to out-of-plane wagging of the phenyl groups that mostly differ in the phase of the vibration. The peak at 2.05 THz is attributed to in-plane phenyl rocking of the PR254 molecules.

Although intermolecular vibrations, such as translational and other lattice motions, are typically found in the assignment of terahertz spectra, these results highlight the importance of internal molecular motions. This appears to be a large factor in the case of conformationally flexible molecules, such as PR3 and PR254, where intermolecular and localized functional group motions can be the main origination of THz features. Despite the similar motions of the predicted vibrations, the measured THz spectra are easily distinguishable between the two pigments.
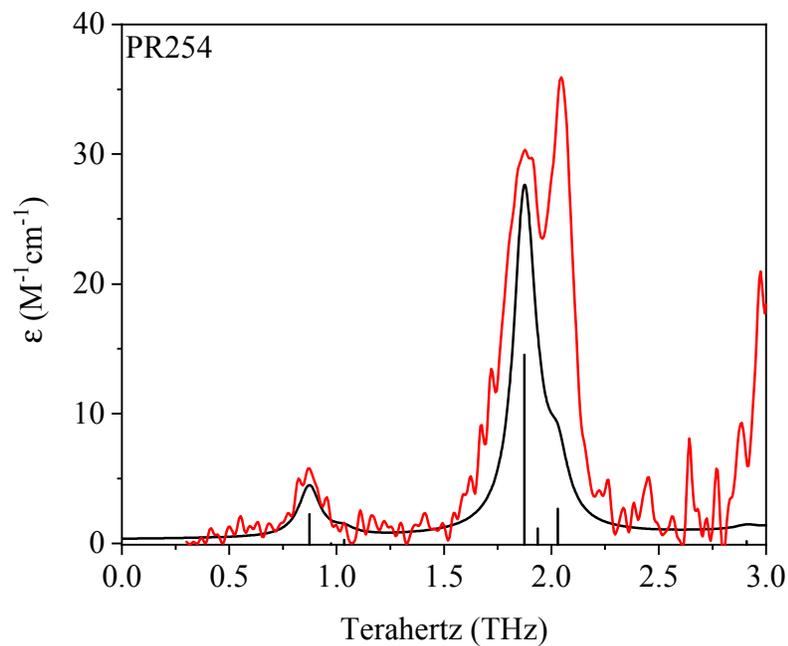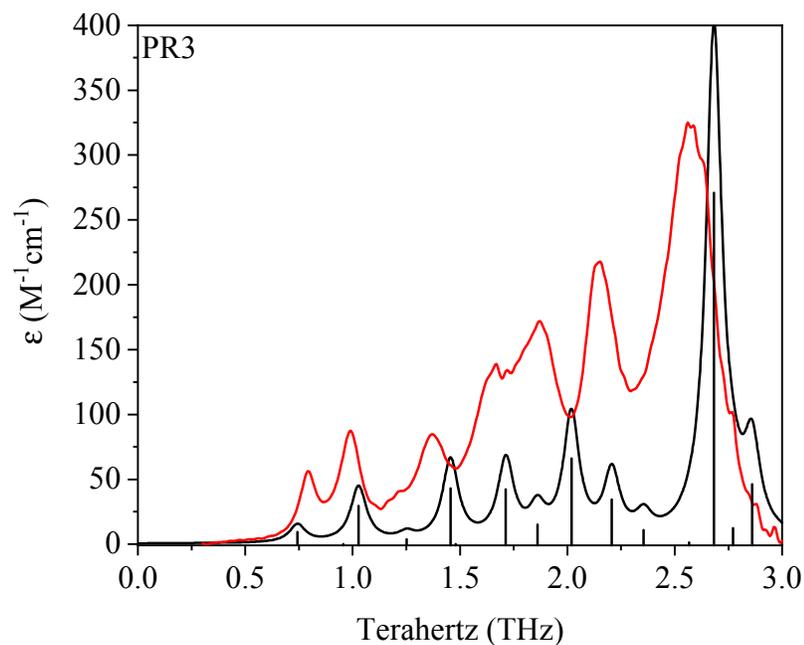
Figure 6-5 Comparison of experimental THz-TDS spectra of PR3 (top panel) and PR254 (bottom panel) with simulated spectra (black). Simulated spectra were convolved with Lorentzian line shapes with FWHM values of 1.5 cm^{-1} for PR3 and 3.23 cm^{-1} for PR254.

Table 6-2 List of experimental and calculated infrared-active modes (THz), infrared intensities (km/mol), mode symmetries, and mode character descriptions for PR3 from 0.5 to 3.0 THz

Exp.	Frequency	Intensity	Symmetry	Mode Character
0.79	0.74	1.48	B_u	Out-of-phase translation along *b*-axis
0.99	0.96	0.00[a]	A_u	Out-of-phase translation along *b*-axis coupled with methyl rotation
	1.03	4.64	A_u	In-plane rotation about the –N=N–
1.22	1.25	0.59	A_u	Out-of-phase wagging
1.37	1.46	6.75	B_u	Rotation about the *a*-axis
	1.48	0.02	A_u	Out-of-phase rocking of naphthol and phenyl groups
1.67	1.71	6.62	B_u	In-phase rocking of naphthol group in *cb*-plane
1.71	1.86	2.38	A_u	Out-of-phase translation along *c*-axis
1.87	2.02	10.37	B_u	Wagging of phenyl and naphthol groups
2.15	2.21	5.41	A_u	Rotation along *a*-axis
	2.36	1.70	B_u	Rotation of phenyl and naphthol groups coupled with methyl rotation
2.57	2.57	0.21	A_u	Rotation of nitro group
	2.68	42.54	B_u	Wagging of nitro and O along *a*-axis
	2.77	1.92	B_u	Out-of-phase rotation of the nitro group
	2.86	7.25	A_u	Rotation of nitro and methyl groups

[a]mode predicted to be infrared active, but of negligible intensity

Table 6-3 List of experimental and calculated infrared-active modes (THz), infrared intensities (km/mol), mode symmetries, and mode character descriptions for PR254 from 0.5 to 3.0 THz

Exp.	Frequency	Intensity	Symmetry	Mode Character
	0.87	0.57	A_u	Out-of-phase wagging of phenyl groups
0.86	0.97	0.00[a]	A_u	Out-of-phase wagging of phenyl groups
	1.03	0.07	B_u	Out-of-phase wagging along *b*-axis
1.88	1.87	3.69	A_u	Wagging of phenyl group and Cl
	1.94	0.29	B_u	Rocking of Cl
2.05	2.03	0.68	B_u	Rotation of phenyl groups
	2.91	0.04	A_u	Wagging of phenyl groups

[a]mode predicted to be infrared active, but of negligible intensity

6.4 Conclusions

THz-TDS and ss-DFT were used to identify and characterize the unique low-frequency vibrational modes of the modern red pigments, PR3 and PR254. In both pigments, these low-frequency modes are primarily due to wagging, twisting, and rocking motions. Although the origins of the spectral features are similar, the THz-TDS spectra are significantly different and can be used to distinguish these two visually similar pigments. These results support increased use of THz-TDS in the field of heritage science and other fields that require nondestructive, chemically specific techniques.

6.5 References

1.   Berrie, B. H.; Lomax, S. Q., Azo Pigments: Their History, Synthesis, Properties, and Use in Artists' Materials. *Studies in the History of Art* **1997**, *57*, 8-33.

2.   Peters, A. T.; Freeman, H. S., *Physico-Chemical Principles of Color Chemistry*; Blackie Academic & Professional, 1996.

3.   Eastaugh, N., *Pigment Compendium: A Dictionary and Optical Microscopy of Historical Pigments*; Butterworth-Heinemann: Oxford, 2008.

4.   Zollinger, H., *Color Chemistry: Syntheses, Properties, and Applications of Organic Dyes and Pigments*; Wiley, 2003.

5.   Kamei, Y.; Shibata, H.; Mizuguchi, J., Azo or Hydrazone Structure in Some Hydrogen-Bonded Azo Pigments. *Journal of Imaging Science and Technology* **2011**, *55*, 30508-1-30508-5.

6.   Khandekar, N.; Mancusi-Ungaro, C.; Cooper, H.; Rosenberger, C.; Eremin, K.; Smith, K.; Stenger, J.; Kirby, D., A Technical Analysis of Three Paintings Attributed to Jackson Pollock. *Studies in Conservation* **2010**, *55*, 204-215.

7.   Learner, T.; Learner, T. J. S.; Smithen, P.; Institute, G. C.; Krueger, J. W.; Art, N. G. o.; Schilling, M. R.; Gallery, T., *Modern Paints Uncovered: Proceedings from the Modern Paints Uncovered Symposium*; Getty Conservation Institute, 2007.

8.   Learner, T.; Institute, G. C., *Analysis of Modern Paints*; Getty Conservation Institute, 2004.

9.   Borg, B.; Dunn, M.; Ang, A.; Villis, C., The Application of State-of-the-Art Technologies to Support Artwork Conservation: Literature Review. *Journal of Cultural Heritage* **2020**.

10.   Bardon, T.; May, R. K.; Taday, P. F.; Strlic, M., Systematic Study of Terahertz Time-Domain Spectra of Historically Informed Black Inks. *Analyst* **2013**, *138*, 4859-4869.

11.   Jackson, J. B.; Bowen, J.; Walker, G.; Labaune, J.; Mourou, G.; Menu, M.; Fukunaga, K., A Survey of Terahertz Applications in Cultural Heritage Conservation Science. *IEEE Transactions on Terahertz Science and Technology* **2011**, *1*, 220-231.

12.   Fukunaga, K.; Ogawa, Y.; Hayashi, S. i.; Hosako, I., Application of Terahertz Spectroscopy for Character Recognition in a Medieval Manuscript. *IEICE Electronics Express* **2008**, *5*, 223-228.

13.   Cosentino, A., Terahertz and Cultural Heritage Science: Examination of Art and Archaeology. *Technologies* **2016**, *4*, 6.

14.   Buzzini, P.; Suzuki, E., Forensic Applications of Raman Spectroscopy for the *in Situ* Analyses of Pigments and Dyes in Ink and Paint Evidence. *Journal of Raman Spectroscopy* **2016**, *47*, 16-27.

15.   Dowsett, M.; Adriaens, A., The Role of Sims in Cultural Heritage Studies. *Nuclear Instruments and Methods in Physics Research Section B* **2004**, *226*, 38-52.

16.   Greening, T., Identification of A-Phase Crystallization Pigment Red 254 in Artist's Paints by Powder X-Ray Diffraction. *Powder Diffraction* **2014**, *29*, 307-310.

17.   Lomax, S. Q., The Application of X-Ray Powder Diffraction for the Analysis of Synthetic Organic Pigments. Part 2: Artists' Paints. *Journal of Coatings Technology and Research* **2010**, *7*, 325-330.

18.   Buchsbaum, C.; Schmidt, M. U., Rietveld Refinement of a Wrong Crystal Structure. *Acta Crystallographica Section B* **2007**, *63*, 926-932.

19.   Bruni, S.; Cariati, F.; Casadio, F.; Toniolo, L., Identification of Pigments on a Xv-Century Illuminated Parchment by Raman and Ftir Microspectroscopies. *Spectrochimica Acta Part A* **1999**, *55*, 1371-1377.

20.   Vagnini, M.; Miliani, C.; Cartechini, L.; Rocchi, P.; Brunetti, B. G.; Sgamellotti, A., Ft-Nir Spectroscopy for Non-Invasive Identification of Natural Polymers and Resins in Easel Paintings. *Analytical and Bioanalytical Chemistry* **2009**, *395*, 2107-2118.

21.   Kendix, E. L.; Prati, S.; Joseph, E.; Sciutto, G.; Mazzeo, R., Atr and Transmission Analysis of Pigments by Means of Far Infrared Spectroscopy. *Analytical and Bioanalytical Chemistry* **2009**, *394*, 1023-1032.

22.   Neelmeijer, C.; Brissaud, I.; Calligaro, T.; Demortier, G.; Hautojärvi, A.; Mäder, M.; Martinot, L.; Schreiner, M.; Tuurnala, T.; Weber, G., Paintings— a Challenge for Xrf and Pixe Analysis. *X-Ray Spectrometry* **2000**, *29*, 101-110.

23.   de Courlon, C.; Ives, S.; Dredge, P., Fields of Colour: The Conservation of Matt, Synthetic Paintings by Michael Johnson. *AICCM Bulletin* **2015**, *36*, 136-146.

24.   Dredge, P.; Ives, S.; Howard, D. L.; Spiers, K. M.; Yip, A.; Kenderdine, S., Mapping Henry: Synchrotron-Sourced X-Ray Fluorescence Mapping and Ultra-High-Definition Scanning of an Early Tudor Portrait of Henry Viii. *Applied Physics A* **2015**, *121*, 789-800.

25.   Rosi, F., et al., An Integrated Spectroscopic Approach for the Non-Invasive Study of Modern Art Materials and Techniques. *Applied Physics A* **2010**, *100*, 613-624.

26.   Jepsen, P. U.; Cooke, D. G.; Koch, M., Terahertz Spectroscopy and Imaging – Modern Techniques and Applications. *Laser Photonics Rev.* **2011**, *5*, 124-166.

27.   Baxter, J. B.; Guglietta, G. W., Terahertz Spectroscopy. *Analytical Chemistry* **2011**, *83*, 4342-4368.

28.   Parrott, E. P. J.; Zeitler, J. A., Terahertz Time-Domain and Low-Frequency Raman Spectroscopy of Organic Materials. *Applied Spectroscopy* **2015**, *69*, 1-25.

29.   Alves-Lima, D.; Song, J.; Li, X.; Portieri, A.; Shen, Y.; Zeitler, J. A.; Lin, H., Review of Terahertz Pulsed Imaging for Pharmaceutical Film Coating Analysis. *Sensors* **2020**, *20*, 1441.

30.   Zeitler, J. A.; Taday, P. F.; Newnham, D. A.; Pepper, M.; Gordon, K. C.; Rades, T., Terahertz Pulsed Spectroscopy and Imaging in the Pharmaceutical Setting ☐ a Review. *J. Pharm. Pharmacol.* **2007**, *59*, 209-223.

31.   King, M. D.; Buchanan, W. D.; Korter, T. M., Identification and Quantification of Polymorphism in the Pharmaceutical Compound Diclofenac Acid by Terahertz Spectroscopy and Solid-State Density Functional Theory. *Anal. Chem.* **2011**, *83*, 3786-3792.

32.   Paul, M. E.; da Silva, T. H.; King, M. D., True Polymorphic Phase Transition or Dynamic Crystal Disorder? An Investigation into the Unusual Phase Behavior of Barbituric Acid Dihydrate. *Crystal Growth & Design* **2019**, *19*, 4745-4753.

33.   Zaczek, A. J.; Catalano, L.; Naumov, P.; Korter, T. M., Mapping the Polymorphic Transformation Gateway Vibration in Crystalline 1,2,4,5-Tetrabromobenzene. *Chem. Sci.* **2019**, *10*, 1332-1341.

34.   Ruggiero, M. T.; Sutton, J. J.; Fraser-Miller, S. J.; Zaczek, A. J.; Korter, T. M.; Gordon, K. C.; Zeitler, J. A., Revisiting the Thermodynamic Stability of Indomethacin Polymorphs with Low-Frequency Vibrational Spectroscopy and Quantum Mechanical Simulations. *Cryst. Growth Des.* **2018**, *18*, 6513-6520.

35.   Squires, A. D.; Kelly, M.; Lewis, R. A., Terahertz Analysis of Quinacridone Pigments. *Journal of Infrared, Millimeter, and Terahertz Waves* **2017**, *38*, 314-324.

36.   Fukunaga, K., *Thz Technology Applied to Cultural Heritage in Practice*; Springer Japan, 2016.

37.   Manceau, J. M.; Nevin, A.; Fotakis, C.; Tzortzakis, S., Terahertz Time Domain Spectroscopy for the Analysis of Cultural Heritage Related Materials. **2008**, *90*, 365-368.

38.   Picollo, M.; Fukunaga, K.; Labaune, J., Obtaining Noninvasive Stratigraphic Details of Panel Paintings Using Terahertz Time Domain Spectroscopy Imaging System. *Journal of Cultural Heritage* **2015**, *16*, 73-80.

39.   Abraham, E.; Fukunaga, K., Terahertz Imaging Applied to the Examination of Artistic Objects. *Stud. Conserv.* **2015**, *60*, 343-352.

40.   Abraham, E.; Younus, A.; Delagnes, J. C.; Mounaix, P., Non-Invasive Investigation of Art Paintings by Terahertz Imaging. **2010**, *100*, 585-590.

41.   Fukunaga, K.; Picollo, M., Terahertz Spectroscopy Applied to the Analysis of Artists' Materials. *Appl. Phys. A* **2010**, *100*, 591-597.

42.   Yang, Y.; Zhai, D.; Zhang, Z.; Zhang, C., Thz Spectroscopic Identification of Red Mineral Pigments in Ancient Chinese Artworks. *J. Infrared, Millimeter, Terahertz Waves* **2017**, *38*, 1232-1240.

43.   Squires, A. D.; Lewis, R. A., Terahertz Analysis of Phthalocyanine Pigments. *Journal of Infrared, Millimeter, and Terahertz Waves* **2019**, *40*, 738-751.

44.   Dampf, S. J.; Korter, T. M., Anomalous Temperature Dependence of the Lowest-Frequency Lattice Vibration in Crystalline Γ-Aminobutyric Acid. *The Journal of Physical Chemistry A* **2019**, *123*, 2058-2064.

45.   Ruggiero, M. T., Invited Review: Modern Methods for Accurately Simulating the Terahertz Spectra of Solids. *Journal of Infrared, Millimeter, and Terahertz Waves* **2020**.

46.   da Silva, T. H.; Rexrode, N. R.; King, M. D., Time-Domain Terahertz Spectroscopy and Solid-State Density Functional Theory Analysis of P-Nitrophenol Polymorphs. *Journal of Infrared, Millimeter, and Terahertz Waves* **2019**.

47.   Kendrick, J.; Burnett, A. D., Exploring the Reliability of Dft Calculations of the Infrared and Terahertz Spectra of Sodium Peroxodisulfate. *Journal of Infrared, Millimeter, and Terahertz Waves* **2019**.

48.   Zhang, W.; Song, Z.; Ruggiero, M. T.; Mittleman, D. M., Assignment of Terahertz Modes in Hydroquinone Clathrates. *Journal of Infrared, Millimeter, and Terahertz Waves* **2020**.

49.   Li, Q.; Zaczek, A. J.; Korter, T. M.; Zeitler, J. A.; Ruggiero, M. T., Methyl-Rotation Dynamics in Metal–Organic Frameworks Probed with Terahertz Spectroscopy. *Chemical Communications* **2018**, *54*, 5776-5779.

50.   Ruggiero, M. T.; Bardon, T.; Strlic, M.; Taday, P. F.; Korter, T. M., Assignment of the Terahertz Spectra of Crystalline Copper Sulfate and Its Hydrates Via Solid-State Density Functional Theory. *J. Phys. Chem. A* **2014**, *118*, 10101-10108.

51.	Squires, A. D.; Lewis, R. A.; Zaczek, A. J.; Korter, T. M., Distinguishing Quinacridone Pigments Via Terahertz Spectroscopy: Absorption Experiments and Solid-State Density Functional Theory Simulations. *J. Phys. Chem. A* **2017**, *121*, 3423-3429.

52.	Kleist, E. M.; Koch Dandolo, C. L.; Guillet, J.-P.; Mounaix, P.; Korter, T. M., Terahertz Spectroscopy and Quantum Mechanical Simulations of Crystalline Copper-Containing Historical Pigments. *J. Phys. Chem. A* **2019**.

53.	Kleist, E. M.; Korter, T. M., Quantitative Analysis of Minium and Vermilion Mixtures Using Low-Frequency Vibrational Spectroscopy. *Analytical Chemistry* **2020**, *92*, 1211-1218.

54.	Herbst, W.; Hunger, K., *Industrial Organic Pigments: Production, Properties, Applications*; Wiley, 2006.

55.	Kobelt, D.; Paulus, E. F.; Kunstmann, W., X-Ray Single-Crystal Structure Analysis of 1,(2-5-Dichorophenylazo)-2-Hydroxy-3-Naphthoic Acid 4-Chloro-2,5-Dimethoxyanilide, Chlorine Derivative of Permanent Brown Fg. *Acta Crystallogr., Sect. B* **1972**, *28*, 1319-24.

56.	Whitaker, A., The Crystal Structure of C.I. Pigment Red 3, 4-Methyl-2-Nitrophenylazo-2-Naphthol. *Z. Kristallogr., Kristallgeom., Kristallphys., Kristallchem.* **1978**, *147*, 99-112.

57.	Whitaker, A., The Crystal Structure of C.I. Pigment Yellow 3, A-(1-Hydroxyethylidene)-2-Chloro-Acetanilide-A-Azo-(4'-Chloro-2'-Nitrobenzene). *Z. Kristallogr.* **1983**, *163*, 19-30.

58.	Whitaker, A., C.I. Pigment Yellow 60, 4-(2-Chlorophenylhydrazono)-3-Methyl-1-Phenyl-5-Pyrazolone. *Acta Crystallogr., Sect. C: Cryst. Struct. Commun.* **1988**, *C44*, 1587-90.

59.	Paulus, E. F.; Rieper, W.; Wagner, D., Molecular and Crystal Structure of the Two Hydrazone Pigments N-(2-Methylphenyl)-2-(2-Methylphenylhydrazono)-3-Oxobutyramide and N-(2-Methoxyphenyl)-2-(2-Methoxyphenylhydrazono)-3-Oxobutyramide. *Z. Kristallogr.* **1983**, *165*, 137-49.

60.	Brown, C. J.; Yadav, H. R., A-(4-Methyl-2-Nitrophenylhydrazono)Acetoacetanilide, C17h16n4o4. *Acta Crystallogr., Sect. C: Cryst. Struct. Commun.* **1984**, *C40*, 564-6.

61.	Whitaker, A., Crystal Structures of Azo Pigments Derived from Acetoacetanilide. *J. Soc. Dyers Colour.* **1988**, *104*, 294-300.

62.	Whitaker, A., Crystal Structure Analysis of Azo Pigments Involving B-Naphthol: A Review. *J. Soc. Dyers Colour.* **1978**, *94*, 431-5.

63.	Ivashevskaya, S., Crystal Structure of Pigment Red 254 from X-Ray Powder Diffraction Data. *Acta Crystallographica Section E* **2017**, *73*, 507-510.

64.	Smith, R., *The Artist's Handbook*; DK Pub., 2003.

65.	Diketopyrrolopyrrole (Dpp) Pigments. In *High Performance Pigments*, pp 165-194.

66.	So, H.-S.; Matsumoto, S., Three Differently Coloured Polymorphs of 3,6-Bis(4-Chlorophenyl)-2,5-Dipropyl-2,5-Dihydropyrrolo[3,4-C]Pyrrole-1,4-Dione. *Acta Crystallographica Section B* **2019**, *75*, 414-422.

67.	Zhang, F.; Wang, H.-W.; Tominaga, K.; Hayashi, M.; Sasaki, T., High-Resolution Thz Spectroscopy and Solid-State Density Functional Theory Calculations of Polycyclic Aromatic Hydrocarbons. *Journal of Infrared, Millimeter, and Terahertz Waves* **2019**.

68.   Macrae, C. F.; Bruno, I. J.; Chisholm, J. A.; Edgington, P. R.; McCabe, P.; Pidcock, E.; Rodriguez-Monge, L.; Taylor, R.; van de Streek, J.; Wood, P. A., Mercury Csd 2.0 - New Features for the Visualization and Investigation of Crystal Structures. *J. Appl. Crystallogr.* **2008**, *41*, 466-470.

69.   Mizuguchi, J.; Grubenmann, A.; Rihs, G., Structures of 3,6-Bis(3-Chlorophenyl)Pyrrolo[3,4-C]Pyrrole-1,4-Dione and 3,6-Bis(4-Chlorophenyl)Pyrrolo[3,4-C]Pyrrole-1,4-Dione. *Acta Crystallographica Section B* **1993**, *49*, 1056-1060.

70.   Bardon, T.; May, R. K.; Taday, P. F.; Strlič, M., Influence of Particle Size on Optical Constants from Pellets Measured with Terahertz Pulsed Spectroscopy. *IEEE Transactions on Terahertz Science and Technology* **2016**, *6*, 408-413.

71.   Sleiman, J., Bou. Terahertz Imaging and Spectroscopy: Application to Defense and Security in Front of the Examination Panel. Université de Bordeaux, 2016.

72.   Dovesi, R., et al., Quantum-Mechanical Condensed Matter Simulations with Crystal. *Wiley Interdiscip. Rev.: Comput. Mol. Sci.* **2018**, *8*, e1360.

73.   Dovesi, R., et al., Crystal17 User's Manual. University of Torino, Torino, 2017.

74.   Perdew, J. P.; Burke, K.; Ernzerhof, M., Generalized Gradient Approximation Made Simple. *Phys. Rev. Lett.* **1996**, *77*, 3865-3868.

75.   Perdew, J. P.; Ruzsinszky, A.; Csonka, G. I.; Vydrov, O. A.; Scuseria, G. E.; Constantin, L. A.; Zhou, X.; Burke, K., Restoring the Density-Gradient Expansion for Exchange in Solids and Surfaces. *Physical Review Letters* **2008**, *100*, 136406.

76.   Schaefer, A.; Horn, H.; Ahlrichs, R., Fully Optimized Contracted Gaussian Basis Sets for Atoms Lithium to Krypton. *J. Chem. Phys.* **1992**, *97*, 2571-7.

77.   Pritchard, B. P.; Altarawy, D.; Didier, B.; Gibson, T. D.; Windus, T. L., New Basis Set Exchange: An Open, up-to-Date Resource for the Molecular Sciences Community. *Journal of Chemical Information and Modeling* **2019**, *59*, 4814-4820.

78.   Feller, D., The Role of Databases in Support of Computational Chemistry Calculations. *Journal of Computational Chemistry* **1996**, *17*, 1571-1586.

79.   Schuchardt, K. L.; Didier, B. T.; Elsethagen, T.; Sun, L.; Gurumoorthi, V.; Chase, J.; Li, J.; Windus, T. L., Basis Set Exchange: A Community Database for Computational Sciences. *Journal of Chemical Information and Modeling* **2007**, *47*, 1045-1052.

80.   Weigend, F.; Ahlrichs, R., Balanced Basis Sets of Split Valence, Triple Zeta Valence and Quadruple Zeta Valence Quality for H to Rn: Design and Assessment of Accuracy. *Physical Chemistry Chemical Physics* **2005**, *7*, 3297-3305.

81.   Grimme, S.; Antony, J.; Ehrlich, S.; Krieg, H., A Consistent and Accurate Ab Initio Parametrization of Density Functional Dispersion Correction (Dft-D) for the 94 Elements H-Pu. *The Journal of Chemical Physics* **2010**, *132*, 154104.

82.   Grimme, S.; Ehrlich, S.; Goerigk, L., Effect of the Damping Function in Dispersion Corrected Density Functional Theory. *Journal of Computational Chemistry* **2011**, *32*, 1456-1465.

83.　　Grimme, S.; Hansen, A.; Brandenburg, J. G.; Bannwarth, C., Dispersion-Corrected Mean-Field Electronic Structure Methods. *Chemical Reviews* **2016**, *116*, 5105-5154.

84.　　Pascale, F.; Zicovich-Wilson, C. M.; Gejo, F. L.; Civalleri, B.; Orlando, R.; Dovesi, R., The Calculation of the Vibrational Frequencies of Crystalline Compounds and Its Implementation in the Crystal Code. *J. Comput. Chem.* **2004**, *25*, 888-897.

85.　　Noel, Y.; Zicovich-Wilson, C. M.; Civalleri, B.; D'Arco, P.; Dovesi, R., Polarization Properties of Zno and Beo: An *Ab Initio* Study through the Berry Phase and Wannier Functions Approaches. *Phys. Rev. B: Condens. Matter Mater. Phys.* **2002**, *65*, 1-9.

86.　　Zicovich-Wilson, C. M.; Pascale, F.; Roetti, C.; Saunders, V. R.; Orlando, R.; Dovesi, R., Calculation of the Vibration Frequencies of A-Quartz: The Effect of Hamiltonian and Basis Set. *J. Comp. Chem.* **2004**, *25*, 1873-1881.

87.　　Monkhorst, H. J.; Pack, J. D., Special Points for Brillouin-Zone Integrations. *Phys. Rev. B: Condens. Matter* **1976**, *13*, 5188-5192.

88.　　Shen, Y. C.; Upadhya, P. C.; Linfield, E. H.; Davies, A. G., Temperature-Dependent Low-Frequency Vibrational Spectra of Purine and Adenine. *Appl. Phys. Lett.* **2003**, *82*, 2350-2352.

89.　　Takahashi, M.; Ishikawa, Y.; Nishizawa, J.-i.; Ito, H., Low-Frequency Vibrational Modes of Riboflavin and Related Compounds. *Chem. Phys. Lett.* **2005**, *401*, 475-482.

Chapter 7. Nondestructive Characterization of Plastic Purses from the Late 19th Century to Modernity: A Collaboration with the Syracuse University Libraries' Plastics and Historical Artifacts Special Collections Research Center

This work is the product of a collaboration between Courtney Asztalos, the Plastics and Historical Artifacts Curator at the Syracuse University Library Special Collections Research Center and members of the chemistry department: Dr. Mary Boyden, Prof. Tim Korter, and graduate student, Elyse Kleist. The goal of this collaboration focused on demonstrating the utility of a portable Raman spectroscopic system as a practical nondestructive method for the unambiguous characterization of plastic artifacts. The identification of the polymer components of these artifacts is essential in the development of conservation strategies for these pieces. Here, the reliability of this Raman spectroscopic method is established via the characterization of a selection of plastic artifacts from the Plastics Collection.

7.1 Introduction

The inclusion of plastic objects in museum collections reflects the growing role of plastics in modern society. The component polymers of these plastic objects range from naturally occurring materials, such as shellac, horn, and ivory, to newer synthetic polymers like polyethylene, polyethylene terephthalate, polystyrene, and polypropylene.[1] Although plastic has been believed to possess long-term physical and chemical durability, curation of these objects has revealed predispositions to deterioration resulting in color changes, physical deformations, increased fragility, as well as the release of volatile organic compounds (VOCs).[2-3] The release of VOCs accelerates deterioration and can induce degradation of nearby objects.[4-5] Additional accelerants include ultra-violet light, high humidity, and environmental pollutants. Increased awareness to the unstable-nature of these polymeric-materials has spawned large-scale research projects focused on developing new tools, techniques, and conservation practices specifically aimed towards the nuances of *in situ* characterization of plastic artifacts.[6-9]

Proper identification and characterization allow for the development of preservation methods, the design of proper storage, and determination of restoration treatments.[10-11] Current identification techniques include a variety of analytical methods such as Raman[4] and infrared spectroscopies,[12-15] gas chromatography/mass spectrometry,[3, 12, 16-18] elemental analysis,[19] and volatile organic compound analysis.[5] Although these methods yield useful data, the instrumentation can be expensive, sampling can be destructive, and operation can be time-consuming or require a specific level of expertise. Ideal identification methods are widely accessible, fast, noninvasive, and nondestructive.[20-22] Portable analytical instruments boast benefits such as small footprints, ease of data collection, and cheaper prices.[22] These advantages have contributed to the implementation of portable spectroscopic instruments within museum

labs. The efficacy of these portable spectroscopic techniques is limited by the availability of comprehensive, high-quality reference spectral libraries that are used in identification. The use of these spectral libraries with commercialized bench top instrumentals allows for the development of procedures that can be readily and consistently followed by all researchers and professionals. This work uses the characterization of a selection of plastic artifacts to highlight the capabilities of a portable Raman system in providing fast and reliable identification of polymer components. Characterization with this system required construction of a comprehensive spectral library from which unknown materials could be identified.

7.2 Materials and Methods

7.2.1 i-Raman Plus Portable Raman System

Spectra were measured with a B&W TEK (Newark, DE) i-Raman Plus Portable Raman System (laser wavelength of 785 nm) equipped with a fiber optic probe, sample stage, and a CCD array detector. Spectra were averaged over 225 acquisitions with a 1-second exposure time at room temperature (298 K) with a spectral range from $65 - 3400$ cm^{-1} and a spectral resolution of 3.5 cm^{-1}. Laser power was varied to avoid damaging polymer samples and artifacts. This spectrometer system includes two software packages, BWSpec and BWID. BWSpec was used for instrument control, spectral acquisition, and peak analysis with spectral smoothing, and baseline corrections. BWID was used for the identification of unknown materials through comparison of collected spectra to user-built spectral libraries.

7.2.2 Spectral Reference Library and Plastic Artifacts

A reference library of over 200 Raman spectra for unique polymer and polymer blends was built from sample kits obtained from Chroma Color Corporation (Dayton, OH); Scientific Polymer Products, Inc. (Ontario, NY); and The Plastics Group of America (Woonsocket, RI).

Five sample artifacts were selected from the Plastics Collection at the Syracuse University Library Special Collections Research Center. The objects, which include plastic purses and pieces, chosen for characterization are shown in **Figure 7-1.** This collection consists of over 2000 artifacts including objects such as toys and industrial building materials to iconic jewelry and fashion pieces. This collection was first established by the Plastics Pioneers' Plastics History and Artifacts Committee and the Greenwald-Haupt Charitable Foundation. Items in the collection have also been contributed by the National Plastics Center and Museum.

Figure 7-1 Plastic objects selected from the Plastics Collection for characterization ― a. clamshell purse (20003.206); b. clear purse (2003.208); c. handbag covers (2010_2005.147); d. colored bamboo-like handles (2010_055.16) ; e. brown purse (2010_055.114).

7.3 Results and Discussion

7.3.1 Spectral Reference Library

The final Raman spectral reference library was composed of over 200 reference polymer samples. A selection of spectra for seven common polymers is shown in **Figure 7-2,** including cellulose acetate (CA); high-density polyethylene (HDPE); polyvinyl chloride (PVC); Nylon-6,6; poly(methyl methacrylate) (PMMA); acrylonitrile butadiene styrene (ABS); styrene acrylonitrile resin (SAN), and polystyrene (PS). The differences between the spectral patterns shown in **Figure 7-2** are exploited by the BWID software for determination of unknown polymer compositions in each artifact.
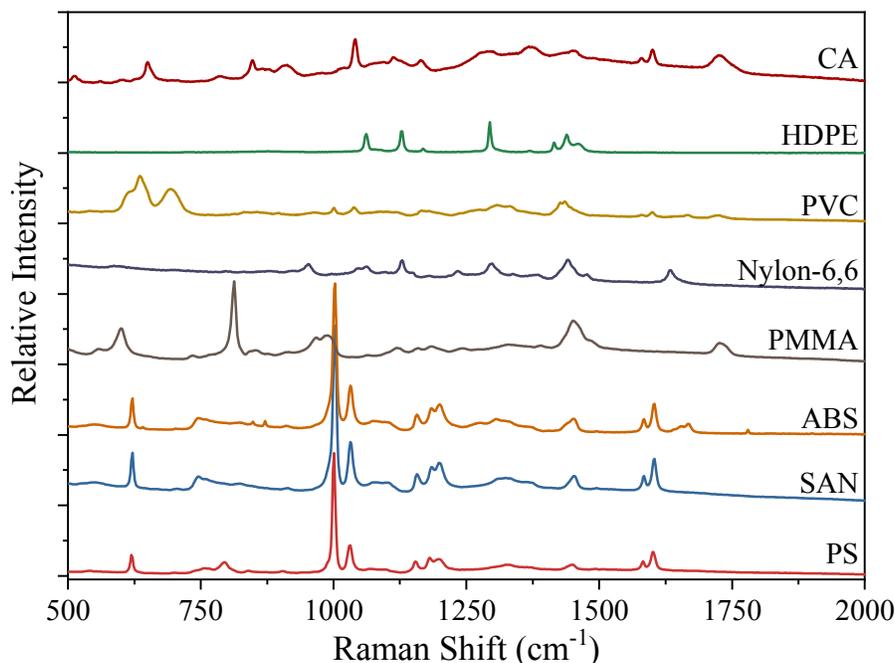
Figure 7-2 Selection of Raman spectra collected with the i-Raman Plus Portable Raman system for seven reference polymers cellulose acetate (CA); high-density polyethylene (HDPE); polyvinyl chloride (PVC); Nylon- 6,6; poly(methyl methacrylate) (PMMA); acrylonitrile butadiene styrene (ABS); styrene acrylonitrile resin (SAN), and polystyrene (PS).

In this work, the spectral range of primary interest is between 500 and 2000 cm^{-1} where peaks correspond to intramolecular motions that can be defined using characteristic group frequencies. These characteristic frequencies enable assignment of the vibrational origins of observed spectral features. For example, **Figure 7-3** shows the reference spectra and structures for PMMA, PS, and CA, and descriptions of the characteristic functional group motions that observed spectral features correspond to.
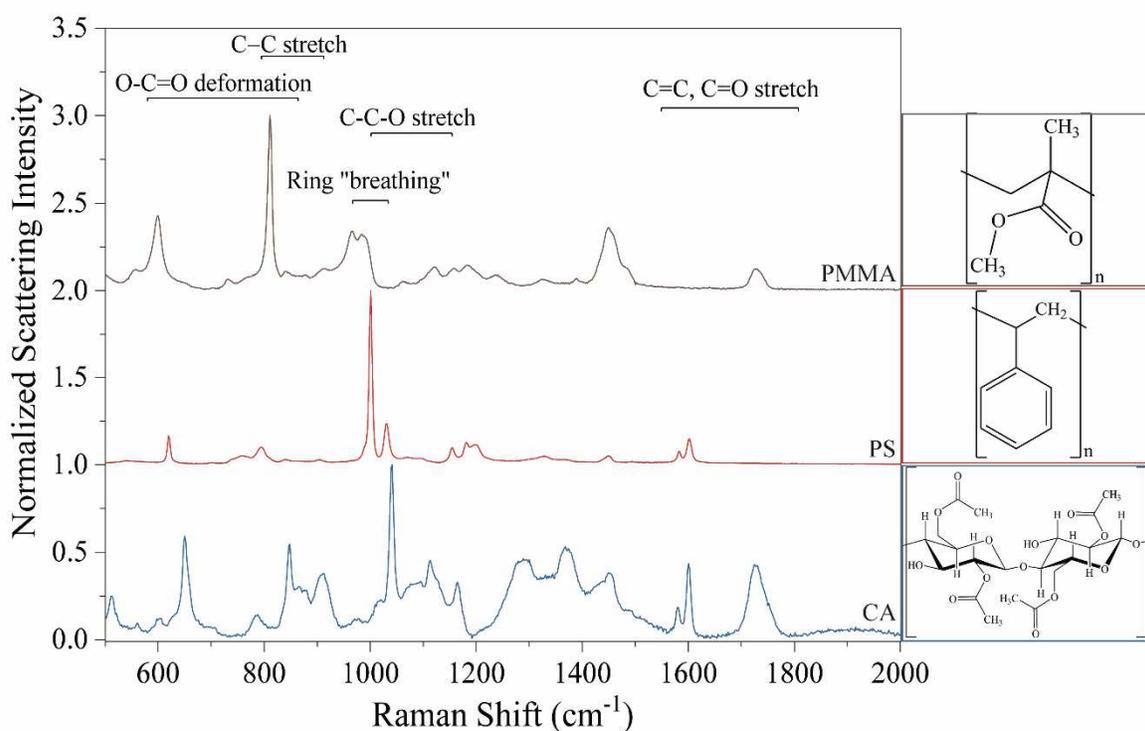
Figure 7-3 Raman spectra and chemical structures of PMMA, PS, and CA. Characteristic molecular vibrations and the associated spectral ranges are labeled.

7.3.2 Composition of Plastic Purses

Prior to this work, there had been minimal detail concerning the composition of these pieces but mentions of prior component identifications will be included where applicable. The polymeric composition of the clear, decorative clamshell purse (2003.206) in **Figure 7-4** had previously been labeled as PMMA. Looking at **Figure 7-4,** the spectrum of PMMA shows

significant activity from 500 – 1000 cm^{-1} which originate from deformations of the ester group in its chemical structure. The collected spectrum for 2003.206 shows a noticeable lack of activity in from 500 – 1000 cm^{-1}. Instead, there is a strong peak centered at 1000 cm^{-1} that is characteristic of a motion commonly observed in aromatic rings. The structure for PMMA (shown in **Figure 7-3**) contains no aromatic rings, but PS does. Upon comparison to the reference spectra for PS and PMMA, it became clear that the 2003.206 had been previously misidentified as PMMA but is actually PS.
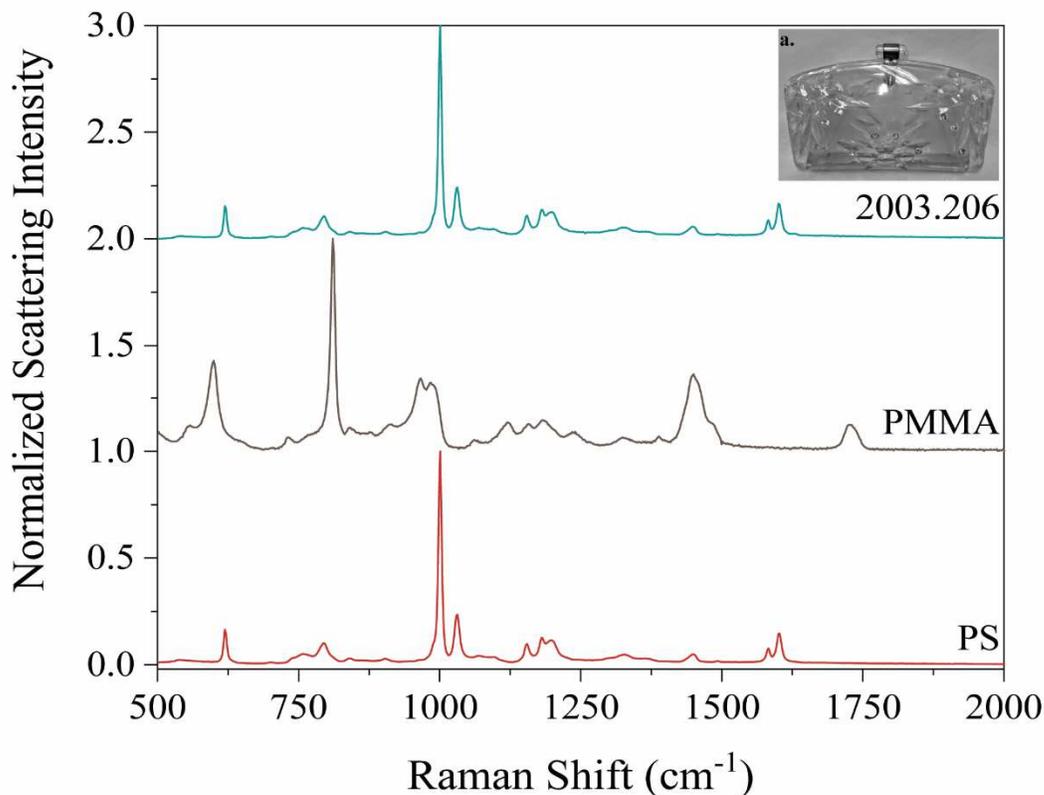
Figure 7-4 Spectral comparison of 2003.206 in comparison to PMMA and PS. Prior to this work, 2003.206 was previously characterized as PMMA.

The purse (2003.208) in **Figure 7-5,** has four parts that were independently characterized: the lid, the base, the handle, and the feet. The lid, base, and handle were all determined to be PMMA by identification of the signature activity from $500 - 1000$ cm^{-1} arising from deformation of the ester functional group. The feet had a drastically different spectral fingerprint, with significant activity from 500 and 2000 cm^{-1}. This complicated spectrum shows features with origins from deformations of an ester groups, stretches of C-C and C-O groups, and ring motions. From these characteristic features, the feet were determined to be CA (structure shown in **Figure 7-3)**.
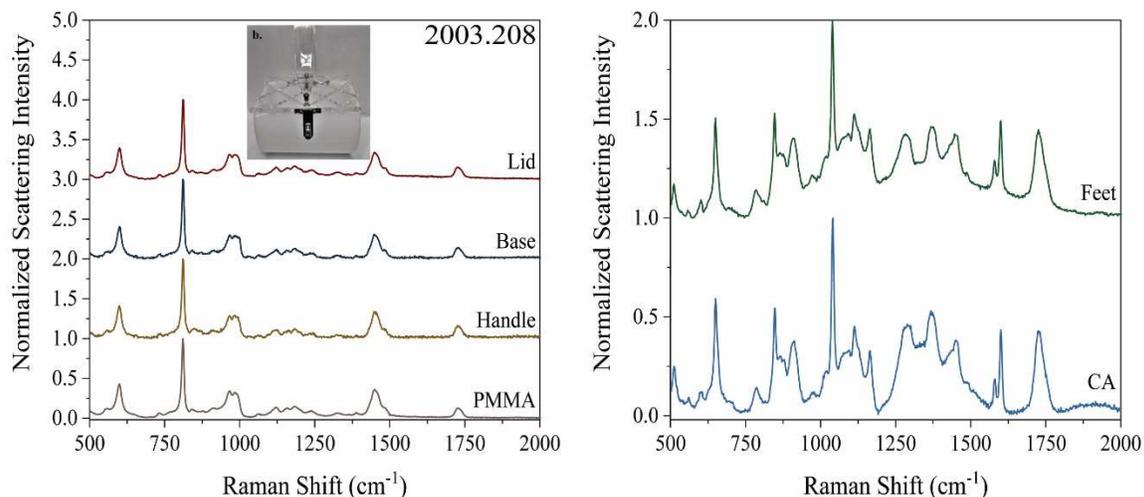
Figure 7-5 Spectral comparison of the four component parts of 2003.208 with PMMA and CA. The base, handle, and lid were determined to be PA and the feet to be cellulose acetate.

Figure 7-6 shows the measured spectrum for the purse covers (2010_2005.147). As seen in previously in **Figure 7-4**, the measured spectrum for 2010_2005.147 is dominated by the peak around 1000 cm^{-1} that corresponds to motion of an aromatic ring, as seen in the spectrum for PS. Prior to this work, 2010_2005.147 had been identified as PS and now was spectroscopically confirmed to be PS.
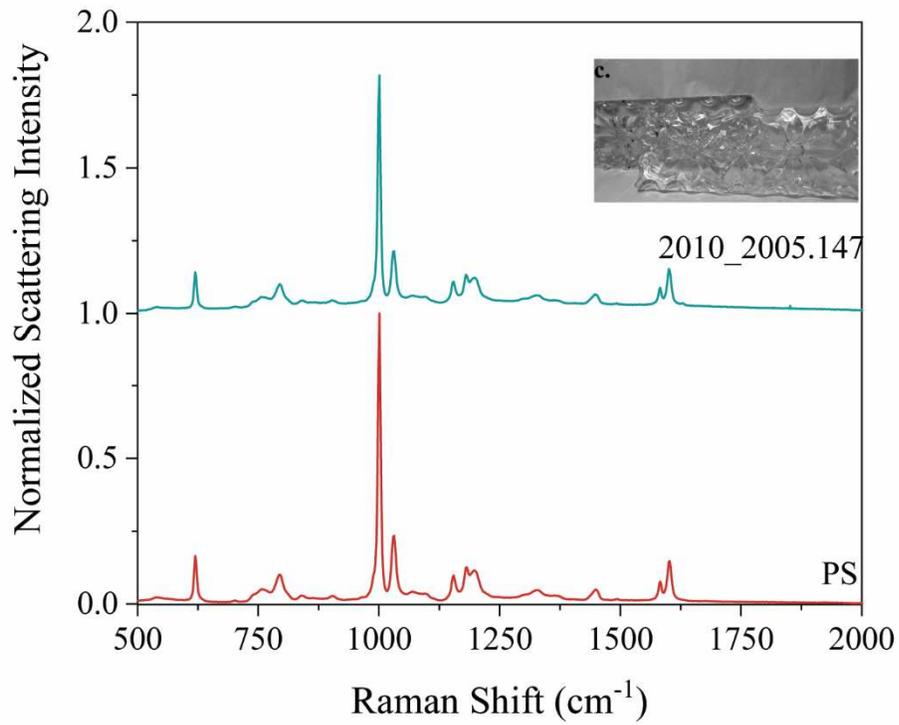
Figure 7-6 Purse covers (2010_2005.147) previously identified as PS were spectroscopically confirmed to be PS.

The four plastic bamboo-like handles (2010_055.16) shown in **Figure 7-1** were previously identified as PS. Spectral measurements shown in **Figure 7-7** found that the spectra for the orange and clear handles were devoid of the characteristic peak for PS around 1000 cm^{-1}. Rather, the collected spectra had many spectral features, similar to those observed in **Figure 7-5,** revealing the primary polymer component as CA.
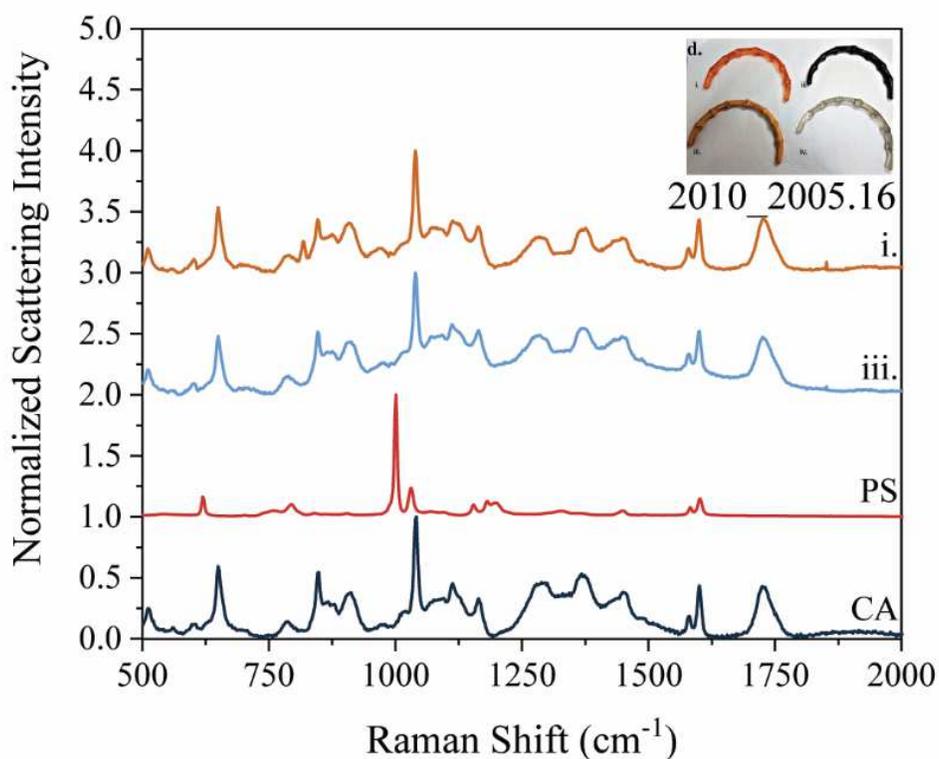
Figure 7.5 Four colored purse handles (2010_055.16) that were previously identified as PS. The spectra for the black and tan handles were inconclusive, but the orange and clear handles were found to be cellulose acetate.

Although the orange and clear handles could be readily identified, spectra for the black and tan handles were inconclusive with no discernable activity (only broad structureless fluorescence was observed). In addition to the lack of spectral features for two of the handles, the

brown purse (2010_055.114) shown in **Figure 7-1**, also lacked any structured features. These pieces fluoresced because they absorbed the 785 nm radiation rather than scattering it.

7.4 Conclusion

The analysis of five plastic artifacts from the Plastics Collection at the Syracuse University Library Special Collections Research Center successfully demonstrated the ability to reliably characterize plastic artifacts with the i-Raman Plus Portable Raman System. These results not only proved that this method is useful in confirming composition identity, but also in revealing composition identities that were unknown or erroneously labeled. One significant limitation that was noted in the examination of the purse handles and brown purse, was sample fluorescence, but that may be mitigated by the use of a different Raman instrument at a different excitation wavelength. The information from this work will be useful in implementing this procedure for large-scale applications for artifact characterization and for designing proper protocols for the preservation of these artifacts.

7.5 References

1.   Dowsett, M.; Adriaens, A., The Role of Sims in Cultural Heritage Studies. *Nuclear Instruments and Methods in Physics Research Section B* **2004**, *226*, 38-52.

2.   Bell, J.; Nel, P.; Stuart, B., Non-Invasive Identification of Polymers in Cultural Heritage Collections: Evaluation, Optimisation and Application of Portable Ftir (Atr and External Reflectance) Spectroscopy to Three-Dimensional Polymer-Based Objects. *Heritage Science* **2019**, *7*, 95.

3.   Lattuati-Derieux, A.; Egasse, C.; Thao-Heu, S.; Balcar, N.; Barabant, G.; Lavédrine, B., What Do Plastics Emit? Hs-Spme-Gc/Ms Analyses of New Standard Plastics and Plastic Objects in Museum Collections. *Journal of Cultural Heritage* **2013**, *14*, 238-247.

4.   Tsang-a, J.-s.; Madden, O.; Coughlin, M.; Maiorana, A.; Watson, J.; Little, N. C.; Speakman, R. J., Degradation of 'Lumarith' Cellulose Acetate. *Studies in Conservation* **2009**, *54*, 90-105.

5.   Curran, K.; Strlič, M., Polymers and Volatiles: Using Voc Analysis for the Conservation of Plastic and Rubber Objects. *Studies in Conservation* **2015**, *60*, 1-14.

6.   Berrie, B. H.; Leona, M.; McLaughlin, R., Unusual Pigments Found in a Painting by Giotto (C. 1266-1337) Reveal Diversity of Materials Used by Medieval Artists. *Heritage Science* **2016**, *4*, 1.

7.   Feller, R. L.; Roy, A., *Artists' Pigments: A Handbook of Their History and Characteristics*; National Gallery of Art: Washington, 1986.

8.   Shashoua, Y., *Conservation of Plastics: Materials Science, Degradation and Preservation*; Elsevier/Butterworth-Heinemann, 2008.

9.   Waentig, F., *Plastics in Art: A Study from the Conservation Point of View*, 2008.

10.   Gottlieb, R.; Maresca, F.; Shoffstall, E., *A Certain Style: The Art of the Plastic Handbag, 1949-59*; Knopf, 1988.

11.   Higgins, P.; Blaser, L., *A Passion for Purses: 1600-2005*; Schiffer Publishing, 2007.

12.   Derrick, M. R.; Stulik, D.; Landry, J. M., *Infrared Spectroscopy in Conservation Science*; Getty Conservation Institute, 2000.

13.   Analytical Methods Committee, A. N., Identification of Plastics in Cultural Heritage Collections by Fourier Transform Infrared Spectroscopy (Ftir). *Analytical Methods* **2018**, *10*, 687-689.

14.   Bardon, T.; May, R. K.; Taday, P. F.; Strlic, M., Systematic Study of Terahertz Time-Domain Spectra of Historically Informed Black Inks. *Analyst* **2013**, *138*, 4859-4869.

15.   Šuštar, V.; Kolar, J.; Lusa, L.; Learner, T.; Schilling, M.; Rivenc, R.; Khanjian, H.; Koleša, D., Identification of Historical Polymers Using near-Infrared Spectroscopy. *Polymer Degradation and Stability* **2014**, *107*, 341-347.

16.   Gage, J., *Color in Art*; Thames & Hudson: London, 2006.

17.   Eastaugh, N., *Pigment Compendium: A Dictionary and Optical Microscopy of Historical Pigments*; Butterworth-Heinemann: Oxford, 2008.

18.   Carvalho, I.; Casanova, C.; Araújo, R.; Lemos, A., Colour Identification, Degradation Processes and Findings in a Fifteenth-Century Book of Hours: The Case Study of *Cofre N.º 31* from Mafra National Palace. *Heritage Science* **2018**, *6*, 9.

19.   Walter, P.; de Viguerie, L., Materials Science Challenges in Paintings. *Nature Materials* **2018**, *17*, 106.

20.   Mitchell, G.; France, F.; Nordon, A.; Tang, P. L.; Gibson, L. T., Assessment of Historical Polymers Using Attenuated Total Reflectance-Fourier Transform Infra-Red Spectroscopy with Principal Component Analysis. *Heritage Science* **2013**, *1*, 28.

21.   Lavédrine, B.; Fournier, A.; Martin, G., *Preservation of Plastic Artefacts in Museum Collections*; Comité Des Travaux Historiques Et Scientifiques, 2012.

22.   Pereira, A.; Candeias, A.; Cardoso, A.; Rodrigues, D.; Vandenabeele, P.; Caldeira, A. T., Non-Invasive Methodology for the Identification of Plastic Pieces in Museum Environment — a Novel Approach. *Microchemical Journal* **2016**, *124*, 846-855.

Appendix A: Supporting Information for Chapter 4

Figure A1. Powder X-ray diffraction data (green) of verdigris sample compared to the predicted powder pattern (black) based on the neutral $Cu(CH_3COO^-)_2 \cdot H_2O$ single-crystal structural data.

Figure A2. Experimental and simulated (black) THz data for malachite.

Figure A3. Azurite unit cell and labeled asymmetric unit.

Figure A4. Malachite unit cell and labeled asymmetric unit.

Figure A5. Unit cell, asymmetric unit, and a labeled asymmetric unit of verdigris.

Figure A6. Baseline corrections for experimental spectra of azurite and verdigris performed using Origin 2018b.

Figure A7. Peak fitting analysis with a Lorentzian line shape for the lowest frequency terahertz absorption of crystalline azurite using Origin 2018b.

Figure A8. Peak fitting analyses with Lorentzian line shapes of the lowest frequency feature (top panel) and broad feature (bottom panel) for verdigris using Origin 2018b.

Table A1. Pellet thickness in millimeters for tablets A-C for azurite, malachite, and verdigris. Each pellet weighed approximately 400 mgs.

Table A2. Cartesian components of dielectric tensor used for calculating LO/TO splitting were simulated with solid-state DFT for azurite, malachite, and verdigris.

Table A3. Solid-state DFT simulated frequencies (including LO/TO splitting) for azurite.

Table A4. Solid-state DFT simulated Raman-active vibrational frequencies for azurite.

Table A5. Solid-state DFT simulated frequencies (including LO/TO splitting) for malachite.

Table A6. Solid-state DFT simulated Raman-active vibrational frequencies for malachite.

Table A7. Solid-state DFT simulated frequencies (including LO/TO splitting) for verdigris.

Table A8. Solid-state DFT simulated Raman-active vibrational frequencies for verdigris.

Table A9. Experimental and solid-state DFT calculated bonds lengths, angles, and torsions for azurite asymmetric unit.

Table A10. Experimental and solid-state DFT calculated bonds lengths, angles, and torsions for malachite asymmetric unit.

Table A11. Experimental and solid-state DFT calculated bonds lengths, angles, and torsions for verdigris with all atoms (top) and only heavy atoms (bottom). Disorder of the methyl rotors in the crystal structure dominates the high RMSD value observed.

Table A1. Pellet thickness in millimeters for tablets A-C for azurite, malachite, and verdigris. Each pellet weighed approximately 400 mgs.

	Pellet thickness (mm)
Azurite	
A	3.34
B	3.44
C	2.72
Malachite	
A	3.28
B	3.36
C	3.24
Verdigris	
A	3.50
B	3.52
C	3.51

Table A2. Cartesian components of dielectric tensor used for calculating LO/TO splitting were simulated with solid-state DFT for azurite, malachite, and verdigris.

	XX	YY	ZZ
Azurite	2.803286	2.724973	3.072791
Malachite	3.387876	3.201275	2.396752
Verdigris	2.209984	2.232644	2.233784

$$\begin{pmatrix} XX & 0 & 0 \\ 0 & YY & 0 \\ 0 & 0 & ZZ \end{pmatrix}$$
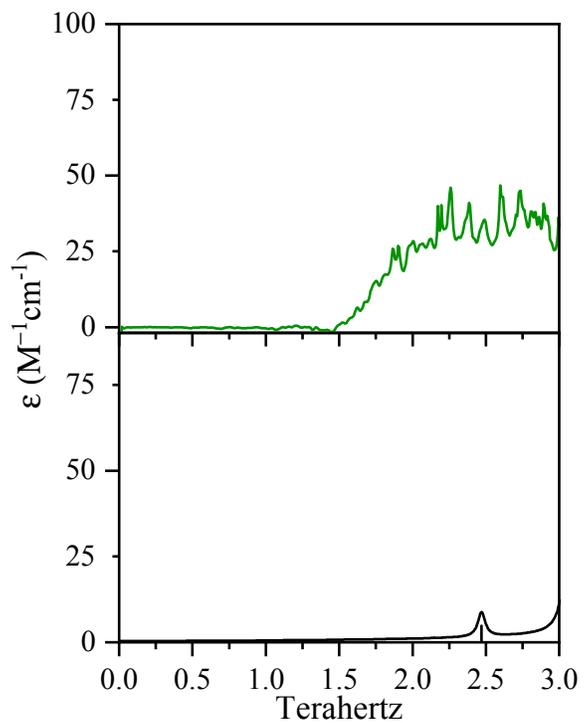
Figure A2. Experimental and simulated (black) THz data for malachite.

Table A3. Solid-state DFT simulated frequencies (including LO/TO splitting) for azurite.

	Longitudinal Optical Modes					Transverse Optical Modes			
	Frequency		Mode	Intensity		Frequency		Mode	Intensity
	cm^{-1}	THz	Symmetry	(km/mol)		cm^{-1}	THz	Symmetry	(km/mol)
1	62.44	1.87	Au	1.6	1	62.86	1.88	Au	0.5
2	76.81	2.30	Bu	5.8	2	116.77	3.50	Au	0
3	116.77	3.50	Au	0.0	3	132.22	3.96	Au	1.6
4	131.32	3.94	Au	9.9	4	152.96	4.59	Au	9.7
5	139.03	4.17	Bu	51.1	5	159.96	4.80	Au	11.8
6	146.88	4.40	Bu	21.0	6	199.64	5.99	Au	24.9
7	147.82	4.43	Au	53.8	7	258.29	7.74	Au	3.7
8	157.59	4.72	Au	10.7	8	272.29	8.16	Au	6.4
9	176.41	5.29	Bu	46.8	9	327.01	9.80	Au	129.7
10	194.17	5.82	Au	49.5	10	364.73	10.93	Au	0.1
11	201.43	6.04	Bu	88.9	11	433.44	12.99	Au	12.7
12	256.23	7.68	Bu	58.8	12	473.49	14.19	Au	58.4
13	257.50	7.72	Au	12.1	13	485.15	14.54	Au	5.5
14	271.04	8.13	Au	19.4	14	542.51	16.26	Au	467.5
15	273.67	8.20	Bu	24.7	15	746.31	22.37	Au	13.8
16	310.48	9.31	Au	225.4	16	776.17	23.27	Au	11.9
17	313.28	9.39	Bu	310.2	17	834.86	25.03	Au	216.6
18	349.93	10.49	Bu	363.3	18	921.70	27.63	Au	46.6
19	364.72	10.93	Au	0.1	19	1080.52	32.39	Au	822.2
20	417.77	12.52	Bu	266.6	20	1119.15	33.55	Au	7.4
21	431.96	12.95	Au	34.7	21	1470.54	44.09	Au	669.2
22	463.81	13.90	Bu	446.6	22	1510.20	45.27	Au	1869.2
23	466.83	14.00	Au	169.7	23	3631.78	108.88	Au	2.2
24	481.45	14.43	Bu	181.8					
25	484.71	14.53	Au	8.9					
26	515.38	15.45	Bu	22.1					
27	515.74	15.46	Au	432.6					
28	745.65	22.35	Au	18.9					
29	756.33	22.67	Bu	58.0					
30	775.60	23.25	Au	17.9					
31	776.11	23.27	Bu	42.1					
32	826.10	24.77	Au	264.4					
33	835.17	25.04	Bu	99.8					
34	915.62	27.45	Bu	939.3					
35	920.01	27.58	Au	57.1					
36	1056.22	31.66	Au	883.1					
37	1058.37	31.73	Bu	166.3					
38	1117.42	33.50	Bu	26.7					
39	1119.01	33.55	Au	3.2					
40	1434.16	43.00	Bu	4294.2					

41	1443.68	43.28	Au	1722.4
42	1489.37	44.65	Au	394.2
43	1503.97	45.09	Bu	6397.2
44	3626.60	108.72	Bu	2423.6
45	3631.76	108.88	Au	2.1

Table A4. Solid-state DFT simulated Raman-active vibrational frequencies for azurite.

	Frequency		Mode
	cm^{-1}	THz	Symmetry
1	92.32	2.77	Ag
2	119.16	3.57	Bg
3	135.60	4.07	Ag
4	149.54	4.48	Bg
5	157.69	4.73	Ag
6	162.95	4.89	Bg
7	181.62	5.44	Ag
8	192.43	5.77	Bg
9	213.65	6.41	Ag
10	233.05	6.99	Bg
11	253.01	7.59	Bg
12	273.17	8.19	Ag
13	279.79	8.39	Ag
14	300.36	9.00	Ag
15	302.66	9.07	Bg
16	340.64	10.21	Bg
17	381.23	11.43	Bg
18	397.18	11.91	Ag
19	411.93	12.35	Bg
20	418.92	12.56	Ag
21	421.31	12.63	Ag
22	428.05	12.83	Bg
23	555.31	16.65	Bg
24	555.35	16.65	Ag
25	745.28	22.34	Ag
26	751.30	22.52	Bg
27	769.82	23.08	Ag
28	773.30	23.18	Bg
29	827.38	24.80	Ag
30	836.87	25.09	Bg
31	922.29	27.65	Bg
32	924.90	27.73	Ag
33	1046.36	31.37	Ag
34	1049.61	31.47	Bg
35	1116.38	33.47	Bg
36	1121.23	33.61	Ag
37	1456.69	43.67	Bg
38	1469.20	44.05	Ag
39	1486.59	44.57	Ag
40	1624.58	48.70	Bg
41	3629.38	108.81	Ag
42	3634.36	108.96	Bg
43	1503.97	45.09	Bu
44	3626.60	108.72	Bu
45	3631.76	108.88	Au

135

Table A5. Solid-state DFT simulated frequencies (including LO/TO splitting) for malachite.

	Longitudinal Optical Modes					Transverse Optical Modes			
	Frequency cm^{-1}	THz	Mode Symmetry	Intensity (km/mol)		Frequency cm^{-1}	THz	Mode Symmetry	Intensity (km/mol)
1	82.39	2.47	Au	0.4	1	82.44	2.47	Au	0.1
2	102.42	3.07	Au	3.5	2	102.76	3.08	Au	0.7
3	123.73	3.71	Bu	9.5	3	126.34	3.79	Au	1.2
4	125.86	3.77	Au	6.4	4	143.12	4.29	Au	2.2
5	142.33	4.27	Au	12.2	5	179.72	5.39	Au	1
6	145.34	4.36	Bu	10.0	6	196.49	5.89	Au	32.4
7	150.81	4.52	Bu	278.8	7	221.94	6.65	Au	28.6
8	164.64	4.94	Bu	41.9	8	232.10	6.96	Au	23.6
9	179.18	5.37	Au	20.2	9	244.07	7.32	Au	3.9
10	184.57	5.53	Bu	100.3	10	283.10	8.49	Au	5.6
11	187.56	5.62	Au	167.8	11	290.51	8.71	Au	0.3
12	216.28	6.48	Bu	75.1	12	375.88	11.27	Au	451.7
13	216.51	6.49	Au	87.1	13	351.77	10.55	Au	39.4
14	229.69	6.89	Au	24.6	14	443.97	13.31	Au	122.2
15	243.65	7.30	Au	5.6	15	501.35	15.03	Au	99.5
16	245.19	7.35	Bu	42.1	16	541.62	16.24	Au	4.5
17	262.57	7.87	Bu	5.3	17	594.31	17.82	Au	264.6
18	278.07	8.34	Bu	113.9	18	721.00	21.62	Au	39.3
19	282.21	8.46	Au	23.7	19	754.91	22.63	Au	5.4
20	290.47	8.71	Au	1.0	20	822.90	24.67	Au	12.8
21	290.87	8.72	Bu	306.5	21	834.57	25.02	Au	6
22	305.37	9.15	Bu	836.4	22	868.37	26.03	Au	0.6
23	328.36	9.84	Bu	108.1	23	931.55	27.93	Au	303
24	332.10	9.96	Au	712.4	24	1089.12	32.65	Au	337.1
25	355.73	10.66	Au	74.4	25	1145.10	34.33	Au	278
26	438.55	13.15	Au	95.2	26	1469.18	44.05	Au	817
27	449.68	13.48	Bu	45.9	27	1578.88	47.33	Au	5124.8
28	497.13	14.90	Au	92.9	28	3554.81	106.57	Au	561.9
29	511.22	15.33	Bu	102.1	29	3675.03	110.17	Au	4275.4
30	526.31	15.78	Bu	484.0					
31	541.42	16.23	Au	5.3					
32	571.41	17.13	Bu	189.9					
33	584.59	17.53	Au	258.6					
34	719.74	21.58	Au	44.9					
35	719.99	21.58	Bu	16.2					
36	751.41	22.53	Bu	238.7					
37	754.75	22.63	Au	6.2					
38	822.50	24.66	Au	18.9					
39	827.60	24.81	Bu	41.2					
40	829.40	24.86	Bu	934.7					
41	834.39	25.01	Au	8.4					
42	868.35	26.03	Au	1.1					
43	869.37	26.06	Bu	643.6					
44	923.07	27.67	Au	430.1					
45	927.68	27.81	Bu	1970.7					
46	1080.62	32.40	Au	524.5					
47	1089.68	32.67	Bu	595.2					
48	1135.80	34.05	Bu	691.8					
49	1139.62	34.16	Au	294.3					
50	1401.51	42.02	Bu	3815.3					
51	1444.96	43.32	Au	2703.9					
52	1522.12	45.63	Au	2672.2					

53	1564.73	46.91	Bu	1525.4
54	3545.08	106.28	Bu	3232.3
55	3550.66	106.45	Au	815.8
56	3651.29	109.46	Au	3731.5
57	3672.05	110.09	Bu	99.5

Table A6. Solid-state DFT simulated Raman-active vibrational frequencies for malachite.

| | Frequency | | Mode |
	cm^{-1}	THz	Symmetry
1	49.80	1.49	Ag
2	80.47	2.41	Bg
3	80.62	2.42	Ag
4	99.17	2.97	Bg
5	113.66	3.41	Ag
6	129.62	3.89	Ag
7	130.76	3.92	Bg
8	132.33	3.97	Ag
9	146.15	4.38	Bg
10	155.83	4.67	Ag
11	156.50	4.69	Bg
12	170.48	5.11	Ag
13	174.65	5.24	Bg
14	189.91	5.69	Bg
15	206.50	6.19	Ag
16	212.41	6.37	Bg
17	229.37	6.88	Bg
18	246.00	7.37	Ag
19	248.20	7.44	Ag
20	249.76	7.49	Bg
21	279.00	8.36	Ag
22	279.65	8.38	Bg
23	287.39	8.62	Bg
24	288.84	8.66	Ag
25	301.25	9.03	Ag
26	310.60	9.31	Bg
27	349.76	10.49	Bg
28	358.47	10.75	Ag
29	440.59	13.21	Bg
30	450.73	13.51	Ag
31	506.47	15.18	Bg
32	520.41	15.60	Ag
33	538.45	16.14	Ag
34	544.96	16.34	Bg
35	567.03	17.00	Ag
36	603.90	18.10	Bg
37	722.02	21.65	Ag
38	724.18	21.71	Bg
39	753.12	22.58	Ag
40	758.06	22.73	Bg
41	802.89	24.07	Ag
42	806.50	24.18	Bg
43	831.09	24.92	Bg
44	832.35	24.95	Ag
45	879.89	26.38	Ag
46	880.21	26.39	Bg
47	1087.82	32.61	Ag
48	1091.93	32.74	Bg
49	1127.76	33.81	Ag
50	1138.60	34.13	Bg

51	1148.14	34.42	Ag
52	1148.34	34.43	Bg
53	1389.25	41.65	Ag
54	1489.20	44.65	Bg
55	1537.67	46.10	Ag
56	1560.98	46.80	Bg
57	3539.91	106.12	Ag
58	3545.97	106.31	Bg
59	3625.93	108.70	Ag
60	3627.85	108.76	Bg

Table A7. Solid-state DFT simulated frequencies (including LO/TO splitting) for verdigris.

	Longitudinal Optical Modes					Transverse Optical Modes			
	Frequency		Mode	Intensity		Frequency		Mode	Intensity
	cm⁻¹	THz	Symmetry	(km/mol)		cm⁻¹	THz	Symmetry	(km/mol)
1	36.52	1.09	Bu	1.5	1	37.08	1.11	Au	0.2
2	36.93	1.11	Au	0.5	2	65.65	1.97	Au	0.1
3	65.59	1.97	Au	0.4	3	71.71	2.15	Au	3.9
4	70.55	2.12	Au	7.0	4	77.90	2.34	Au	0.0
5	71.55	2.15	Bu	5.7	5	91.47	2.74	Au	0.0
6	77.90	2.34	Au	0.0	6	118.74	3.56	Au	0.4
7	78.23	2.35	Bu	3.5	7	133.84	4.01	Au	8.1
8	83.75	2.51	Bu	6.1	8	143.21	4.29	Au	0.3
9	91.46	2.74	Au	0.0	9	176.13	5.28	Au	0.1
10	104.22	3.12	Bu	2.5	10	188.70	5.66	Au	0.1
11	118.66	3.56	Au	0.9	11	199.57	5.98	Au	1.5
12	127.54	3.82	Bu	2.5	12	226.46	6.79	Au	0.3
13	132.57	3.97	Au	14.2	13	240.32	7.20	Au	10.8
14	143.16	4.29	Au	0.5	14	255.26	7.65	Au	4.0
15	144.77	4.34	Bu	4.2	15	272.72	8.18	Au	17.3
16	167.66	5.03	Bu	13.7	16	283.22	8.49	Au	16.7
17	176.12	5.28	Au	0.2	17	305.40	9.16	Au	71.6
18	186.07	5.58	Bu	31.8	18	336.85	10.10	Au	11.3
19	188.68	5.66	Au	0.2	19	380.35	11.40	Au	152.6
20	194.25	5.82	Bu	61.8	20	529.55	15.88	Au	8.8
21	199.41	5.98	Au	2.9	21	570.24	17.10	Au	5.1
22	226.42	6.79	Au	0.8	22	622.05	18.65	Au	313.2
23	226.79	6.80	Bu	10.0	23	643.24	19.28	Au	189.2
24	239.25	7.17	Au	24.7	24	646.42	19.38	Au	46.9
25	245.73	7.37	Bu	29.6	25	689.93	20.68	Au	51.3
26	252.91	7.58	Bu	35.7	26	695.82	20.86	Au	146.1
27	254.88	7.64	Au	9.2	27	747.83	22.42	Au	55.4
28	271.08	8.13	Au	45.1	28	789.73	23.68	Au	713.0
29	272.70	8.18	Bu	49.4	29	952.84	28.57	Au	0.4
30	276.29	8.28	Bu	253.9	30	957.27	28.70	Au	0.1
31	281.93	8.45	Au	30.9	31	1048.57	31.44	Au	14.8
32	300.93	9.02	Au	100.9	32	1055.59	31.65	Au	56.6
33	304.29	9.12	Bu	4.8	33	1075.35	32.24	Au	61.6
34	319.47	9.58	Bu	352.3	34	1083.23	32.47	Au	0.7
35	336.21	10.08	Au	16.6	35	1400.51	41.99	Au	47.5
36	371.11	11.13	Bu	96.0	36	1404.62	42.11	Au	13.7
37	373.27	11.19	Au	187.0	37	1439.09	43.14	Au	11.7
38	525.90	15.77	Bu	1.0	38	1456.29	43.66	Au	252.6
39	529.20	15.87	Au	15.8	39	1480.29	44.38	Au	22.2
40	566.56	16.99	Bu	5.6	40	1489.87	44.67	Au	182.9
41	570.02	17.09	Au	12.8	41	1499.01	44.94	Au	386.5
42	604.88	18.13	Bu	71.3	42	1503.08	45.06	Au	183.5
43	609.85	18.28	Au	653.0	43	1533.91	45.99	Au	132.3
44	636.56	19.08	Bu	51.9	44	1663.21	49.86	Au	2146.4
45	638.96	19.16	Au	134.6	45	1714.69	51.41	Au	6.8
46	644.79	19.33	Bu	29.4	46	3058.09	91.68	Au	6.8
47	646.01	19.37	Au	5.7	47	3060.11	91.74	Au	4.2
48	657.45	19.71	Bu	110.0	48	3116.45	93.43	Au	1.5
49	688.02	20.63	Au	115.6	49	3124.48	93.67	Au	3.3
50	691.47	20.73	Bu	80.4	50	3162.23	94.80	Au	2.2
51	693.36	20.79	Au	68.1	51	3177.13	95.25	Au	3.8

52	705.19	21.14	Bu	817.4		52	3518.81	105.49	Au	590.6
53	739.74	22.18	Bu	70.4		53	3656.24	109.61	Au	1932.8
54	746.39	22.38	Au	82.6						
55	777.04	23.30	Au	545.7						
56	952.78	28.56	Bu	6.4						
57	952.84	28.57	Au	0.3						
58	957.00	28.69	Bu	0.1						
59	957.26	28.70	Au	0.1						
60	1048.31	31.43	Au	19.7						
61	1048.87	31.44	Bu	3.2						
62	1054.14	31.60	Bu	56.8						
63	1054.75	31.62	Au	56.1						
64	1074.50	32.21	Au	55.5						
65	1077.24	32.30	Bu	24.0						
66	1083.22	32.47	Au	0.5						
67	1083.87	32.49	Bu	84.1						
68	1391.92	41.73	Bu	20.8						
69	1399.14	41.95	Bu	43.1						
70	1399.82	41.97	Au	79.2						
71	1404.46	42.10	Au	15.8						
72	1438.89	43.14	Au	28.5						
73	1445.30	43.33	Bu	1171.4						
74	1451.16	43.50	Bu	926.7						
75	1452.64	43.55	Au	440.5						
76	1477.28	44.29	Bu	138.5						
77	1479.00	44.34	Bu	108.5						
78	1479.84	44.36	Au	77.6						
79	1486.52	44.56	Au	441.5						
80	1486.56	44.57	Bu	197.1						
81	1495.23	44.83	Au	246.3						
82	1499.76	44.96	Bu	62.5						
83	1502.25	45.04	Au	29.6						
84	1532.72	45.95	Au	101.4						
85	1540.24	46.18	Bu	60.5						
86	1625.02	48.72	Bu	4504.2						
87	1644.71	49.31	Au	1752.6						
88	1691.81	50.72	Bu	182.5						
89	1714.65	51.40	Au	3.2						
90	3057.70	91.67	Bu	30.4						
91	3058.06	91.68	Au	6.9						
92	3060.09	91.74	Au	4.1						
93	3060.22	91.74	Bu	9.2						
94	3116.38	93.43	Bu	0.4						
95	3116.44	93.43	Au	1.5						
96	3123.46	93.64	Bu	68.1						
97	3124.46	93.67	Au	3.4						
98	3161.83	94.79	Bu	12.5						
99	3162.22	94.80	Au	2.2						
100	3177.07	95.25	Bu	8.9						
101	3177.11	95.25	Au	3.9						
102	3516.05	105.41	Au	645.5						
103	3519.45	105.51	Bu	3892.7						
104	3648.21	109.37	Au	1802.4						
105	3650.46	109.44	Bu	2068.6						

Table A8. Solid-state DFT simulated Raman-active vibrational frequencies for verdigris.

	Frequency		Mode
	cm^{-1}	THz	Symmetry
1	51.80	1.55	Bg
2	53.70	1.61	Bg
3	57.11	1.71	Ag
4	59.65	1.79	Ag
5	81.26	2.44	Bg
6	83.04	2.49	Ag
7	99.77	2.99	Ag
8	101.51	3.04	Bg
9	103.97	3.12	Ag
10	109.24	3.27	Bg
11	124.16	3.72	Bg
12	124.27	3.73	Ag
13	126.88	3.80	Bg
14	134.98	4.05	Ag
15	142.72	4.28	Bg
16	144.28	4.33	Ag
17	147.28	4.42	Bg
18	147.52	4.42	Ag
19	179.01	5.37	Bg
20	181.70	5.45	Ag
21	181.88	5.45	Bg
22	190.39	5.71	Ag
23	190.43	5.71	Bg
24	203.56	6.10	Ag
25	218.26	6.54	Bg
26	220.21	6.60	Ag
27	233.10	6.99	Ag
28	233.13	6.99	Bg
29	244.26	7.32	Ag
30	244.33	7.33	Bg
31	257.97	7.73	Ag
32	259.80	7.79	Bg
33	266.11	7.98	Ag
34	269.52	8.08	Bg
35	277.34	8.31	Bg
36	277.55	8.32	Ag
37	306.69	9.19	Ag
38	310.41	9.31	Bg
39	322.85	9.68	Bg
40	325.04	9.74	Ag
41	541.95	16.25	Bg
42	547.51	16.41	Ag
43	569.07	17.06	Bg
44	569.29	17.07	Ag
45	595.64	17.86	Bg
46	610.15	18.29	Ag
47	626.09	18.77	Bg
48	627.55	18.81	Ag
49	651.43	19.53	Bg
50	651.44	19.53	Ag
51	669.10	20.06	Bg
52	684.52	20.52	Ag

53	698.78	20.95	Bg
54	708.71	21.25	Ag
55	722.55	21.66	Bg
56	771.31	23.12	Bg
57	773.47	23.19	Ag
58	782.10	23.45	Ag
59	948.83	28.45	Bg
60	949.35	28.46	Ag
61	963.50	28.89	Ag
62	963.52	28.89	Bg
63	1048.74	31.44	Ag
64	1050.81	31.50	Bg
65	1058.30	31.73	Bg
66	1058.76	31.74	Ag
67	1072.72	32.16	Ag
68	1076.52	32.27	Bg
69	1083.89	32.49	Bg
70	1085.28	32.54	Ag
71	1394.57	41.81	Bg
72	1400.83	42.00	Ag
73	1403.97	42.09	Bg
74	1406.55	42.17	Ag
75	1439.91	43.17	Ag
76	1442.31	43.24	Bg
77	1445.51	43.34	Ag
78	1458.70	43.73	Bg
79	1473.51	44.17	Bg
80	1479.98	44.37	Bg
81	1480.11	44.37	Ag
82	1485.90	44.55	Bg
83	1486.73	44.57	Ag
84	1488.23	44.62	Ag
85	1504.35	45.10	Bg
86	1504.87	45.11	Ag
87	1552.09	46.53	Bg
88	1553.39	46.57	Ag
89	1558.21	46.71	Ag
90	1559.33	46.75	Bg
91	1698.18	50.91	Bg
92	1720.61	51.58	Ag
93	3057.57	91.66	Bg
94	3057.61	91.66	Ag
95	3059.91	91.73	Bg
96	3060.41	91.75	Ag
97	3116.37	93.43	Ag
98	3116.50	93.43	Bg
99	3122.79	93.62	Bg
100	3123.93	93.65	Ag
101	3161.50	94.78	Bg
102	3161.78	94.79	Ag
103	3177.14	95.25	Bg
104	3177.32	95.25	Ag
105	3516.96	105.44	Ag
106	3533.06	105.92	Bg
107	3643.72	109.24	Ag
108	3650.28	109.43	Bg

Table A9. Experimental and solid-state DFT calculated bonds lengths, angles, and torsions for azurite asymmetric unit.

Atom1	Atom2	Atom3	Atom4	Length (Å)		Angle (°)		Torsion Angle (°)	
				Exp.	Calcd.	Exp.	Calcd.	Exp.	Calcd.
Cu2	O2	C	O4	2.758	2.79	74.21	73.87	-7.72	-8.2
Cu2	O4	C	O3	1.940	1.950	112.89	113.86	-167.84	-167.94
O2	C	Cu2	O1	1.280	1.288	78.72	79.16	-62.12	-63.01
O3	C	Cu2	O2	1.287	1.284	160.14	160.08	-158.15	-159.44
O4	C	Cu2	O2	1.277	1.277	41.34	40.80	169.79	169.01
O1	Cu2	O4	C	1.967	1.968	96.69	96.92	-73.59	-75.53
H	O1	Cu2	O4	0.973	0.976	113.05	113.59	66.97	68.75
Cu1	O2	C	Cu2	1.939	1.935	120.29	121.01	-151.38	-150.07
				RMSD	0.012	RMSD	0.55	RMSD	1.22

Figure A3. Azurite unit cell and labeled asymmetric unit.

Table A10. Experimental and solid-state DFT calculated bonds lengths, angles, and torsions for malachite asymmetric unit.

Atom1	Atom2	Atom3	Atom4	Length (Å) Exp.	Calcd.	Angle (°) Exp.	Calcd.	Torsion Angle (°) Exp.	Calcd.
Cu2	O2	Cu1	O5	2.110	2.124	94.74	91.73	8.73	5.35
Cu1	O5	Cu2	O4	1.911	1.922	106.41	105.42	103.67	103.20
O2	Cu1	O5	H2	2.053	2.581	79.43	79.99	-131.35	-140.02
O3	C	O2	Cu1	1.266	1.265	119.66	119.78	-34.32	-80.42
O4	Cu2	O2	C	2.372	1.928	92.09	95.76	46.22	55.04
O1	C	O2	Cu2	1.287	1.291	118.87	118.84	19.42	21.70
H1	O4	Cu2	O2	0.975	0.978	99.32	115.06	-158.24	-168.78
H2	O5	Cu1	O2	0.969	0.972	123.65	123.24	-131.35	-140.02
C	O2	Cu1	O5	1.313	1.305	124.29	129.04	-128.26	-129.02
				RMSD	0.230	RMSD	5.72	RMSD	16.61
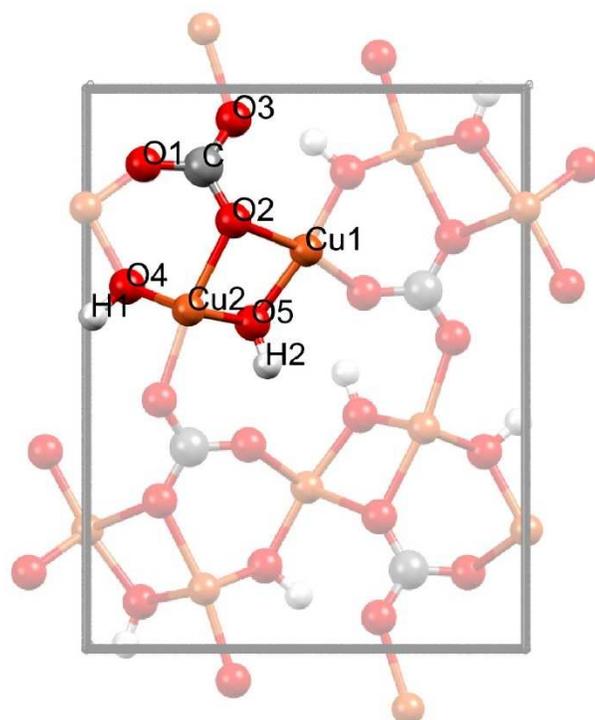
Figure A4. Malachite unit cell and labeled asymmetric unit.

Table A11. Experimental and solid-state DFT calculated bonds lengths, angles, and torsions for verdigris with all atoms (top) and only heavy atoms (bottom). Disorder of the methyl rotors in the crystal structure dominates the high RMSD value observed.

Atom1	Atom2	Atom3	Atom4	Length (Å) Exp.	Length (Å) Calcd.	Angle (°) Exp.	Angle (°) Calcd.	Torsion Angle (°) Exp.	Torsion Angle (°) Calcd.
O3	Cu	O1	C1	1.994	1.95	89.05	87.01	-81.37	-86.25
O1	Cu	O5	H8	1.95	2.01	93.33	100.22	44.93	20.61
C4	C3	O3	Cu	1.495	1.502	117.04	117.73	-173.89	-178.66
C2	C1	O1	Cu	1.506	1.505	118.78	119.08	177.52	177.15
H5	C4	C3	O3	1.064	1.087	116.54	111.26	35.35	4.99
H4	C4	C3	O3	0.874	1.090	117.80	109.30	-175.42	126.75
H6	C4	C3	O3	0.996	1.090	106.63	109.27	-61.87	-116.35
H2	C2	C1	O1	0.977	1.085	110.31	112.27	63.23	-3.91
H1	C2	C1	O1	1.003	1.091	106.94	108.44	-47.97	-125.87
H3	C2	C1	O1	1.022	1.091	103.35	109.97	-171.60	117.84
H8	O5	Cu	O3	0.860	0.973	115.09	133.15	-44.29	-67.94
H7	O5	Cu	O1	0.880	0.979	128.54	115.91	-115.07	-134.03
O4	C3	O3	Cu	1.251	1.269	124.22	125.06	5.95	1.84
C3	**O3**	Cu	O1	1.269	1.265	124.90	122.49	78.70	87.36
C1	O1	Cu	O3	1.248	1.269	124.85	121.03	-81.37	-86.25
O2	C1	O1	Cu	1.274	1.267	125.45	124.10	-1.96	-2.39
				RMSD	0.083	RMSD	6.70	RMSD	109.32

Atom1	Atom2	Atom3	Atom4	Length (Å) Exp.	Length (Å) Calcd.	Angle (°) Exp.	Angle (°) Calcd.	Torsion Angle (°) Exp.	Torsion Angle (°) Calcd.
O3	Cu	O1	C1	1.994	1.95	89.05	87.01	-81.37	-86.25
C4	C3	O3	Cu	1.495	1.502	117.04	117.73	-173.89	-178.66
C2	C1	O1	Cu	1.506	1.505	118.78	119.08	177.52	177.15
O4	C3	O3	Cu	1.251	1.269	124.22	125.06	5.95	1.84
C3	O3	Cu	O1	1.269	1.265	124.90	122.49	78.70	87.36
C1	O1	Cu	O3	1.248	1.269	124.85	121.03	-81.37	-86.25
O2	C1	O1	Cu	1.274	1.267	125.45	124.10	-1.96	-2.39
				RMSD	0.020	RMSD	1.99	RMSD	4.82
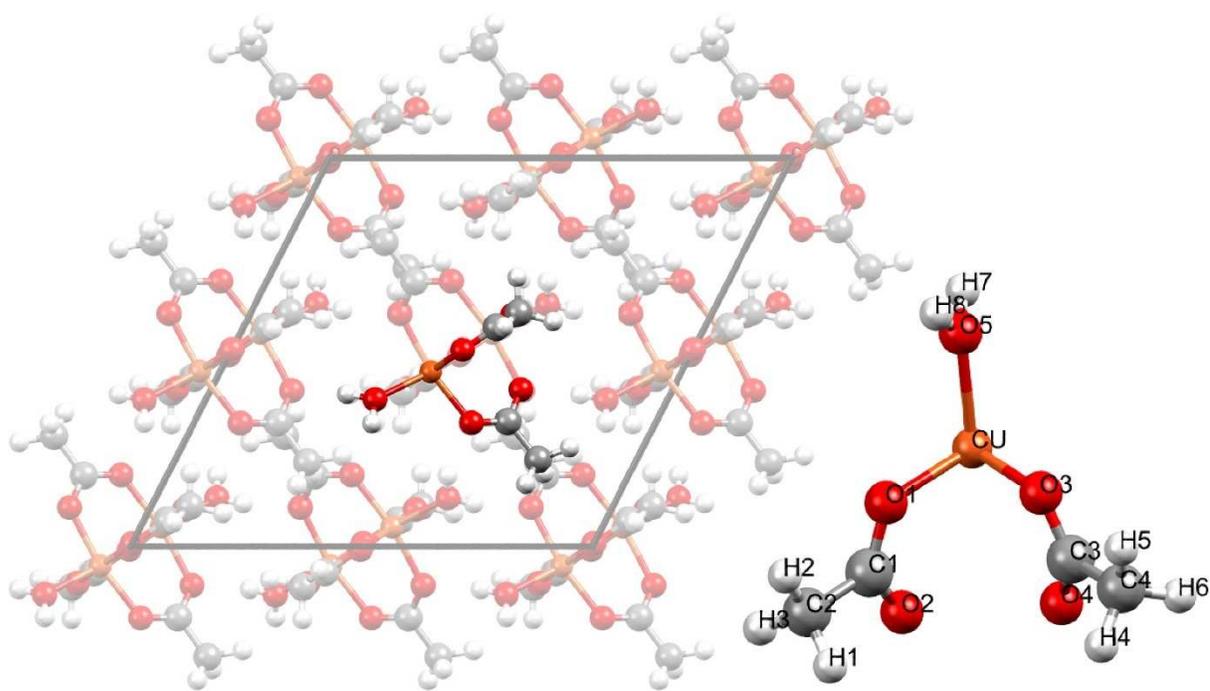
Figure A5. Unit cell, asymmetric unit, and a labeled asymmetric unit of verdigris.
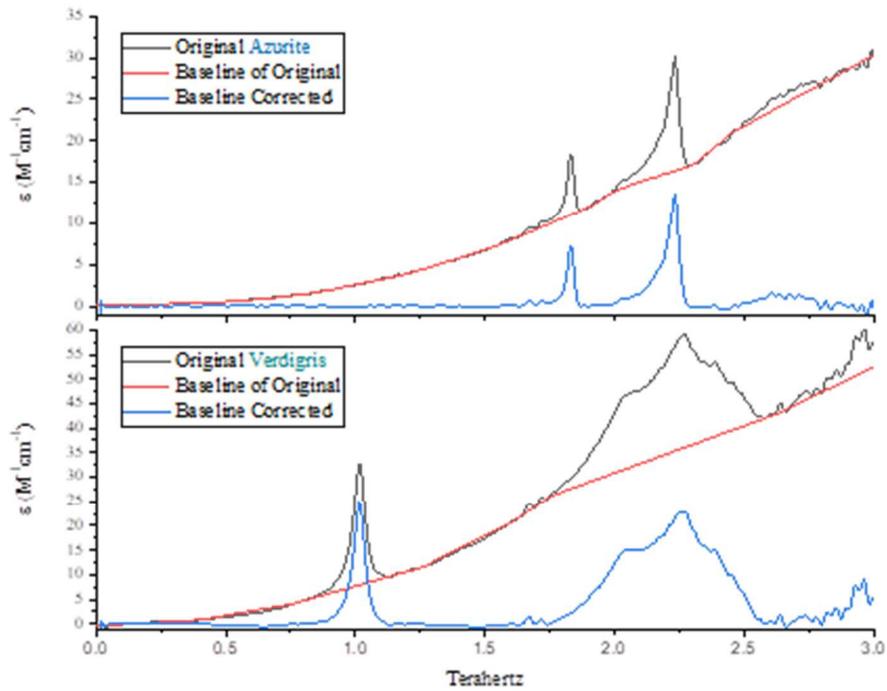
Figure A6. Baseline corrections for experimental spectra of azurite and verdigris performed using Origin 2018b.
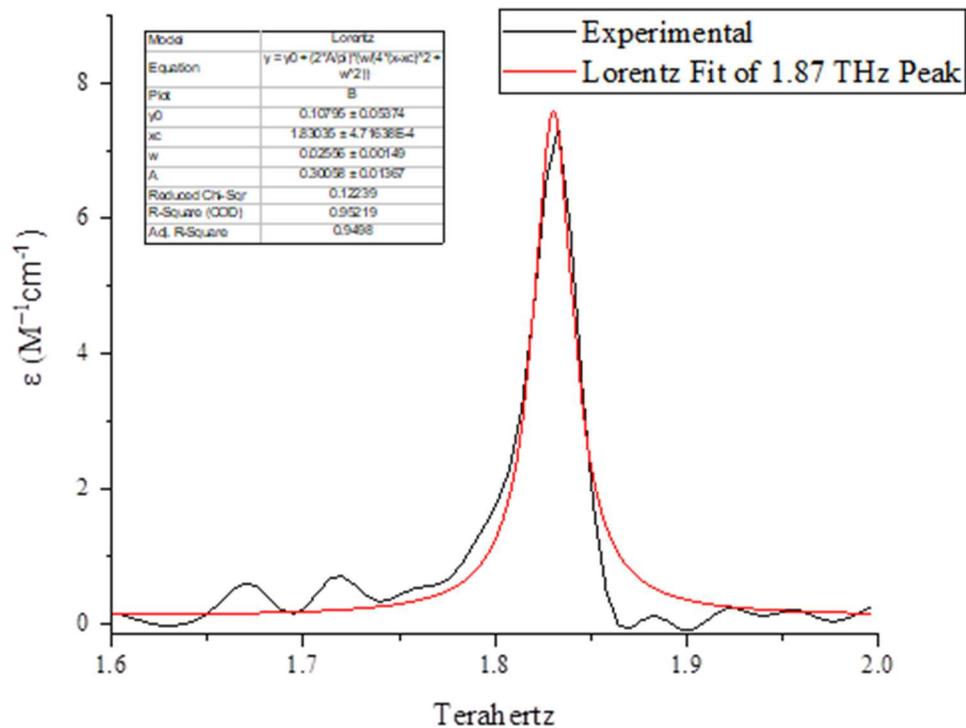
Figure A7. Peak fitting analysis with a Lorentzian line shape for the lowest frequency terahertz absorption of crystalline azurite using Origin 2018b.
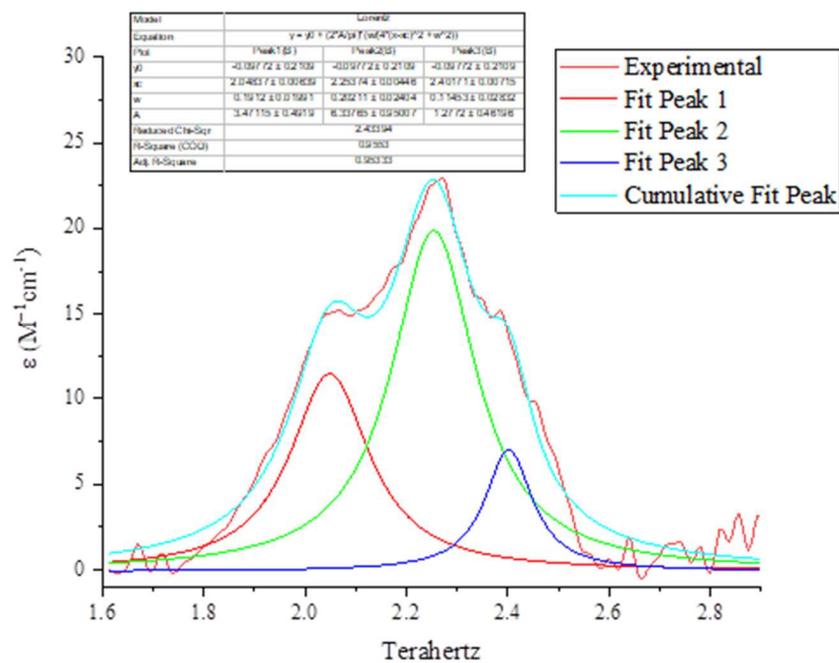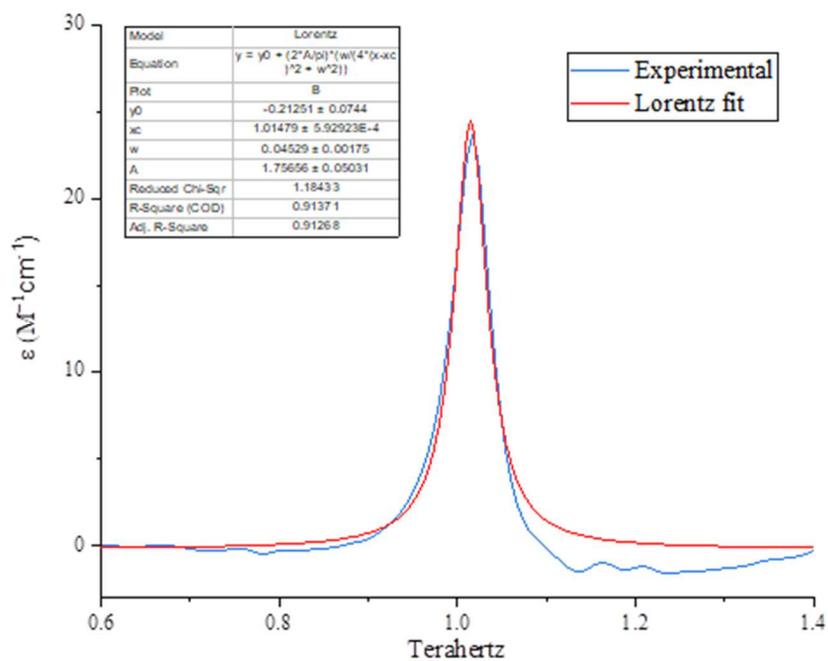
Figure A8. Peak fitting analyses with Lorentzian line shapes of the lowest frequency feature (top panel) and broad feature (bottom panel) for verdigris using Origin 2018b.

Appendix B: Supporting Information for Chapter 5

Figure B1. Powder X-ray diffraction data (red) of minium (top panel) and vermilion (bottom panel) samples compared to the predicted powder patterns (black) based on the single-crystal structural data.

Table B1. Pellet thickness (in millimeters) for pure and mixed sample pellets. Each pellet weighed approximately 800 mgs.

Table B2. SS-DFT simulated dielectric tensor components for minium and vermilion.

Table B3. Solid-state DFT simulated IR-active frequencies (including LO/TO splitting) for minium.

Table B4. Solid-state DFT simulated Raman-active frequencies and normalized intensities (including LO/TO splitting) for minium.

Figure B2. THz-TDS spectra simulated with PBE were convolved using empirically determined Lorentzian line shapes with a FWHM of 2.15 cm^{-1} for minium (top-panel) and 1.85 cm^{-1} for vermilion (bottom panel).

Table B5. Solid-state DFT simulated IR-active frequencies (including LO/TO splitting) for vermilion.

Table B6. Solid-state DFT simulated Raman-active frequencies and normalized intensities (including LO/TO splitting) for vermilion.

Figure B3. LFRS spectra simulated with PBE were convolved using Voigt profiles for minium (top-panel) and vermilion (bottom panel).

Figure B4. Experimental 290 K THz-TDS spectra of pure vermilion (top) and minium (bottom).

Figure B5. Peak fitting with Lorentzian line shapes of specific THz-TDS spectral range in minium and vermilion mixture sample, 1:2, using Origin 2018b.

Figure B6. Peak fitting with Lorentzian line shapes of specific THz-TDS spectral range in minium and vermilion mixture sample, 2:3, using Origin 2018b.

Figure B7. Peak fitting with Lorentzian line shapes of specific THz-TDS spectral range in minium and vermilion mixture sample, 1:1, using Origin 2018b.

Figure B8. Peak fitting with Lorentzian line shapes of specific THz-TDS spectral range in minium and vermilion mixture sample, 3:2, using Origin 2018b.

Figure B9. Peak fitting with Lorentzian line shapes of specific THz-TDS spectral range in minium and vermilion mixture sample, 2:1, using Origin 2018b.

Figure B10. Parameters for linear least squares fit of THz-TDS calibration curves for minium (top) and vermilion (bottom).

Figure B11. Experimental 290 K LFRS spectra of pure vermilion (top) and minium (bottom) before normalization.

Figure B1. Powder X-ray diffraction data (red) of minium (a) and vermilion (b) samples compared to the predicted powder patterns (black) based on the single-crystal structural data.

Table B1. Pellet thickness (in millimeters) for pure and mixed sample pellets. Each pellet weighed approximately 800 mgs.

	Pellet thickness (mm)
Minium	2.89
Vermilion	2.82
Blank (PTFE)	2.90
3:2	2.85
1:1	2.86
2:3	2.95
1:2	2.56
2:1	2.70

Table B2. SS-DFT simulated dielectric tensor components for minium and vermilion.

	Minium			Vermilion		
	XX	YY	ZZ	XX	YY	ZZ
PBE	5.594	5.594	5.594	7.911	7.911	9.949
PBE0	4.620	4.620	4.726	6.249	6.249	7.494

Table B3. Solid-state DFT simulated IR-active frequencies (including LO/TO splitting) for minium.

	PBE				PBE0			
	Frequency (THz)	(cm^{-1})	Mode Symmetry	Intensity (km/mol)	Frequency (THz)	(cm^{-1})	Mode Symmetry	Intensity (km/mol)
Transverse Optical Modes	1.61	53.55	E$_u$	92.18	1.75	58.22	E$_u$	35.72
	1.73	57.56	E$_u$	151.38	1.81	60.23	E$_u$	220.35
	1.99	66.25	A$_{2u}$	79.91	2.22	74.17	A$_{2u}$	40.81
	2.33	77.85	E$_u$	111.37	2.57	85.77	E$_u$	100.03
	3.18	105.94	A$_{2u}$	365.30	3.48	116.19	E$_u$	1.62
	3.30	109.96	E$_u$	0.31	3.92	130.83	A$_{2u}$	449.88
	4.30	143.53	E$_u$	739.04	4.59	153.12	E$_u$	829.10
	5.67	189.26	E$_u$	3.16	6.50	216.82	E$_u$	43.09
	8.04	268.21	E$_u$	2584.91	8.51	283.78	E$_u$	2796.69
	9.31	310.52	E$_u$	2693.80	9.82	327.68	E$_u$	2450.93
	9.94	331.49	A$_{2u}$	5428.33	11.14	371.68	A$_{2u}$	5905.17
	11.10	370.24	E$_u$	1235.97	11.88	396.14	E$_u$	801.66
	11.90	396.86	E$_u$	3469.52	12.94	431.72	E$_u$	4542.89
	13.40	446.87	A$_{2u}$	2237.98	14.17	472.59	A$_{2u}$	1903.39
	14.87	495.85	E$_u$	802.10	16.13	538.06	E$_u$	1640.97
	15.25	508.75	E$_u$	678.40	16.31	543.93	E$_u$	42.67
Longitudinal Optical Modes	1.64	54.66	E$_u$	1.80	1.75	58.45	E$_u$	0.20
	1.89	62.90	E$_u$	29.20	2.02	67.42	E$_u$	28.80
	2.08	69.53	A$_{2u}$	8.40	2.28	76.09	A$_{2u}$	4.70
	2.43	81.22	E$_u$	33.40	2.66	88.81	E$_u$	23.40
	3.58	119.49	A$_{2u}$	85.10	3.48	116.21	E$_u$	0.20
	3.30	109.97	E$_u$	0.10	4.38	146.25	A$_{2u}$	90.60
	4.62	154.15	E$_u$	179.80	4.97	165.82	E$_u$	165.40
	5.68	189.30	E$_u$	0.90	6.51	217.27	E$_u$	7.60
	8.46	282.21	E$_u$	254.10	9.01	300.45	E$_u$	225.60
	10.02	334.23	E$_u$	816.10	10.64	354.91	E$_u$	818.90
	11.95	398.66	A$_{2u}$	953.20	12.03	401.25	E$_u$	154.60
	11.30	376.85	E$_u$	205.50	13.17	439.26	A$_{2u}$	566.90
	13.48	449.63	E$_u$	4475.60	14.79	493.20	E$_u$	3425.60
	15.05	501.93	E$_u$	376.10	16.30	543.78	E$_u$	5.80
	15.94	531.56	E$_u$	6189.50	17.41	580.79	A$_{2u}$	7637.00
	16.01	534.01	A$_{2u}$	7064.80	17.45	582.20	E$_u$	8649.50

Table B4. Solid-state DFT simulated Raman-active frequencies and normalized intensities (including LO/TO splitting) for minium.

|	PBE				PBE0			
	Frequency		Mode	Intensity	Frequency		Mode	Intensity
	(THz)	(cm^{-1})	Symmetry	(km/mol)	(THz)	(cm^{-1})	Symmetry	(km/mol)
Transverse Optical Modes	1.61	53.85	B$_{1g}$	87.78	0.67	22.43	E$_g$	6.59
	1.84	61.47	E$_g$	74.75	1.72	57.37	B$_{1g}$	52.86
	1.97	65.76	A$_{1g}$	6.29	2.01	66.95	E$_g$	120.32
	2.00	66.79	B$_{1g}$	1.06	2.16	72.11	B$_{1g}$	0.41
	2.27	75.88	E$_g$	0.14	2.19	72.91	A$_{1g}$	19.64
	2.54	84.77	B$_{2g}$	34.46	2.64	88.06	B$_{2g}$	14.62
	3.10	103.48	E$_g$	10.65	2.68	89.24	E$_g$	8.74
	3.61	120.49	A$_{1g}$	1000.00	3.65	121.67	E$_g$	10.80
	3.69	123.25	B$_{2g}$	5.01	3.86	128.61	A$_{1g}$	1000.00
	4.45	148.30	E$_g$	29.53	3.96	132.15	B$_{2g}$	20.53
	4.55	151.61	B$_{1g}$	0.08	4.76	158.79	E$_g$	63.40
	6.19	206.34	B$_{1g}$	18.44	5.09	169.84	B$_{1g}$	8.50
	6.93	231.08	A$_{1g}$	36.96	7.02	234.02	B$_{1g}$	14.17
	7.45	248.56	B$_{1g}$	0.10	7.11	237.26	A$_{1g}$	189.25
	9.24	308.24	E$_g$	67.35	7.86	262.13	B$_{1g}$	6.55
	9.50	317.00	B$_{2g}$	3.60	9.89	329.80	B$_{2g}$	39.12
	11.15	372.05	E$_g$	14.74	9.91	330.48	E$_g$	164.92
	11.46	382.32	A$_{1g}$	95.52	12.29	409.81	A$_{1g}$	190.55
	13.36	445.72	E$_g$	43.01	12.37	412.57	E$_g$	42.75
	13.40	447.14	B$_{1g}$	9.57	14.36	478.95	E$_g$	57.83
	13.88	463.14	B$_{2g}$	0.09	14.84	495.17	B$_{1g}$	26.13
	13.92	464.27	E$_g$	0.43	15.03	501.27	B$_{2g}$	0.35
	15.38	513.13	B$_{2g}$	2.77	15.19	506.56	E$_g$	9.38
	15.39	513.48	A$_{1g}$	651.68	16.58	553.19	B$_{1g}$	43.09
	15.65	522.04	B$_{1g}$	60.42	17.22	574.51	A$_{1g}$	371.62
					17.24	575.24	B$_{2g}$	0.19
Longitudinal Optical Modes	1.64	54.66	E$_u$	0.00	1.75	58.45	A$_{2u}$	0.00
	1.89	62.90	E$_u$	0.00	2.02	67.42	E$_u$	0.00
	2.08	69.53	A$_{2u}$	0.00	2.28	76.09	E$_u$	0.00
	2.43	81.22	E$_u$	0.00	2.66	88.81	E$_u$	0.00
	3.58	119.49	A$_{2u}$	0.00	3.48	116.21	A$_{2u}$	0.00
	3.30	109.97	E$_u$	0.00	4.38	146.25	E$_u$	0.00
	4.62	154.15	E$_u$	0.00	4.97	165.82	E$_u$	0.00
	5.68	189.30	E$_u$	0.00	6.51	217.27	A$_{2u}$	0.00
	8.46	282.21	E$_u$	0.00	9.01	300.45	E$_u$	0.00
	10.02	334.23	E$_u$	0.00	10.64	354.91	E$_u$	0.00
	11.95	398.66	A$_{2u}$	0.00	12.03	401.25	E$_u$	0.00
	11.30	376.85	E$_u$	0.00	13.17	439.26	E$_u$	0.00
	13.48	449.63	E$_u$	0.00	14.79	493.20	A$_{2u}$	0.00
	15.05	501.93	E$_u$	0.00	16.30	543.78	A$_{2u}$	0.00
	15.94	531.56	E$_u$	0.00	17.41	580.79	E$_u$	0.00
	16.01	534.01	A$_{2u}$	0.00	17.45	582.20	E$_u$	0.00

Figure B2. THz-TDS spectra simulated with PBE were convolved using empirically determined Lorentzian line shapes with a FWHM of 2.15 cm^{-1} for minium (top-panel) and 1.85 cm^{-1} for vermilion (bottom panel).

Table B5. Solid-state DFT simulated IR-active frequencies (including LO/TO splitting) for vermilion.

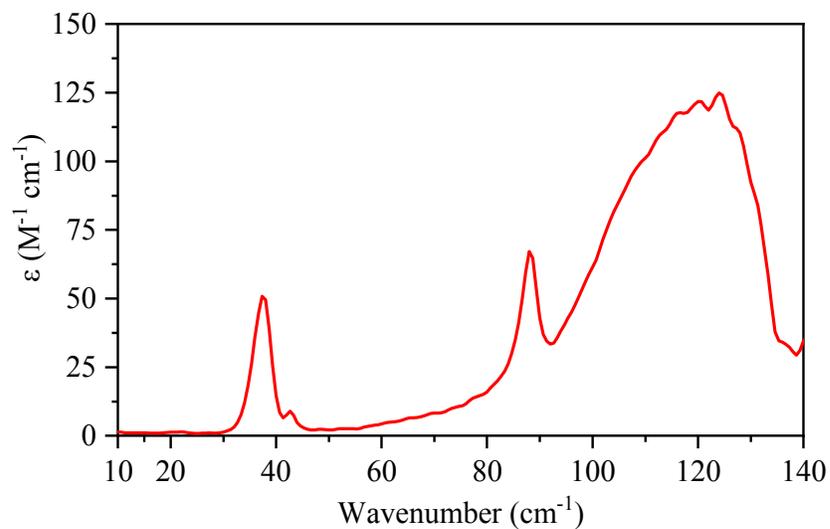| | PBE | | | | PBE0 | | | |
| | Frequency | | Mode | Intensity | Frequency | | Mode | Intensity |
	(THz)	(cm^{-1})	Symmetry	(km/mol)	(THz)	(cm^{-1})	Symmetry	(km/mol)
Transverse Optical Modes	1.10	36.61	A$_2$	22.09	1.05	35.08	A$_2$	32.50
	1.37	45.71	E	1.32	1.39	46.52	E	3.47
	2.58	85.99	E	63.1	2.72	90.61	E	83.67
	3.38	112.78	E	452.67	3.34	111.27	E	401.53
	3.41	113.74	A$_2$	242.42	3.34	111.54	A$_2$	200.40
	7.85	261.98	E	192.11	8.61	287.04	E	228.19
	9.44	315.02	A$_2$	365.85	10.28	342.74	A$_2$	375.70
	9.51	317.17	E	197.01	10.49	349.95	E	171.36
Longitudinal Optical Modes	1.25	41.78	A$_2$	6.20	1.33	44.39	A$_2$	7.60
	1.37	45.84	E	0.30	1.41	46.92	E	0.50
	2.65	88.50	E	6.20	2.81	93.62	E	4.20
	4.45	148.46	E	381.00	4.60	153.53	E	352.50
	4.28	142.73	A$_2$	188.30	4.33	144.50	A$_2$	157.50
	8.09	270.02	E	196.70	8.94	298.28	E	233.90
	9.77	325.75	E	322.00	10.76	358.97	E	297.10
	10.08	336.21	A$_2$	435.80	11.08	369.58	A$_2$	443.60

Table B6. Solid-state DFT simulated Raman-active frequencies and normalized intensities (including LO/TO splitting) for vermilion.

| | PBE | | | | PBE0 | | | |
| | Frequency | | Mode | Intensity | Frequency | | Mode | Intensity |
	(THz)	(cm^{-1})	Symmetry	(km/mol)	(THz)	(cm^{-1})	Symmetry	(km/mol)
Transverse Optical Modes	1.32	44.06	A$_1$	558.08	1.37	45.86	A$_1$	548.63
	1.37	45.71	E	1.93	1.39	46.52	E	20.81
	2.58	85.99	E	1.93	2.72	90.61	E	18.91
	3.38	112.78	E	68.54	3.34	111.27	E	204.55
	7.12	237.46	A$_1$	1000.00	7.86	262.05	A$_1$	1000.00
	7.85	261.98	E	115.24	8.61	287.04	E	87.45
	9.51	317.17	E	265.78	10.49	349.95	E	293.38
Longitudinal Optical Modes	1.25	41.78	A$_2$	0.00	1.33	44.39	A$_2$	0.00
	1.37	45.84	E	2.10	1.41	46.92	E	20.41
	2.65	88.50	E	1.18	2.81	93.62	E	20.06
	4.45	148.45	E	147.99	4.60	153.53	E	325.76
	4.28	142.73	A$_2$	0.00	4.33	144.50	A$_2$	0.00
	8.09	270.02	E	161.01	8.94	298.28	E	135.86
	9.77	325.75	E	243.13	10.76	358.97	E	269.32
	10.08	336.21	A$_2$	0.00	11.08	369.58	A$_2$	0.00
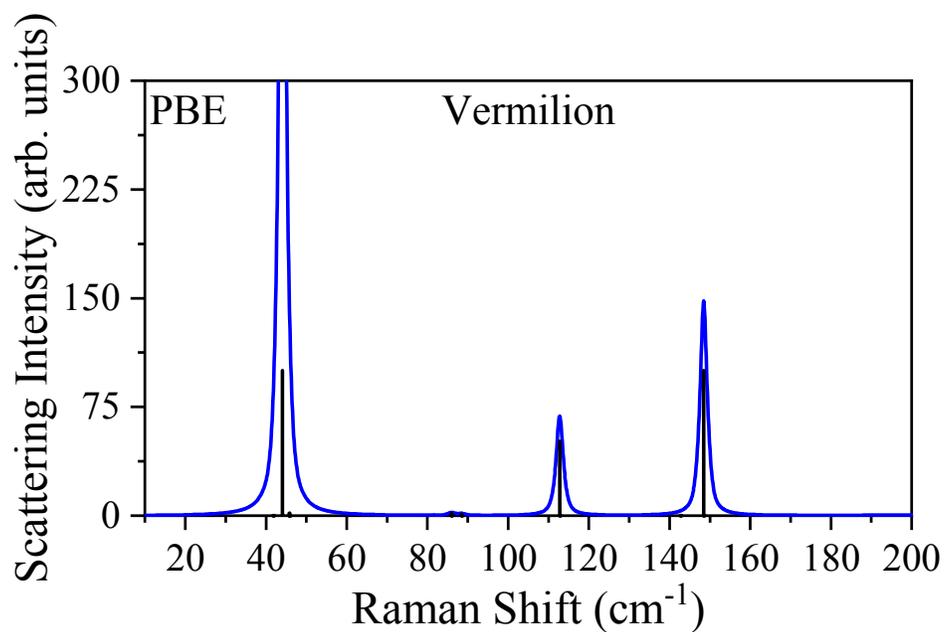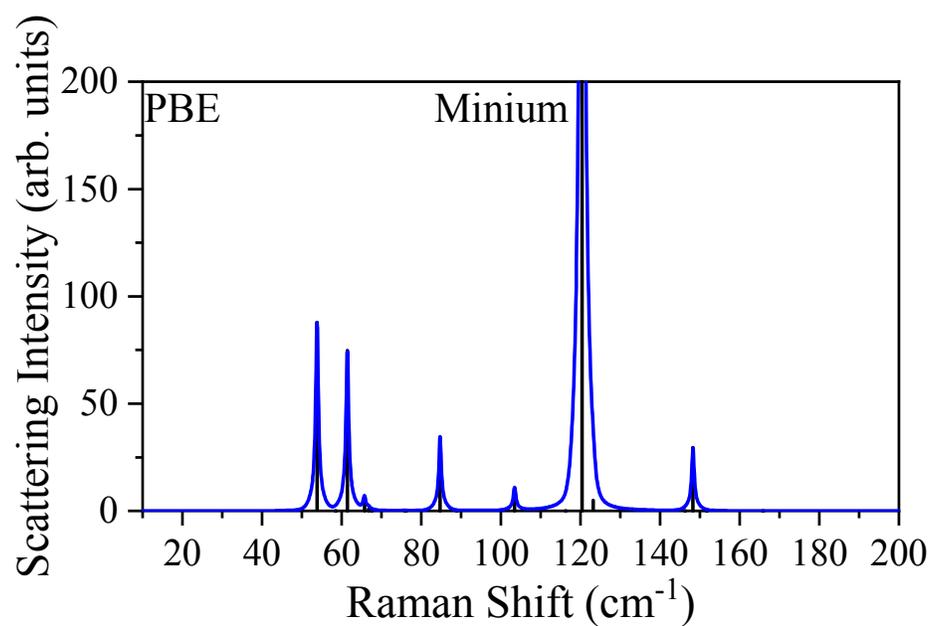
Figure B3. LFRS spectra simulated with PBE were convolved using Voigt profiles for minium (top-panel) and vermilion (bottom panel).
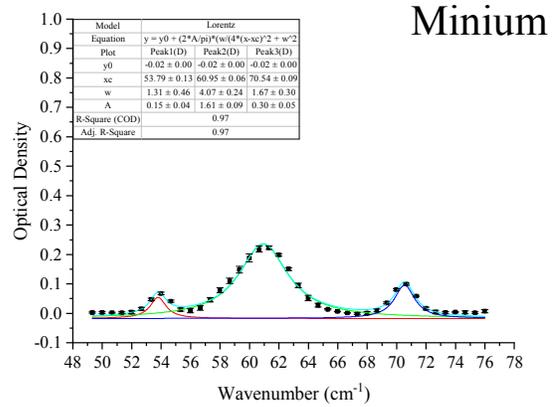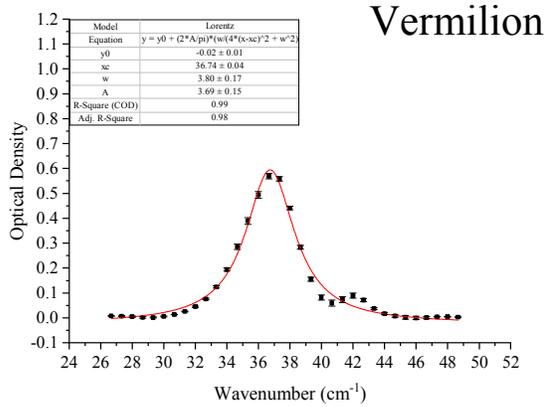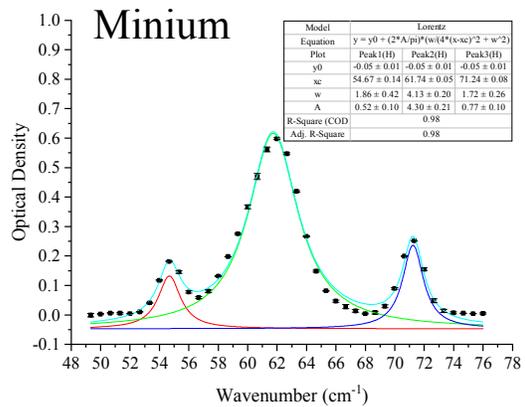
Vermilion Exp. Peaks (cm^{-1})
37.3
42.7
88.0
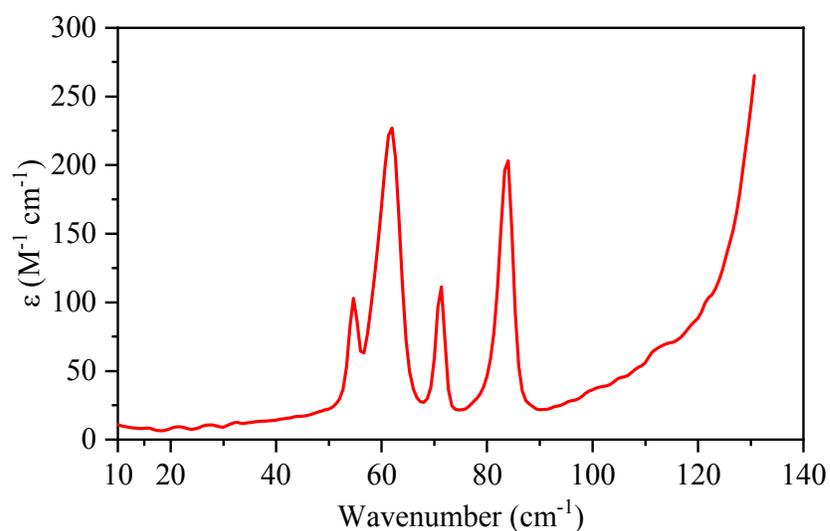
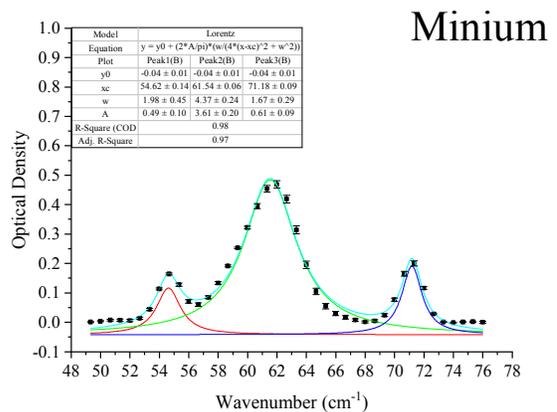| Minium Exp. Peaks (cm^{-1}) |
|---|
| 54.7 |
| 62.0 |
| 71.3 |
| 84.0 |

Figure B4. Experimental 290 K THz-TDS spectra of pure vermilion (top) and minium (bottom).

Vermilion

Model	Lorentz
Equation	y = y0 + (2*A/pi)*(w/(4*(x-xc)^2 + w^2)
y0	-0.02 ± 0.01
xc	36.74 ± 0.04
w	3.80 ± 0.17
A	3.69 ± 0.15
R-Square (COD)	0.99
Adj. R-Square	0.98

Minium

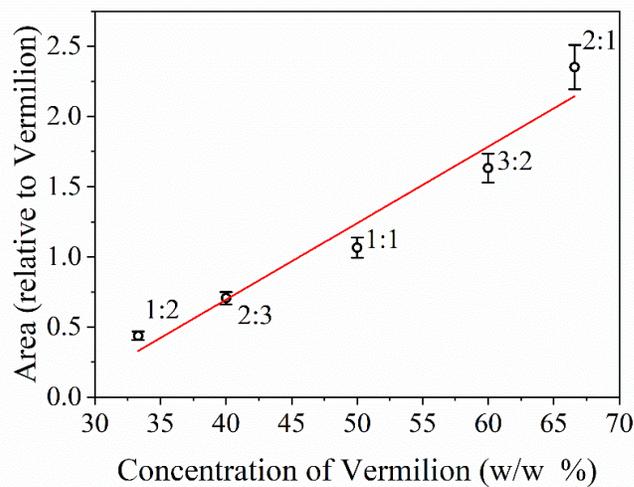| Model	Lorentz		
Equation	y = y0 + (2*A/pi)*(w/(4*(x-xc)^2 + w^2		
Plot	Peak1(D)	Peak2(D)	Peak3(D)
y0	-0.02 ± 0.00	-0.02 ± 0.00	-0.02 ± 0.00
xc	53.79 ± 0.13	60.95 ± 0.06	70.54 ± 0.09
w	1.31 ± 0.46	4.07 ± 0.24	1.67 ± 0.30
A	0.15 ± 0.04	1.61 ± 0.09	0.30 ± 0.05
R-Square (COD)	0.97		
Adj. R-Square	0.97		

Figure B5. Peak fitting with Lorentzian line shapes of specific THz-TDS spectral range in minium and vermilion mixture sample, 1:2, using Origin 2018b.
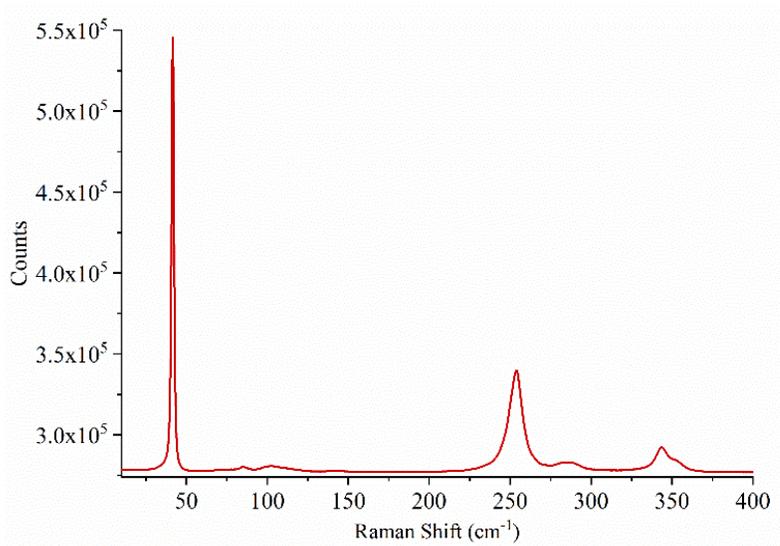
Vermilion

Model	Lorentz
Equation	y = y0 + (2*A/pi)*(w/(4*(x-xc)^2 + w^2))
y0	-0.04 ± 0.01
xc	37.45 ± 0.04
w	3.67 ± 0.16
A	6.08 ± 0.24
R-Square (COD)	0.99
Adj. R-Square	0.99

Minium

Model	Lorentz		
Equation	y = y0 + (2*A/pi)*(w/(4*(x-xc)^2 + w^2))		
Plot	Peak1(H)	Peak2(H)	Peak3(H)
y0	-0.05 ± 0.01	-0.05 ± 0.01	-0.05 ± 0.01
xc	54.67 ± 0.14	61.74 ± 0.05	71.24 ± 0.08
w	1.86 ± 0.42	4.13 ± 0.20	1.72 ± 0.26
A	0.52 ± 0.10	4.30 ± 0.21	0.77 ± 0.10
R-Square (COD)	0.98		
Adj. R-Square	0.98		

Figure B6. Peak fitting with Lorentzian line shapes of specific THz-TDS spectral range in minium and vermilion mixture sample, 2:3, using Origin 2018b.

Vermilion

Model	Lorentz
Equation	y = y0 + (2*A/pi)*(w/(4*(x-xc)^2 + w^2))
y0	-0.02 ± 0.01
xc	37.33 ± 0.05
w	3.91 ± 0.18
A	3.39 ± 0.14
R-Square (COD)	0.99
Adj. R-Square	0.98

Minium

Model	Lorentz		
Equation	y = y0 + (2*A/pi)*(w/(4*(x-xc)^2 + w^2))		
Plot	Peak1(B)	Peak2(B)	Peak3(B)
y0	-0.04 ± 0.01	-0.04 ± 0.01	-0.04 ± 0.01
xc	54.62 ± 0.14	61.54 ± 0.06	71.18 ± 0.09
w	1.98 ± 0.45	4.37 ± 0.24	1.67 ± 0.29
A	0.49 ± 0.10	3.61 ± 0.20	0.61 ± 0.09
R-Square (COD)	0.98		
Adj. R-Square	0.97		

Figure B7. Peak fitting with Lorentzian line shapes of specific THz-TDS spectral range in minium and vermilion mixture sample, 1:1, using Origin 2018b.

Figure B8. Peak fitting with Lorentzian line shapes of specific THz-TDS spectral range in minium and vermilion mixture sample, 3:2, using Origin 2018b.

Figure B9. Peak fitting with Lorentzian line shapes of specific THz-TDS spectral range in minium and vermilion mixture sample, 2:1, using Origin 2018b.

| Equation	y=a+b*x
Intercept	-1.44657±0.48731
Slope	0.05166 ± 0.00947
Residual Sum of Squares	0.20291
Pearson's r	0.95313
R-Square (COD)	0.90846

Equation	y=a+b*x
Intercept	-1.48511 ± 0.3564
Slope	0.0545 ± 0.00692
Residual Sum of Squares	0.10853
Pearson's r	0.97663
R-Square (COD)	0.9538

Figure B10. Parameters for linear least squares fit of THz-TDS calibration curves for minium (top) and vermilion (bottom).

Vermilion Exp. Peaks (cm^{-1})
41.7
84.5
101.9
253.8
282.3
288.4
343.2
351.8
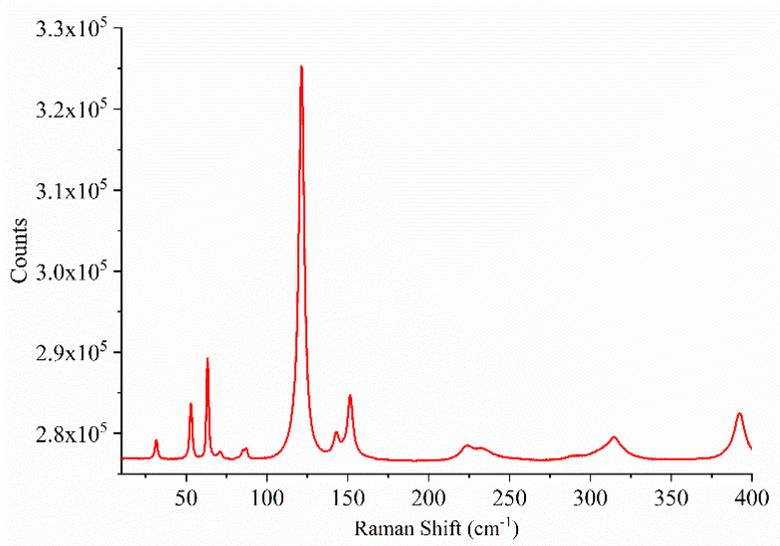
Minium Exp. Peaks (cm^{-1})
31.8
53.4
63.2
71.2
84.9
87.4
121.0
142.7
151.8
223.7
232.8
289.9
314.4
391.8

**Figure B11.** Experimental 290 K LFRS spectra of pure vermilion (top) and minium (bottom) before normalization.
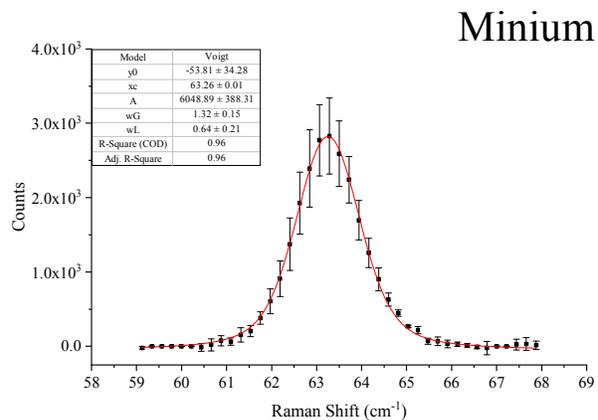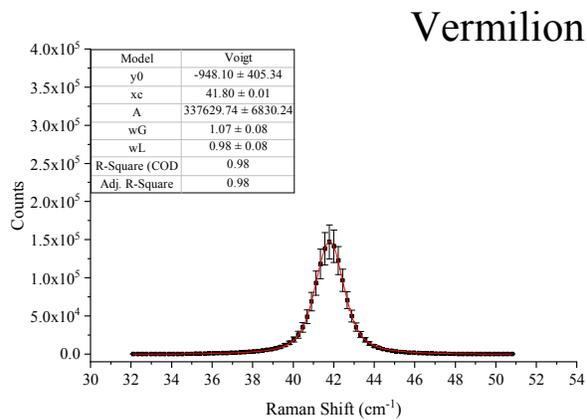
Figure B12. Peak fitting with Voigt line shapes of specific LFRS spectral range in minium and vermilion mixture sample, 1:2, using Origin 2018b.
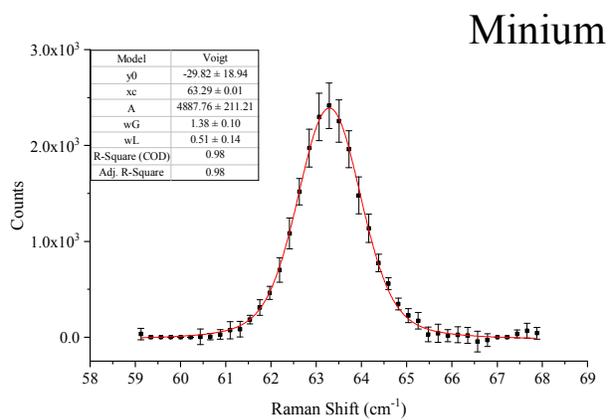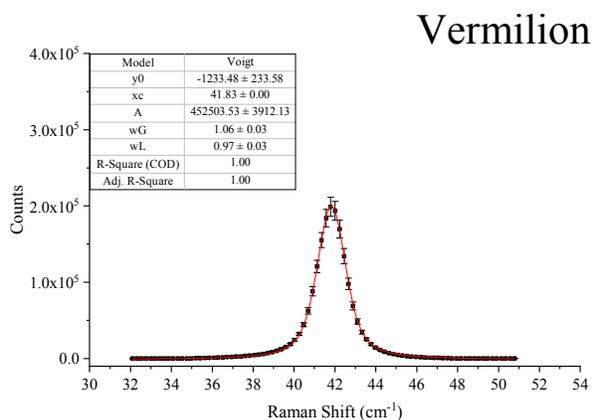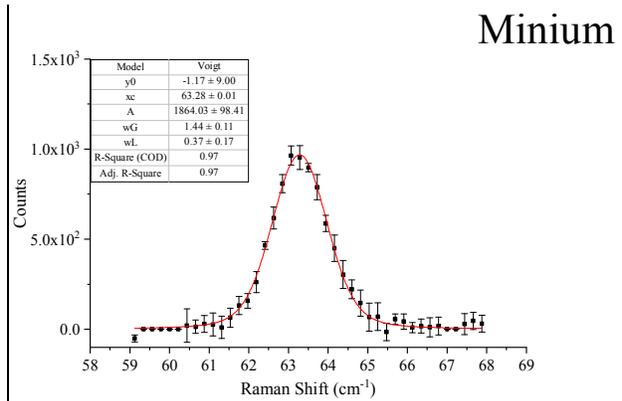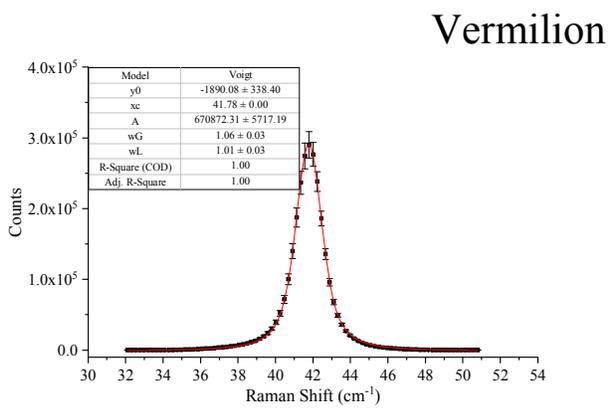

Figure B13. Peak fitting with Voigt line shapes of specific LFRS spectral range in minium and vermilion mixture sample, 2:3, using Origin 2018b.
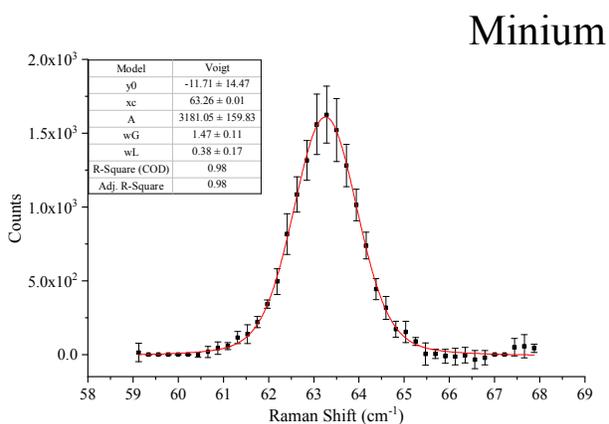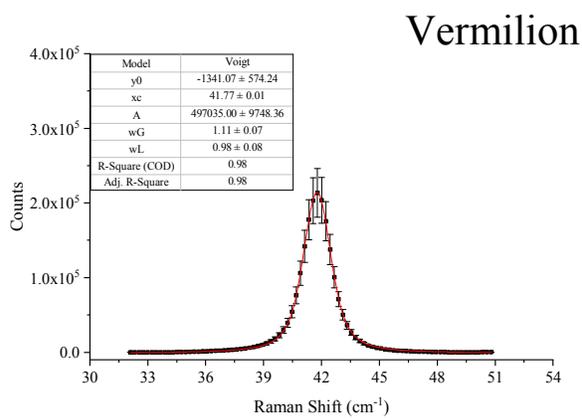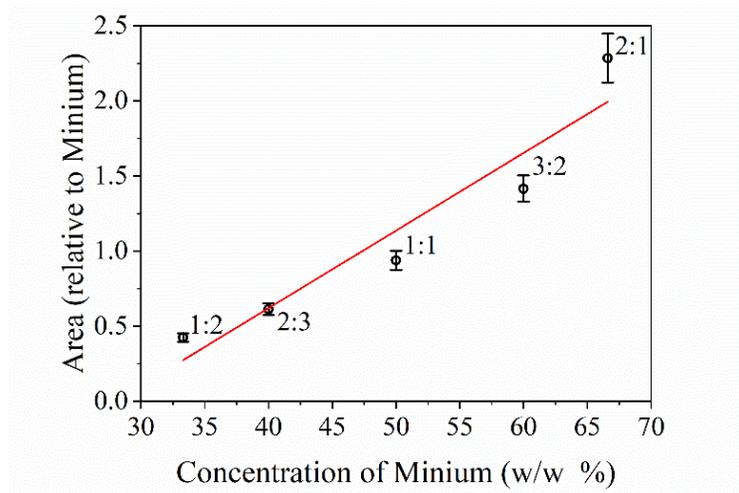

Figure B14. Peak fitting with Voigt line shapes of specific LFRS spectral range in minium and vermilion mixture sample, 1:1, using Origin 2018b.
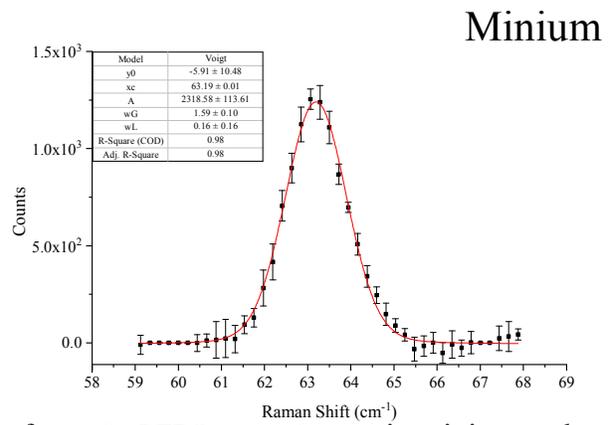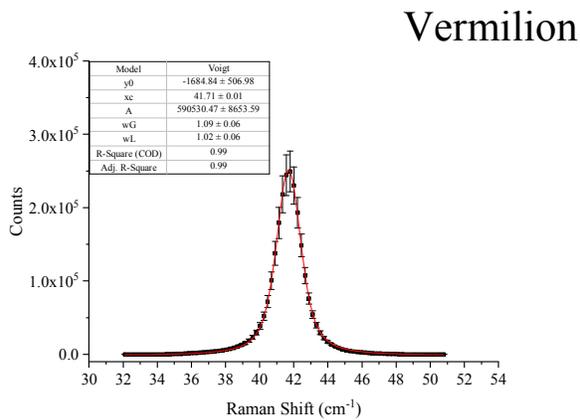
Figure B15. Peak fitting with Voigt line shapes of specific LFRS spectral range in minium and vermilion mixture sample, 3:2, using Origin 2018b.

Figure B16. Peak fitting with Voigt line shapes of specific LFRS spectral range in minium and vermilion mixture sample, 2:1, using Origin 2018b.

Equation	y=a+b*x
Intercept	-1.44657±0.48731
Slope	0.05166 ± 0.00947
Residual Sum of Squares	0.20291
Pearson's r	0.95313
R-Square (COD)	0.90846
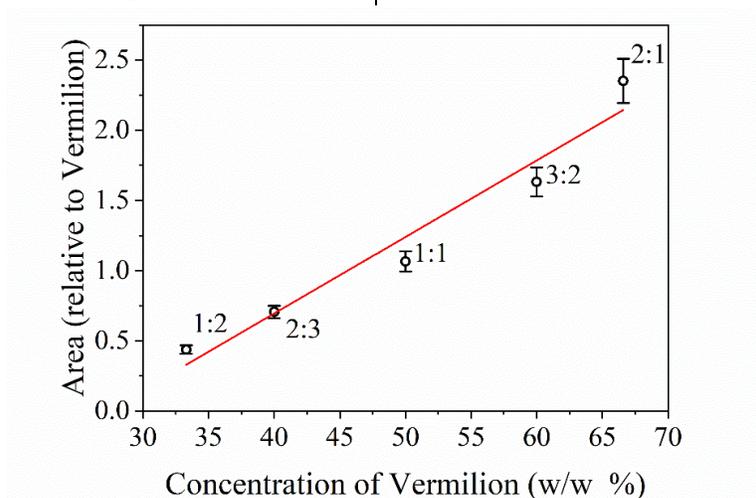
| Equation	y=a+b*x
Intercept	-1.48511 ± 0.3564
Slope	0.0545 ± 0.00692
Residual Sum of Squares	0.10853
Pearson's r	0.97663
R-Square (COD)	0.9538

Figure B17. Parameters for linear least squares fit of LFRS calibration curves for minium (top) and vermilion (bottom).

Table B7. Experimental and solid-state DFT calculated bonds lengths and angles for minium asymmetric unit.

Bond Length (Å)		Exp.	Calcd.	
Atom1	Atom2		PBE	PBE0
Pb4+	O1	2.13	2.18	2.14
Pb4+	O2	2.21	2.26	2.20
Pb2+	O2	2.73	2.38	2.73
Pb2+	O1	2.22	2.27	2.23
		RMSD	0.18	0.01

| Bond Angle (°)			Exp.	Calcd.	
Atom1	Atom2	Atom3		PBE	PBE0
Pb4+	O1	Pb2+	112.32	111.25	112.28
Pb2+	O2	Pb4+	93.51	94.84	94.00
O1	Pb4+	O2	83.35	82.42	83.31
O1	Pb2+	O2	70.56	71.28	70.21
			RMSD	1.04	0.30
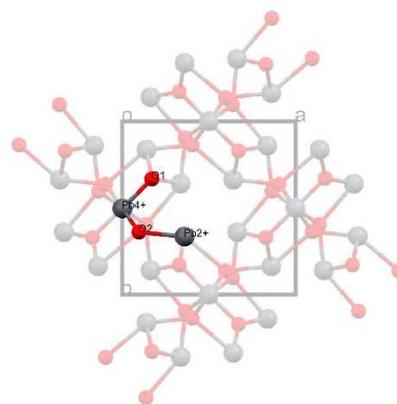
Table B8. Experimental and solid-state DFT calculated bonds length for vermilion asymmetric unit.

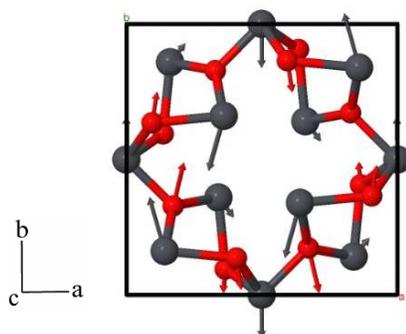| Bond Length (Å)		Exp.	Calcd.	
Atom1	Atom2		PBE	PBE0
S	Hg	2.37	2.44	2.41
		% Error	3.17	1.73

169
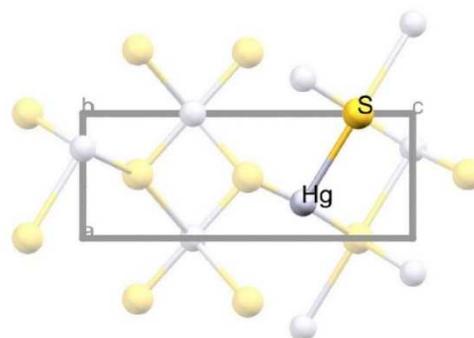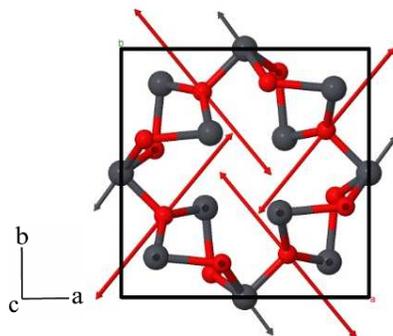
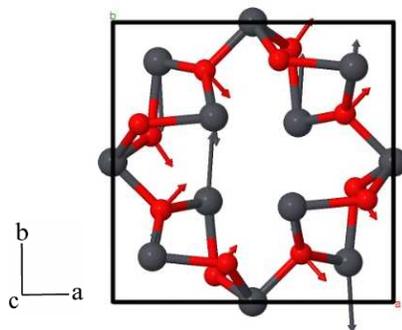**Figure B18.** Eigenvector plot for Raman-active mode, 22.43 cm^{-1}, in minium.
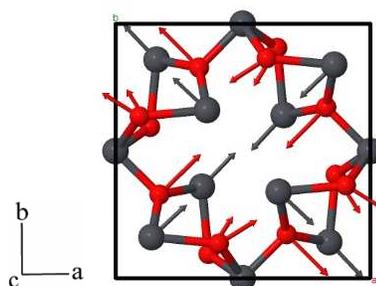
Figure B19. Eigenvector plot for Raman-active mode, 57.37 cm^{-1}, in minium.

Figure B20. Eigenvector plot for IR-active mode, 58.22 cm^{-1}, in minium.

Figure B21. Eigenvector plot for IR-active mode, 60.23 cm^{-1}, in minium.

Figure B22. Eigenvector plot for Raman-active mode, 66.95 cm^{-1}, in minium.

Figure B23. Eigenvector plot for Raman-active mode, 72.11 cm^{-1}, in minium.

Figure B24. Eigenvector plot for Raman-active mode, 72.91 cm^{-1}, in minium.

Figure B25. Eigenvector plot for IR-active mode, 74.17 cm^{-1}, in minium.

171

Figure B26. Eigenvector plot for IR-active mode, 85.77 cm^{-1}, in minium.
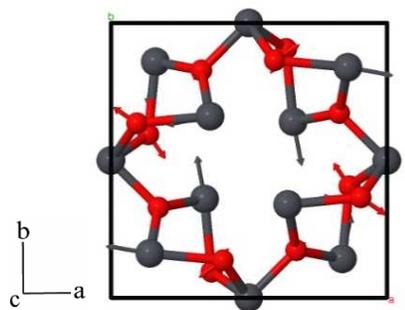
Figure B27. Eigenvector plot for Raman -active mode, 88.06 cm^{-1}, in minium.
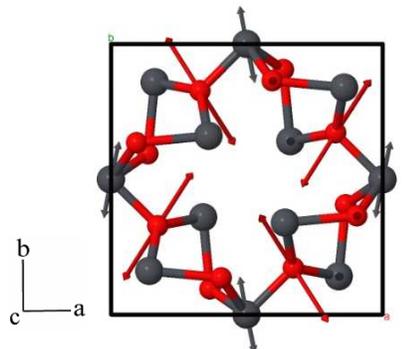
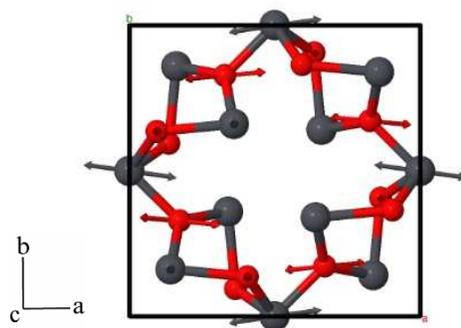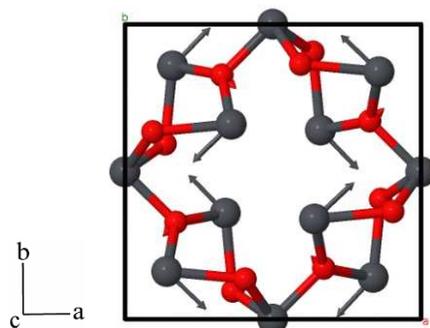
Figure B28. Eigenvector plot for Raman -active mode, 89.24 cm^{-1}, in minium.
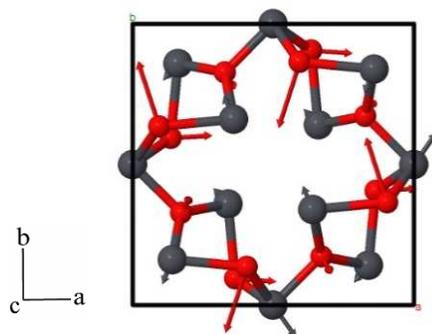
Figure B29. Eigenvector plot for IR-active mode, 116.19 cm^{-1}, in minium.
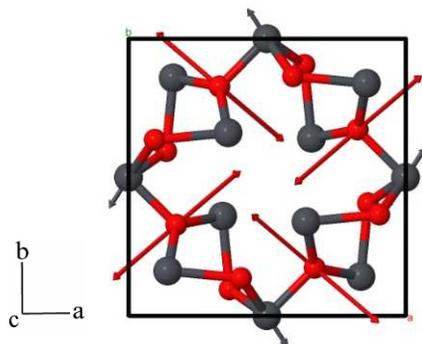
Figure B30. Eigenvector plot for Raman-active mode, 121.67 cm⁻¹, in minium.
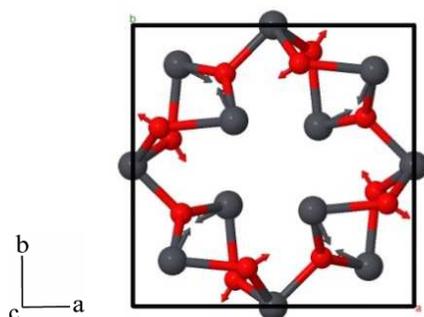
Figure B31. Eigenvector plot for Raman-active mode, 128.60 cm⁻¹, in minium.
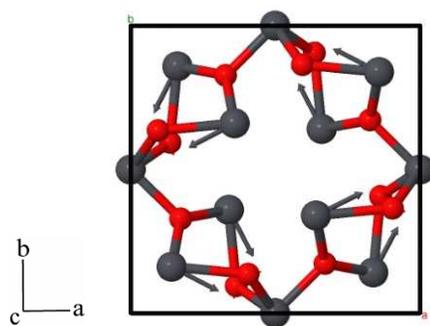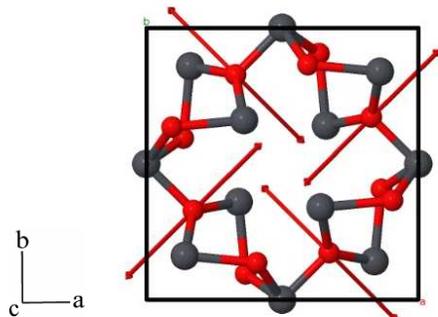

Figure B32. Eigenvector plot for IR-active mode, 130.83 cm⁻¹, in minium.
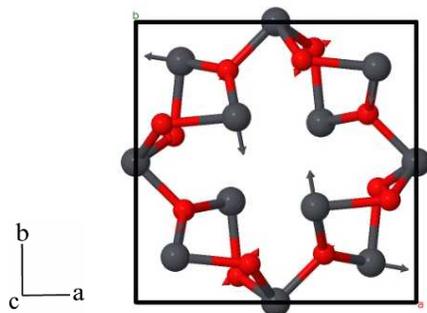
Figure B33. Eigenvector plot for Raman-active mode, 132.15 cm⁻¹, in minium.

173
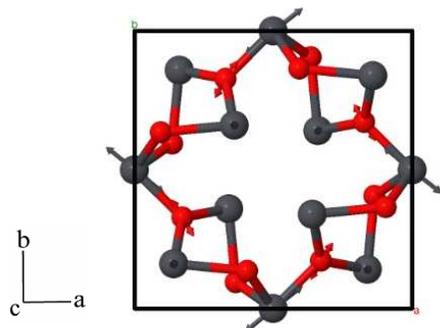
Figure B34. Eigenvector plot for Raman-active mode, 158.79 cm^{-1}, in minium.
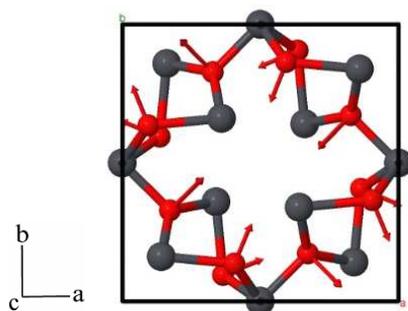
Figure B35. Eigenvector plot for Raman-active mode, 169.84 cm^{-1}, in minium.
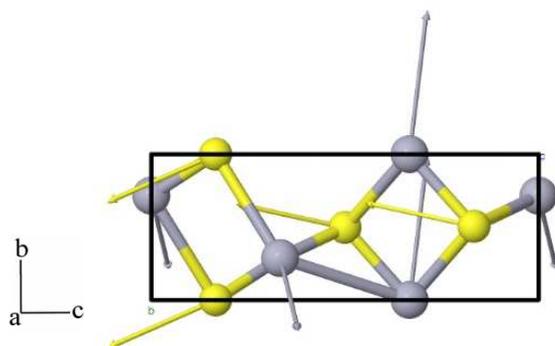
Figure B36. Eigenvector plot for IR-active mode, 35.08 cm^{-1}, in vermilion.
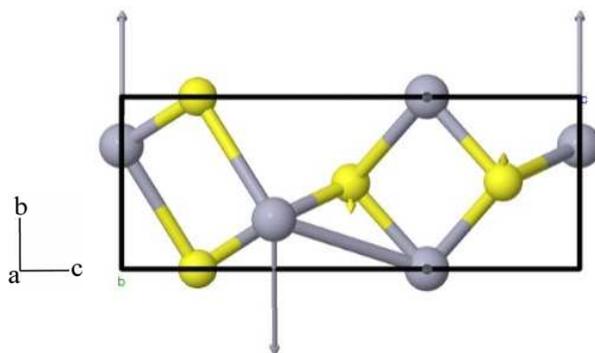
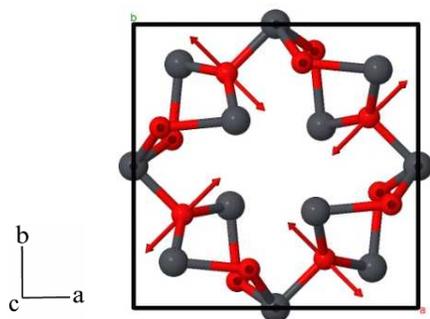**Figure B37.** Eigenvector plot for Raman-active mode, 45.86 cm^{-1}, in vermilion.
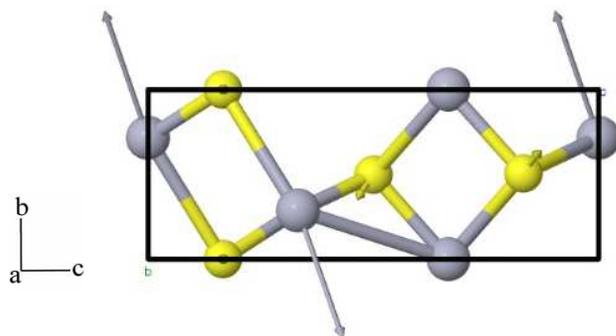
Figure B38. Eigenvector plot for Raman & IR-active mode, 46.52 cm^{-1}, in vermilion.
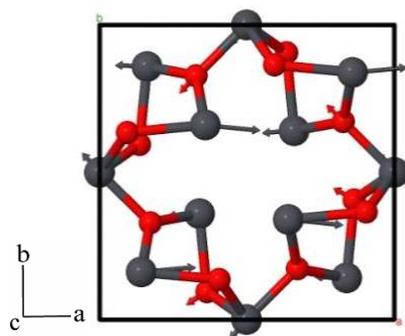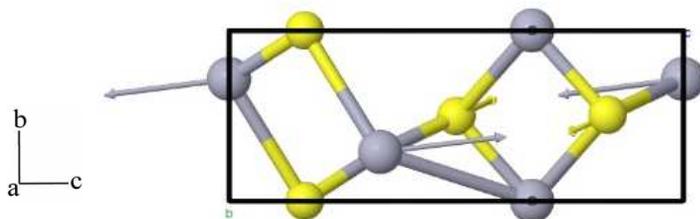

Figure B39. Eigenvector plot for Raman & IR-active mode, 90.61 cm^{-1}, in vermilion.
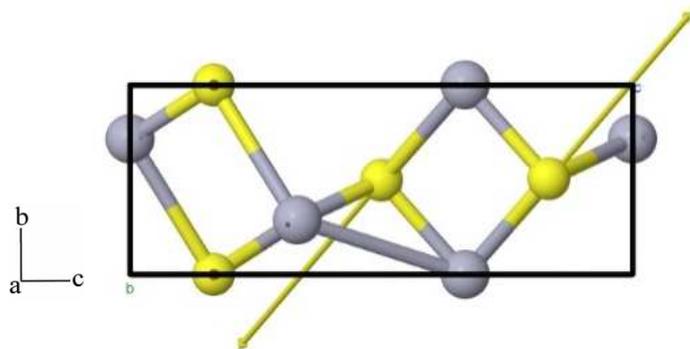
Figure B40. Eigenvector plot for Raman & IR-active mode, 111.27 cm^{-1}, in vermilion.
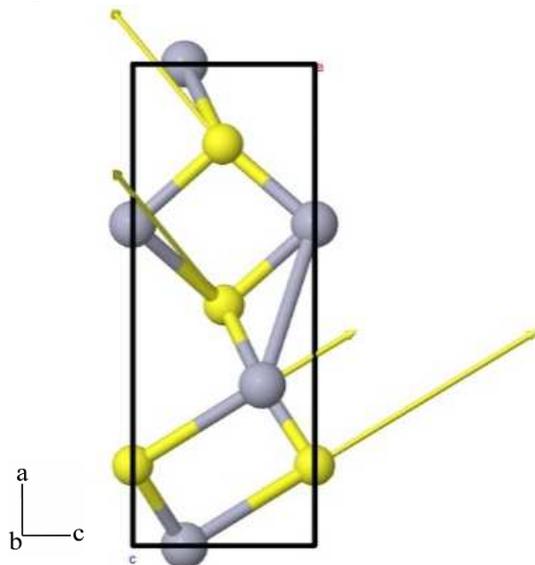
Figure B41. Eigenvector plot for IR-active mode, 111.54 cm^{-1}, in vermilion.

Appendix C: Supporting Information for Chapter 6

Figure C1. Experimental and predicted powder X-ray diffraction patterns of PR3.

Figure C2. Experimental and predicted powder X-ray diffraction patterns of PR254.

Table C1. . Pellet thickness in millimeters for tablets A-C for PR3 and PR254. Each pellet weighed approximately 400 mgs

Table C3. Solid-state DFT simulated frequencies for PR3.

Table C4. Solid-state DFT simulated frequencies for PR254.

Table C5. Solid-state DFT simulated frequencies (including LO/TO splitting) for verdigris.
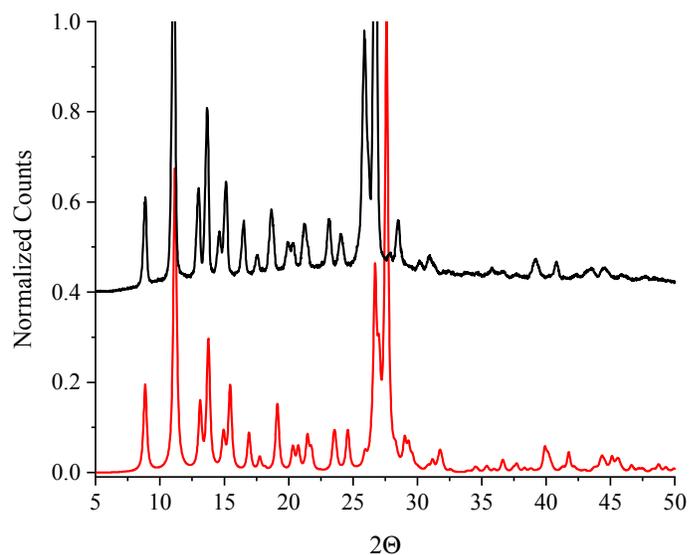
Figure C1. Experimental and predicted powder X-ray diffraction patterns of PR3.
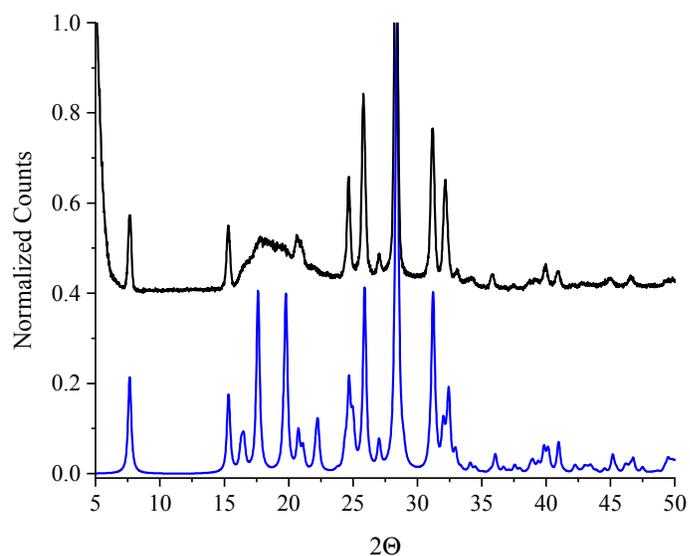
Figure C2. Experimental and predicted powder X-ray diffraction patterns of PR254.

Table C1. Pellet thickness in millimeters for tablets A-C for PR3 and PR254. Each pellet weighed approximately 400 mgs.

	Pellet thickness (mm)
PR3	
A	3.53
B	3.72
C	3.59
PR254	
A	3.88
B	3.82
C	3.88

Table C2. Solid-state DFT simulated frequencies for PR3.

Frequency		Intensity	Symmetry
THz	cm^{-1}		
0.74	24.79	1.48	Bu
0.96	31.92	0.00	Au
1.03	34.29	4.64	Au
1.25	41.73	0.59	Au
1.46	48.57	6.75	Bu
1.48	49.38	0.02	Au
1.71	57.18	6.62	Bu
1.86	62.09	2.38	Au
2.02	67.36	10.37	Bu
2.21	73.65	5.41	Au
2.36	78.59	1.70	Bu
2.57	85.64	0.21	Au
2.68	89.52	42.54	Bu
2.77	92.49	1.92	Bu
2.86	95.45	7.25	Au
3.33	111.18	0.15	Au
3.34	111.40	0.10	Bu
3.54	118.16	6.67	Bu
3.59	119.61	1.17	Au
4.10	136.89	4.54	Bu
4.14	138.18	15.87	Au
4.37	145.71	2.44	Au
4.52	150.64	1.95	Bu
4.58	152.85	0.49	Bu
4.79	159.61	1.54	Au
4.96	165.34	13.64	Bu
4.99	166.32	32.18	Au
5.66	188.87	35.65	Bu
5.80	193.37	17.61	Au
5.90	196.72	17.98	Au
5.95	198.62	1.28	Bu
6.85	228.56	17.28	Bu
6.94	231.49	1.40	Au
7.63	254.53	2.18	Au
7.66	255.60	19.38	Bu
8.67	289.22	28.73	Bu
8.71	290.63	2.32	Au

10.02	334.24	3.05	Au
10.11	337.37	1.46	Bu
10.24	341.63	24.22	Bu
10.29	343.14	3.54	Au
10.89	363.22	2.87	Au
10.89	363.31	13.71	Bu
11.45	381.82	0.32	Au
11.45	382.04	20.51	Bu
12.03	401.31	23.32	Au
12.08	402.99	23.09	Bu
12.23	408.09	0.24	Au
12.31	410.46	11.34	Bu
12.67	422.49	62.16	Bu
12.67	422.68	11.56	Au
12.92	431.00	0.29	Bu
12.93	431.15	0.00	Au
13.63	454.79	9.52	Bu
13.66	455.76	3.92	Au
14.29	476.62	46.42	Au
14.32	477.79	12.74	Bu
14.85	495.34	283.98	Bu
14.85	495.44	2.00	Au
14.93	498.00	7.87	Au
14.99	500.00	30.63	Bu
15.68	522.94	1.52	Au
15.74	524.93	33.94	Bu
15.93	531.24	1.74	Au
15.98	532.93	4.54	Bu
16.07	536.20	23.75	Bu
16.08	536.21	0.54	Au
18.47	615.96	5.85	Au
18.47	616.14	24.19	Bu
19.38	646.30	0.02	Au
19.39	646.83	9.96	Bu
20.00	667.27	4.05	Bu
20.01	667.44	0.70	Au
20.21	674.25	13.26	Au
20.26	675.94	0.45	Bu
20.32	677.80	26.25	Bu
20.33	678.12	0.09	Au
21.66	722.52	27.36	Bu

21.67	722.74	73.31	Au
21.94	731.85	6.43	Au
21.97	732.99	277.21	Bu
22.18	739.97	1.76	Au
22.23	741.44	146.12	Bu
22.29	743.37	38.60	Bu
22.31	744.32	140.84	Bu
22.32	744.50	134.25	Au
22.37	746.18	18.37	Au
23.62	787.90	10.28	Bu
23.62	787.94	31.91	Au
24.16	805.93	13.42	Au
24.20	807.17	363.58	Bu
24.81	827.56	162.72	Bu
25.01	834.26	6.05	Au
25.05	835.69	25.76	Bu
25.06	836.01	32.18	Au
25.52	851.17	40.18	Au
25.65	855.58	18.53	Bu
25.95	865.52	159.45	Au
25.97	866.34	70.06	Bu
26.53	885.06	2.18	Bu
26.54	885.16	12.93	Au
27.69	923.68	49.06	Bu
27.74	925.29	36.85	Au
27.90	930.48	13.95	Au
27.95	932.46	169.60	Bu
28.12	938.10	209.10	Bu
28.12	938.10	17.61	Au
28.45	948.87	24.66	Bu
28.47	949.52	2.53	Au
28.76	959.40	7.91	Bu
28.77	959.64	0.68	Au
29.51	984.47	22.81	Bu
29.52	984.78	137.34	Au
29.57	986.49	16.10	Bu
29.59	986.91	3.66	Au
30.05	1002.37	42.52	Bu
30.07	1002.92	4.08	Au
31.11	1037.75	5.46	Au
31.11	1037.78	55.55	Bu

31.21	1040.94	40.17	Bu
31.22	1041.35	0.07	Au
32.24	1075.29	325.66	Au
32.27	1076.46	20.25	Bu
32.71	1091.19	208.26	Bu
32.83	1094.92	148.99	Au
33.58	1120.26	827.91	Au
33.61	1121.21	98.75	Bu
33.79	1127.11	75.86	Au
33.82	1128.27	56.57	Bu
34.56	1152.95	159.63	Bu
34.57	1153.12	16.45	Au
35.10	1170.87	228.92	Au
35.19	1173.76	40.63	Bu
35.71	1191.09	104.05	Bu
35.82	1194.77	2109.84	Au
36.40	1214.32	5.06	Au
36.41	1214.58	287.09	Bu
36.70	1224.13	23.25	Au
36.70	1224.32	190.57	Bu
37.26	1242.82	47.78	Bu
37.26	1242.92	581.41	Au
37.61	1254.62	108.67	Bu
37.61	1254.66	7.18	Au
38.27	1276.40	27.12	Bu
38.27	1276.69	257.10	Au
38.63	1288.45	1802.14	Bu
38.72	1291.57	3291.42	Au
39.32	1311.64	252.14	Bu
39.34	1312.34	119.14	Au
40.55	1352.70	27.21	Bu
40.57	1353.11	510.43	Au
40.71	1358.06	250.34	Bu
40.71	1358.08	170.78	Au
41.07	1370.02	21.71	Bu
41.09	1370.76	141.82	Au
41.48	1383.68	1141.75	Au
41.55	1386.04	24.30	Bu
41.65	1389.20	479.00	Bu
41.74	1392.22	138.87	Au
42.28	1410.31	700.73	Bu

42.37	1413.37	189.95	Au
42.94	1432.33	337.20	Bu
42.95	1432.50	1356.85	Au
43.09	1437.18	210.17	Bu
43.16	1439.61	303.39	Au
43.27	1443.48	84.54	Au
43.33	1445.38	67.34	Bu
43.54	1452.28	421.08	Bu
43.71	1458.12	689.59	Au
44.12	1471.67	336.03	Au
44.14	1472.44	41.59	Bu
44.38	1480.37	1898.78	Au
44.59	1487.48	370.62	Bu
45.00	1501.00	277.82	Au
45.03	1501.95	5.38	Bu
46.22	1541.83	1376.95	Au
46.28	1543.65	124.84	Bu
46.31	1544.86	368.12	Bu
46.35	1546.06	33.36	Au
46.85	1562.79	16.39	Au
46.89	1564.00	114.97	Bu
47.92	1598.59	17.35	Bu
47.94	1598.99	485.10	Au
48.08	1603.85	149.81	Au
48.10	1604.40	116.08	Bu
48.28	1610.50	55.62	Au
48.42	1615.12	30.53	Bu
88.78	2961.34	50.63	Bu
88.78	2961.50	0.79	Au
90.75	3027.12	8.54	Au
90.75	3027.14	18.95	Bu
91.08	3038.13	653.41	Bu
91.09	3038.33	588.31	Au
92.16	3074.19	10.72	Bu
92.16	3074.24	18.89	Au
92.94	3100.18	12.12	Au
92.95	3100.33	4.15	Bu
93.02	3102.72	58.59	Au
93.02	3102.79	89.89	Bu
93.22	3109.39	8.34	Bu
93.22	3109.53	2.42	Au

93.23	3109.65	2.12	Au
93.23	3109.68	5.66	Bu
93.82	3129.56	9.79	Bu
93.82	3129.65	8.43	Au
94.14	3140.19	2.40	Bu
94.14	3140.32	4.15	Au
94.40	3148.89	6.46	Au
94.40	3148.95	9.10	Bu
94.56	3154.10	0.05	Bu
94.56	3154.17	0.63	Au
94.78	3161.39	367.57	Au
94.78	3161.39	23.35	Bu

Table C3. Solid-state DFT simulated frequencies for PR254.

Frequency		Intensity	Symmetry
THz	cm-1		
0.87	29.12	0.57	Au
0.97	32.47	0.00	Au
1.03	34.51	0.07	Bu
1.87	62.54	3.69	Au
1.94	64.61	0.29	Bu
2.03	67.72	0.68	Bu
2.91	97.10	0.04	Au
3.40	113.55	0.42	Bu
3.47	115.81	0.01	Au
3.93	131.15	12.29	Bu
3.96	132.07	7.58	Au
5.30	176.87	0.61	Au
5.31	177.05	15.72	Bu
6.74	224.74	9.07	Bu
6.74	224.88	0.36	Au
7.06	235.33	86.25	Bu
7.06	235.41	1.57	Au
8.12	270.95	13.84	Au
8.15	271.90	11.10	Bu
8.91	297.33	1.20	Au
8.92	297.70	0.16	Bu
9.72	324.07	150.93	Bu
9.77	325.87	22.91	Au

11.95	398.70	4.63	Bu
11.98	399.71	1.61	Au
12.94	431.77	41.35	Au
12.95	431.96	131.16	Bu
14.13	471.36	85.22	Bu
14.19	473.44	49.97	Au
15.40	513.59	64.17	Au
15.43	514.59	258.39	Bu
18.22	607.92	31.94	Au
18.23	608.11	72.82	Bu
18.67	622.61	1.11	Bu
18.68	623.08	0.12	Au
20.56	685.72	59.79	Bu
20.56	685.80	36.72	Au
21.21	707.57	34.80	Au
21.21	707.60	86.16	Bu
21.28	709.68	325.66	Bu
21.36	712.34	43.31	Au
22.67	756.16	7.92	Au
22.67	756.28	35.01	Bu
23.75	792.18	152.98	Bu
23.77	792.76	9.05	Au
24.38	813.08	605.00	Bu
24.40	813.85	67.07	Au
24.63	821.56	292.90	Au
24.69	823.54	329.79	Bu
24.76	825.85	0.62	Au
24.82	827.74	851.15	Bu
27.84	928.71	26.55	Bu
27.85	928.85	0.43	Au
28.67	956.34	14.14	Bu
28.69	957.00	0.34	Au
30.03	1001.66	64.23	Bu
30.07	1003.00	169.57	Au
31.13	1038.35	55.79	Au
31.15	1039.02	41.03	Bu
32.32	1077.95	136.61	Bu
32.41	1081.13	409.31	Au
33.42	1114.85	227.81	Bu
33.46	1116.24	27.08	Au
33.71	1124.54	82.69	Au

33.72	1124.74	617.70	Bu
35.87	1196.64	22.08	Au
35.88	1196.96	72.73	Bu
36.14	1205.58	151.20	Au
36.18	1206.72	91.76	Bu
39.16	1306.07	1.20	Bu
39.19	1307.35	0.78	Au
39.73	1325.40	333.78	Bu
39.74	1325.47	0.72	Au
40.47	1349.92	15.16	Au
40.47	1350.05	295.13	Bu
42.13	1405.43	31.59	Bu
42.14	1405.58	54.18	Au
43.74	1458.92	65.29	Au
43.75	1459.41	1433.82	Bu
44.44	1482.29	841.43	Au
44.59	1487.48	453.59	Bu
46.38	1546.95	100.94	Bu
46.38	1547.15	82.70	Au
47.55	1586.25	708.76	Au
47.62	1588.46	1815.12	Bu
47.67	1590.04	105.86	Au
47.69	1590.61	1939.59	Bu
48.59	1620.82	268.16	Au
48.64	1622.51	5026.13	Bu
92.15	3073.84	272.48	Au
92.17	3074.59		Bu
93.04	3103.34	26.43	Au
93.04	3103.36	183.24	Bu
93.69	3125.32	550.22	Bu
93.70	3125.41	6.83	Au
94.06	3137.44	228.25	Bu
94.06	3137.67	11.36	Au
94.37	3147.92	0.54	Bu
94.39	3148.42	31.87	Au

Curriculum Vitae

Elyse Kleist

Phone: 717-798-2240
ekleist2000@gmail.com
linkedin.com/in/elysekleist

EDUCATION

PhD   Syracuse University, Chemistry
2020

MPhil   Syracuse University, Chemistry
2015

BS   Indiana University of Pennsylvania, Chemistry
2013
Robert E. Cook Honors College
Cum laude, Dean's List

RESEARCH EXPERIENCE

Research Assistant, Syracuse University, Syracuse, NY, USA   2020
Dissertation: <u>Characterization of Crystalline Pigments with Low-Frequency Vibrational Spectroscopy and Solid-State Density Functional Theory</u>
Advisor: Prof. Tim Korter
- Characterized solid-state behaviors of heavy-metal oxides and sulfides, copper complexes, azobenzene and diketopyrrolopyrrole dyes with low-frequency spectral methods
- Uncovered originations of low-frequency vibrational behaviors with solid-state density functional theory
- Proficient in terahertz spectroscopy, low-frequency Raman spectroscopy, and X-ray crystallography
- Catalogued spectral library of polymers
- Identified polymeric composition of plastics from the late 19th century to modernity

Research Assistant, Syracuse University, Syracuse, NY, USA
Thesis: <u>Predicting Deuterium Isotope Shifts in Small, Rigid Peptides</u>   2015
Advisor: Prof. Bruce Hudson
- Predicted nuclear magnetic isotopic shifts with quantum mechanical models
- Measured deuterium isotope effects for ^{13}C, ^{15}N, ^{17}O nuclei
- Synthesized polyenes via a reductive dimerization of vinyl iodides
- Experienced in NMR, FT-IR, and FT-Raman spectroscopies

Research Assistant, Indiana University of Pennsylvania, Indiana, PA, USA 2013
Thesis: <u>An Evaluation of Mini Gas Chromatographs in the Undergraduate Organic Chemistry Laboratory</u>
Advisor: Prof. Justin Fair

- Diversified organic chemistry laboratory curriculum with procedures employing modern analytical instruments
- Surveyed chemists across industries to identify desired skills in college graduates and compared these skills to the current curricula in the United States

PEER-REVIEWED PUBLICATIONS

Journal Publications

E. M. Kleist, T. M. Korter. Analysis of minium and vermilion mixtures with low-frequency vibrational spectroscopy. *Analytical Chemistry,* **2020,** *92*, 1211-1218.

E. M. Kleist, C. L. Koch Dandolo, J.-P. Guillet, P. Mounaix, T. M. Korter. Terahertz spectroscopy and quantum mechanical simulations of crystalline copper-containing historical pigments. *Journal of Physical Chemistry A,* **2019**. *123, 6*, 1225-1232.

J. D. Fair, **E. M. Kleist,** D. M. Stoy, A survey of industrial organic chemists: understanding the chemical industry's needs of current bachelor-level graduates. *Journal of Chemical Education,* **2014**, *91*, 2084-2092.

Journal Papers (Submitted)

A. D. Stephens, M. N. Qaisrani, M. T. Ruggiero, S. T. E. Jones, E. Poli, A. D. Bond, P. J. Woodhams, **E. M. Kleist**, L. Grisanti, R. Gebauer, J. A. Zeitler, D. Credgington, A. Hassanali, and G. S. Kaminski-Schierle. Intrinsic fluorescence in non-aromatic peptide structures is induced by collective vibrations, charge reorganisation and short hydrogen bonds, as shown in a new glutamine-related structure**.** *Science,* Submitted, 2020. Preprint Available on BioRxiv.

Journal Papers in Progress

E. M.Kleist, C. L. Koch Dandolo, J.-P.Guillet, P. Mounaix, T. M. Korter, T. Characterization of the modern pigments red 3 and 254 with terahertz spectroscopy and quantum mechanics. *In progress.*

Conference Papers

E. M. Kleist, T. M. Korter, Analysis of minium and vermilion mixtures with low-frequency vibrational spectroscopy. *44th International Conference on Infrared, Millimeter, and Terahertz Waves.* Paris, France, 2019, pp. 1-1.

E. M. Kleist, C. L. Koch Dandolo, T. M. Korter, P. Mounaix, Terahertz spectroscopy and quantum mechanical simulations of crystalline historical pigments. *43rd International Conference on Infrared, Millimeter, and Terahertz Waves.* Nagoya, Japan, 2018, pp. 1-1.

HONORS AND AWARDS

Graduate Dean's Award for Excellence in Research and Creative Work	2020
William and Audrey Madia Scholarship	2012
Chemistry Alumni Research Fund Award	2011
Robert E. Cook Honors College Enhancement Fund	2010
International Education Scholarship	2010
Board of Governors Tuition Scholarship	2009
New Economy Technology Scholarship Program SciTech Scholarship	2009

COMMUNITY SERVICE

Bellevue Farmer's Market/Feeding Neighbors Program
Co-Organizer/Volunteer, Pittsburgh, Pennsylvania, 2020-Present
- Developed program to address immediate food insecurity because of COVID-19
- Prepared, packaged, and distributed over 30,000 meals
- Managed over 75 volunteers in safely packaging meals
- Planned and regulated meal design, large food orders and delivery, enforced adherence to current ServSafe® standards

Helping Hounds Dog Rescue
Volunteer, Dewitt, New York, 2015-2018
- Recorded medical records for incoming dogs
- Trained new volunteers
- Handled difficult rescues as a member of the Behavioral Assessment Team

Alpha Chi Sigma-Bringing STEM to the Classroom
Volunteer/Co-organizer, Indiana, Pennsylvania, 2011-2012
- Promoted STEM education to elementary, middle, and high-school students
- Designed engaging presentations and demonstrations
- Organized college student volunteers

Syracuse University, Syracuse, New York   2013-2019
Teaching Assistant, Department

- Taught physical chemistry (quantum mechanics) laboratory and lecture
- Developed laboratory experiments and lectures and graded scientific reports
- Managed experimental set-up, waste disposal, pre- and post- laboratory assistance
- Moderated general chemistry lecture sections and led recitation sections
- Supervised organic chemistry laboratory sections

Indiana University of Pennsylvania, Indiana, Pennsylvania   2010-2013
Teacher's Assistant, Chemistry

- Supervised undergraduate organic and general chemistry lab sections
- Prepared instruments, reagents, and materials
- Established methods for collection and disposal of hazardous waste

PROFESSIONAL TRAINING

MSSC2018-Ab Initio Modelling in Solid State Chemistry
University of Turin, Turin, Italy, 2018

PROFESSIONAL AFFILIATIONS

Women in Science and Engineering Future Professionals Program

Alpha Chi Sigma

American Chemical Society

CONTRIBUTED TALKS

E. M. Kleist, T. M. Korter. "Analysis of minium and vermilion mixtures with low-frequency vibrational spectroscopy." *44th International Conference on Infrared, Millimeter, and Terahertz Waves.* Paris, France. 2019.

E. M. Kleist, B. S. Hudson. "Efforts towards prediction of NH(D) and CH(D) isotope effects on ^{13}C NMR spectra of *cis* and *trans* lactams via computational chemistry." 48th Midwest Theoretical Chemistry Conference. Pittsburgh, Pennsylvania. 2016.

E. M. Kleist, B. S. Hudson. "Computational and experimental studies of NH(D) and CH(D) isotopic exchange effects on ^{13}C NMR spectra of small, rigid peptides." Pacifichem 2015: Biomolecular Structure and Dynamics: Recent Advances. Honolulu, Hawaii. 2015.

E. M. Kleist, O. M. Melton, B. S. Hudson. "Effects of deuterium substitution on ^{13}C isotopic shifts in small, rigid peptides." 14th Upstate NMR Symposium. Syracuse, New York. 2015.

CONTRIBUTED POSTERS

E. M. Kleist, T. M. Korter. "Interpreting the low-frequency vibrational fingerprints of crystalline pigments" MSSC2018 - Ab Initio Modelling in Solid State Chemistry, 2018.

E. M. Kleist, T. M. Korter. "Interpreting the low-frequency vibrational fingerprints of crystalline pigments." 256th American Chemical Society National Meeting and Exposition, 2018.

E. M. Kleist, B. S. Hudson. "Prediction of multiple *cisoid* and *transoid* conformations of caprylolactam in solution by density functional theory and FTIR." 253rd American Chemical Society National Meeting and Exposition, 2017.

E. M. Kleist, B. S. Hudson. "Efforts towards prediction of NH(D) and CH(D) isotopic exchange effects on ^{13}C NMR spectra of small, rigid peptides via computational quantum chemistry." 251st American Chemical Society National Meeting and Exposition, 2016.

E. M. Kleist, B. S. Hudson. "Computation of CH and NH isotopic exchange effects on ^{13}C NMR spectra of small, rigid peptides." 250th American Chemical Society National Meeting and Exposition, 2015.

E. M. Kleist, O. M. Melton, B. S. Hudson. "Effects of deuterium substitution on ^{13}C isotopic shifts in small, rigid peptides." 248th American Chemical Society National Meeting and Exposition, 2014.

E. M. Kleist, J. D. Fair. "Evaluation of mini gas chromatographs in the undergraduate organic chemistry laboratory." 43rd Middle Atlantic Regional Meeting of the American Chemical Society, 2012.